

https://dspace.org/

Synthesis of Tungsten Oxide Nanostructures by Laser Pyrolysis

Govender, Malcolm

2012-02-01
http://hdl.handle.net/10539/11220

Downloaded from a DSpace repository. https://dspace.org/

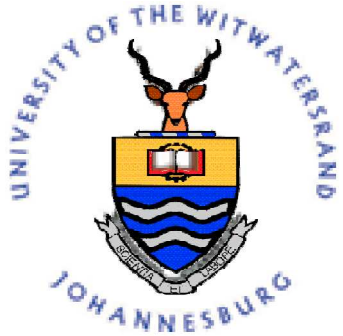
Synthesis of Tungsten Oxide Nanostructures by Laser Pyrolysis

Malcolm Govender

School of Physics

University of the Witwatersrand, Johannesburg

Republic of South Africa



7 October 2011

A thesis submitted to the Faculty of Science, University of the Witwatersrand, Johannesburg, in the Republic of South Africa, in fulfillment of the Degree of Master of Science.

Abstract

This dissertation discusses the synthesis method known as laser pyrolysis. The theory on laser pyrolysis has been inferred since 1975, but it is insufficient in predicting the products that can be formed. This is due to the use of a laser, which leads to indecisive reaction pathways from precursor to product. In this work, the laser wavelength and power are varied to initiate a starting point in understanding the complex nature of the laser–precursor interaction, in addition to studying the resulting nanomaterial that is formed by the corresponding laser pyrolysis parameters. The results are justified based on linear and nonlinear optical processes, as well as photophysical and photochemical processes. Experiments to produce tungsten trioxide nanowires were conducted, but similar products could not be achieved, due to the difficulty in emulating ‘sensitive’ variables such as gas pressure and flow rates. However, it was discovered for the first time using this method that six-sided tungsten oxide “stars” can be grown.

To my mum

Declaration

I declare that this thesis is truly my own original, unaided work. It is being submitted for the Degree of Master of Science to the University of the Witwatersrand, Johannesburg, South Africa. This work has not been submitted for any degree or examination in any other university or academic institution.

_____

This

_____

day of

_____

in the year of our Lord

_____

Acknowledgements

There are many people that I would like to thank, and in particular:

- My co-supervisor, Dr. Bonex Mwakikunga for the support, encouragement and advice.
- My supervisors, Prof. Andrew Forbes and Prof. Elias Sideras-Haddad for the guidance and mentorship, and for the invaluable input in putting this work together.
- My lab partner, Lerato Shikwambana, it was a pleasure working with him.
- Special thanks to Darryl Naidoo for having embarked on this journey with me, and for the support, help and sharing all the great times we've had together these past two years.
- My colleagues at the National Laser Centre (NLC) who are too many to mention, it was an honour and pleasure to work alongside some of the greatest minds in the field.
- NLC for making this work possible.
- My aunt, Yogie, for being there for me when I needed her the most.
- My parents, for bringing me up with love and respect.
- My brother, for taking interest in my work.
- My family, for always believing in me and for the constant prayers that pulled me through.

Table of Contents

List of Figures ..... **x**

List of Tables ..... **xv**

List of Acronyms ..... **xvi**

List of Outputs by Candidate ..... **xviii**

1 Literature Review **1**

1. Introduction **1**

1.1 Nanoscience and Nanotechnology **2**

1.1.1 Instruments used to study Nanomaterials 3

1.1.2 Ways of Synthesizing Nanomaterials 3

1.2 Tungsten Trioxide (WO_3) **5**

1.2.1 Material Properties tend to differ at the Nanoscale 6

1.2.2 Characteristics of Tungsten Oxides 7

1.2.3 Production of nano-WO_3 8

1.3 Laser Pyrolysis **10**

1.3.1 Theory of Laser Pyrolysis 10

1.3.2 The Application of Laser Pyrolysis 11

2 Laser–Matter Interaaction **13**

2.1 Linear and Nonlinear Optical Processes **13**

2.1.1 Linear and Nonlinear Polarization of a material system induced by an optical field 13

2.1.2 Linear and Nonlinear Absorption of a material system 14

2.1.3 Open and Closed Two-level atom 15

2.2 Photochemistry and Photophysics **19**

2.2.1 Photophysical Processes 19

2.2.2 Photochemical Processes 21

2.2.2.1 Multiphoton Infrared Excitation 22

2.3 Summary **24**

3 Characterization Techniques 25

3.1 Introduction 25

3.2 Fourier Transform Infrared Spectroscopy (FTIR) 25

3.3 Raman Spectroscopy 28

3.4 X-ray Diffraction (XRD) 31

3.5 The Transmission Electron Microscope (TEM) 33

3.6 The Scanning Electron Microscope (SEM) 35

3.7 Energy Dispersive X-ray Spectroscopy (EDS/EDX) 37

3.8 Summary 40

4 The Carbon Dioxide (CO_2) Laser 41

4.1 Introduction 41

4.2 Theory of CO_2 Laser operation 42

4.3 The PL6 CO_2 Laser 44

4.4 Characterization of Lasers 45

4.4.1 Properties of Gaussian-like Beams 45

4.4.2 Two Experimental Methods used to Characterize Lasers 47

4.4.2.1 The Scanning Slit Method 47

4.4.2.2 The Pyrocam Method 49

4.4.3 Results of the Laser Parameters 50

4.5 Laser Polarization 55

4.6 Determination of the Laser Wavelengths 57

4.6.1 The Experimental Setup used to determine the Wavelength Spectrum of the PL6 Laser 57

4.6.2 Results for the Wavelength Spectrum of the PL6 Laser 59

4.7 Summary of Laser Characterization 59

4.8 Conclusion 60

5 Experimental 61

5.1 Introduction 61

5.2 Methodology and Setup of the Laser Pyrolysis method 62

5.3 Estimation of the Laser Interaction Volume 66

5.4 The Chemical Precursor 66

5.4.1 Preparation of Tungsten (VI) Ethoxide Precursor 66

5.4.2 Properties of Tungsten (VI) Ethoxide Precursor 68

5.4.3 Spectroscopic analysis of Tungsten (VI) Ethoxide Precursor 68

5.5 Summary 69

6 Results and Discussion 70

6.1 Laser Pyrolysis carried out at varying Wavelength and Power 70

6.2 Sample Morphology and Topography 72

6.2.1 Wavelength Variation 72

6.2.2 Power Variation 80

6.3 Sample Phase Composition and Crystal Structure 82

6.4 Sample Vibrational Information and Molecular Identification 87

6.5 Repetition experiments at the Higher Power Regime 90

6.6 Conclusion 96

7 Conclusion and Future Work 98

Appendix A 102

Appendix B 118

Appendix C 128

Appendix D 135

Appendix E 145

Appendix F 147

Appendix G 157

Appendix H 160

References 167

List of Figures

Figure 1.1 Scanning electron micrographs of less-common and hierarchical structures of **(a)** nanopine (Fe_2O_3), **(b)** nanowheels (Pt), **(c)** nanoflower (ZnO) and **(d)** a nanotree (ZnO) 4
Figure 1.2 Scanning electron micrograph of post-annealed tungsten trioxide nanowires synthesized by laser pyrolysis showing a thin film that has flaked up into slabs between which are numerous nano-wires. Insets: **(a)** shows a close look at the nanowires in between the slabs, **(b)** zooms in onto the nano-wire area and **(c)** display one nano-wire's end. 5
Figure 1.3 The current-voltage (*I-V*) characteristics of nanometre-sized WO_3 (nm-WO_3) and micrometre-sized WO_3 (μm-WO_3) 6
Figure 1.4 Crystallite size effect on temperature phase transition. α refers to tetragonal phase, β refers to monoclinic phase and γ refers to orthorhombic phase of WO_3 7
Figure 1.5 The increasing trend of laser pyrolysis publications over the past three decades . 10
Figure 1.6 Representation of the maximum productivity predicted by the model based on aerosol theory and the experimental conditions required for the production of iron nanocrystals of a given size 12

Figure 2.1 Near-resonant excitation of a two-level atom..... 15
Figure 2.2 Relaxation processes of the closed two-level atom 16
Figure2.3 Relaxation processes of the open two-level atom 17
Figure 2.4 Molecular orbital energy level diagram, which shows the various photophysical processes that may be involved in a molecule 20
Figure 2.5 Energy levels and transitions involved in the multiphoton infrared dissociation of a diatomic molecule 23

Figure 3.1 Illustration of the layout and components of an interferometer used in FTIR 26
Figure 3.2 FTIR transmittance spectrum of ethanol, showing the characteristic peaks arising from the different chemical bond frequencies 28
Figure 3.3 An illustration of the layout and components of a Raman spectrometer..... 30
Figure 3.4 Raman spectrum of WO_3, showing the characteristic peaks arising from the vibrational modes of the compound..... 30

Figure 3.5 Incident x-rays diffracting off the planes in a crystal at distinct angles of θ depending on d' 31
Figure 3.6 The components of a diffractometer with the beam path in the $\theta/2\theta$ mode..... 32
Figure 3.7 XRD diffractogram or spectrum of WO_3, showing the characteristic diffraction angles and Miller indexes. The broad underlying peak results from the substrate on which the WO_3 sits 33
Figure 3.8 An illustration of the layout and components of a transmission electron microscope 34
Figure 3.9 TEM micrographs of a **(a)** nanorod and **(b)** nanotube..... 35
Figure 3.10 An illustration of the layout and components of a scanning electron microscope 36
Figure 3.11 A secondary electron mode SEM micrograph of various tungsten oxide nanostructures 37
Figure 3.12 The electron orbits of an atom with the electron shells designated by K, L and M, with quantum numbers *n* equal to 1, 2 and 3, respectively. A K-shell electron is excited to the empty M-shell, and an L-shell electron fills the K-shell vacancy in a de-excitation process.. 38
Figure 3.13 A schematic diagram of an EDX detector and its signal processing circuitry 39
Figure 3.14 An EDX spectrum of a tungsten oxide, where the tungsten peaks are represented by W and the oxygen peak are represented by O. The carbon (C) results from carbon-coating the sample to make it conductive, and the sodium (Na) and silicon (Si) are present in the substrate 40

Figure 4.1 The properties that distinguish **(a)** white light from **(b)** laser light..... 41
Figure 4.2 An illustration of the three possible vibrational modes of the CO_2 molecule..... 42
Figure 4.3 The three energy levels of the CO_2 molecule with the subdivided levels caused by rotations in the vibrating molecule and also shown here are the lasing transitions from two of the resonant modes..... 43
Figure 4.4 A picture of the PL6 laser, power supply and the cylinder containing the CO_2-N_2-He gas mixture 44
Figure 4.5 An illustration of a Gaussian intensity profile over an arbitrary radial distance... 45
Figure 4.6 A schematic diagram of beam propagation through a lens 47
Figure 4.7 A schematic of the setup used to characterize the CO_2 laser beam using a thin slit. The inset shows the slit size relative to a South African one rand coin..... 48

Figure 4.8 The setup used to characterize the laser beam using a pyrocam. The inset shows a picture of the pyrocam with a chopper attached to the front of it 49
Figure 4.9 An image taken by the pyrocam showing the heat distribution of the beam by the different colours and the intensity distribution on the x and y axes are also shown 50
Figure 4.10 (a)-(b) Plots of the power for varying slit positions at various propagation distances between the focusing mirror and thin slit 51
Figure 4.10 (c)-(d) Plots of the power for varying slit positions at various propagation distances between the focusing mirror and thin slit 52
Figure 4.11 The second-order quadratic fit from the data of the pyrocam method 53
Figure 4.12 The picture shows the layout and beam propagation through the windows in an attenuator and the inset shows a home-made attenuator 56
Figure 4.13 The total intensity transmission for the attenuated angles for the theoretical, normalized experimental data and the fitted theoretical curves for the experimental data of the PL6 laser 56
Figure 4.14 A schematic of the setup used to determine the wavelength spectrum 57
Figure 4.15 A picture of CO_2 Spectrum Analyzer (16-A) from Macken Instruments 58
Figure 4.16 A picture of CO_2 Spectrum Analyzer's display screen with the cover on the casing opened 58
Figure 4.17 The wavelength spectrum of the PL6 CO_2 laser 59

Figure 5.1 A cross-section of the reaction chamber during laser pyrolysis using the cross flow geometry 61
Figure 5.2 The reaction chamber inside which laser pyrolysis is carried out 62
Figure 5.3 (a) The inside of the chamber cap 63
Figure 5.3 (b) A close-up of the three-way nozzle 64
Figure 5.4 The aerosol generator holds the precursor liquid, and argon gas is passed through the bottom inlet creating a fine aerosol that emerges from the top 64
Figure 5.5 The setup used to carry out laser pyrolysis 65
Figure 5.6 The pictures show the colour changes as the reaction proceeds to form tungsten (VI) ethoxide precursor 67
Figure 5.7 The FTIR spectrum of the tungsten ethoxide precursor (blue) and pure ethanol (green). The shaded region represents the wavelength range of the CO_2 laser and the dashed red line represents the CO_2 laser's 10.6 μm wavelength 69

Figure 6.1 The varying laser parameters are represented by the respective points on the graph, used to investigate the effects on the morphology and chemical composition of the products 70
Figure 6.2 The comparison of the FTIR transmittance spectrum of the tungsten ethoxide precursor and the CO_2 laser radiation absorbance data of tungsten (VI) ethoxide as a function of wavelength 72
Figure 6.3 (a) The annealed sample prepared at the 9.22 µm wavelength and 51.2 W/cm^2 .. 73
Figure 6.3 (b) The EDX spectrum on the area of the sample prepared at the 9.22 µm wavelength and constant power density of 51.2 W/cm^2, which shows the presence of calcium (Ca), magnesium (Mg), carbon coating (C), sodium (Na), silicon (Si) and sulphur (S), which most probably come from the Corning glass. The oxygen (O) could have come from the substrate and the sample and tungsten (W) results from the sample 74
Figure 6.4 The average spherical particle sizes as a function of wavelength at the 51.2 W/cm^2 power density 78
Figure 6.5 (a) A TEM micrograph showing a nanorod and **(b)** the EDX spectrum taken of the rod 79
Figure 6.6 The average spherical particle sizes as a function of power density at the 10.6 µm wavelength 81
Figure 6.7 The XRD spectrum for the post-annealed sample, prepared at the 9.22 µm wavelength and 51.2 W/cm^2 power density 83
Figure 6.8 A zoomed in view of the most intense XRD peak of Figure 6.7 with a Gaussian fit to this peak. The full width at half maximum, and the angle at which the peak is most intense, are then extracted and converted to radians 85
Figure 6.9 The particulate sizes for the samples shown in the SEM micrographs above, were calculated from the XRD spectra for the respective samples and Scherrer's formula, for the various **(a)** wavelengths at the 51.2 W/cm^2 power density and **(b)** power densities at the 10.6 µm wavelength 86
Figure 6.10 The Raman spectrum of a cleaned corning glass substrate 88
Figure 6.11 The Raman spectrum for the post-annealed sample, prepared at the 9.22 µm wavelength and 51.2 W/cm^2 power density 89
Figure 6.12 SEM micrographs of the pre-annealed sample, at 5000 times magnification, prepared at the 10.6 µm wavelength and power density of 2.2 kW/cm^2 92

Figure 6.13 SEM micrographs (×11230) of the post-annealed sample showing the stars that formed during annealing, prepared at the 10.6 µm wavelength and power density of 2.2 kW/cm^2 93
Figure 6.14 SEM micrographs of the post-annealed sample showing structures growing between slabs, at 10130 times magnification, prepared at the 10.6 µm wavelength 94
Figure 6.15 The XRD spectrum for the post-annealed sample containing the stars, slabs and the growths between the slabs 95
Figure 6.16 The Raman spectrum for the post-annealed sample containing the stars, slabs and the growths between the slabs 96

List of Tables

Table 4.1. The parameters for the PL6 laser obtained from the pyrocam method and the parameters for the Synrad laser obtained from the scanning slit method 60

Table 6.1. The results obtained from the XRD spectra for the varied set of laser parameters 84

Table 6.2. The results obtained from the Raman spectra for the varied set of laser parameters 90

List of Acronyms (*in order of appearance*)

SANi	South African Nanotechnology Initiative
Nanotech	Nanotechnology
XRD	X-ray diffraction
TEM	Transmission electron microscpe
SEM	Scanning electron microscope
EDX/EDS	Energy dispersive x-ray spectroscopy
STM	Scanning tunnelling microscope
AFM	Atomic force microscope
FTIR	Fourier Transform Infrared Spectroscopy
UV	Ultraviolet/visible/near infrared
FET	Field-effect transistor
$\mathcal{F}(\delta)$	Fourier Transform
ω	Frequency of a monochromatic light
d	Sample thickness
ϑ	Induced dipole moment
α_0	Weak-field absorption coefficient
t	Measure of time
$\vec{P}(t)$	Polarization
ψ_0	Polarizability
E_0	Incident electric field amplitude
Q_0	Maximum physical displacement of atoms about their equilibrium position
h	Planck's constant
λ	Wavelength of light
p	Momentum
m	Mass
v	Velocity
Z	Atomic number
d'	Interplanar spacing
2θ	Diffraction angle
CO_2	Carbon dioxide

J	Rotational quantum number
TEM_{00}	Fundamental Transverse Electromagnetic Mode
I	Laser beam intensity after interaction with matter
I_0	Laser beam incident intensity
P_0	Peak power density
ρ	Radial position
z	Distance on the laser beam propagation axis
$\omega(z)$	Beam radius at propagation distance z
ω_0	Beam waist
z_0	Distance on the laser beam propagation axis where the beam waist is located
z_R	Rayleigh range
M^2	Laser beam quality or propagation factor
φ	Laser beam divergence angle
ZnSe	Zinc selenide
Cu	Copper
Mo	Molybdenum
θ_B	Brewster's angle
θ_b	Angle that satisfies Bragg's law
n_1, n_2	Refractive indices
HeNe	Helium-Neon
c	Speed of light
pH	Measure of acidity or alkalinity of a solution
l	Nozzle diameter from which the precursor exits
sccm	Standard cubic centimetres per minute
Tr	Trace of an n-by-n square matrix
Im	Image of a subspace

List of Outputs by Candidate

Posters presented:

Govender, M., Shikwambana, L., Forbes, A., Mwakikunga, B.W., and Sideras-Haddad, E. Photochemical investigation of tungsten trioxide nano-wires synthesized by laser-induced pyrolysis, SAIP, UKZN, Durban Westville , 2009.

Govender, M., Shikwambana, L., Forbes, A., Mwakikunga, B.W., Sideras-Haddad, E., and Erasmus, R.M. Morphological and structural properties of tungsten oxide ($WO_{3\pm x}$) nanostructures synthesized by laser pyrolysis at controlled laser power and wavelength, Villa-Conference on Interaction Among Nanostructures, Santorini, Greece, 2010.

Govender, M., Shikwambana, L., Forbes, A., Mwakikunga, B.W., Sideras-Haddad, E., and Erasmus, R.M. Optimizing the formation of WO_{3-x} nanostructures: stars and spheres, SAIP, CSIR-ICC, Pretoria, 2010.

Orals presented:

Govender, M., Shikwambana, L., Forbes, A., Mwakikunga, B.W., Sideras-Haddad, E., and Erasmus, R.M. Synthesis of Tungsten Trioxide (WO_3) nanostructures by Laser Pyrolysis, Lasers in Chemistry, Irene, Pretoria, 2010.

Govender, M., Shikwambana, L., Forbes, A., Mwakikunga, B.W., Sideras-Haddad, E., and Erasmus, R.M. Optical absorption properties of Tungsten (VI) Ethoxide precursor by laser pyrolysis at controlled laser power and wavelength, Optical Techniques and Nano-Tools for Material and Life Sciences, Minsk, Belarus, 2010.

Publication:

Govender, M., Shikwambana, L., Mwakikunga, B.W., Sideras-Haddad, E., Erasmus, R.M., and Forbes, A. Formation of tungsten oxide nanostructures by laser pyrolysis: stars, fibres and spheres, *Nanoscale Research Letters*, **6** (166), 2011, pp. 1-8. *See Appendix H*

Chapter 1

Literature Review

1. Introduction

The focus of this work was to set up the nanosynthesis method known as laser pyrolysis, to synthesize thin films and nanostructures of tungsten oxide. The method produces nanomaterials of high quality and purity [1], by intersecting a laser beam with a chemical precursor. The motivation for using the laser pyrolysis method was the observation of tungsten trioxide nanowires and nanorods by our group in 2008 [2]. Tungsten trioxide is a "smart material" which finds potential applications in sensor devices, and nano-sized tungsten trioxide introduces unique properties at ambient conditions [3]. Besides producing different shaped nanostructures, understanding of the dynamics of the laser–precursor interaction could reveal the potentials of this method for producing various nano-materials.

To bring this work into perspective, a review is first carried out on the field of nanoscience and nanotechnology, the properties of tungsten trioxide and the laser pyrolysis method. Then a detailed look is given to laser–matter interaction which helps to understand the possible processes that take place when the laser beam is intersected by the chemical precursor and forms the crux of this work. The setup and operation of the instruments used to identify and characterize the synthesized products is covered in detail. The laser used to carry out laser pyrolysis is then introduced and much detail is given to determine all the characteristics of this laser. A comprehensive analysis is given of the experimental setup and shows how the laser and chemical precursor are brought together to carry out laser pyrolysis. Finally, the results obtained from the laser pyrolysis parameters are given and discussed with respect to the processes involved in the laser–matter interaction.

1.1 Nanoscience and Nanotechnology

Nanoscience and nanotechnology are exciting and cutting edge fields of research dealing with the study, synthesis and development of materials with special characteristics. The vast applications of these materials are of immense interest and range from nano-electronics and nano-mechanics, to next generation sensors and bio-medical applications. In South Africa, it is regarded as an emerging field, with isolated projects having been carried out in the past decade. In 2002, the South African Nanotechnology Initiative (SANi) was founded [4]. This formally introduced nanoscience and nanotechnology as a research field in South Africa, providing a network for scientists, engineers and academics from universities, science councils and the private sector to interact and collaborate on projects.

Nanoscience refers to the study of very tiny structures, having physical dimensions in the range of tens to hundreds of nanometres (10^{-9} m) [5]. Scientists in this area, work with atoms and molecules rather than bulk materials. When working on the nanometer scale, physical properties such as quantum mechanical and thermodynamic properties play an important role. By studying the individual molecular properties, advanced nanostructured materials having new and amazing characteristics, can be synthesised.

Nanotechnology is closely related to nanoscience and involves the actual manipulation, application and development of nanometre-sized structures for specific technologies and applications [6]. When the properties of nanostructures are realised, attention is drawn to nanotechnology. Richard Feynman was one of the first scientists to introduce the concept of nanotechnology in 1959, in his famous talk entitled “There’s Plenty of Room at the Bottom” [7]. He spoke about developing a process that could manipulate individual atoms and molecules using special sets of tools to construct and control other proportionally smaller sets.

Nanotechnology is very common in electronics and device physics, because there is a trend to engineer smaller and more compact solutions. Nanomaterials have found useful applications in many fields from medicine to energy production. However, since nanomaterials and nanoparticles are not readily detectable, many concerns have been raised regarding their

toxicity and environmental impacts, and to whether or not special regulations on nanotechnology need to be implemented [8].

1.1.1 *Instruments used to study Nanomaterials*

The tools used in nanoscience and nanotechnology are of great importance, since they enable us to 'see' and 'touch' at this scale. These instruments are also used to measure, observe, and manipulate atoms and molecules [5]. Electron microscopy is a well known technique used to obtain the topography of nanomaterial at very high magnification and resolution. Energy dispersive x-ray spectroscopy (EDS or EDX), uses x-ray spectroscopic capability for identifying the elemental composition of the material. W. C. Röntgen and M. von Laue developed a technique known as x-ray diffraction (XRD) which is useful for analyzing the three-dimensional crystal structure of materials [5]. The scanning tunnelling microscope (STM) and atomic force microscope (AFM) was developed by G. Binnig and H. Rohrer [5]. STM is used to determine the topological map of a conductive surface and AFM is used to image, measure and manipulate nanostructures. All these techniques have improved drastically over the years to the point where the instruments are commercially available.

1.1.2 *Ways of Synthesizing Nanomaterials*

The two main approaches used for the synthesis of nanostructured materials are the bottom-up approach and the top-down approach. The bottom-up approach uses atoms and molecules as the starting species that are chemically constructed to the nanometre scale while the top-down approach uses larger particles that are physically disintegrated to the nanometre scale. The approach that will be considered in this study is the bottom-up approach.

Some of the bottom-up techniques adopted to synthesize nanostructured materials to date are vapour condensation and gas-phase synthesis [9], plasmochemical synthesis [10] (which includes the laser pyrolysis technique), deposition from colloidal solutions [11], conventional pyrolysis [12], mechanosynthesis [13], detonation-induced synthesis [14], self-propagating high-temperature synthesis [15] and nanopowder compaction [16]. The top-down techniques include amorphous alloy crystallisation [17], severe plastic deformation [18], Coulomb explosion [19] and nanolithography [20]. The nanostructured materials that these techniques

can produce are nanowires [21], nanorods [22], nanobelts [23], nanotubes [24], nanoribbons [25], nanoflowers [26] and other hierarchical structures [27] like those pictured in Figure 1.1.

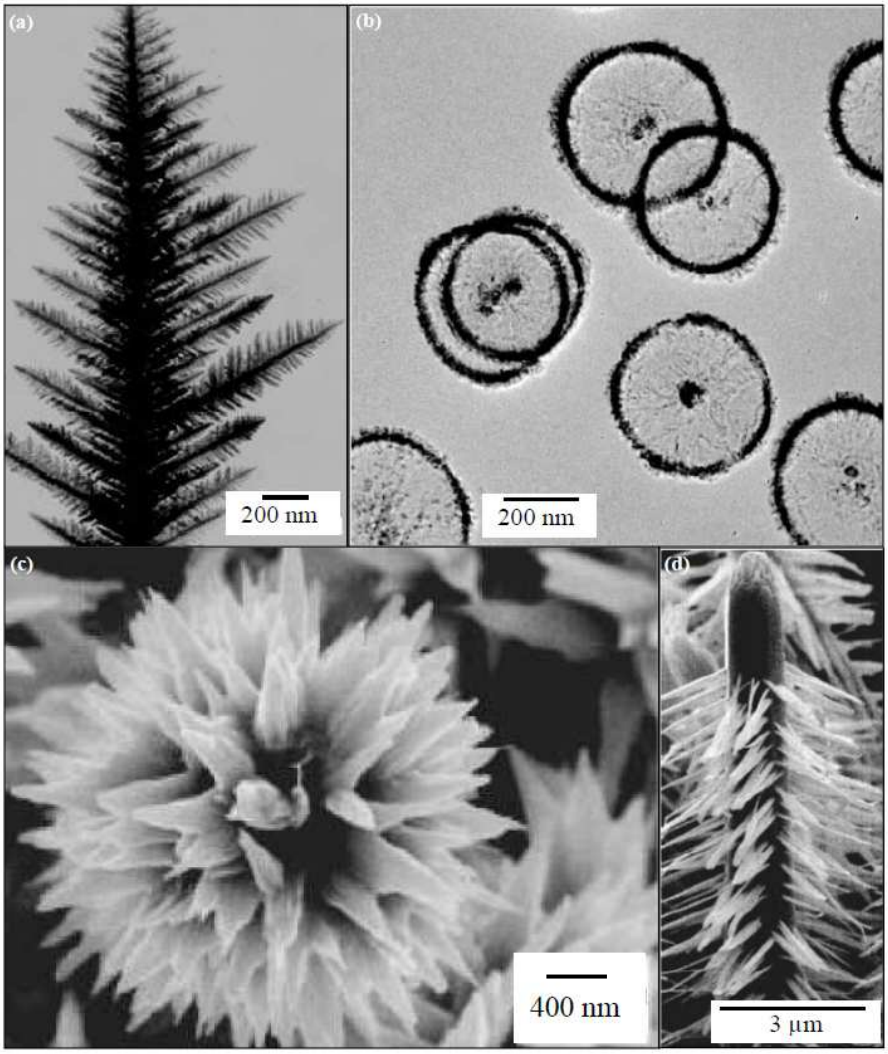


Figure 1.1 Scanning electron micrographs of less-common and hierarchical structures [27] of **(a)** nanopine (Fe_2O_3), **(b)** nanowheels (Pt), **(c)** nanoflower (ZnO) and **(d)** a nanotree (ZnO).

The type of nanomaterials studied here are thin films, which are characterized as two-dimensional quantum structures with length and width but without apparent thickness. The production of thin films of tungsten trioxide can be used to manufacture sensor devices, but it was also found that tungsten trioxide nanowires, pictured in Figure 1.2, could be grown within the film during annealing [2, 21], which introduces other interesting properties. Nanowires are defined as structures that have diameters constrained to tens of nanometers and arbitrary length, and represent the smallest objects for the efficient transport of electrons and excitons [28].

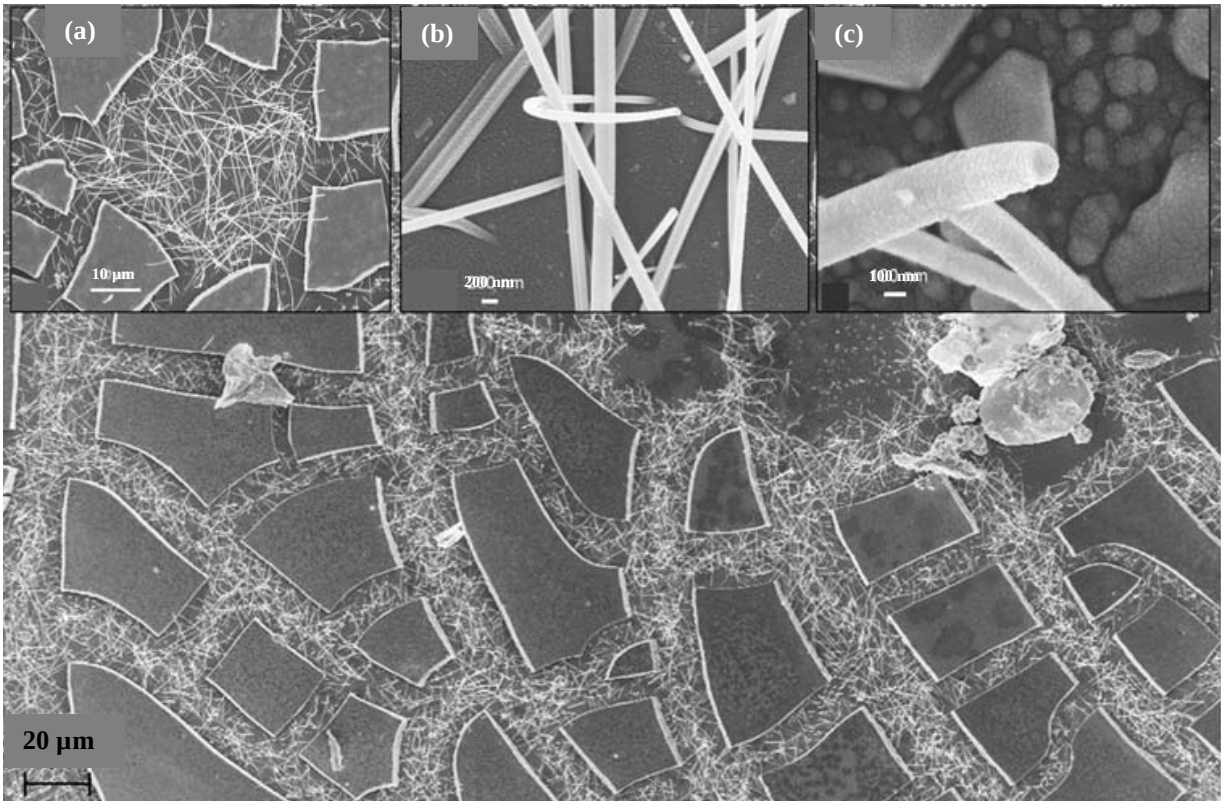


Figure 1.2 Scanning electron micrograph of post-annealed tungsten trioxide nanowires synthesized by laser pyrolysis showing a thin film that has flaked up into slabs between which are numerous nano-wires [21]. Insets: **(a)** shows a close look at the nanowires in between the slabs, **(b)** zooms in onto the nano-wire area and **(c)** display one nano-wire's end.

Thin films fall under the group known as 'Advanced Materials' [5], which are usually tougher, harder, more durable and elastic when compared to conventional materials. The other interesting properties of advanced materials include electrochromic, gasochromic and photochromic properties, and the materials that exhibit these properties are so-called 'smart materials'. Smart materials have the ability to reversibly change its colour or transparency in response to an electric current, certain gases or electromagnetic radiation, and tungsten trioxide is one such compound that is known to exhibit these properties [2].

1.2 Tungsten Trioxide (WO_3)

Tungsten trioxide (WO_3) is yellow in colour with a temperature dependent crystalline structure. At temperatures between 17^{o}C and 330^{o}C, it exhibits its most common monoclinic structure [29]. WO_3 finds application in the production of 'smart windows', which is a special type of tinted window. A thin coating of WO_3 on electrically switchable glass can change

light transmission through the window with an applied voltage, which essentially controls the amount of heat and light passing through it [30]. WO_3 can also be used in gas sensors, fireproofing fabrics [31] and pigments [32]. The electrochromic property, as well as the gasochromic and photochromic properties of WO_3, can be explained using the colour bleach process [33]. The colour bleach process involves a redox reaction of the thin films and the injection or ejection of either a cation or an anion and an electron. The material thus behaves like a mixed conductor with thinner films having faster bleaching processes.

1.2.1 *Material Properties tend to differ at the Nanoscale*

WO_3 is known to occur naturally as a hydrate [34] but the need for an appropriate, inexpensive and effective synthesis method is required to produce high quality yield within a specific nano-size scale. Figure 1.3 illustrates how micrometre-sized and nanometre-sized tungsten trioxide influences the electrical properties, owing to the ironic relaxation polarization mechanism [35].

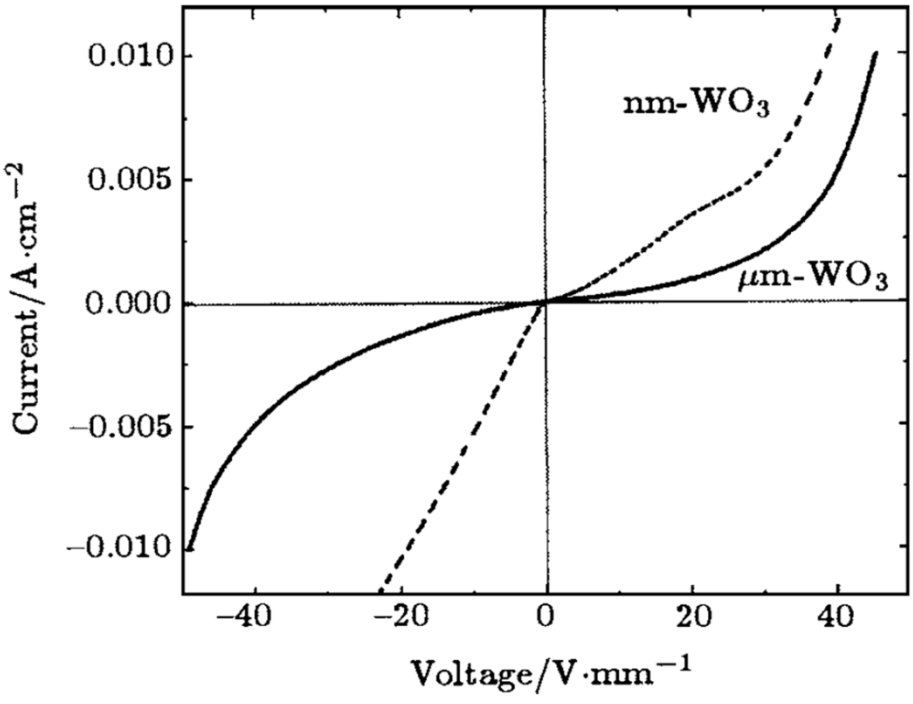


Figure 1.3 The current-voltage (*I-V*) characteristics of nanometre-sized WO_3 (nm-WO_3) and micrometre-sized WO_3 (μm-WO_3) [35].

Figure 1.4 summarizes the WO_3 phase transitions from Raman spectroscopy as a function of temperature. The results conclude that the larger particle sizes require higher temperatures to induce a phase change [3], and so it would be advantageous to produce materials that undergo phase changes closer to room temperature.

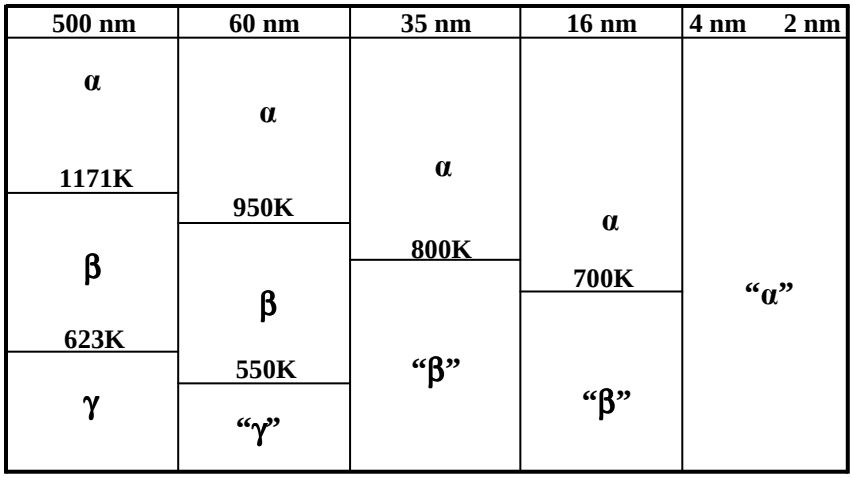


Figure 1.4 Crystallite size effect on temperature phase transition. α refers to tetragonal phase, β refers to monoclinic phase and γ refers to orthorhombic phase of WO_3 [3].

The change in transition temperature for the phase changes can be explained using the Gibbs-Thomson relationship [3]. The Gibbs-Thomson relationship relates the lowering of the melting temperature ($\Delta T = T - T^0$) to the radius (in nm) of the crystals by,

$$\frac{\Delta T}{T^0} = \frac{2V_\alpha}{\Delta H_{\alpha-\beta}} \sigma \frac{1}{r}, \qquad (1.1)$$

where V_α is the molar volume of the crystalline phase, $\Delta H_{\alpha-\beta}$ is the free molar melting enthalpy, σ is the liquid–solid interfacial energy, and r is the radius of the small crystals.

There is more evidence of substantial differences between a nanomaterial and its bulk material. For instance, nanoparticles interact with each other in a different fashion from the bulk, because the nanoparticle sizes are comparable to the distances at which interactions occur in electron, phonon and magnon subsystems. Furthermore, the atomic-molecular structures of the energetic nanoparticles do not attain thermodynamic equilibrium. The properties of same-sized nanoparticles are dependent on synthesis conditions and the temperature variation during synthesis [7]. The energy gap of nano-sized WO_3 is found to be

1.5 eV which is substantially lower than bulk WO_3 energy gap of 2.6-3.5 eV [36]. The nano-sized WO_3 offers better quality and catalytic stability in some applications compared to the bulk material [37].

1.2.2 *Characteristics of Tungsten Oxides*

Tungsten oxides can occur in several stoichiometric and non-stoichiometric compounds with the composition WO_{3-x} ($0.1 \leq x \leq 1$), known as Magneli phases [38], which appear with rather similar structures [10, 39]. These compounds can be verified using spectroscopic techniques such as Fourier Transform Infrared (FTIR) spectroscopy and Raman spectroscopy. FTIR Spectroscopic analysis of thin films and nanostructures of tungsten trioxide [10, 33, 40, 41] shows a W=O vibrating mode between 950-990 cm^{-1} wavenumbers, a W–O–W vibrating mode between 600-780 cm^{-1} wavenumbers and a W–O–W vibrating mode at 806 cm^{-1} wavenumber. It should be noted that the vibrational modes are particle size dependent so the wavenumbers can up or down-shift slightly as a result of Heisenberg's Uncertainty Principle. Raman studies show that the fundamental WO_3 vibrational mode is found between 705-715 cm^{-1} and 805-815 cm^{-1}. The O–W–O stretching mode is found between 260-274 cm^{-1} and 327-334 cm^{-1} wavenumbers [10, 37]. XRD analysis suggests that the Miller indices for nanorod growth is along the (0 2 0) plane [25] and nanowire growth is along the (0 1 0) plane [26]. This is of interest for the prediction of a scheme for the growth of nanorods and nanowires.

1.2.3 *Production of nano-WO_3*

In recent years, many techniques for the production of WO_3 nanostructures and films have been introduced and extensively studied. Reactive radio-frequency magnetron sputtering deposition of pure tungsten, using a plasma of argon as carrier gas and oxygen as reactive gas, is one of the most successful techniques for producing WO_3 thin films and nanowires [42]. The pressure and gas flow rates of this technique influence the properties of the thin films.

The sol-gel technique [37], also known as chemical solution deposition, is a wet-chemical technique that is primarily used to fabricate metal oxide materials. This method requires a lower pH for faster aggregation of the nanostructures.

Simple pyrolysis [43] involves the recrystallization of a tungsten containing precursor in a hot organic solvent. The crystals are then heated in a furnace for three hours at 450^{o}C to produce the tungsten trioxide nanorods.

Solvothermal synthesis [39, 44] is conducted in a stainless steel autoclave with the starting precursor solution contained in it. The autoclave is placed in a furnace for six hours at 200^{o}C to initiate synthesis of the nanowires. By varying the reaction temperature, reaction time, solvent type, surfactant type and precursor type, it is possible to control the shape, size distribution, surface area and crystallinity of the product. It is believed that a lower solution concentration leads to lower supersaturation of the precursor and thus promotes the growth of tungsten oxide nanowires [39, 44].

Ultrasonic spray pyrolysis [45] uses a transducer that produces ultrasound waves, which are focused on the surface of the precursor. This converts the liquid precursor into a vapour of ultra-small droplets. The vapour is carried by argon gas into a quartz tube which is attached to a furnace. The vapour is annealed in the high temperature region of the furnace, and the product is collected on a substrate at the exit of the quartz tube. The vapour is annealed for 17 hours at different temperatures between 100^{o}C and 700^{o}C. It was observed that at temperatures below 650^{o}C, tungsten oxide nano-wires were grown probably due to Ostwald ripening.

The laser pyrolysis technique [2, 21] which will be explained in detail in the next section, involves the interaction between a laser beam and a precursor to induce a chemical reaction. The resulting “ablated material” is then placed in a furnace for 17 hours at 500^{o}C. The laser power, laser wavelength, precursor concentration, precursor flow rate and annealing conditions influence the size, shape and composition of the synthesized tungsten oxide.

1.3 Laser Pyrolysis

Laser pyrolysis was first reported by Bachman *et. al.* [46] in 1975. In 1981, Haggerty and Cannon [1] reported on an improved laser pyrolysis setup. As the synthesis technique's potential increased, the number of publications also increased over the years until 2006. The decrease in trend since 2006 could be owed to the complex nature of using a laser for material synthesis. Some of the nanomaterials that have been produced are tungsten [47], tungsten oxides [2, 21, 48], vanadium oxides [48, 49], ceramics [50-55], iron oxides [56-60], titanium oxides [61-65], silicon [66-69] and carbon [70-76] have been synthesized with enhanced properties over other synthesis methods.

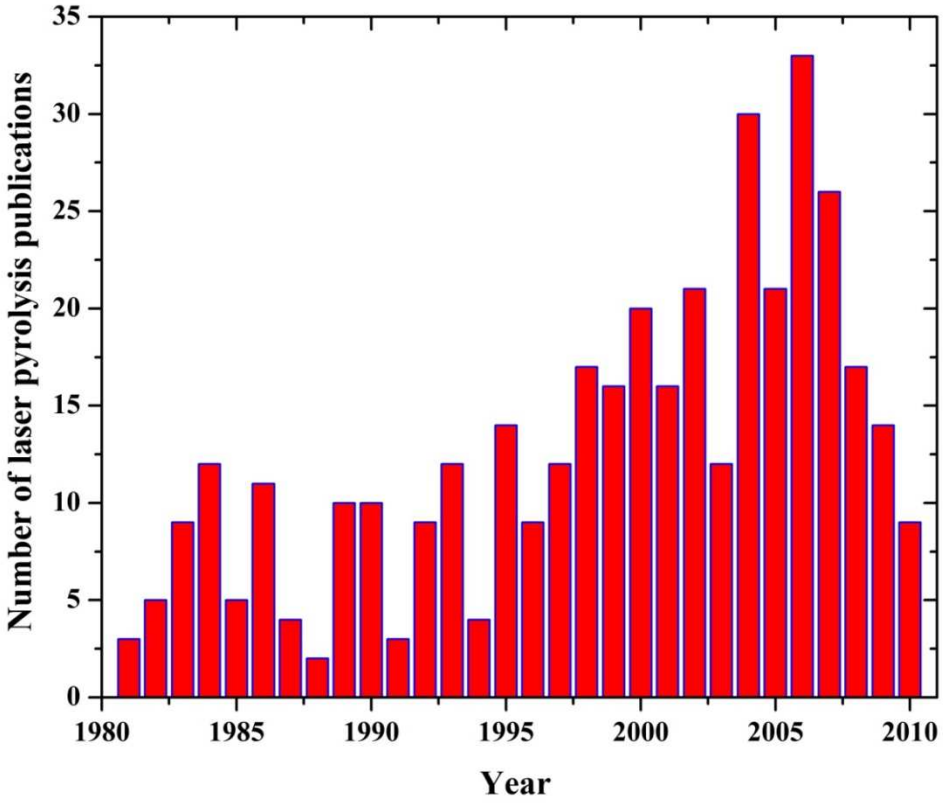


Figure 1.5 The increasing trend of laser pyrolysis publications over the past three decades.

1.3.1 *Theory of Laser Pyrolysis*

Laser pyrolysis is based on photon-induced chemical reactions, which relies on the resonant interaction between a laser beam's emission line and a precursor's absorption band, such that a photochemical reaction is activated [2]. The photochemical reaction enables an otherwise inaccessible reaction pathway towards a specific product, either by dissociation, ionization or

isomerisation of the precursor compound. The laser pyrolysis process is conducted within a reaction chamber, either under vacuum or at atmospheric pressure.

The multiple photon energy transfer increases the internal energy of the ground electronic state of the absorbing precursor molecules, causing the evolution of vibrational states through collisional relaxation processes and photochemical reactions. It has been shown, that for an environment where multiple collisions occur on the time scale of a chemical reaction, such as in the case of multiphoton transfer, that the vibrational modes of the polyatomic molecule will reach equilibrium and the reaction will occur without energy localization in a single mode [77].

If the precursor does not directly absorb the laser radiation, a sensitizer gas is added to couple the laser radiation to the absorbing system. The laser beam could possibly act as a highly localized heat source which could photo-thermally dissociate the precursor. The dissociated molecules of the supersaturated gas phase precursor form radicals that react and assemble into nanoparticles by homogenous nucleation via a bottom-up process [1].

1.3.2 *The Application of Laser Pyrolysis*

Some of the advantages of laser pyrolysis are the production of extremely fine and pure products with small size distributions, a well defined reaction zone that is free from impurities and contaminants. In recent years, many models [78, 79] have been derived to explain the temperature gradient induced by the laser and its effects on the synthesis of the nanomaterial.

The experimental variables that are still under investigation include [80-84] (i) the power density of the laser beam which is proportional to the temperature gradient, (ii) the gas precursor velocities, (iii) precursor residence time in the laser beam, (iv) the reaction chamber pressure and gas composition. These variables are material specific, and the overall effects on the synthesized material's morphology vary accordingly. It was found in some cases that as the laser power density increased, the size of the nanoparticles decreased. This is because the spontaneous reaction temperature increases to higher levels, causing the nucleation rate to increase proportionally faster than the growth rate. It was also found that laser wavelength and power density introduces competing processes, such as photochemical and photothermal

processes [76]. It was found in some cases, that increased reaction chamber pressure [72, 82, 84] and increased gas velocity [66, 72, 82] cause a decrease in nanoparticle size. This is due to a faster nucleation rate and a decrease in dissociation and collisions between molecules. Furthermore, it was found that in most cases, that diluted precursors formed smaller nanoparticles [66, 74, 83, 84], because there is a decrease in collisions between molecules and thus a decreased growth rate. Figure 1.6 shows the simulated results for laser pyrolysis derived from aerosol theory and are specific to the formation of iron nanoparticles [79].

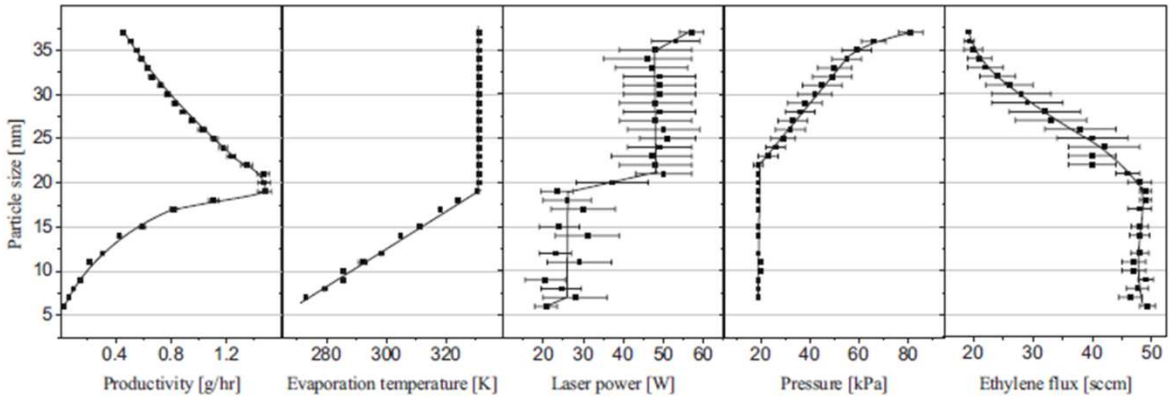


Figure 1.6 Representation of the maximum productivity predicted by the model based on aerosol theory and the experimental conditions required for the production of iron nanocrystals of a given size [79].

Chapter 2

Laser–Matter Interaction

2.1 Linear and Nonlinear Optical Processes

Linear optical processes occur when the response of a material system to an applied optical field depends linearly on the strength of the optical field (such as a laser field), while nonlinear optical processes involves a material system behaving in a nonlinear manner on the strength of an optical field [85]. Some linear and nonlinear processes will be looked at in the sections to follow so that the interaction between the laser beam and chemical precursor in laser pyrolysis can be better understood from this perspective.

2.1.1 Linear and Nonlinear Polarization of a material system induced by an optical field

To understand what is meant by optical nonlinearity, consider the dipole moment per unit volume or polarization $\vec{P}(t)$ of a material system, and its dependence on the strength $\vec{E}(t)$ of an applied optical field. For the linear case, the induced polarization depends linearly on the applied optical field strength, and the relationship is given by [85]

$$\vec{P}(t) = \epsilon_0 \chi^{(1)} \vec{E}(t), \tag{2.1}$$

where $\chi^{(1)}$ is the constant of proportionality known as the linear susceptibility, and ϵ_0 represents the permittivity of free space. For the nonlinear case, the expression in equation (2.1) can be generalized, such that the polarization can be expressed as a power series in the optical field strength. The nonlinear relationship is given by [85]

$$\begin{aligned}\vec{P}(t) &= \epsilon_0\left[\chi^{(1)} \vec{E}(t) + \chi^{(2)} \vec{E}^2(t) + \chi^{(3)} \vec{E}^3(t) + \cdots\right] \\ &\equiv \vec{P}^{(1)}(t) + \vec{P}^{(2)}(t) + \vec{P}^{(3)}(t) + \cdots,\end{aligned} \tag{2.2}$$

where $\chi^{(2)}$, $\chi^{(3)}$ are known as the second and third-order nonlinear optical susceptibilities, respectively. The fields $\vec{P}(t)$ and $\vec{E}(t)$ are taken to be scalar quantities in equations (2.1) and (2.2) for simplicity, and it is assumed that the polarization at time *t* depends only on the instantaneous value of the optical field strength. The assumption that the material system responds instantaneously also suggests that the material system must be lossless and dispersionless. The nonlinear susceptibilities generally depend on the frequencies of the applied fields, but under the assumption of instantaneous response, the susceptibilities are taken to be constant.

The second nonlinear optical interactions (such as the second order nonlinear polarization, which is written as $\vec{P}^{(2)}(t) = \epsilon_0 \chi^{(2)} \vec{E}^2(t)$, cannot occur in material systems that display inversion symmetry or centrosymmetry, such as liquids, gases and amorphous solids [85]. Therefore, the $\chi^{(2)}$ susceptibility vanishes for such material systems, and so these materials cannot produce second-order nonlinear optical interactions. The third-order nonlinear optical interactions (described by the $\chi^{(3)}$ susceptibility), however, can occur for both centrosymmetric and noncentrosymmetric material systems. For the specific case where the laser interacts with a centrosymmetric vapourized precursor (which is the material system studied in this work), the possible change in polarization is brought into perspective to get a basic idea of the changes induced by the laser beam on the chemical precursor.

2.1.2 Linear and Nonlinear Absorption of a material system

Since the precursor absorbs laser radiation, it is possible for the absorption to be either linear or nonlinear, and the various possibilities will be covered here. For a saturable absorber, the absorption coefficient α is related to the applied optical field intensity (which is written as $I = 2n\epsilon_0 c|E|^2$ where n is the refractive index of the material system). In a saturable absorber, the rate of excitation exceeds the rate of decay such that the ground state becomes depleted and the absorption subsequently saturates. The intensity-dependant linear absorption relationship is given by [85]

$$\alpha = \frac{\alpha_0}{1 + I/I_S}, \tag{2.3}$$

where α_0 is the weak-field absorption coefficient, and I_S is an optical constant known as the saturation intensity. For the nonlinear case, equation (2.3) can be expanded in a power series to give [85]

$$\alpha = \alpha_0[1 - (I/I_S) + (I/I_S)^2 - (I/I_S)^3 + \cdots]. \qquad (2.4)$$

This series converges only for $I < I_S$, and only in this limit can saturable absorption be described by means of a power series, like that given by equation (2.2).

Describing the atomic system is simplified by using the two-level approximation which considers only two levels, and so there is no need to perform the sum over all atomic states. Note that the chemical precursor used in the study is a polyatomic molecule and the two-level approximation provides a starting point to the more complex nature of the precursor. The situation in which a monochromatic beam of frequency ω interacts with a collection of two-level atoms is dealt with in detail in Appendix A, and the results will be given here. The case for a monochromatic beam describes the case of the laser–precursor interaction used in laser pyrolysis, and so this will be considered.

2.1.3 Open and Closed Two-level atom

The interaction that is considered is illustrated in Figure 2.1 where the excitation frequency ω of the atomic system is near-resonance to the absorption frequency of the atom. The lower atomic level is denoted by ***a*** and the upper atomic level is denoted by ***b***.

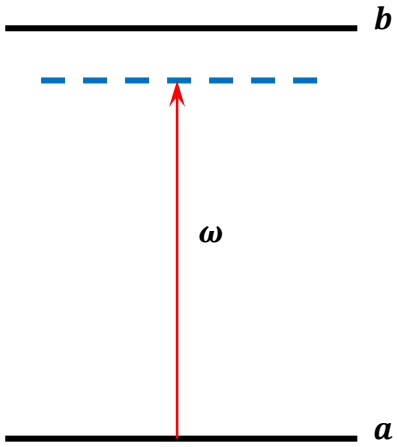


Figure 2.1 Near-resonant excitation of a two-level atom [85].

A two-level system is referred to as closed when any population that leaves the upper level ***b*** enters the lower level ***a*** and the relaxation processes for a closed two-level system is illustrated schematically in Figure 2.2. It is assumed that the upper level decays at a rate Γ_{ba} to the lower level, such that the lifetime of the upper level can be written as $T_1 = 1/\Gamma_{ba}$ [85], and the decay of the upper level would typically be due to spontaneous emission. It is also assumed that the atomic dipole moment is dephased in the characteristic time T_2, leading to a transition line width (in the case of weak applied fields) of characteristic width $\gamma_{ba} = 1/T_2$.

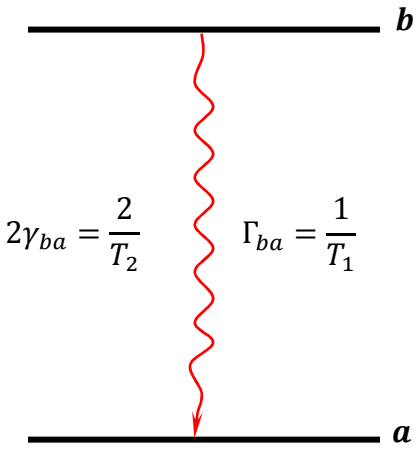


Figure 2.2 Relaxation processes of the closed two-level atom [85].

T_1 (known as the relaxation time where the population inversion relaxes from its initial value to its equilibrium value) and T_2 (known as the dephasing time where the dipole moments oscillation frequency decays to zero) are related to the collisional dephasing rate γ_c by

$$\frac{1}{T_2} = \frac{1}{2T_1} + \gamma_c. \qquad (2.5\text{ a})$$

For an atomic vapour, γ_c can be described accurately by the formula

$$\gamma_c = C_s N + C_f N_f, \qquad (2.5\text{ b})$$

where N is the number density of atoms having resonance frequency ω_{ba}, and N_f is the number density of any "foreign" atoms of a different resonance frequency. The parameters C_s and C_f are coefficients describing self-broadening and foreign-gas broadening, respectively. As an example, for the resonance line of atomic sodium ($3s \rightarrow 3p$ transition), $T_1 = 16$ ns,

$C_s = 1.50 \times 10^{-7}\,\mathrm{cm}^3/\mathrm{s}$, and for foreign-gas broadening by collisions with argon atoms, $C_f = 2.53 \times 10^{-9}\,\mathrm{cm}^3/\mathrm{s}$ [85].

A two-level system is referred to as open when the population that leaves the upper level ***b*** does not necessarily enter the lower level ***a***. Examples of such systems are magnetic sublevels or hyperfine levels associated with states ***a*** and ***b***. The open two-level atom is shown schematically in Figure 2.3. This model is often encountered when the upper level or both levels are assumed to acquire population at some controllable pump rates, which is taken to be λ_b and λ_a for levels ***b*** and ***a***, respectively. As in the case of the closed two-level atom, it is assumed that the induced dipole moment relaxes in a characteristic time T_2.

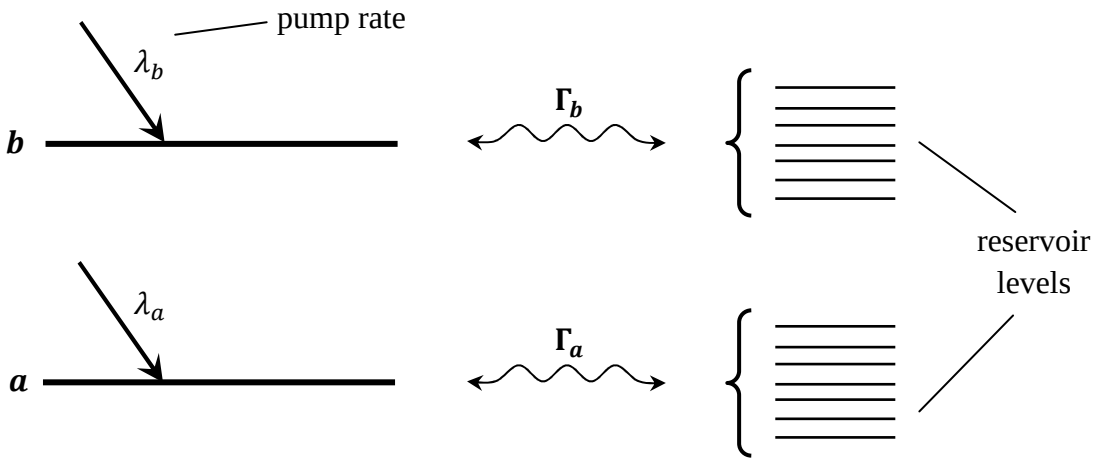


Figure 2.3 Relaxation processes of the open two-level atom [85].

The relaxation rates for the open two-level atom are related to the collisional dephasing rate and population rates Γ_b and Γ_a (for upper levels ***b*** and lower level ***a***, respectively), and the relationship is given by [85]

$$\frac{1}{T_2} = \frac{1}{2}(\Gamma_b + \Gamma_a) + \gamma_c. \tag{2.6}$$

To get an idea of the magnitudes of some of the physical quantities for a steady-state response of a two-level atom in a laser beam, an example will be considered. Assuming that the dipole moment $|\mu_{ba}| = 2.5ea_0 = 2.0 \times 10^{-29}$ C m (as it is for the $3s \rightarrow 3p$ transition of atomic sodium) and that the laser intensity I is measured in $\mathrm{W/cm^2}$, this relationship gives the numerical rabi frequency Ω of [85]

$$\Omega[\mathrm{rad/sec}] = 2\pi(1 \times 10^9)\left(\frac{I[\mathrm{W/cm^2}]}{127}\right)^{1/2}. \tag{2.7}$$

Hence, whenever the intensity I exceeds $127\ \mathrm{W/cm^2}$, $\Omega/2\pi$ becomes greater than 1 GHz, which is a typical value of the Doppler-broadened linewidth of an atomic transition. Intensities this large are available from a focused output of even low-power continuous wave lasers.

The saturation intensity I_S^0 of an atomic transition can be quite small. Again using $|\mu_{ba}| = 2.0 \times 10^{-29}$ C m, and assuming that $T_1 = 16$ ns (the value for the $3s \rightarrow 3p$ transition of atomic sodium) and that $T_2/T_1 = 2$ (the ratio for a radiatively broadened transition), it is found that [85]

$$I_S^0 = 52.7\ \frac{\mathrm{W}}{\mathrm{m^2}}. \tag{2.8}$$

The previous equations and results physically describe the possible change in polarization, as well as linear and nonlinear absorption of a laser beam during the laser–precursor interaction in laser pyrolysis. The next section looks at photochemistry and photophysics, which also describes the laser–precursor interaction, but more explicitly accounts for molecular changes and the chemistry that result in the material system, induced by the optical field or laser beam.

2.2. Photochemistry and Photophysics

Another field that describes light–matter interaction is photochemistry and photophysics. Photochemistry is the study of the chemical changes induced by the interaction with light. Photophysics refers to a variety of physical transformations induced by light-interaction that may occur between and within molecules prior to any chemical changes [86].

The difference between the two processes is that the photochemical process involves the breaking and reforming of chemical bonds (photosynthesis describes such a process), while the photophysical process involves physical changes in the molecular system interacting with the light (such as the conversion of light energy to heat or fluorescence and phosphorescence without any chemical changes) [87].

For a photochemical or photophysical process to occur according to the Grotthus-Draper law (derived in the early 1800s by Christian von Grotthus and John Draper), a single molecule must first absorb a photon of light. In a photochemical process according to the Stark-Einstein law (derived in the early 1900s by Johannes Stark and Albert Einstein), one molecule absorbs one and only one photon of light. The exception to this law is observed only when extremely high light intensity sources are used, such as lasers, where multiphoton absorption by a single molecule is possible [87].

2.2.1 Photophysical Processes

Figure 2.4 schematically describes the various photophysical processes for a typical molecule. Absorption refers to the process where a material system absorbs a photon of light, or alternatively, multiphoton absorption occurs when a material system absorbs more than one photon. In the case of one-photon absorption process, the energy of the absorbed photon is greater than or equal to the energy difference between the ground vibrational level of the material system and the excited vibrational level of the material system. The vibrational excited level can emit a photon that is equal to or lower in energy than that of absorption and de-excite to some vibrational level of the ground singlet state, which is referred to as fluorescence. Lower lying excited singlet states have mean lifetimes on the order of nanoseconds or as short as femtoseconds, whereas the corresponding triplet state $\mathcal{T}_1$ of the

same material system may have a lifetime from microseconds to many seconds. It is also possible for an electron in the molecule to undergo a spin transition and become a triplet system, in a process known as intersystem crossing. Once in the triplet state, the material system can emit a photon of light of less energy than that involved in the fluorescence process, and return to the ground singlet state. This emission is referred to as phosphorescence. Internal conversion is similar to intersystem crossing in that the de-excitation process is radiationless, but the molecular spin state for internal conversion remains the same and the excitation energy is transformed into heat. Vibrational cascade refers to the sequence of spontaneous decays by an excited atom.

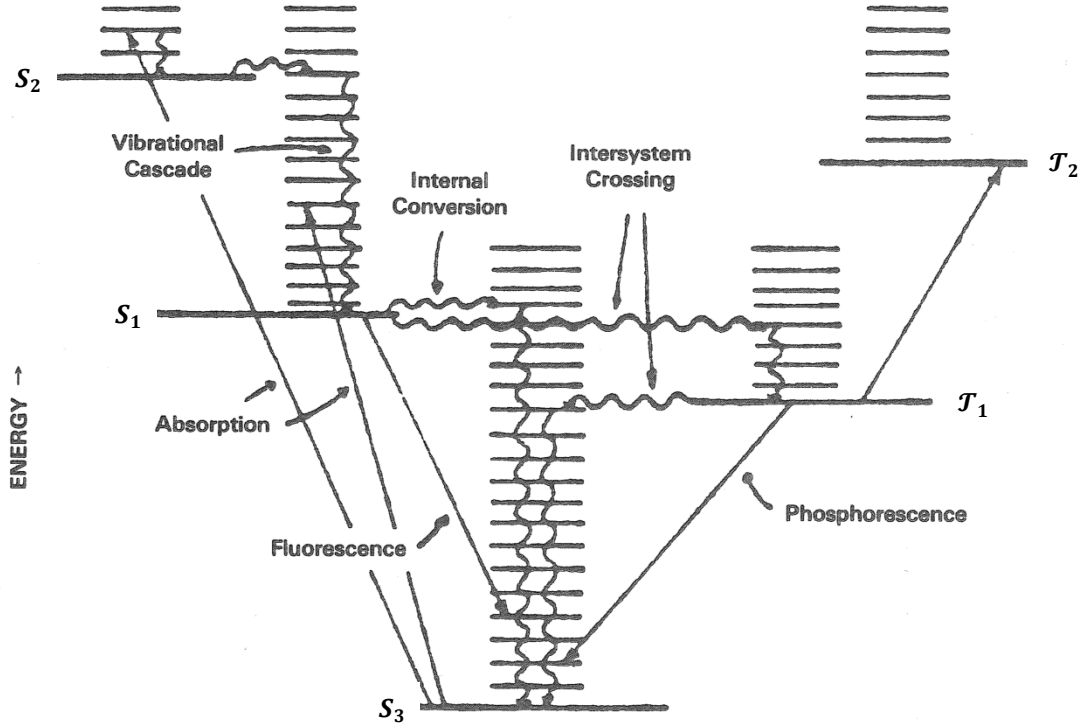


Figure 2.4 Molecular orbital energy level diagram, which shows the various photophysical processes that may be involved in a molecule [86].

2.2.2 Photochemical processes

After the molecule absorbs a photon of light and after the subsequent photophysical processes, it is possible for the molecule to undergo a chemical change rather than return to its ground state [88]. De-excitation or relaxation may lead to ionization, isomerisation, or dissociation, as illustrated for a polyatomic molecule ABC by the scheme given as [89]

$$\text{Photoabsorption: } ABC + \text{nh}\nu \rightarrow ABC^{*} \qquad (n \geq 1), \tag{2.9 a}$$

$$\text{Autoionisation: } ABC^{*} \rightarrow ABC^{+} + \text{e}^{-}, \tag{2.9 b}$$

$$\text{Isomerisation: } ABC^{*} \rightarrow ACB^{*}, \tag{2.9 c}$$

$$\text{Dissociation: } ABC^{*} \rightarrow AB^{\ddagger} + C^{\ddagger}, \tag{2.9 d}$$

where $\text{h}\nu$ represents a photon of some energy and e^{-} represents an electron. The last process of the scheme, given in equation (2.9 d), results in bond fission and produces the fragments AB and C, which are both in vibrationally or possibly electronically excited states [89]. Dissociation represents the simplest kind of photochemical reaction, and it also provides the mechanism for the first step in many more complex types of photochemistry. However, many polyfunctional compounds can exhibit more than one type of dissociation, leading to a mixture of products.

The discussion above considered unimolecular reactions, but lasers are known to induce bimolecular reactions in which either one or both of the reactants are initially excited by the absorption of laser light [89]. Even if the photoabsorption only takes place in one of the reactants before the collisional reaction, the laser excitation can still play a crucial role in ‘state preparation’, since the chemistry of excited molecules differs from its ground state counterpart. This state preparation discussed here, will be referred to in the results and discussion chapter as there is some motivation of this occurring. Infrared lasers are usually used to promote each reactant to various energy levels, allowing for the sometimes, inaccessible reaction pathways. This is one of the reasons that the carbon dioxide gas laser is

used in laser pyrolysis experiments, as it “lases” in the far infrared region of the electromagnetic spectrum.

2.2.2.1 *Multiphoton Infrared Excitation*

Multiphoton processes can be induced by intense radiation of lower-than-the-interband-energy photons, and become extremely efficient if one or more resonance conditions are satisfied by the molecular energy levels [89]. Vibrational levels are more or less equally spaced for the lowest levels of excitation, and so with infrared radiation of appropriate wavelength, multiphoton absorption can become highly significant.

The case of multiphoton infrared absorption by a diatomic molecule is considered, as there is only one vibrational frequency. The appropriate energy levels are illustrated in Figure 2.5, where the arrows represent the absorption of infrared photons with the same frequency. Note that spacing between adjacent levels in the vibrational state starts off fairly constant, but thereafter diminishes at an increasing rate from a polynomial to an exponential trend. Also note that each vibrational level contains more closely spaced rotational levels. Because each of these levels has an associated linewidth, this results in a quasi-continuum of states, which is represented by the shaded region in Figure 2.5. Eventually, there is a limit at which point there is no longer any restoring force as the two atoms move apart, leading to dissociation. The system referred to here is anharmonic.

The process of multiphoton absorption displays different characteristics over different regions of the energy scale, and the regions are commonly referred to as region I, II, and III as illustrated in Figure 2.5. In region I, the vibrational levels are widely spaced, and the spacing is greater than the overall absorption bandwidth. However, the spacing is non-uniform, and so the photon energy soon gets out of step, allowing for multiphoton processes. For example, in Figure 2.5, the transitions $v = 0 \rightarrow 1$, $1 \rightarrow 2$, $2 \rightarrow 3$, $3 \rightarrow 4$ and $4 \rightarrow 5$ all require energies close to that of a single photon and lying within the overall bandwidth. These transitions therefore all take place by the process of single-photon absorption. However, the energy required for the $5 \rightarrow 6$ transition, is sufficiently different, as it lies outside the bandwidth and cannot take place by absorption of one photon. Excitation can still proceed up to the $v = 10$ level, as indicated by direct $5 \rightarrow 10$ transition involving four-photon absorption. This is the

main characteristic of region I that such concerted multiphoton processes take place on the way up the vibrational ladder [89].

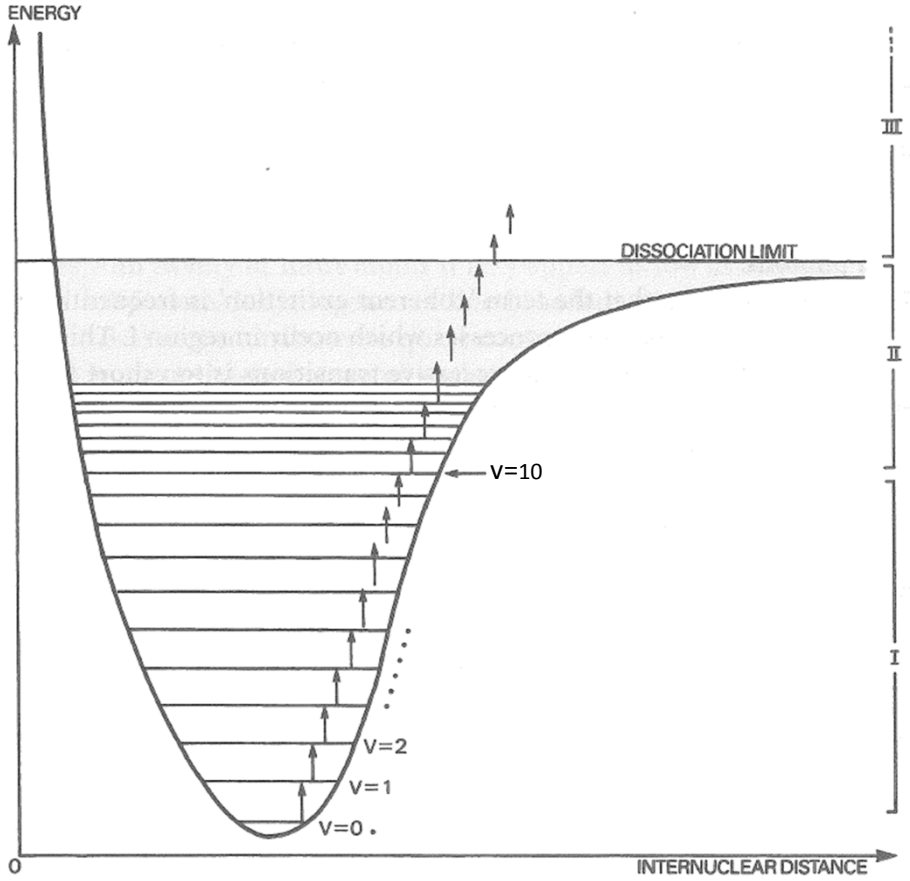


Figure 2.5 Energy levels and transitions involved in the multiphoton infrared dissociation of a diatomic molecule [89].

Region II is characterized by a quasi-continuum behavior resulting from the fact that vibrational energy level spacing has become less than the bandwidth. Successive photons can be absorbed here in a series of energetically allowed single-photon transitions. Since energy conservation is satisfied at every step, the molecule can at each point exist for a finite lifetime before absorbing the next photon. Therefore, excitation through this region does not necessitate the enormously large photon flux which might have first appeared. Once the level of excitation has reached the dissociation threshold, a true energy level continuum is encountered, and more photons can be absorbed in the short time before the atoms separate. The region where more photons can be absorbed in the short time before the atoms separate is known as region III behaviour [89].

Considering the case of polyatomic molecules, many of the same principles for the diatomic molecule apply, but many additional factors come into play. In polyatomic molecules containing N atoms, there are generally $(3N-6)$ modes of vibration (or degrees of freedom), and each mode has its own ladder of vibrational and associated rotation-vibration levels. This makes it possible to induce multiphoton excitation at a number of different wavelengths, corresponding to each of these various vibrational modes. There can also be many different processes of dissociation involving the fission of different chemical bonds leading to different types of fragmentation. Further multiphoton excitation may occur in any fragment with suitable vibrational levels, and can represent a fourth stage in the overall process of multiphoton decomposition [89]. As one can see, the complexity of understanding the polyatomic molecule increases as more and more detailed theory is added. It is possible at this stage, however, to gauge on the microscopic level, the dynamics that occurs within the chemical precursor used in laser pyrolysis.

2.3. Summary

The nature of light and laser interactions with matter was dealt with here. During such interactions, it is possible for linear and nonlinear optical processes to occur in the material system, and the cases for polarization and absorption were discussed. This introduces and gives a theoretical description of the possible processes that can occur when the laser beam interacts with the chemical precursor. The fields of photochemistry and photophysics were also introduced, and the resulting processes were highlighted to get an overview of the laser precursor interaction on a microscopic scale. These formulations form the basis in explaining the experimental results.

Chapter 3

Characterization Techniques

3.1 Introduction

The characterization techniques used in this study are Fourier Transform Infrared Spectroscopy (FTIR), Raman spectroscopy, X-ray Diffraction (XRD), Transmission and Scanning Electron Microscopy, and Energy Dispersive X-ray Spectroscopy (EDS/EDX). FTIR is a well-known technique which is non-destructive, and is used to identify compounds both quantitatively and qualitatively in quick scanning time [90]. Raman spectroscopy is ideal for identifying compound stoichiometries [91] and together with XRD [92], the sample composition and crystal structure can be positively identified. The electron microscopes, namely the Transmission Electron Microscope (TEM) and Scanning Electron Microscope (SEM), are used to image, in high resolution and magnification, the morphology and topography of thin films and nanostructures [93]. The electron microscopes house the EDX identification technique, which can identify the elements making up a sample [93].

3.2 Fourier Transform Infrared Spectroscopy (FTIR)

The method of infrared spectroscopy is used to analyze materials based on the molecular absorption and transmission of infrared radiation [90]. Compounds are made up of a unique combination of atoms, and so the bonds between the atoms making up the compound have characteristic vibrational frequencies. When infrared radiation is passed through a sample, a unique combination of absorption peaks corresponding to the vibrational frequencies can be collected and used to identify the compound.

A FTIR spectrometer consists of a beamsplitter, a fixed mirror, a moving mirror, a laser and a detector [90]. The beamsplitter reflects about half of the incident light source and transmits the remainder of the beam as shown in Figure 3.1. The reflected beam travels to a fixed mirror while the transmitted beam travels to a moving mirror, which moves back and forth at a constant velocity. This velocity is timed according to the very precise laser wavelength in

the system, which also acts as an internal wavelength calibration. Both the mirrors reflect the beams back to the beamsplitter where they recombine, and because the moving mirror has traveled a different distance than the beam from the fixed mirror, some of the wavelengths recombine constructively and some destructively.

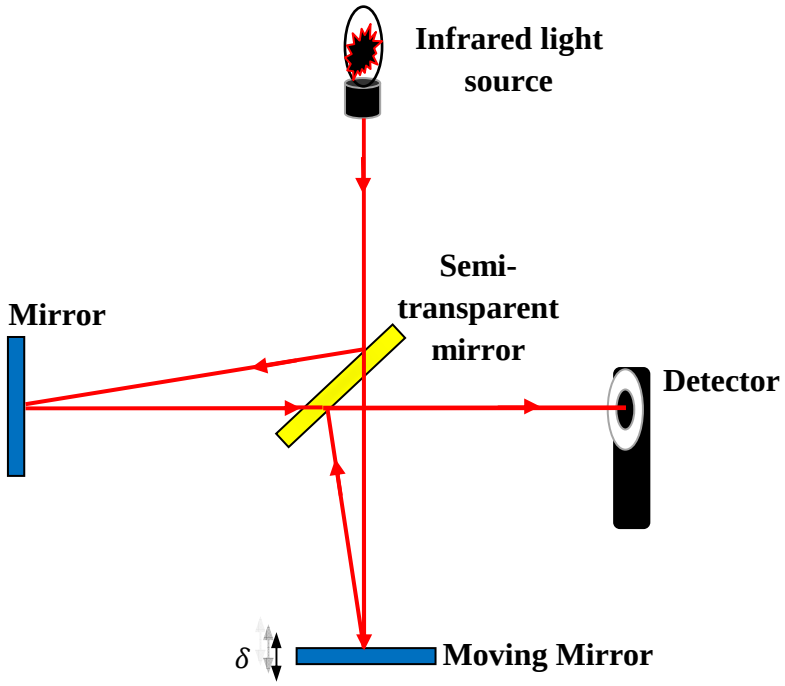


Figure 3.1 Illustration of the layout and components of an interferometer used in FTIR [90].

If the two beams interfere constructively, this results in a maximum in the detector signal intensity [90]. If the position of the moving mirror is such that the optical pathlength of the beam from the moving mirror is different from that of the beam from the fixed mirror by half a wavelength $(1/2\ \lambda)$, then the two beams will interfere destructively, resulting in a minimum in the detector signal intensity. The resulting interference pattern is known as an interferogram. The interferogram then goes from the beamsplitter to the sample, where some radiation is absorbed and the remainder transmitted. The transmitted portion reaches the detector, which reads information about every wavelength in the infrared range simultaneously. To obtain the infrared spectrum, the detector signal is sent to a computer, and an algorithm called a Fourier transform is performed on the interferogram to convert it into a single beam spectrum. A reference single beam (obtained by scanning air) is also collected without a sample and the sample single beam is ratioed to the background single beam to produce a transmittance or "%T" spectrum.

If $I(\delta)$ is the intensity of the beam at the detector, δ is the mirror displacement in centimeters and $B(\omega)$ is the intensity of the source as a function of frequency ω in cm^{-1}, then the equation for the signal is expressed as [90]

$$\mathcal{F}(\delta) = B(\omega)\cos(2\pi\delta\omega). \tag{3.1}$$

When frequencies are added up to an infinite number (ie. Polychromatic source), the detector will respond to the sum of all cosine waves: [90]

$$\mathcal{F}(\delta) = \int_{-\infty}^{\infty} B(\omega)\cos(2\pi\delta\omega)\, d\omega, \tag{3.2}$$

where [90]

$$B(\omega) = \int_{-\infty}^{\infty} I(\delta)\cos(2\pi\delta\omega)\, d\delta. \tag{3.3}$$

The relationship between the interferogram and the spectrum is defined by equations (3.2) and (3.3).

FTIR was carried out on ethanol and the resulting FTIR transmittance spectrum as a function of frequency that was obtained is shown Figure 3.2. The ethanol compound and the fingerprint peaks corresponding to the bonds in the compound and their relative abundances is shown on the spectrum. The knowledge of the absorption bands of the precursor is imperative for laser pyrolysis, and will be dealt with in later chapters.

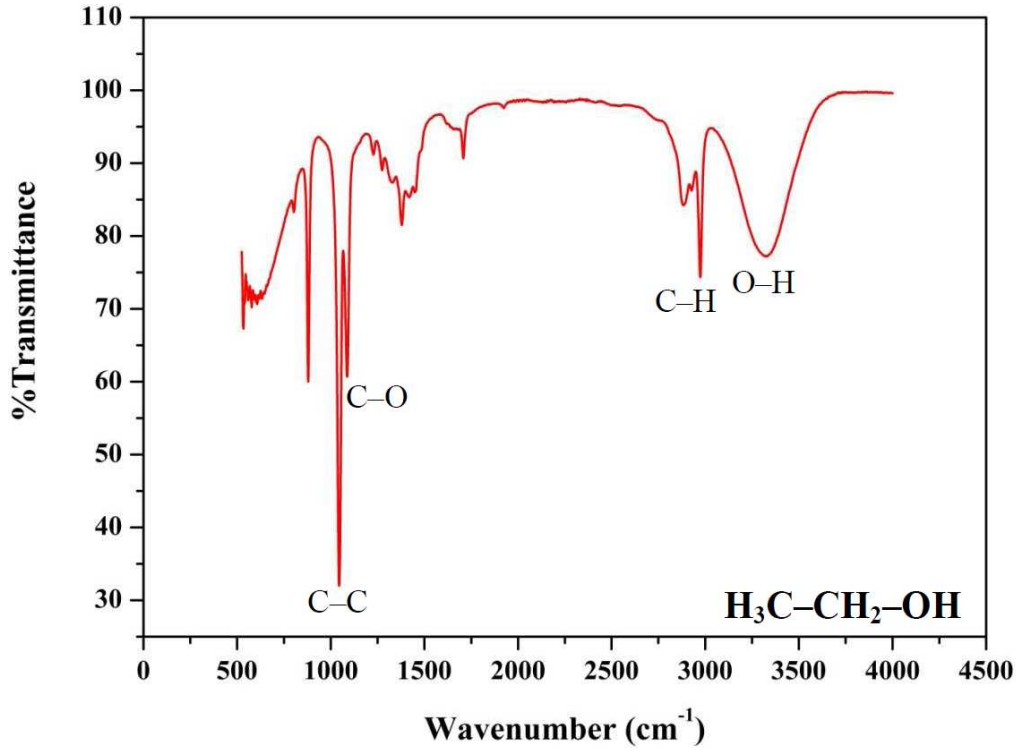


Figure 3.2 FTIR transmittance spectrum of ethanol, showing the characteristic peaks arising from the different chemical bond frequencies.

3.3 Raman Spectroscopy

Raman spectroscopy is based on the phenomenon of Raman scattering, which was first observed in 1928 by C. V. Raman and K. S. Krishnan [94-96]. When light is incident on a sample, it is scattered according to the nature of the bonds in the compound. Raman spectroscopy focuses on the Raman scattered light to create a spectrum that is unique for every compound.

The sample is exposed to a laser beam, and the interaction causes a periodic perturbation of the electron orbits in the molecules, which further causes the electron cloud to oscillate and induce a dipole moment [91]. The oscillating dipole moment is itself a source of electromagnetic radiation, and emerges as scattered light. The scattered light depends on the oscillating dipole moment which is a function of polarizability. Polarizability depends on the sample's molecular structure and nature of the chemical bonds making up a compound. The majority of the scattered light has the identical frequency as the incident radiation, and this type of radiation is known as Rayleigh scattering.

The scattered light that has different frequencies from the incident radiation could be Compton or Raman scattered light [96]. Raman scattered light results from the interaction between the incident photon and matter, whereas Compton scattered light results from the transfer of energy from the incident photon to a free electron, thus altering the photon energy. In Raman spectroscopy, only the interaction between light and matter is considered, so Raman scattered light is isolated and analyzed.

The Raman scattered light that has a frequency lower than the incident light is called Stokes Raman bands, and the Raman scattered light that has a frequency higher than the incident light is called anti-Stokes Raman bands. The equation for the induced dipole moment ϑ that takes into account all the scattered frequencies is given by [91]

$$\vartheta = \psi_0 E_0 \cos(2\pi\nu_0 t) + \left(\frac{d\alpha}{dQ}\frac{Q_0 E_0}{2}\right)\{\cos[2\pi(\nu_0 - \nu_{\text{vib}})t] + \cos[2\pi(\nu_0 + \nu_{\text{vib}})t]\}, \tag{3.4}$$

where ψ_0 is the polarizability of the molecule, E_0 is the electric field amplitude of the incident radiation, Q_0 is the maximum physical displacement of the atoms about their equilibrium position, ν_0 is the incident frequency, ν_{vib} is the scattered frequency and t is a measure of time. The first term of equation (3.2) represents elastic scattering (Rayleigh scattering), the second term represents down-shifted frequency (Stokes scattering) and the third term represents up-shifted frequency (anti-Stokes scattering).

In a Raman spectrometer, an optical microscope is used to focus and image a sample as depicted in Figure 3.3. The incident beam of a single wavelength, is tightly focused (beam diameter of ~1 μm) onto the sample, and the back-scattered radiation from the sample is directed onto a detector. The elastic scattered light is filtered out, and a fingerprint Raman spectrum is obtained, and looks like the spectrum shown in Figure 3.4. This technique is considered to be non-destructive.

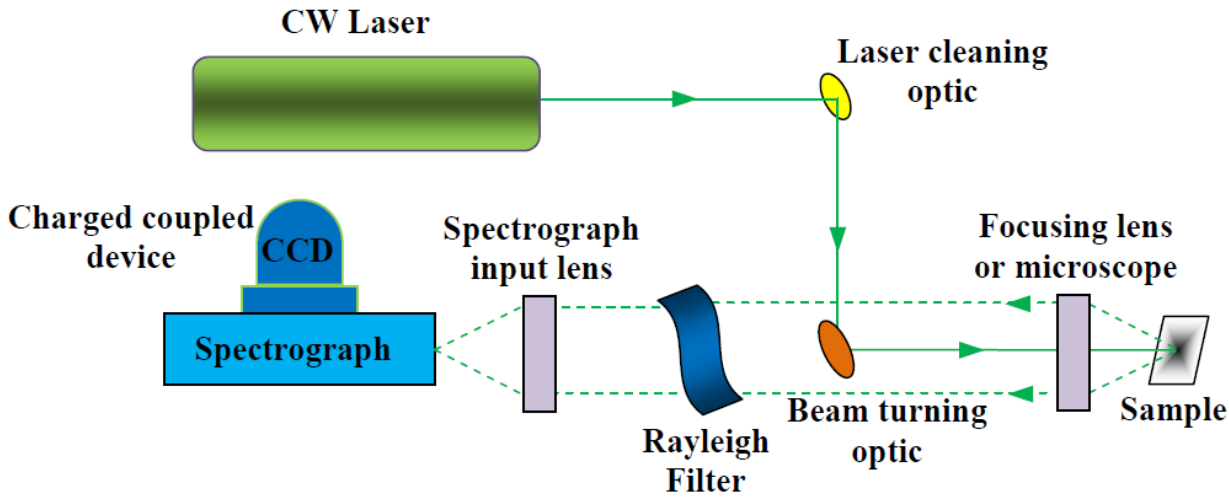


Figure 3.3 An illustration of the layout and components of a Raman spectrometer [94].

Raman spectroscopy was carried out on a sample of WO_3 and the resulting Raman spectrum as a function of frequency is shown in Figure 3.4. The WO_3 compound and the combination of characteristic peaks corresponding to the vibrational modes in the compound acts as a fingerprint, allowing for the identification of the compound.

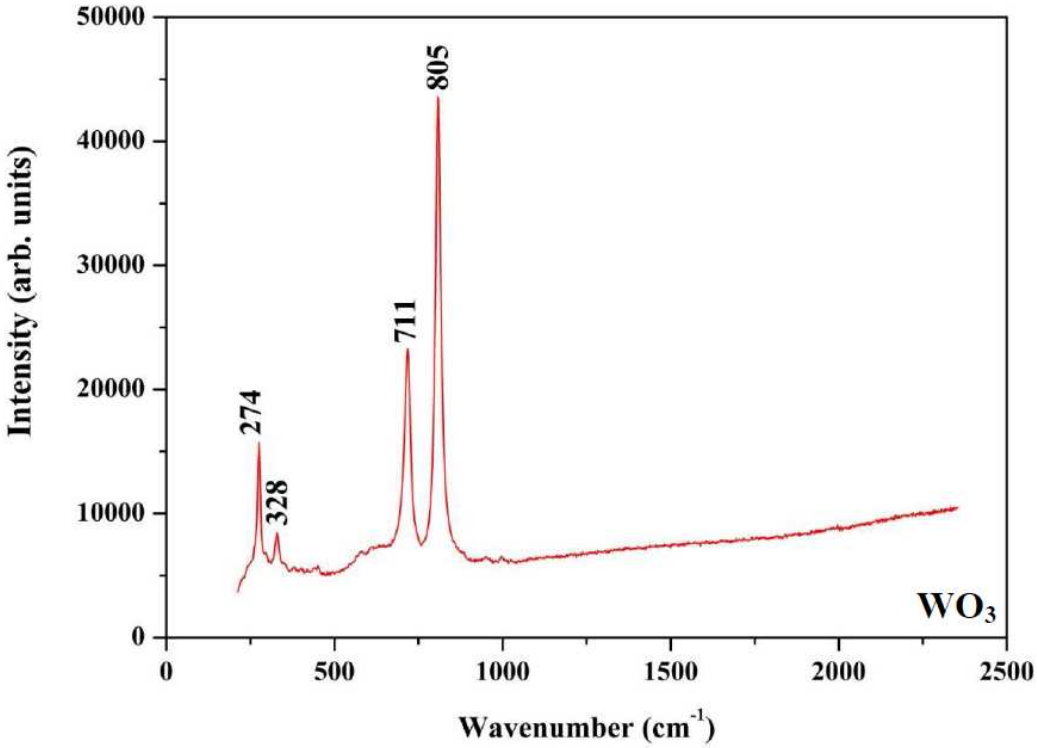


Figure 3.4 Raman spectrum of WO_3, showing the characteristic peaks arising from the vibrational modes of the compound.

3.4 X-ray Diffraction (XRD)

X-rays were discovered in 1895 by W. C. Röntgen and the technique of x-ray diffraction (XRD) was discovered in 1912 by W. L. Bragg [92]. XRD is a versatile, non-destructive analytical technique used for Miller indexing of crystal structures, microstructure analysis, and the determination of the degree of crystallinity.

This technique involves the interaction of x-ray photons with atoms from a sample, and so the photons can then be scattered, diffracted, reflected or absorbed and in the case of diffraction, the incident x-ray photon is scattered by atoms in distinct angles. Figure 3.5 shows a crystal with atoms arranged in planes, where beam *1* and *1a* are incident x-ray beams at angle θ to the plane normal. The incident photons interact with atom K and P from the uppermost plane, respectively. Constructive interference between the two incident beams will only take place if *1́* and *1á* are in phase, and this only occurs when the scattering angle is equal to the angle of incidence. If more planes are taken into consideration (beams *1*, *1a*, *2*), diffraction will only occur for distinct angles of θ depending on the interplanar spacing d'. The condition of diffraction from a regular 3D crystal is explained by Bragg's law, which is given by [92]

$$m\lambda = 2d' \sin\theta, \tag{3.5}$$

where λ is the x-ray wavelength, m is an integer called the order of diffraction, and θ is the angle of x-ray incidence measured from the reflecting plane.

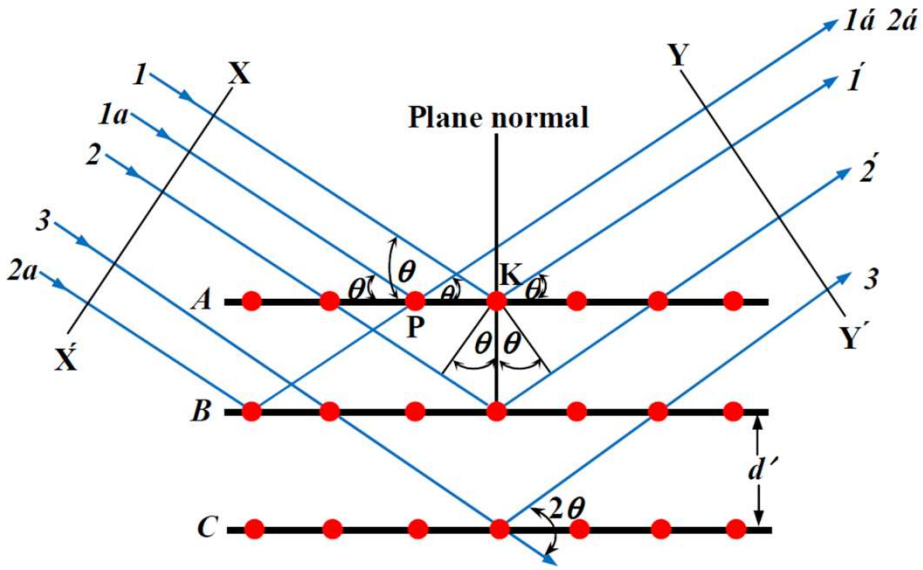


Figure 3.5 Incident x-rays diffracting off the planes in a crystal at distinct angles of θ depending on d' [92].

By varying the angle θ, the Bragg's law conditions are satisfied by different interplanar spacing in polycrystalline materials, which is dependent on the periodicity of the crystal. The periodicity of the crystal determines the diffraction direction which is the position of the possible 2θ angles, and a schematic of a diffractometer is shown in Figure 3.6. A further description on the components of Figure 3.6 will not be given here, but for more information refer to [97]. Plotting the angular positions against the relative intensities I of the resultant diffracted peaks, a characteristic pattern of the sample is obtained like the diffractogram shown in Figure 3.7 with the PDF number and Miller indices. The XRD peaks on a diffractogram are compared against Powder Diffraction Files (PDF), which are maintained by the International Centre for Diffraction Data (ICDD), to identify the sample.

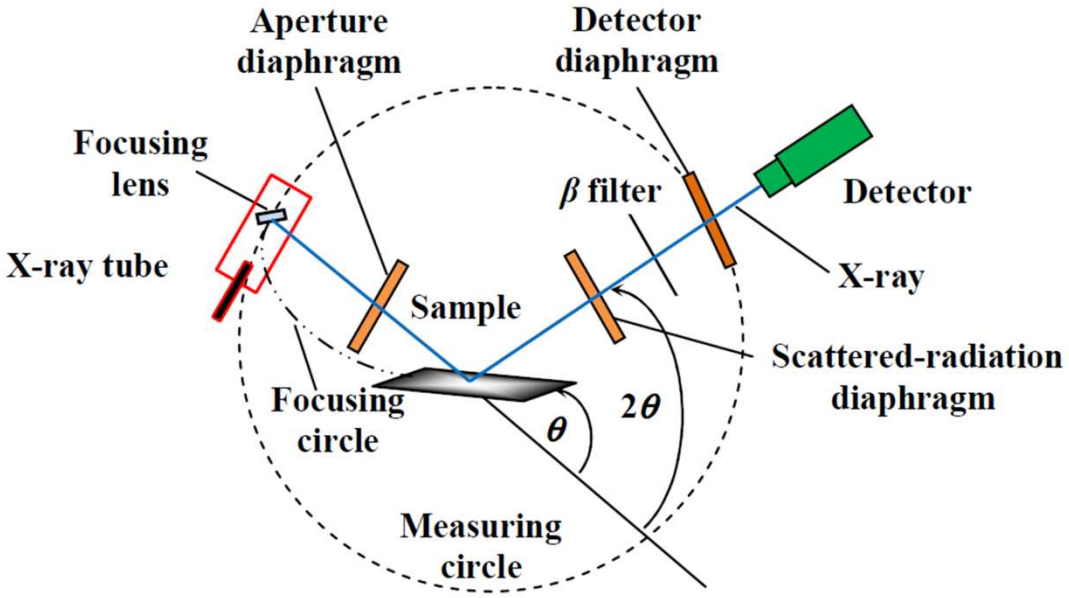


Figure 3.6 The components of a diffractometer with the beam path in the $^{\theta}/_{2\theta}$ mode [97].

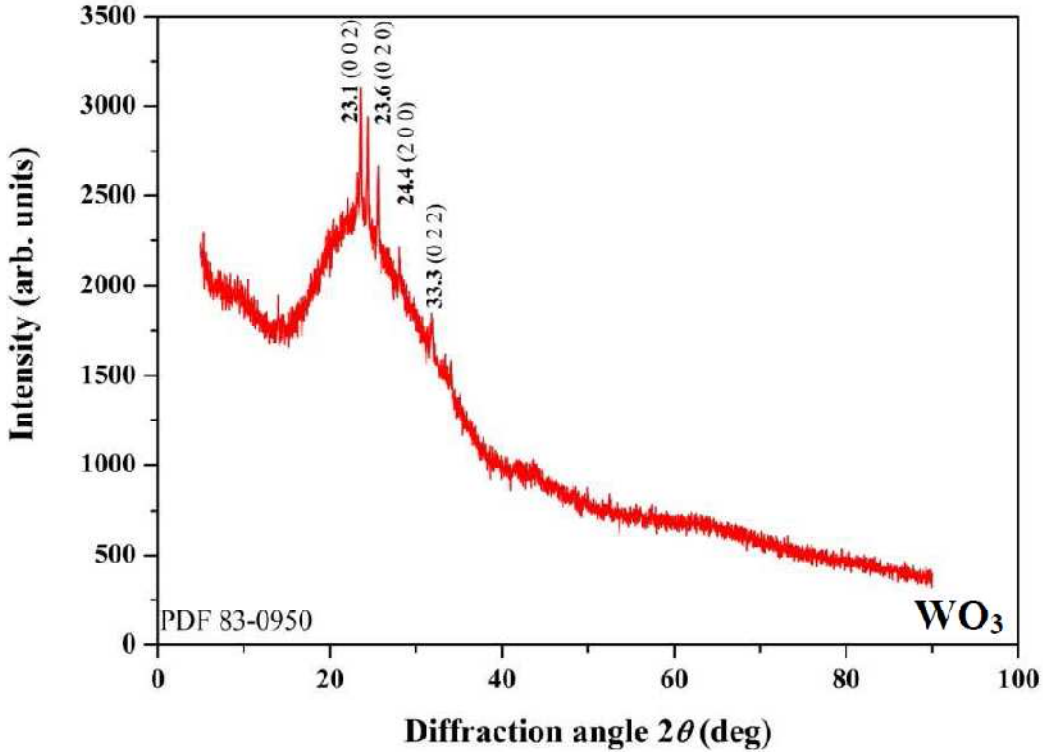


Figure 3.7 XRD diffractogram or spectrum of WO_3, showing the characteristic diffraction angles and Miller indexes. The broad underlying peak results from the substrate on which the WO_3 sits.

3.5 The Transmission Electron Microscope (TEM)

TEM was invented in 1931 by M. Knoll and E. Ruska, when it was realised that material particles such as electrons possess a wavelike character [95]. This technique is used to image sample materials at the atomic-scale. Louis de Broglie proposed that electrons have a wavelength λ given by

$$\lambda = \frac{\mathrm{h}}{p} = \frac{\mathrm{h}}{(mv)}, \tag{3.6}$$

where h is Planck's constant, p, m and v are the electron's momentum, mass and velocity, respectively. The velocity of the electrons can be increased by accelerating them through a potential difference, which in turn decreases the wavelength according to Equation (3.4). The wavelength becomes comparable to atomic dimensions, and so they are strongly diffracted from the regular array of atoms at the surface of a crystal. Increasing the accelerating potential causes the higher-energy electrons to penetrate deeper into a sample. It is therefore

possible to form a transmission electron diffraction pattern from the electrons that have passed through a thin sample, and the focused electron beam improves the spatial resolution.

Only a minute amount of material is needed for TEM analysis. The material is usually sonicated in an organic solvent to homogenise it (it is thus a destructive technique), and a drop of the resulting solution is put onto a copper grid. The sample is then placed onto the sample stage, depicted in Figure 3.8. The TEM comprises of an illumination system, the sample stage and the imaging system. The illumination system is made up of an electron gun and two or more condenser lenses that focus the electrons onto the sample. The system must be carried out under vacuum to eliminate any dust particles from the column, and more importantly, the vacuum extracts the air that rapidly decomposes the electron beam. The sample stage allows the sample to be held stationery or to be moved, and so a specific area of the sample can be imaged. The imaging system contains at least three lenses stacked vertically, forming a lens column that produces a magnified image (or a diffraction pattern) of the sample on a fluorescent screen. TEM was carried out on a sample prepared by laser pyrolysis and the resulting TEM micrographs are shown in Figure 3.9.

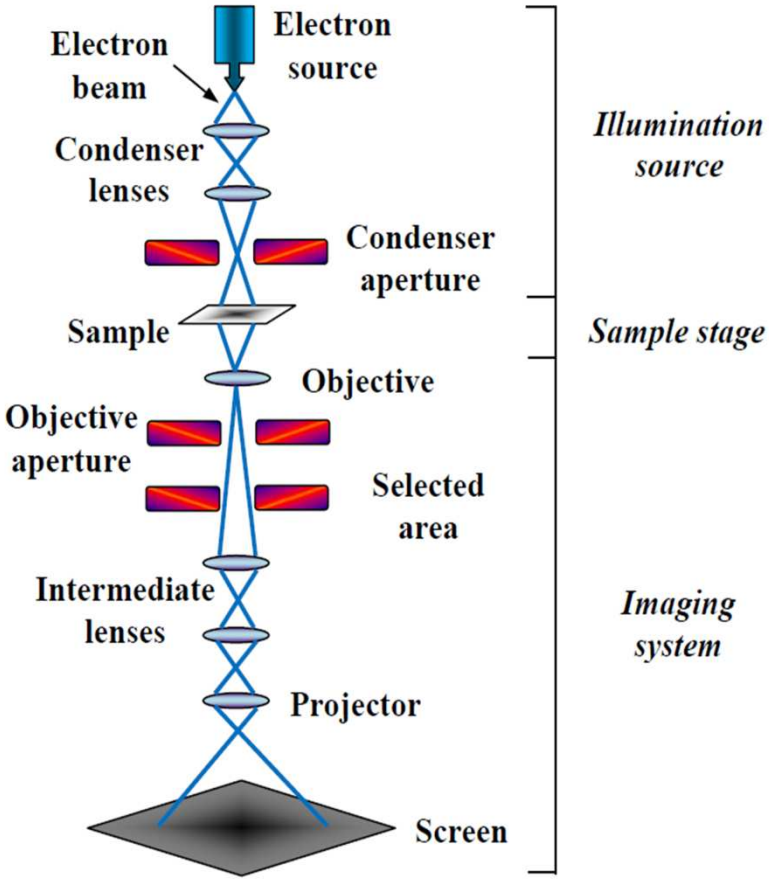


Figure 3.8 An illustration of the layout and components of a transmission electron microscope [95].

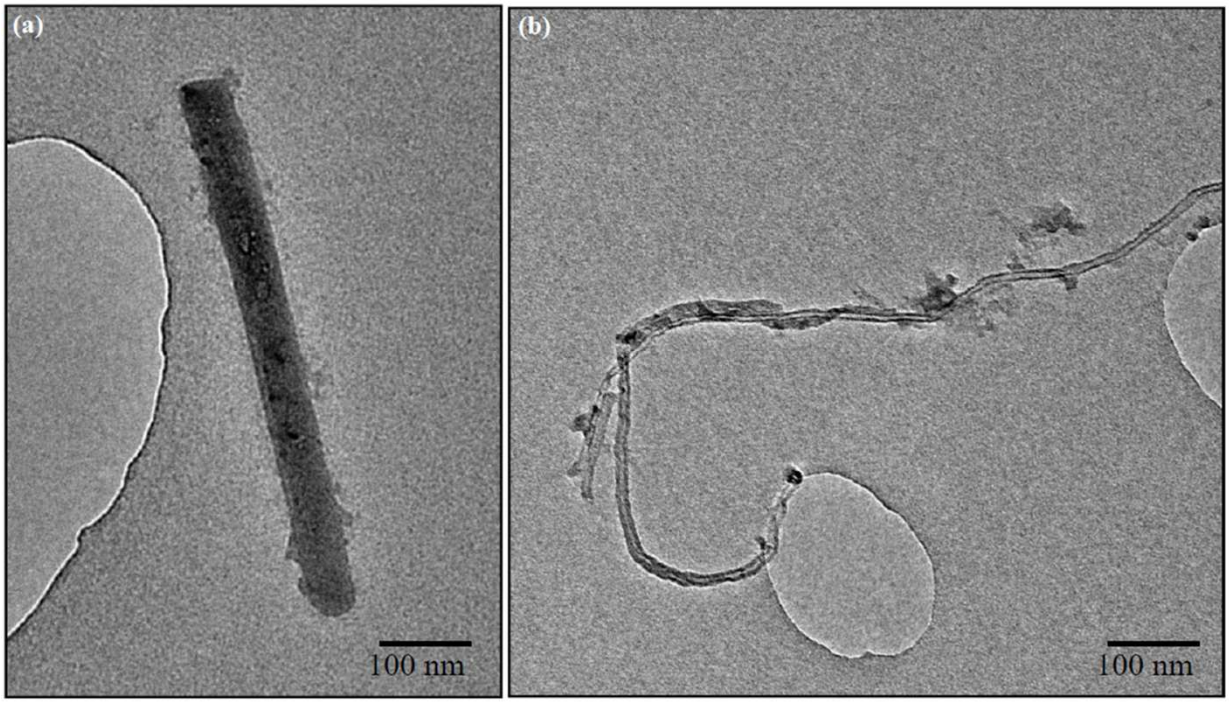


Figure 3.9 TEM micrographs of a **(a)** nanorod and **(b)** nanotube.

3.6 The Scanning Electron Microscope (SEM)

The first commercial SEM was built in 1938 by M. von Ardenne. It is a non-destructive analytical technique used to image samples at the micron-scale. SEM relies on the detection of backscattered or secondary electrons from relatively thick (so-called bulk samples composed of nanomaterials) samples [95], unlike TEM, which can only analyze very thin samples.

The sample is bombarded with a focused beam of incoming (primary) electrons from an electron source as depicted in Figure 3.10. The primary electron transfers energy to the sample, which causes electrons from the sample to be dislodged. These dislodged electrons are known as secondary electrons, and are attracted and collected by a positively biased secondary electron detector, and converted to a signal.

The secondary electrons are emitted with a range of energies making it difficult to focus them onto an image by electron lenses, so a scanning principle is used to form an image. This principle involves the focusing of primary electrons into a small-diameter electron probe that is scanned across the sample and electrostatic and magnetic fields applied at right angles to

the beam change the electrons direction of travel. By scanning simultaneously in two perpendicular directions, a square or rectangular area of the sample (known as a raster) can be covered, and an image of this area can be formed by collecting secondary electrons from each point on the sample. Secondary electrons are used mainly to resolve topographic and charging information. SEM was carried out on a sample prepared by laser pyrolysis and the resulting SEM micrograph taken in secondary electron mode is shown in Figure 3.11.

Apart from secondary electrons, the bombardment of primary electrons also results in the emission of backscattered electrons from the sample. Backscattered electrons are more energetic than secondary electrons, and have a definite direction. Backscattered electrons can only be detected if the detector is in the path of travel of the primary electrons as depicted in Figure 3.10. Backscattered electrons are used mainly to enhance compositional contrast and crystal orientation. SEM images have a relatively large depth of focus which results from the fact that electrons in the SEM travel very close to the optic axis which creates good image resolution.

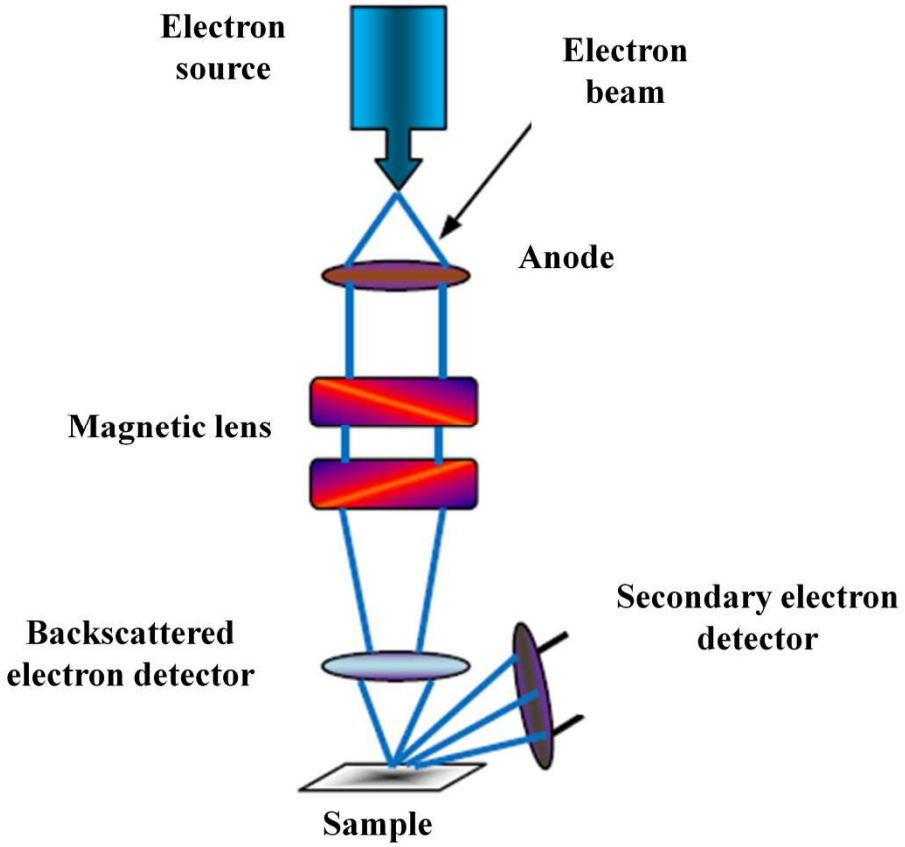


Figure 3.10 An illustration of the layout and components of a scanning electron microscope [95].

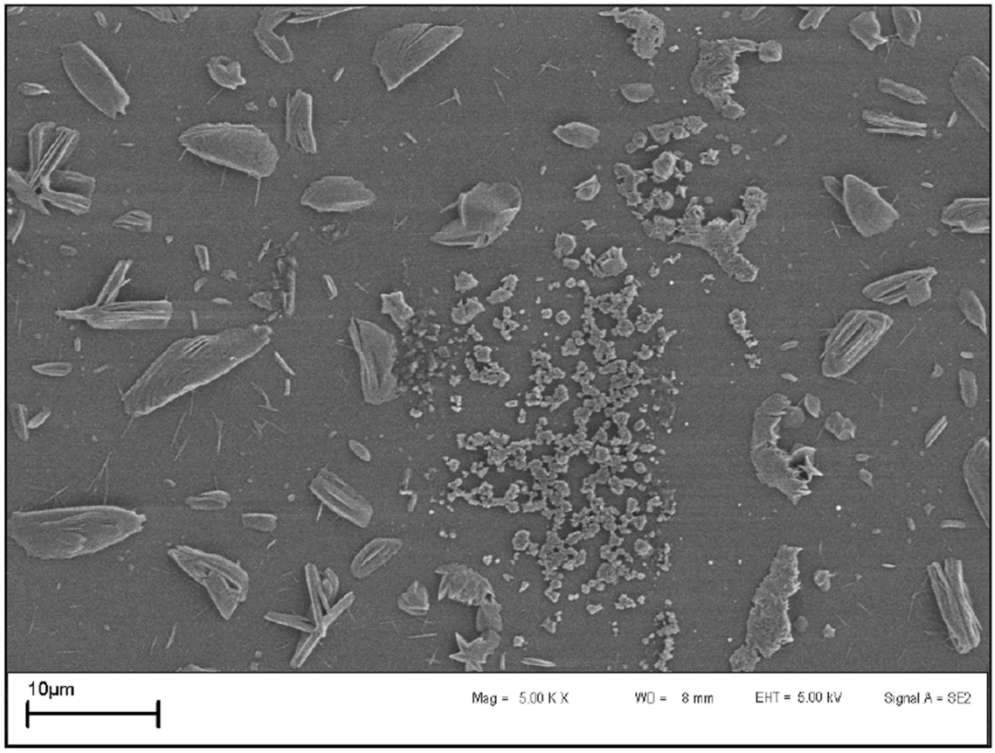


Figure 3.11 A secondary electron mode SEM micrograph of various tungsten oxide nanostructures.

3.7 Energy Dispersive X-ray Spectroscopy (EDS/EDX)

EDX was discovered in 1951, and combines the electron microscope capability with that of x-ray spectroscopy. It is a non-destructive technique used for chemical characterization and to quantify the atomic composition of a sample [92], and so it can be used to confirm the results from FTIR, Raman spectroscopy and XRD.

When a primary electron is incident on a sample, it has a probability of being scattered inelastically by an inner-shell (such as a K-shell) electron. The K-shell electron can undergo a transition to a higher-energy orbit, creates an electron vacancy (hole) in its inner-shell as depicted in Figure 3.12. The inner-shell vacancy can quickly be filled by other atomic electrons by making a downward transition from a higher energy level. During the de-excitation process, energy is released as a photon whose energy ($h\nu$) is that of x-rays, which arises from the difference between the upper and lower energy levels. The energy of the characteristic x-ray photon therefore, depends on the atomic number Z of the atom and on the quantum numbers of the energy levels involved in the transition.

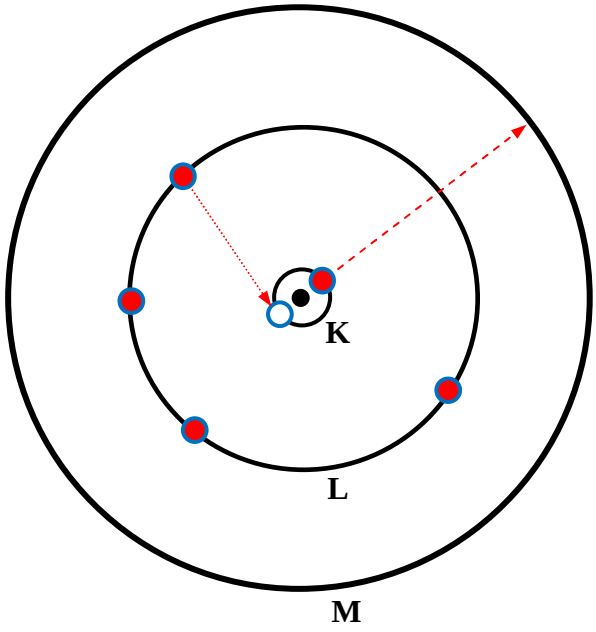


Figure 3.12 The electron orbits of an atom with the electron shells designated by K, L and M, with quantum numbers *n* equal to 1, 2 and 3, respectively. A K-shell electron is excited to the empty M-shell, and an L-shell electron fills the K-shell vacancy in a de-excitation process.

EDX has other closely related analytical techniques such as Auger Electron Spectroscopy (AES) and X-ray Photoelectron Spectroscopy (XPS). AES does not focus on x-ray emission as in EDX, but instead focuses on another species called an Auger electron. XPS focuses on the kinetic energy of ejected electrons, such as Auger electrons, and determines the binding energy from the kinetic energy which is element-specific.

In EDX, the dispersive device is a semiconductor diode which allows the x-ray emitted from the atom to penetrate the diode's transition region (between p and n-doped material), and the x-ray energy can release a considerable number of outer-shell (valence) electrons from the confinement of a particular atomic nucleus [92]. This process is equivalent to exciting electrons from the valence to the conduction band (which creates electron-hole pairs) and results in electrical conduction by both electrons and holes. To ensure that maximum amount of x-rays are absorbed and generate current pulses in an external circuit, the p-n transition region is made much wider than most semiconductor diodes. The diodes are cooled to ~140 K to eliminate the contribution of electronic noise caused by thermal generation of electron-hole pairs. A thin protective window in front of the diode prevents water vapour and hydrocarbon molecules (present at low concentration in a SEM or TEM vacuum) from

condensing onto the diode. The current pulses collected by the detector are fed into a field-effect transistor (FET) preamplifier which is located just behind the diode. To further reduce noise, the FET acts as a charge-integrating amplifier and as each photon is absorbed, the output voltage increases proportionally to its input voltage, which is proportional to the number of electron-hole pairs or photon energy. The sensitivity of the EDX to detect the presence of an element above background noise is on the order of parts per million or 0.1 weight-weight percentage. Figure 3.13 shows the basic layout of the components used for EDX and the technique was carried out on a sample prepared by laser pyrolysis and the resulting EDX spectrum of the tungsten oxide sample on a substrate is shown in Figure 3.14.

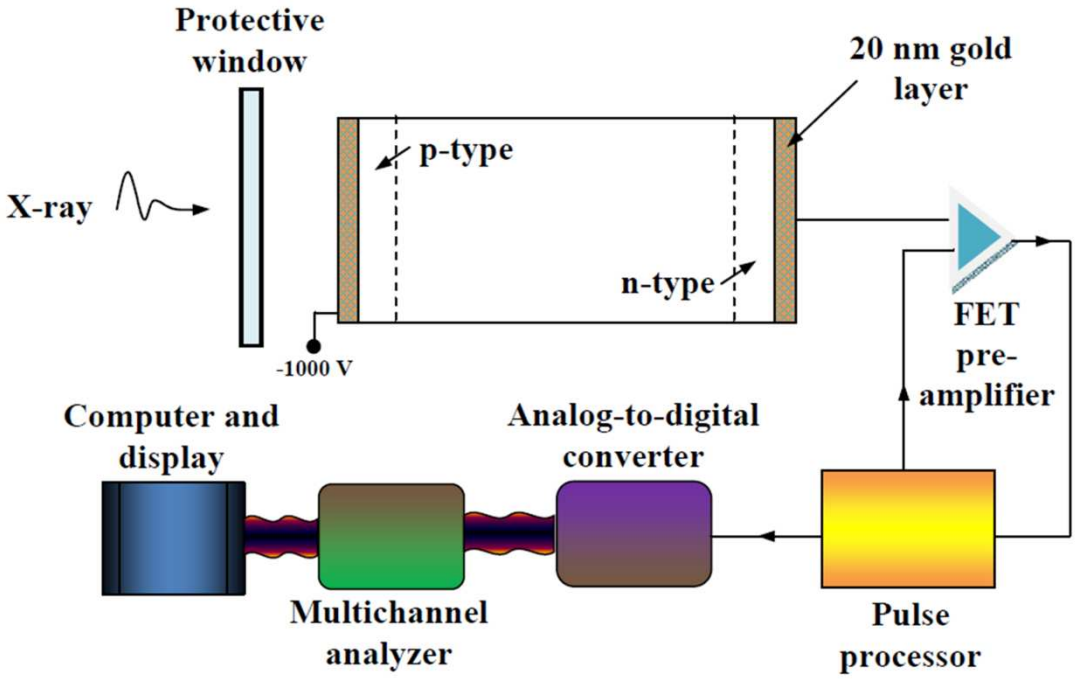


Figure 3.13 A schematic diagram of an EDX detector and its signal processing circuitry [92].

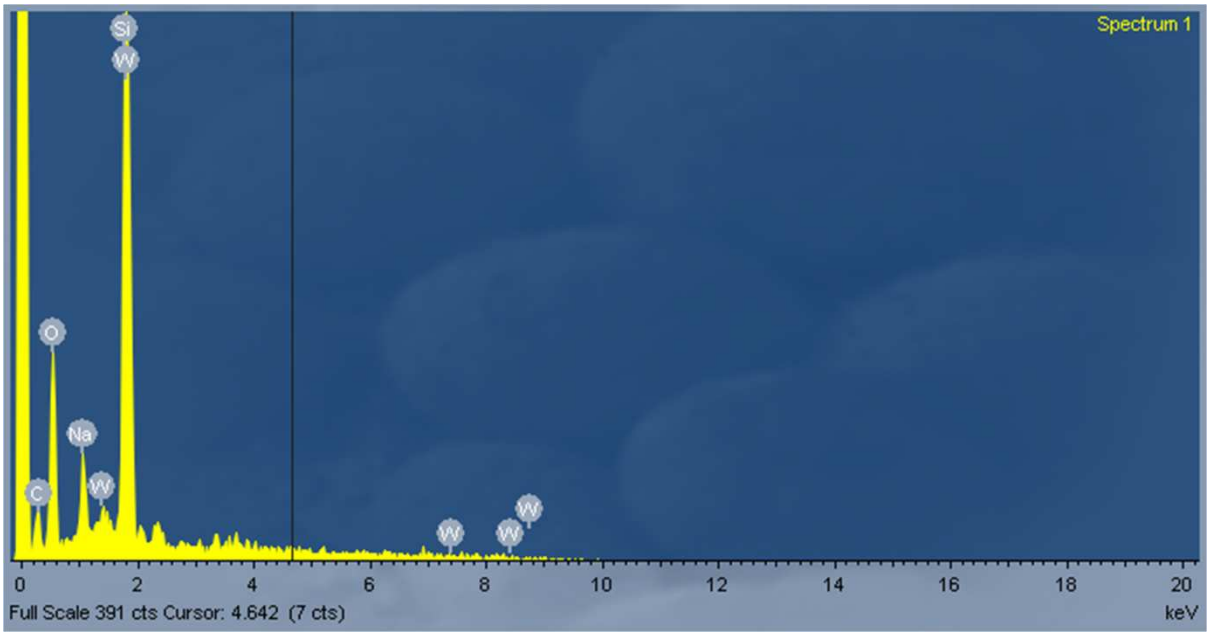


Figure 3.14 An EDX spectrum of a tungsten oxide, where the tungsten peaks are represented by W and the oxygen peak are represented by O. The carbon (C) results from carbon-coating the sample to make it conductive, and the sodium (Na) and silicon (Si) are present in the substrate.

3.8 Summary

The various characterization techniques used in this study were covered in detail. FTIR provides information about the absorption band frequency of the chemical precursor and so it can be determined into which band the laser wavelength is distributed. Raman spectroscopy and XRD helps to accurately identify the chemical composition with the aid of literature and PDFs, respectively. The electron microscopes give a description of the morphology and topography of the products and EDX confirms that the product contains the expected elements and eliminates the possibility of foreign particle contributions such as dust. The characterization techniques will be applied to observe and analyze the reactants and products applicable to the laser pyrolysis technique.

Chapter 4

The Carbon Dioxide (CO_2) Laser

4.1 Introduction

Light Amplification by the Stimulated Emission of Radiation, commonly known by the acronym 'LASER', describes a variety of unique radiation emitting devices. Laser light differs from white light in that laser light is monochromatic, coherent, and slowly diverging. A comparison of the properties between white light and laser light is illustrated in Figure 4.1. One class of lasers is infrared gas lasers, such as the carbon dioxide (CO_2) laser which "lases" in the far-infrared region of the electromagnetic spectrum. The wavelengths (9-11 μm) of this laser are readily absorbed by most materials, which allows for applications such as material processing, cutting, cladding and welding [98]. Apart from the favourable wavelength, efficiency and stability, CO_2 gas lasers are some of the most powerful commercially available lasers with thousands of watts of power output. In this study we make use of a CO_2 laser to carry out laser pyrolysis.

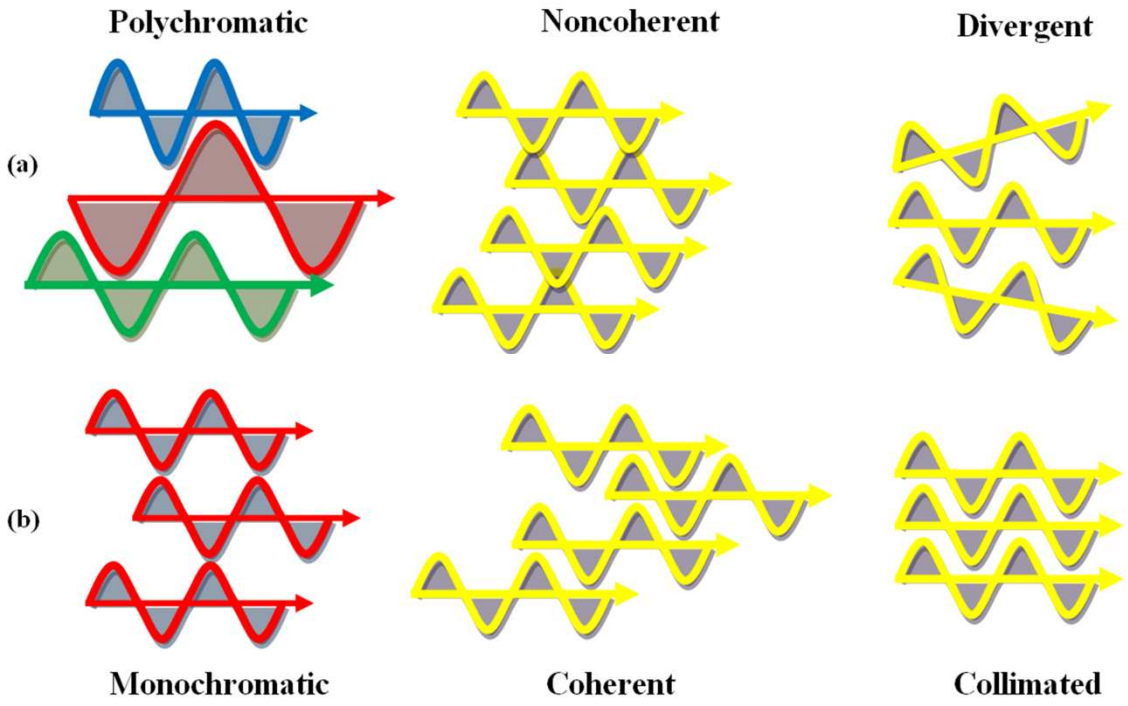


Figure 4.1 The properties that distinguish **(a)** white light from **(b)** laser light [99].

4.2 Theory of CO_2 Laser operation

The atoms of the CO_2 molecule are arranged adjacent to each other to form a geometrically linear and symmetric structure, and this geometry gives rise to three possible vibrational modes as shown in Figure 4.2.

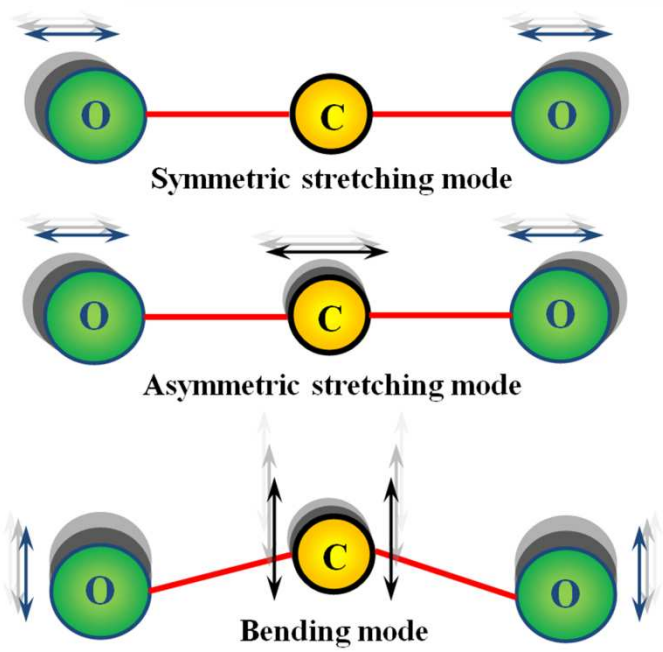


Figure 4.2 An illustration of the three possible vibrational modes of the CO_2 molecule [100].

The symmetric stretching, asymmetric stretching and bending vibrational modes of the CO_2 molecule gives rise to the 1388 cm^{-1} (0.17 eV), 2349 cm^{-1} (0.29 eV) and 667 cm^{-1} (0.08 eV) wavenumbers, respectively. The three respective wavenumbers for the three modes produce the three-level system shown in Figure 3.3, and are represented by the quantum numbers ($n_1n_2n_3$) 010, 020 and 001. The first quantum number (n_1) represents the quantum level or excitation number of the symmetric stretching mode, the second quantum number (n_2) refers to the bending mode and the third quantum number (n_3) refers to the excitation number of the asymmetric mode.

The vibrational modes can further undergo rotational vibrations that cause degeneracy and further subdivide the whole series of levels into quantized levels specified by the rotational quantum number *J*. The selection rule states that *J* can change by ±1 for the vibrational-rotational transitions. Transitions where *J* increases by one (+1) are referred to as the dominant *P*-branch transitions and the transitions where *J* decreases by one (-1) are referred to as the *R*-branch transitions. The *P*-branch transition has more gain than the competing *R*-branch and thus outputs more power. The simultaneous change of the vibrational and rotational quantum states causes the highest gain at the ~10.6 µm transition. The competition between these branches causes a possible wavelength range between 9 µm and 11 µm and a single wavelength can be selected with the use of a diffraction grating [100].

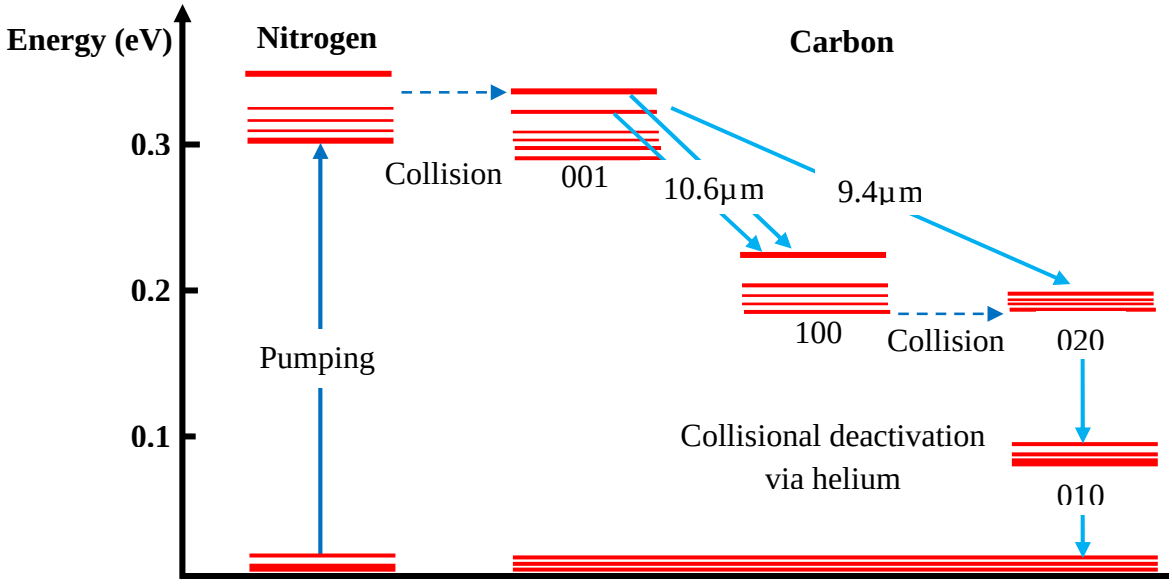


Figure 4.3 The three energy levels of the CO_2 molecule with the subdivided levels caused by rotations in the vibrating molecule and also shown here are the lasing transitions from two of the resonant modes [100].

The active lasing medium of CO_2 lasers is composed of a mixture of three gases as suggested in Figure 4.3. For the CO_2 laser used in this experiment, the gas mixture was composed of 7% CO_2 gas, 18% nitrogen gas and helium gas constitutes the remainder of the mixture. The gas mixture flows inside a plasma tube that is pumped by a high current excitation source which affects the energy levels as depicted in Figure 4.3. The first excited energy level of nitrogen has a long-lived metastable state (~2 ms) that makes collisional transfer of energy very efficient to the CO_2 molecule. The nitrogen molecule can only transfer its energy to the CO_2 by resonant scattering and collisions because homonuclear molecules like nitrogen cannot

lose energy by photon emission. The energy from the nitrogen's first excited vibrational state is transferred to the carbon dioxide's asymmetric stretching mode since there is only an 18 cm^{-1} energy gap between the two levels. After this energy transfer, the nitrogen now exists in a lower excited energy state and collisions with helium bring the nitrogen down to the ground state. The energy collected by the helium is then extracted as heat into the atmosphere by an external air or water-cooled system that is connected to the plasma tube. The helium also assists in bringing the carbon dioxide molecules from the second energy level down to the ground state and enhances the thermal conductivity of the gas mixture [101].

4.3 The PL6 CO_2 Laser

The model of CO_2 laser used is the PL6-030 laser from Edinburgh Instruments, pictured in Figure 4.4, and this laser was chosen because it is wavelength tunable. Because wavelengths produced are in the far-infrared region of the electromagnetic spectrum, the mirrors are coated with either gold, copper or molybdenum, and the other optics such as lenses are zinc selenide. The totally and partially reflecting coated mirrors are mounted on either end of two plasma tubes forming a resonator and the active lasing gas mixture flows continuously through the plasma tubes at a pressure of 25 mbar and is evacuated to an outlet pipe. A high voltage supply (LPS-2000) supplies currents of 40 mA on two-channels, one for each plasma tube via an anode and cathode connection. This high current is converted to a laser power of 65 W in a continuous wave laser beam. A water-cooling chiller constantly circulates water through the outer cavity of the plasma tubes to expend the heat. It takes about 10 minutes for this laser to reach thermal equilibrium, and the output beam profile of the PL6 laser is ~90% TEM_{00} transverse electromagnetic mode due to the design of the laser.

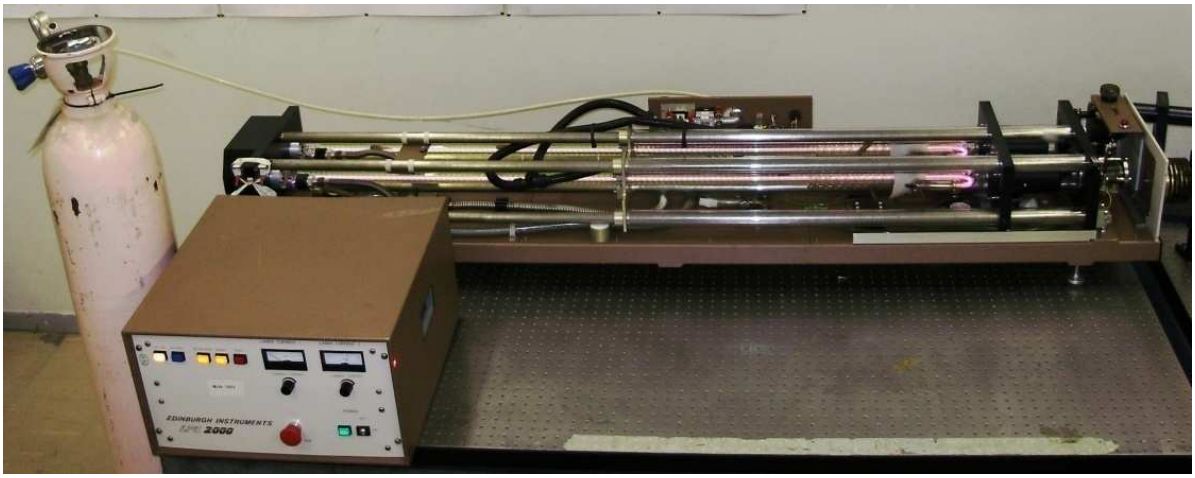


Figure 4.4 A picture of the PL6 laser, power supply and the cylinder containing the CO_2-N_2-He gas mixture.

4.4 Characterization of Lasers

The laser beam propagation parameters are important for experimental purposes because it helps to understand the laser dynamics. There are various laser beam profiling techniques available for various laser types and here two possible techniques used for CO_2 lasers will be considered.

4.4.1 *Properties of Gaussian-like Beams*

A laser beam with a TEM_{00} mode has a Gaussian-like intensity profile similar to the one shown in Figure 4.5. At any position z on the propagation axis, the intensity profile I is defined by

$$I(\rho, z) = I_0 \left[\frac{\omega_0}{\omega(z)}\right]^2 \exp\left[-2\frac{\rho^2}{\omega^2(z)}\right], \tag{4.1}$$

which is a function of the radial position $\rho\ (= \sqrt{x^2 + y^2})$ and the exponential term defines a Gaussian distribution, I_0 is the square of the electric field of the light wave and is the peak intensity on the beam axis, $\omega(z)$ is the beam radius at propagation distance z and ω_0 is the minimum beam radius or waist at position z_0.

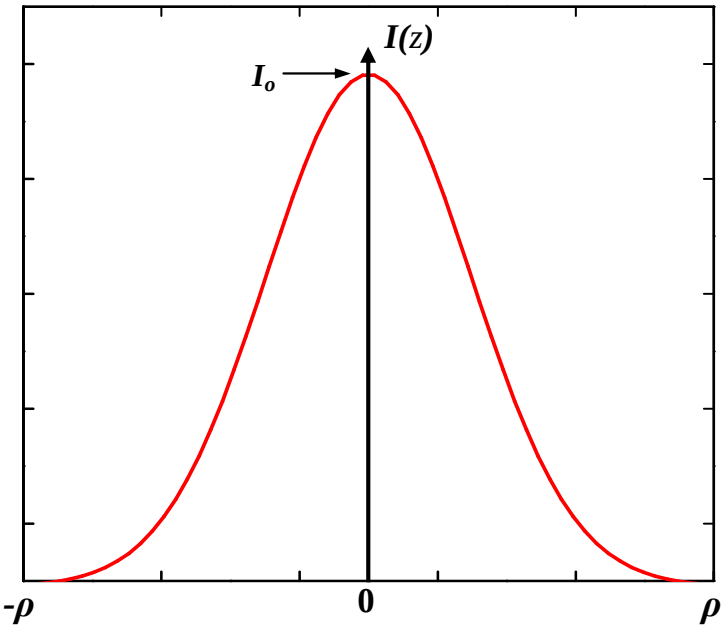


Figure 4.5 An illustration of a Gaussian intensity profile over an arbitrary radial distance.

The peak power density on the beam axis in terms of peak intensity I_0 contained in the laser beam can be defined by

$$P_d(z) = I_0 \frac{\omega_0^2}{\omega^2(z)}. \tag{4.2}$$

The respective beam radii denoted by $\omega(z)$ and ω_0 are illustrated in Figure 4.6. The beam radius at some propagation distance z is given by

$$\omega(z) = \omega_0 \sqrt{1 + \left(\frac{z - z_0}{z_R}\right)^2}, \tag{4.3}$$

where z_R is the so-called Rayleigh range. The Rayleigh range is related to the beam quality factor M^2 and the wavelength of the laser beam through the relation

$$z_R = \frac{\pi\omega_0^2}{M^2\lambda}. \tag{4.4}$$

The Rayleigh range is the distance at which the cross-sectional area of the laser beam doubles after z_0 and is often interpreted as a measure of how far the laser beam propagates without significant divergence. Thus a long Rayleigh range is favourable for experimental purposes. The beam quality factor M^2 is a measure of how many modes are oscillating in the laser beam and impacts on the space beam width product [102]. For an ideal TEM_{00} mode, M^2 equals 1, and for Gaussian-like beams M^2 is greater than 1.

The angle between the tangent line to the diverging laser beam and the central propagation axis shown in Figure 4.6 is known as the divergence angle φ and is given by

$$\varphi = \frac{M^2\lambda}{\pi\omega_0}. \tag{4.5}$$

The divergence angle gives an indication of how collimated the beam is or if it diverges quickly.

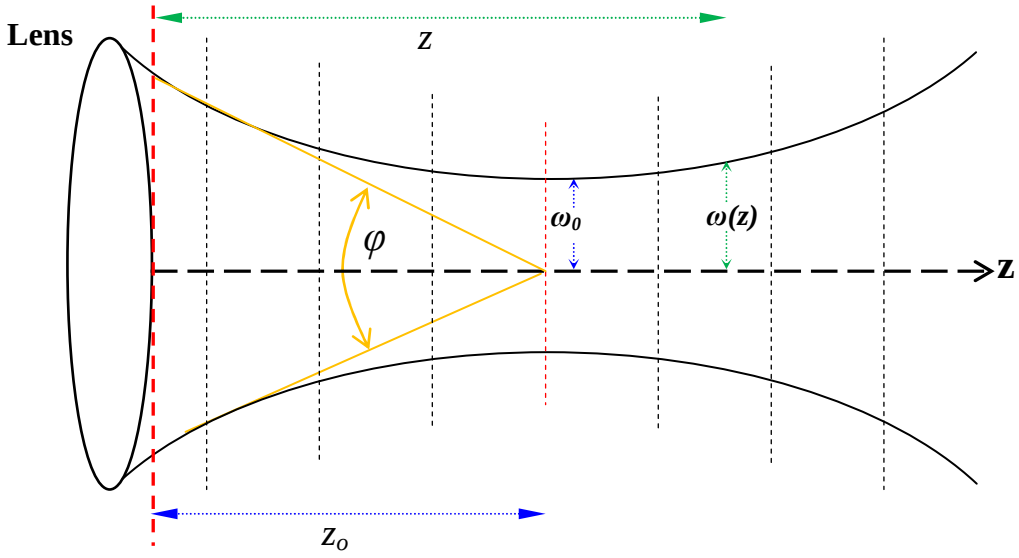


Figure 4.6 A schematic diagram of beam propagation through a lens.

4.4.2 Two Experimental Methods used to Characterize Lasers

The characterization of the laser beam was carried out using two methods. The first method is the scanning slit method which uses a thin slit and power meter to measure beam intensity passing through a thin slit for incrementally adjacent positions to the beam at chosen axial or propagation distances away from a focusing mirror in the x and y-direction. The second method is the pyrocam method which uses an infrared camera to capture an image of the laser beam at chosen axial or propagation distances away from a focusing mirror and the beam diameter is extracted from the data.

4.4.2.1 *The Scanning Slit Method*

The scanning slit method is a suitable and accurate profiling technique that works best for Gaussian-like laser beams, because non-Gaussian beams have convergence problems associated with beam profiles that contain discontinuities [103]. The slit width must be at most 10% of the beam diameter for accurate profiling.

The Gaussian-like profile is traced out with a thin slit by integrating the intensity of the beam over the area of the slit width. The resulting measurement from the thin slit width is equivalent to the original cross section convolved with the profile of the slit. This measurement is carried out over the whole beam profile, and a least-squares Gaussian fit is

applied to the measured data to determine the beam radius at different propagation distances. By squaring the beam radii and plotting it against its propagation distances, the relevant beam parameters can be extracted.

This method is simple and has many advantages over other profiling methods. The thin slit acts as a natural attenuator, which is advantageous because it is possible to measure high powered beams directly without decreasing sensitivity and without increasing noise of the signal. There is also no need to differentiate the signal with respect to position to obtain the beam profile. These two advantages make this method superior to other known methods, and is the preferred choice for Gaussian-like beam profiling.

The scanning slit method has a very simple setup and the layout for the case of CO_2 laser beam profiling is depicted in Figure 4.7. The CO_2 laser is co-aligned with a helium neon laser beam in order to follow the path of the CO_2 beam. The helium neon beam is combined with the carbon dioxide beam by using a beam combiner that transmits the wavelengths of the CO_2 beam but reflects the 633 nm wavelength of the helium neon beam. The two aligned beams are projected onto a copper coated focusing mirror which has a 1 m radius of curvature, which is effectively a lens with a focal length of 500 mm. This mirror focuses the beam through the slit (slit width of 60 μm measured with a travelling microscope) and onto a power meter (Ophir L50A) that measures the resulting power.

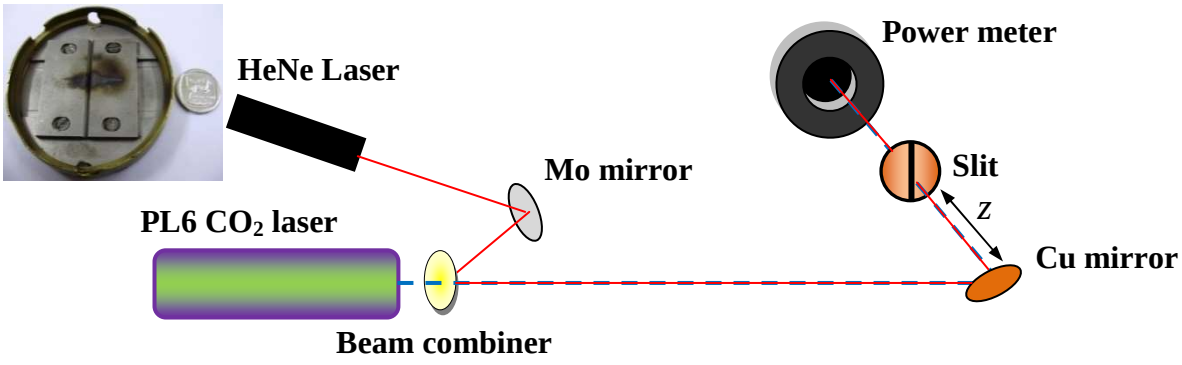


Figure 4.7 A schematic of the setup used to characterize the CO_2 laser beam using a thin slit. The inset shows the slit size relative to a South African one rand coin.

4.4.2.2 *The Pyrocam Method*

The Pyrocam (PY-III-C-A) is a solid state, high performance pyroelectric camera that can measure and analyze low-level and high-level signals of an infrared laser beam. This camera has a uniform infrared response and can capture thermal images of hot sources in real-time. Since it measures in real-time, it can be used for pulsed lasers or continuous wave lasers. For continuous wave lasers however, an external chopper has to be attached to the pyrocam to pulse the beam and synchronize it to the rate at which the camera captures frames. Each frame of the camera detector has 124×124 pixels on 100 μm centres that respond to wavelengths from 1 μm to 1000 μm. The image frame is mathematically analyzed by computer software that implements peak, centroid or knife edge methods [104]. This profiling technique can be used to characterize Gaussian-like and non-Gaussian laser beams, which make this method versatile.

The setup used for the pyrocam method for the specific case of CO_2 laser profiling is shown in Figure 4.8. This setup is a little more complicated than that used for the scanning slit method, because the high-powered beam needs to be externally attenuated. Attenuators, reflecting wedges and high reflectors are needed to reduce the laser power from 75 W down to 100 mW, because high powers will burn out the camera's pixels. An image captured by the pyrocam is pictured in Figure 4.9.

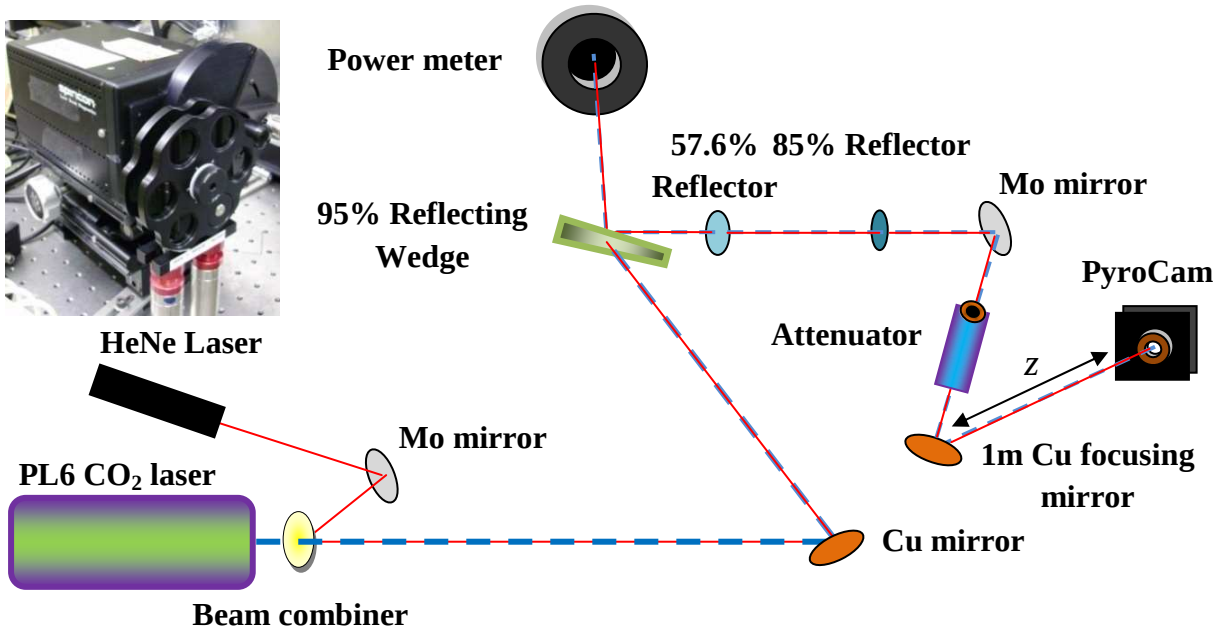


Figure 4.8 The setup used to characterize the laser beam using a pyrocam. The inset shows a picture of the pyrocam with a chopper attached to the front of it.

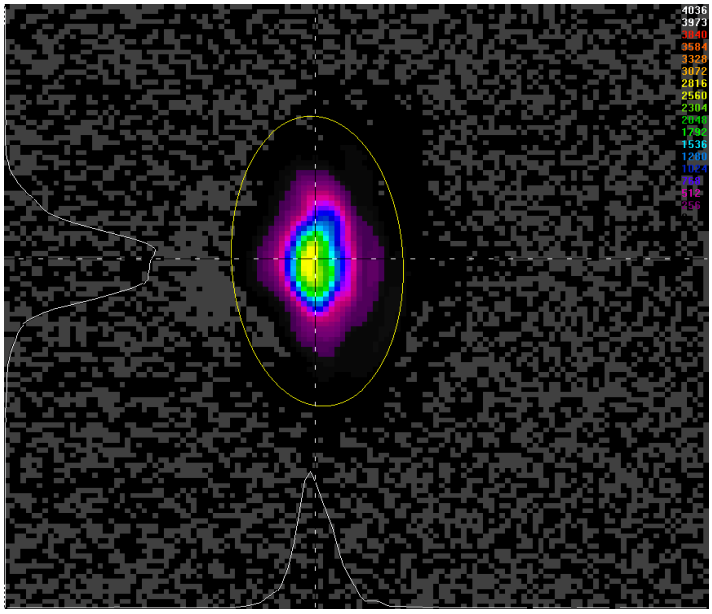


Figure 4.9 An image taken by the pyrocam showing the heat distribution of the beam by the different colours and the intensity distribution on the x and y axes are also shown.

4.4.3 Results of the Laser Parameters

The results for the scanning slit method are presented first. The laser beam profiles in the y-direction only are plotted for each propagation distance z, and the profile at four propagation distances are shown in Figures 4.10 (a)-(d) with reference to the 1 m radius of curvature mirror that has a predicted focal length f ~50 cm. The beam profiles were fitted with a least squares Gaussian function so that the beam radii for the propagation distances can be extracted, halved, then squared and plotted against its respective propagation distance.

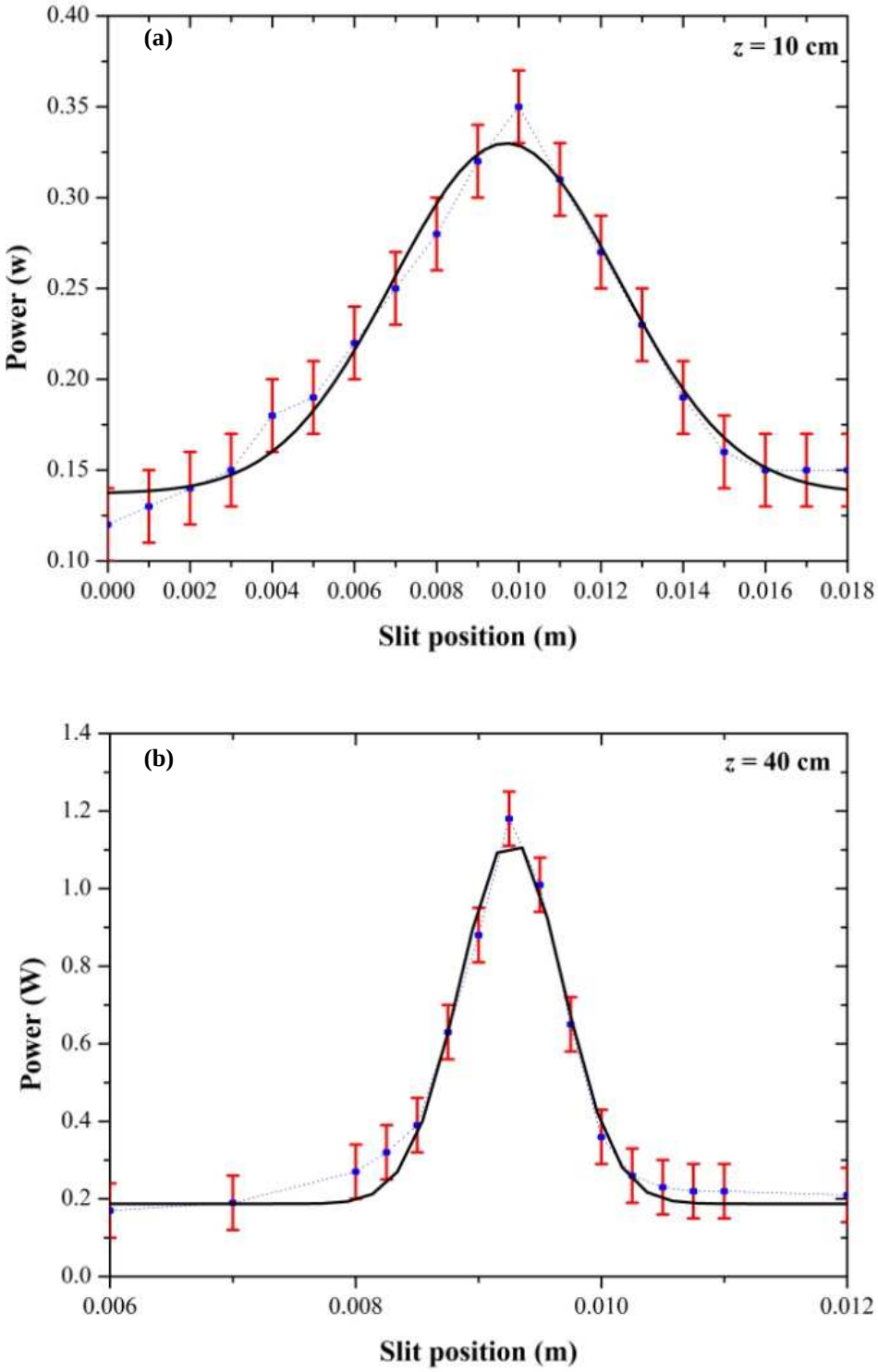
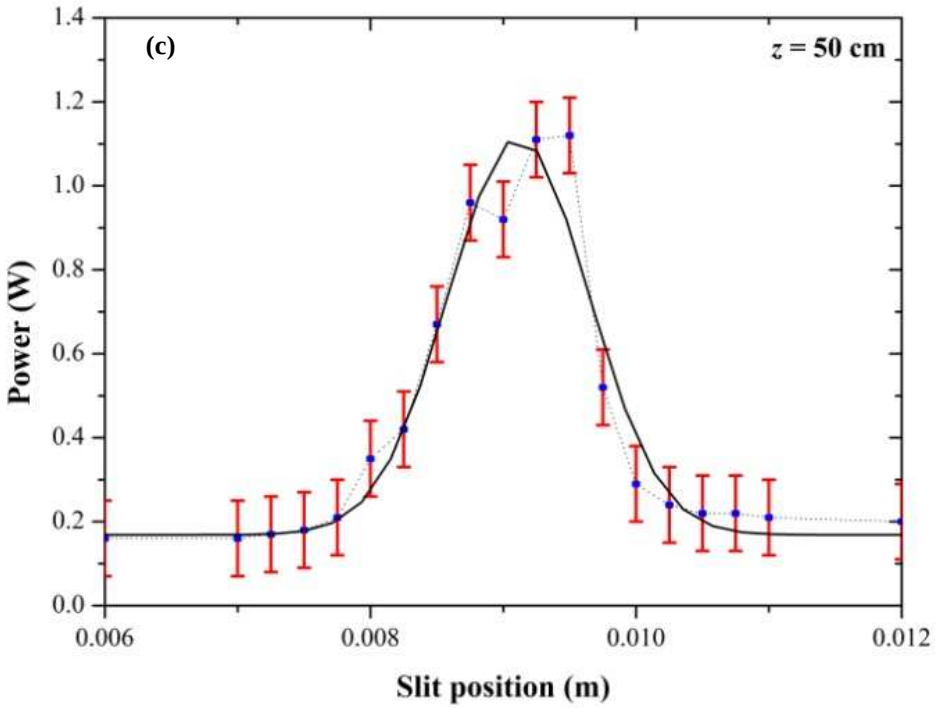


Figure 4.10 (a)-(b) Plots of the power for varying slit positions at various propagation distances between the focusing mirror and thin slit.



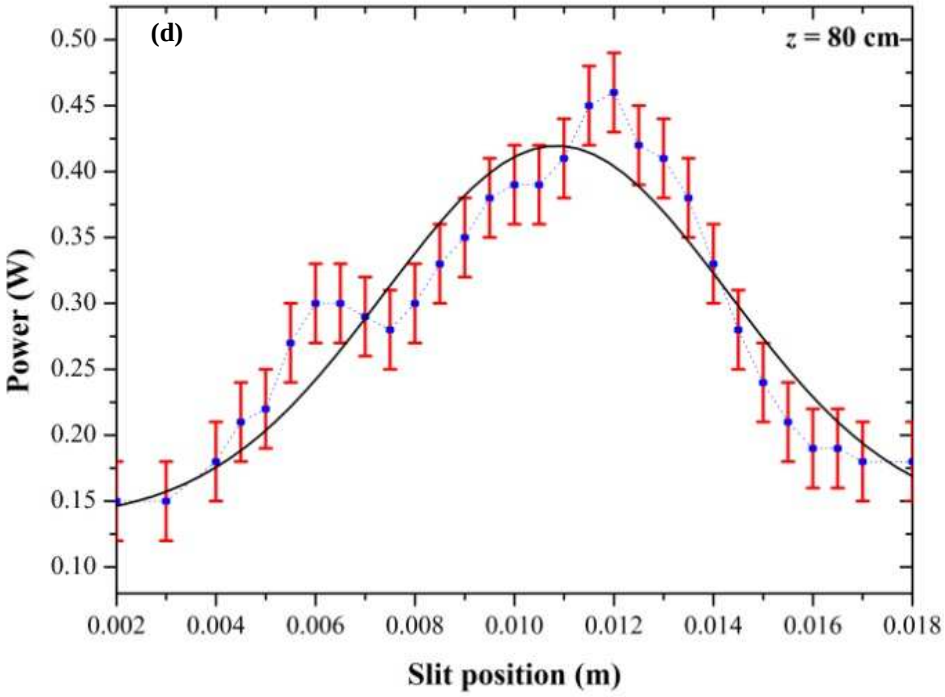


Figure 4.10 (c)-(d) Plots of the power for varying slit positions at various propagation distances between the focusing mirror and thin slit.

The beam profiles are Gaussian-like before the focal plane of the focusing mirror, as evident in Figures 4.10 (a)-(b), as opposed to the beam profiles from the focal plane of the focusing mirror which show multiple peaks depicted in Figures 4.10 (c)-(d). The scanning slit method was also used to compare the PL6 laser to a Synrad (D 48-2-115) laser, which has a Gaussian-like beam profile. The results are discussed in section 4.7.

The characterization of the PL6 laser was then carried out using the pyrocam method. Images of the beam for the same propagation distances that were chosen in the scanning slit method were captured by the infrared camera. The beam diameters from the images were halved, and then squared and plotted against its respective propagation distance as shown in Figure 4.11.

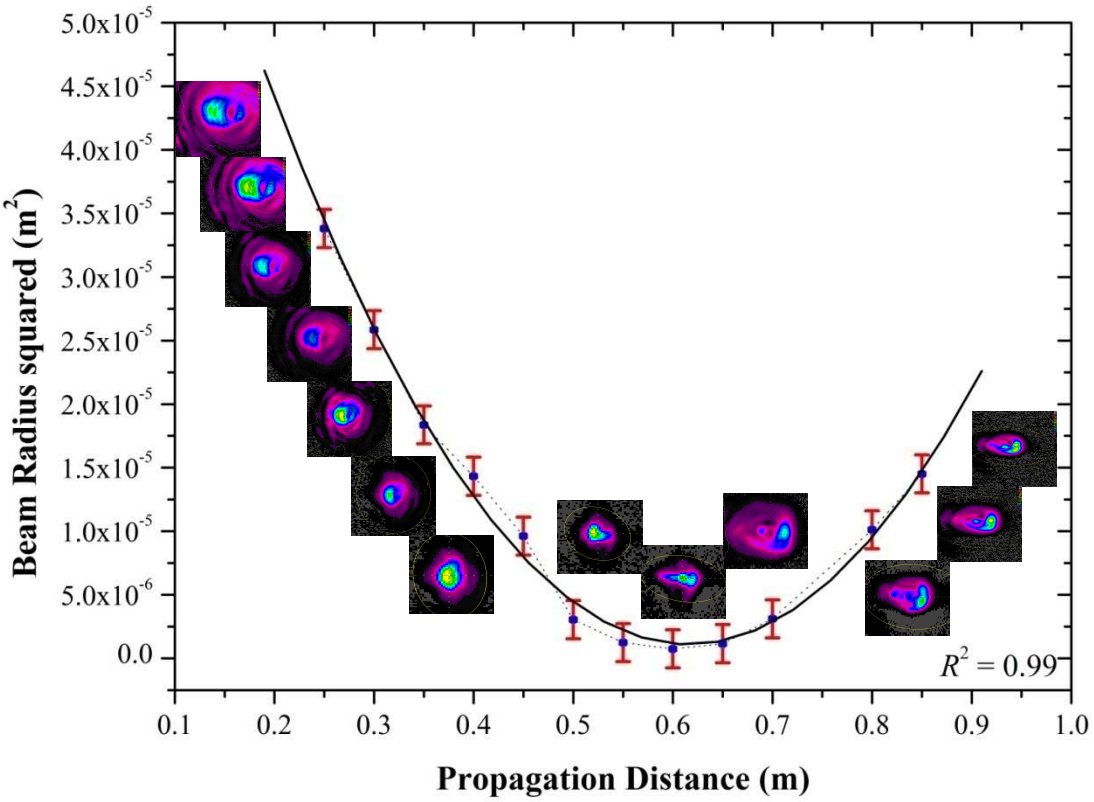


Figure 4.11 The second-order quadratic fit from the data of the pyrocam method.

To utilize the results of this plot, equation (4.3) needs to be rearranged to a quadratic equation to coincide with the parameters extracted from the graph of Figure 4.11. The quadratic form of equation (4.3) is given by

$$\omega^2(z) = \left(\frac{M^2\lambda}{\pi\omega_0}\right)^2 - 2z_0\left(\frac{M^2\lambda}{\pi\omega_0}\right)^2 z + \left(\frac{M^2\lambda}{\pi\omega_0}\right)^2 z_0^2 + \omega_0^2. \tag{4.6}$$

Extracting the data from the equation of the polynomial fit of Figure 4.11 and equation (4.6), the following data was obtained:

$$\left(\frac{M^2\lambda}{\pi\omega_0}\right)^2 = 2.489 \times 10^{-4},$$

$$-2z_0\left(\frac{M^2\lambda}{\pi\omega_0}\right)^2 = -3.065 \times 10^{-4}\ \text{m}, \tag{4.7}$$

and

$$\left(\frac{M^2\lambda}{\pi\omega_0}\right)^2 z_0^2 + \omega_0^2 = 9.547 \times 10^{-5}\ \text{m}^2.$$

Solving equations (4.7) simultaneously, the beam waist position z_0 was found to be 0.616 m±7%. The value of z_0 was found to be ~19% more than *f*, which explains why the graph of Figure 4.11 is asymmetric. This discrepancy between the expected focal point could be a result of a fast diverging beam. The beam waist ω_0 for the 1 m radius of curvature mirror was found to be 1.054×10^{-3} m±13% while the unfocused beam radius was found to be 6.11×10^{-3} m±25% which implies that the 1 m focusing mirror made the beam radius six times smaller. Using equation (4.5), the divergence angle φ was found to be 16 mrad±8% which confirms that the beam has high divergence. The Rayleigh range z_R was found to be 0.066 m±1% and thus the area of the beam doubles at a distance of 0.682 m away from the focusing mirror. The beam quality factor M^2 was found to be 4.93±0.8% which suggests that the PL6 laser outputs a non-Gaussian beam.

4.5 Laser Polarization

Light waves are composed of an electric field and magnetic field and their respective vectors are perpendicular to each other and to the direction of propagation of the light wave. Polarized light is dependent on the electric field vector since the magnetic field vector is always confined perpendicular to the electric field [105].

One way of achieving laser power variability is by using a polarization based attenuator shown in the inset of Figure 4.12. This attenuator consists of two zinc selenide windows which are represented in Figure 4.12. The incident laser beam first propagates through air which has a refractive index n_1 of 1.00, and then through the zinc selenide window which has a refractive index n_2 of 2.40. The windows are mounted at Brewster's angle θ_B ($= \tan[n_2/n_1]$) which is found to be 1.18 rad. The laser beam is refracted between two different media, and so two windows are used to correct for refraction and make the incoming and outgoing beam collinear.

The laser beam moves through the four surfaces T_1, T_2, T_3 and T_4 of the two windows alternatively getting refracted between the air and zinc selenide media. The laser beam strikes the surface T_1 at incident angle θ_i and is refracted by an angle θ_t in the zinc selenide window. The beam then strikes surface T_2 at the refracted angle θ_t and leaves at angle θ_i. The laser beam then undergoes the same transformation in surfaces T_3 and T_4 and eventually emerges from the attenuator with the same incident angle θ_i. Since the windows are fixed at Brewster's angle in this case, the angle of incidence always equals Brewster's angle, and as the attenuator is rotated, the windows are also rotated adjacent to the laser beam. The laser beam always strikes the window at Brewster's angle throughout the rotation, such that only the plane of the light is affected. The transmission power of the beam varies sinusoidally with the attenuation angle. Therefore, the rotation angle that allows full transmission of the laser beam coincides with the angle of the plane of light which corresponds to the polarization of the light beam.

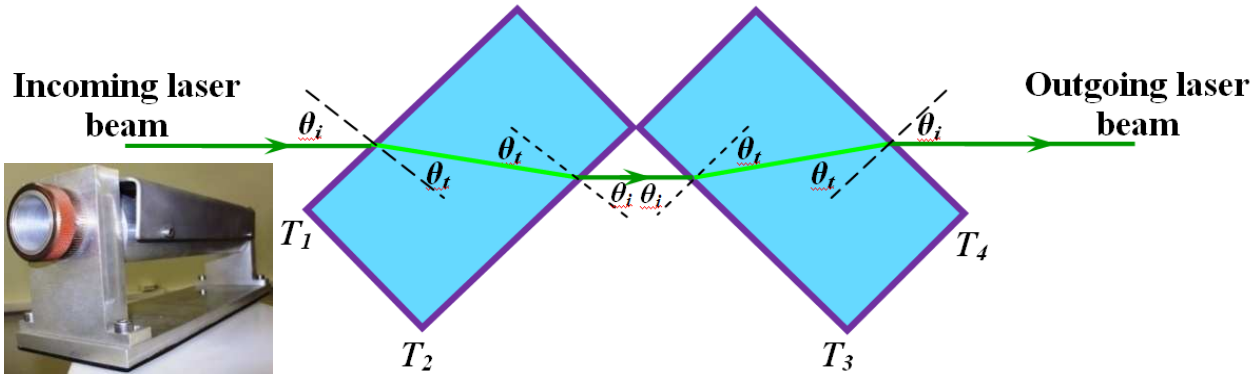


Figure 4.12 The picture shows the layout and beam propagation through the windows in an attenuator and the inset shows a home-made attenuator.

Figure 4.13 illustrates the determination of the polarization of the PL6 laser. The attenuator is rotated and the relative intensity is plotted. From Figure 4.13, it is seen that the polarization is vertical, since maximum transmission is found at 0 rad (or 0 deg), 3.14 rad (or 180 deg) and 6.28 rad (or 360 deg).

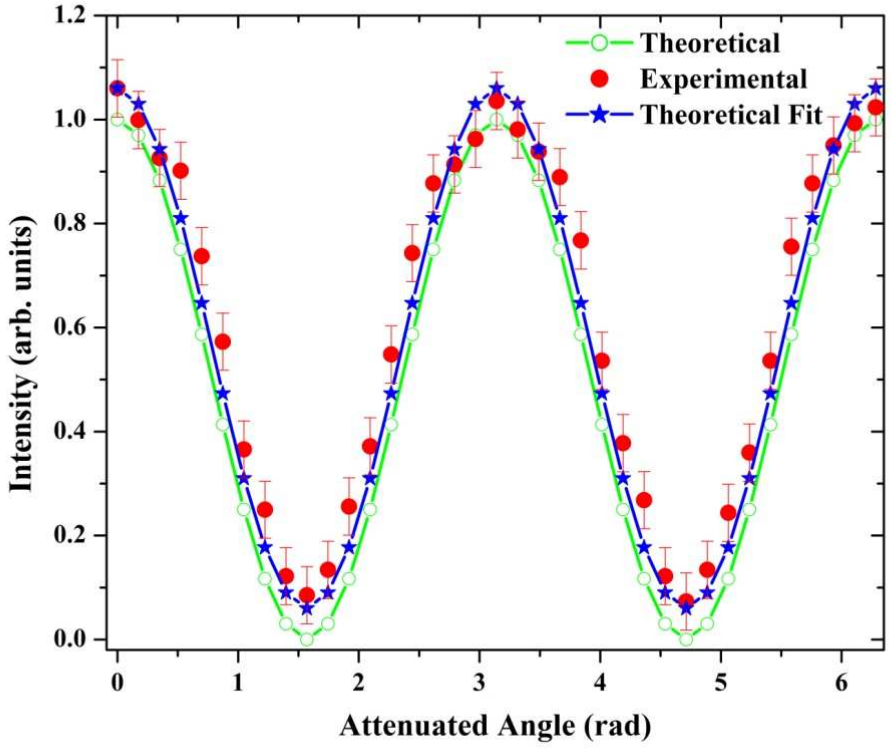


Figure 4.13 The total intensity transmission for the attenuated angles for the theoretical, normalized experimental data and the fitted theoretical curves for the experimental data of the PL6 laser.

4.6 Determination of the Laser Wavelengths

4.6.1 *The Experimental Setup used to determine the Wavelength Spectrum of the PL6 Laser*

The experimental setup used to determine the wavelength spectral range is shown in Figure 4.14 which is similar to the setups used before with the addition of a CO_2 spectrum analyzer and a pop-up folding mirror. The pop-up folding mirror directs the laser beam either to the power meter or the spectrum analyzer so the varying power or varying wavelengths can be recorded. The wavelength is varied by rotating the grating in the PL6 laser until the wavelength and branch line is displayed by the spectrum analyzer. The power changes because different branches have different gains.

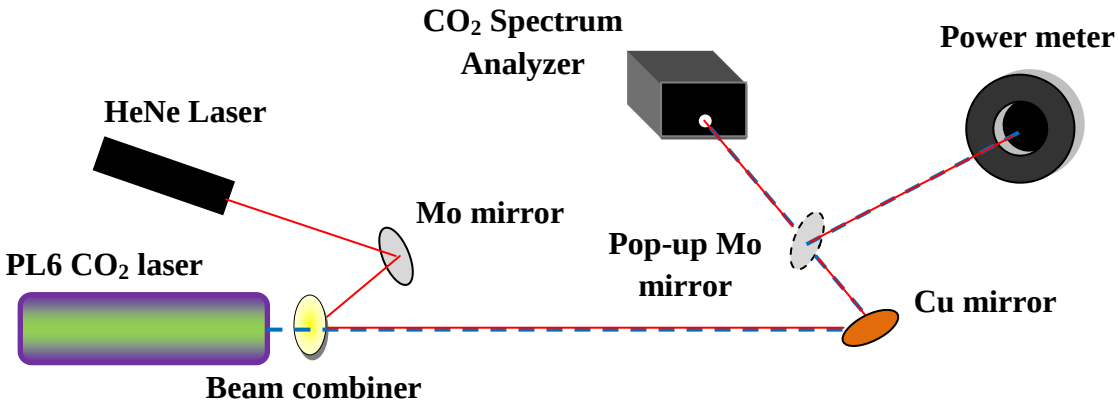


Figure 4.14 A schematic of the setup used to determine the wavelength spectrum.

To determine the wavelength spectrum of the CO_2 laser, a CO_2 Spectrum Analyzer from Macken Instruments (Model-16A) shown in Figure 4.15 is used to display all the lasing transitions of the CO_2 laser. The spectrum analyzer uses a grating spectroscope to identify the rotational lines of the *P* and *R* branches and wavelengths between 9.10 µm and 11.30 µm. The laser beam enters the front of the spectrum analyzer through a 1 cm diameter aperture and just a portion of the beam passes through a variable slit. The light that does not pass through the slit is absorbed by the casing of the spectrum analyzer [106].



Figure 4.15 A picture of CO_2 Spectrum Analyzer (16-A) from Macken Instruments.

The spectrum analyzer uses a UV excited thermal sensitive screen which is depicted in Figure 4.16 and the rotational line and wavelength of the laser beam appears as a darkened area on this screen. This darkened area lies between two scales with the upper scale of the screen showing the rotational lines and the lower scale displays the wavelength in micrometers.



Figure 4.16 A picture of CO_2 Spectrum Analyzer's display screen with the cover on the casing opened.

4.6.2 *Results for the Wavelength Spectrum of the PL6 Laser*

The wavelength versus power graph is plotted in Figure 4.17 which shows how the power varies for each wavelength transition as well as the possible wavelength transitions of this laser. The 9R24 rotational line at 9.25 µm gave the highest power for that branch, the 9P20 rotational line at 9.54 µm gave the highest power for that branch, the 10R18 rotational line at 10.26 µm gave the highest power for that branch and the 10P20 rotational line at 10.60 µm gave the highest power of 60.5 W for the entire spectrum.

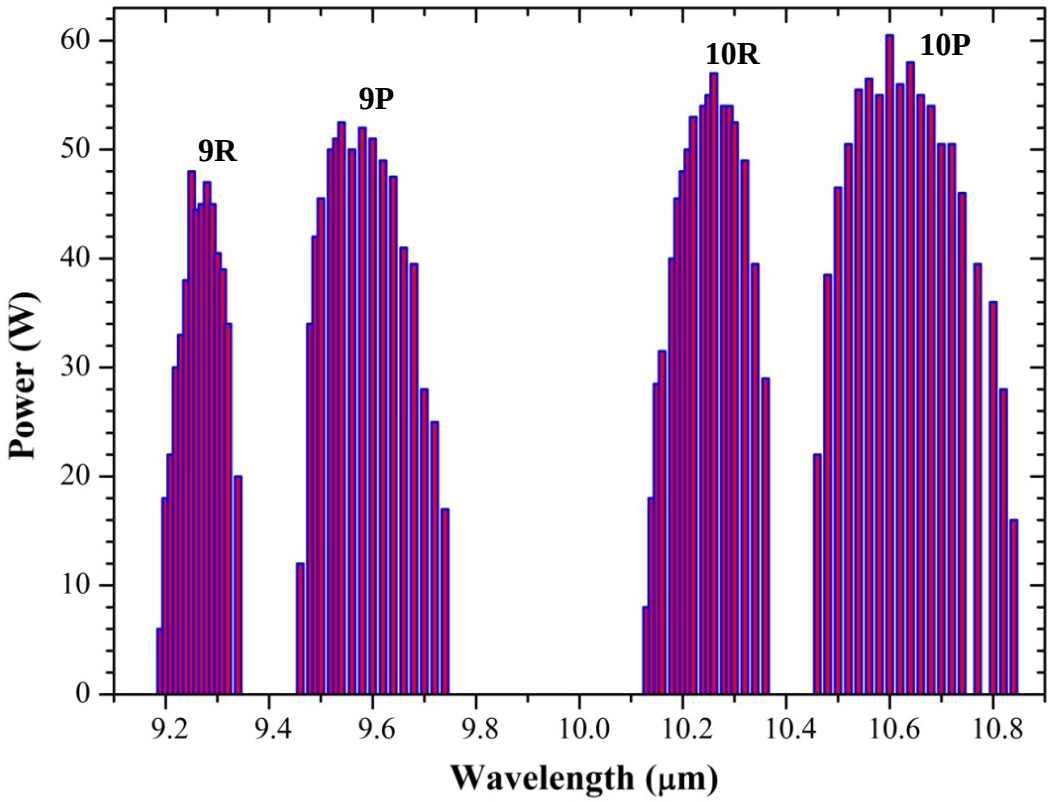


Figure 4.17 The wavelength spectrum of the PL6 CO_2 laser.

4.7 Summary of Laser Characterization

The PL6 laser was found to have non-Gaussian properties before and after the focal plane of the focusing mirror unlike the Synrad (D 48-2-115) CO_2 laser which was found to output a Gaussian-like beam. The polarization of the lasers was determined using the attenuator. The calculated parameters of both the lasers are tabulated in Table 4.1.

Table 4.1. The parameters for the PL6 laser obtained from the pyrocam method and the parameters for the Synrad laser obtained from the scanning slit method.

Laser Model	**Propagation parameters**			**Wavelength**	**Polarization**		**Maximum Power**
	ω_0 (m)	z_0 (m)	M^2	λ (μm)	*Vertical* (%)	*Horizontal* (%)	*P (W)*
PL6	1.054×10^{-3}	0.616	4.93	9.19-10.84	93	7	65
Synrad	8.059×10^{-4}	0.500	1.04	10.60	92	8	30

The PL6 laser beam waist is about 24% larger than the Synrad laser beam waist and the z_0 values indicate that the Synrad laser beam diverges slower than the PL6 laser beam. The Synrad laser has a fixed wavelength unlike the wavelength tunable PL6 laser which is why the PL6 laser was chosen. Both the lasers are linearly polarized with similar percentages of parallel and perpendicular polarizations.

4.8 Conclusion

A review was given on CO_2 laser theory. A comparison was made between the PL6 and Synrad lasers using the scanning slit and pyrocam characterization techniques. The laser polarization was obtained with the use of a home-made attenuator. The laser wavelength was determined using a CO_2 spectrum analyzer. The results from the characterization techniques revealed that the PL6 and Synrad laser have a vast difference in the beam quality factor due to the different laser designs.

Chapter 5

Experimental

5.1 Introduction

Several experimental geometries have been proposed to carry out laser pyrolysis, but the cross flow geometry was found to be the most advantageous [1]. Cross flow geometry, shown in Figure 5.1, requires a horizontal propagating laser beam to orthogonally intersect a vertically flowing 'vapour' precursor such that the effects exerted by gravity on the dissociated precursor can be controlled. The details on Figure 5.1 will be covered in the next section. This geometry also provides a very stable reaction and steady interaction zone where the laser beam and precursor intersect.

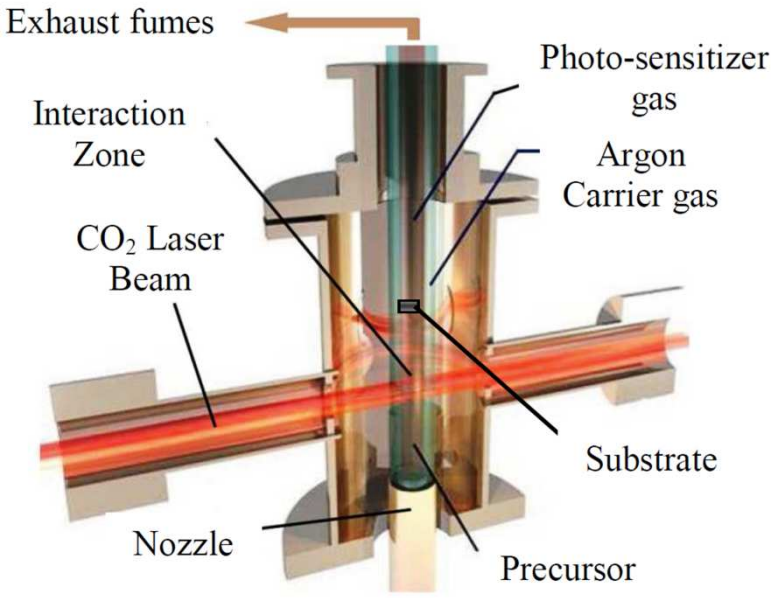


Figure 5.1 A cross-section of the reaction chamber during laser pyrolysis using the cross flow geometry [107].

An unfavourable condition for this geometry occurs when the laser beam is progressively absorbed as it passes through the thickness of the precursor stream. The precursor is thus exposed to varying laser intensity, which can cause non-uniformities in nanoparticulate formation. This condition is overcome however, since the residence time is very short, and so any variation in laser intensity is negligible. The cross flow geometry is applied in this study, as it is by far the most efficient configuration.

5.2 Methodology and Setup of the Laser Pyrolysis method

The cross flow geometry is achieved with a custom-made reaction chamber, shown in Figure 5.2, within which laser pyrolysis is carried out at atmospheric pressure. The stainless-steel six-arm chamber (dimensions 590 mm ×130 mm ×230 mm) is constructed with adjacent arms perpendicular to each other. Two of the longer opposite arms (labelled *1* and *2* in Figure 5.2) are each mounted with a 2-inch zinc selenide window. The first window serves as an entry point for the laser beam into the reaction chamber towards the interaction zone which is located at the centre of the two arms, and then exits the chamber through the second window. There is also a gas inlet on each of the long arms that allows carrier gas to flow in and protect the two zinc selenide windows from any scattered precursor and pyrolized products.

Horizontally and adjacent to the long arms is another pair of shorter opposite arms, one arm mounted with a 2-inch calcium fluoride window for viewing ultraviolet or visible emissions arising from the interaction zone, and the other arm is mounted with a 2-inch zinc selenide window to view infrared emissions from the interaction zone.

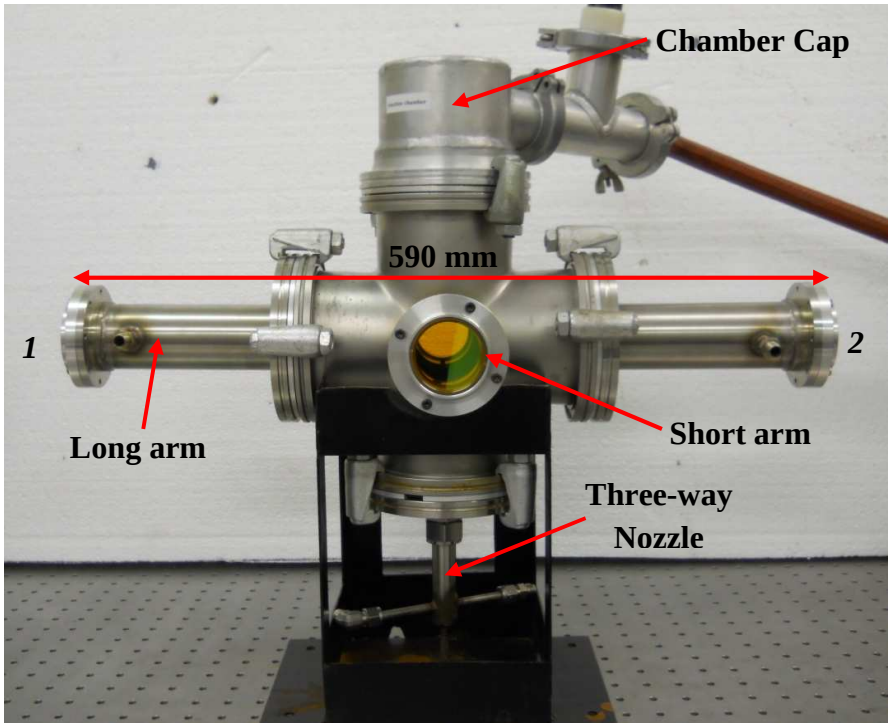


Figure 5.2 The reaction chamber inside which laser pyrolysis is carried out.

The top vertical arm has a removable cap that houses a substrate as shown in Figure 5.3 (a), and evacuates gases and fumes from the chamber. The bottom vertical arm holds a three-way nozzle (dimensions 46 mm×190 mm) shown in Figure 5.3 (b), which is used to direct the sensitizer gas, encasing gas and precursor towards the laser beam and substrate. The encasing gas (which is argon in this case) flows through the outermost ring (area of nozzle for emerging carrier gas is 1.32 cm^2) of the nozzle and minimizes the distribution and spreading of the contents from the inner nozzle outlets. The sensitizer gas (which is usually required when a precursor does not directly absorb the laser emission wavelength) flows through the middle ring (area of nozzle for emerging sensitizer gas is 0.31 cm^2) of the nozzle and acts as an energy transfer agent for the precursor. The precursor flows through the innermost ring (area of nozzle for emerging precursor gas is 0.20 cm^2) of the nozzle and is carried by argon gas because argon is inert and thought to act as a buffer gas that broadens the absorption bands of the precursor [78].

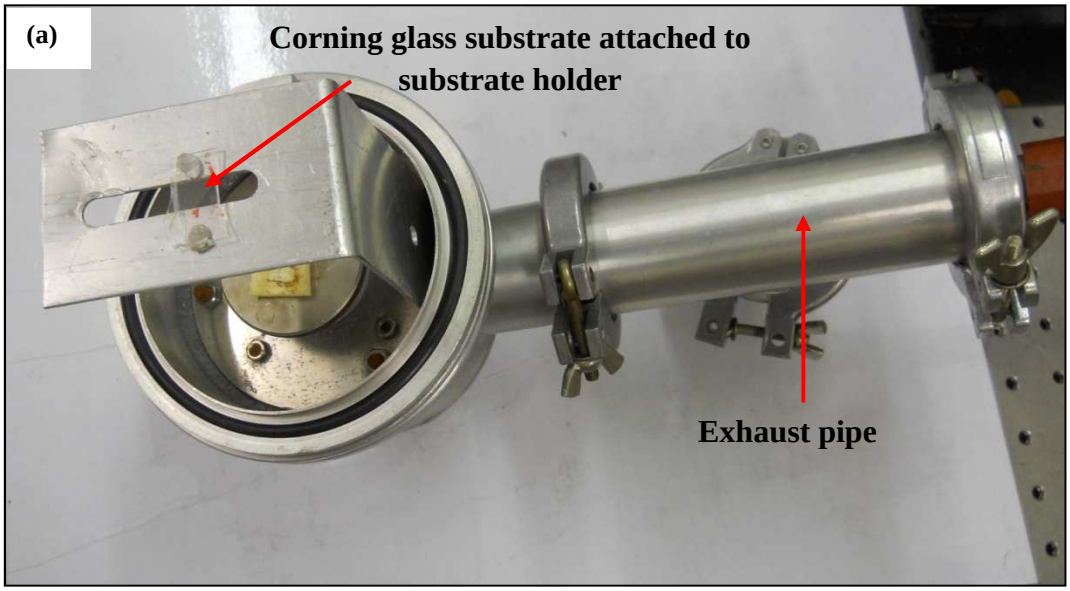


Figure 5.3 (a) The inside of the chamber cap.

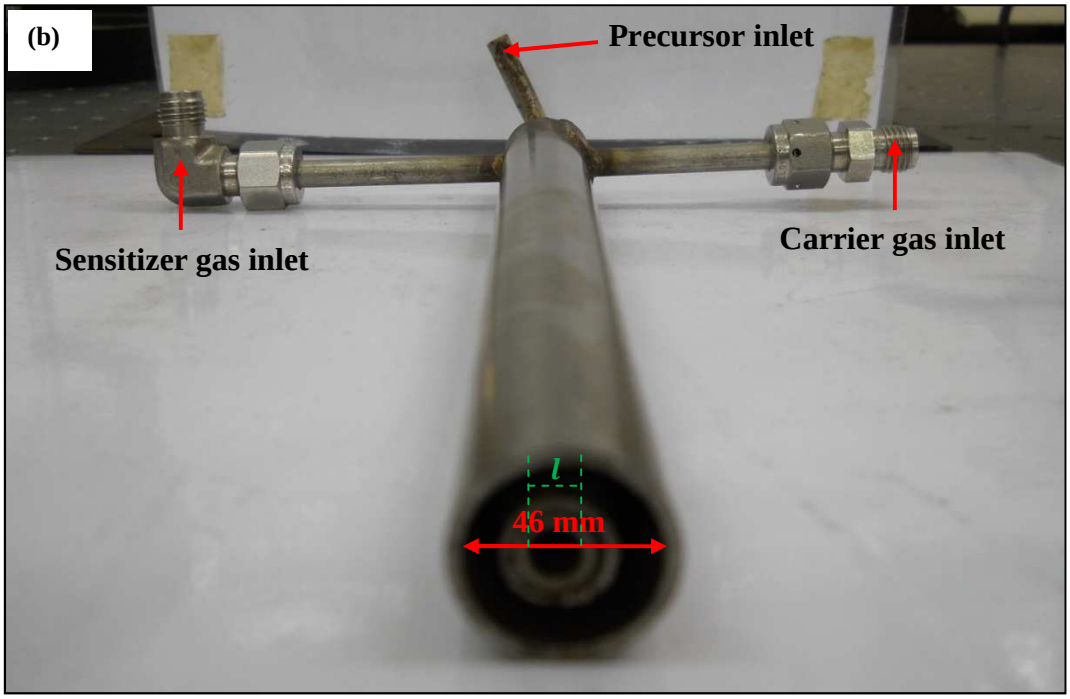


Figure 5.3 (b) A close-up of the three-way nozzle.

The laser pyrolysis setup requires the precursor to be in a gaseous phase to make the process effective. The liquid precursor is converted into a fine spray before entering the nozzle using the aerosol generator (Micro Mist®, Hudson RCI) shown in Figure 5.4. Argon gas is pumped through the aerosol generator which converts the liquid into small droplets (droplets have a diameter of 5 μm according to the manufacturer).

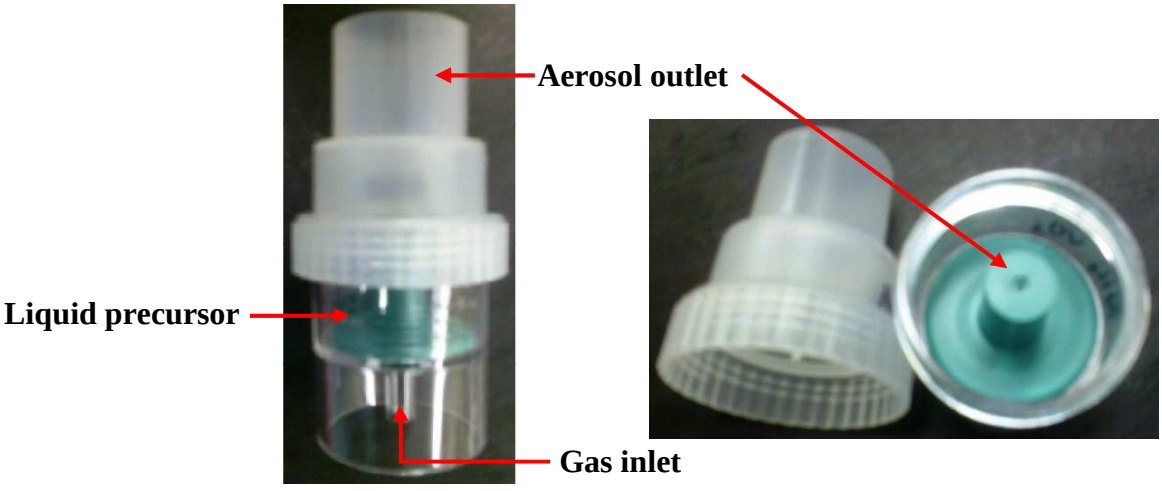


Figure 5.4 The aerosol generator holds the precursor liquid, and argon gas is passed through the bottom inlet creating a fine aerosol that emerges from the top.

The reaction chamber fits into the experimental setup as shown in Figure 5.5. The attenuator is used to vary the laser power entering the chamber while the power meter monitors the laser power before and during laser-precursor interaction. The laser beam is positioned 3 cm above the nozzle and 5.5 cm below the substrate to hinder the precursor from deviating off the nozzle axis. The gas flow rates are variable and are optimized according to the density of the precursor. The amount of time that the precursor is allowed to flow for, determines the thickness of the film that collects on the substrate. The samples are annealed in a furnace for 17 hours at 500^{o}C, and the products are characterized by the techniques discussed in Chapter 2.

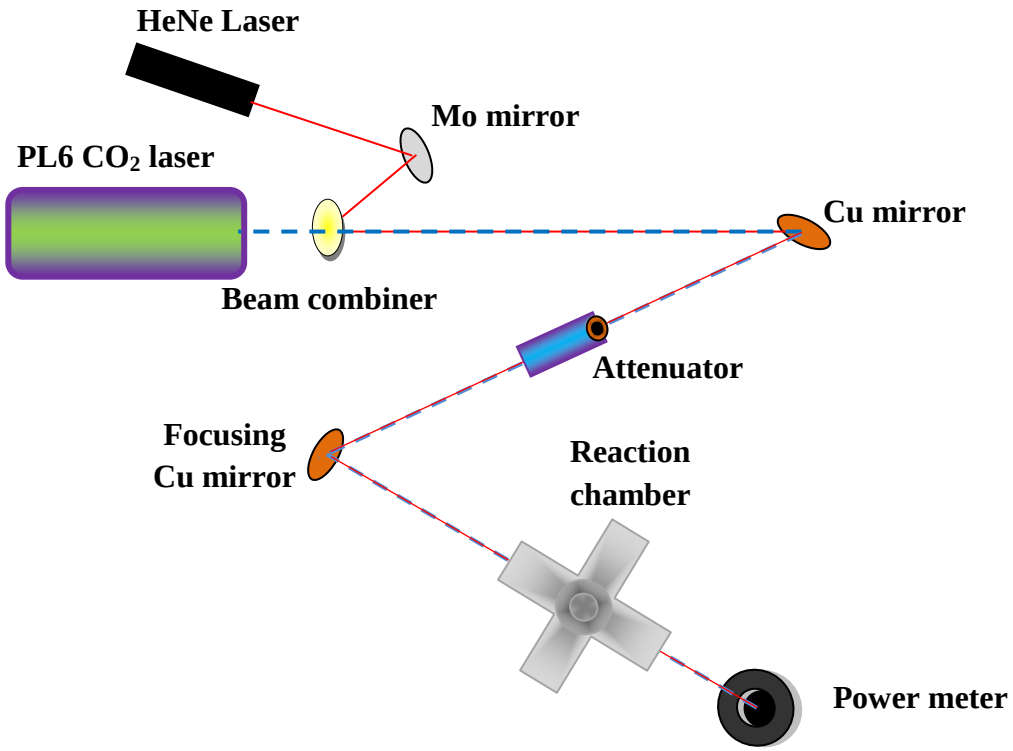


Figure 5.5 The setup used to carry out laser pyrolysis.

5.3 Estimation of the Laser Interaction Volume

The laser interaction volume *V* is the volume occupied in the laser beam by the precursor. The laser interaction volume was modified from literature [2] to give

$$V = \pi \int_{z_0-\frac{1}{2}l}^{z_0+\frac{1}{2}l} \omega^2(z)\, dz = \frac{\pi l^3}{12}\left(\frac{M^2\lambda}{\pi\omega_0}\right)^2 + \pi\omega_0^2 l, \qquad (5.1)$$

where *l* is the diameter of the nozzle from which the precursor exits and the other symbols have been defined in section 4.4.1. For the unfocused PL6 laser beam whose parameters were given in section 4.4.3 and for *l* equal to 2.5 mm (diameter of inner nozzle), the interaction volume comes out to be 0.29 cm^3±10%.

5.4 The Chemical Precursor

A chemical precursor is a compound that participates in a chemical reaction to produce another compound. We aim to fabricate tungsten trioxide from tungsten (VI) ethoxide precursor, that is, $W(OC_2H_5)_6 \rightarrow WO_3$ via the laser pyrolysis method. Tungsten (VI) ethoxide is a well known precursor for producing tungsten trioxide and its chemical properties are suitable to be used in laser pyrolysis. It is known that heat treatment of this precursor at temperatures above 100^{o}C converts this precursor to WO_3 [108], so it is interesting to investigate the conversion of the precursor by a laser.

5.4.1 *Preparation of Tungsten (VI) Ethoxide Precursor*

Tungsten (VI) ethoxide was prepared by mixing 0.11 g of greyish-blue anhydrous tungsten hexachloride (WCl_6, Sigma Aldrich, >99.9%) powder in 100 mL of absolute ethanol (C_2H_5OH, Sigma Aldrich, >99.9%) which gave a molarity of 2.5 mM. A precursor with a 27 μM concentration was also prepared to repeat experiments from literature [2]. The reaction was carried out under argon atmosphere because tungsten hexachloride reacts violently with oxygen and moisture from the air. The colour of the solution was yellow immediately after mixing the solute in solvent, and then changed to dark blue 15 minutes later. The blue colour

faded away over several days, and eventually became colourless with light yellow tungsten (VI) ethoxide colloids in solution.

The colour changes of the reaction are depicted in Figure 5.6, and the reaction steps are given by [108]

$$WCl_6 + x\,C_2H_5OH \rightarrow WCl_{6-x}(OC_2H_5)_x + x\,HCl \qquad (5.2)$$

(yellow to dark blue)

and

$$WCl_{6-x}(OC_2H_5)_x + (6-x)\,C_2H_5OH \rightarrow W(OC_2H_5)_6 + (6-x)\,HCl \qquad (5.3)$$

(blue) (light yellow colloids)

where x goes from 1 to 6 as the reaction proceeds.



Figure 5.6 The pictures show the colour changes as the reaction proceeds to form tungsten (VI) ethoxide precursor.

5.4.2 *Properties of Tungsten (VI) Ethoxide Precursor*

Tungsten (VI) ethoxide is a light yellow solid with a melting point of 105-110^{o}C. The precursor made here is actually tungsten (VI) ethoxide suspended in a large excess of ethanol (~11 times), and so the precursor is a volatile 'liquid'. The precursor is so diluted by ethanol, that it assumes most of the ethanol properties. The density of the precursor was verified and found to be 0.79 g cm^{-3}. The boiling point is 78.1^{o}C and the pH is 6.

5.4.3 *Spectroscopic analysis of Tungsten (VI) Ethoxide Precursor*

It is important in laser pyrolysis to determine the absorption bands of the precursor, and so FTIR was carried out on the liquid precursor using a Perkin Elmer Spotlight 400 FTIR Imaging System in the wavelength range 500-4000 cm^{-1}. The green spectrum in Figure 5.7 shows ethanol background and the blue spectrum shows the tungsten (VI) ethoxide precursor plus ethanol contribution. The two spectra are contrasted to understand the contributions of the ethanol peaks. The peak labelled 1 in Figure 5.7 found at 1087 cm^{-1} (9.20 μm), is indicative of a carbon-oxygen (C–O) bond, and the peak labelled 2 found at 1045 cm^{-1} (9.57 μm), is indicative of a carbon-carbon (C–C) bond [109]. The peak labelled 3, which is found outside the wavelength range of the laser at 805 cm^{-1} (12.43 μm), most probably represents the tungsten-oxygen (W–O) bond in a very small quantity. The shaded region of the FTIR spectrum shows the wavelength range of the CO_2 laser and the dashed line refers to the 10.6 μm wavelength of the laser beam. This overlap of laser wavelength with the precursor absorption band is a prerequisite for laser pyrolysis method, and will be discussed in detail in the following chapter.

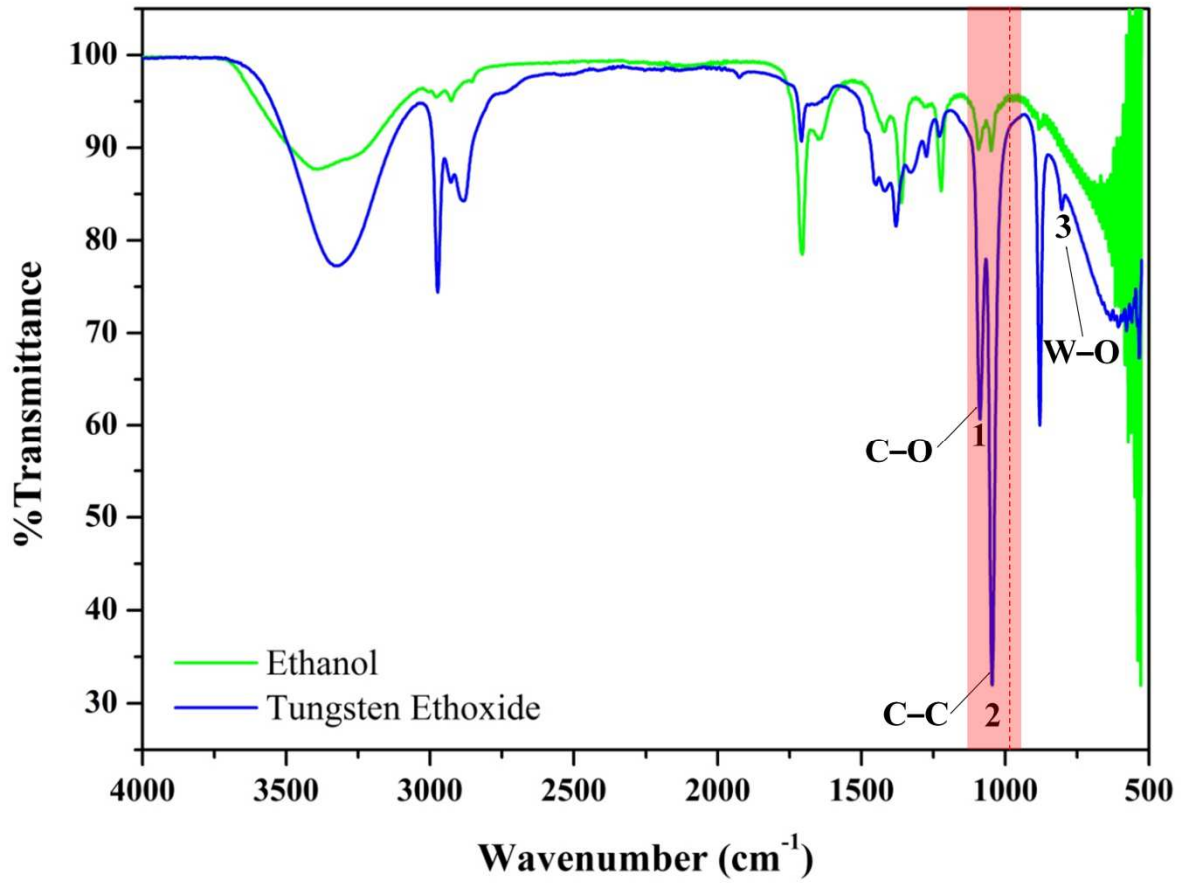


Figure 5.7 The FTIR spectrum of the tungsten ethoxide precursor (blue) and pure ethanol (green). The shaded region represents the wavelength range of the CO_2 laser and the dashed red line represents the CO_2 laser's 10.6 μm wavelength.

5.5 Summary

The cross flow geometry was chosen to carry out laser pyrolysis, and all the components necessary for this configuration was shown and discussed. The volume of the laser-precursor interaction was found to be 0.29 cm^3. The preparation of the tungsten (VI) precursor was outlined, and spectroscopic analysis of the precursor reveals that the absorption bands of the precursor overlaps with the emission lines of the PL6 laser, which is a requisite for laser pyrolysis.

Chapter 6

Results and Discussion

6.1 Laser Pyrolysis carried out at varying Wavelength and Power

The first set of experiments involved varying the wavelength (9.22-10.82 μm) at a fixed power density of 51.2 W/cm^2±5% (a power of 30 W in a beam radius of 6.11 mm) and the second set of experiments involved varying the power density (17-110 W/cm^2±10%) at a fixed wavelength of 10.6 μm to investigate the morphology and chemical composition of the products as a function of the laser parameters. The set of parameters chosen are illustrated in Figure 6.1.

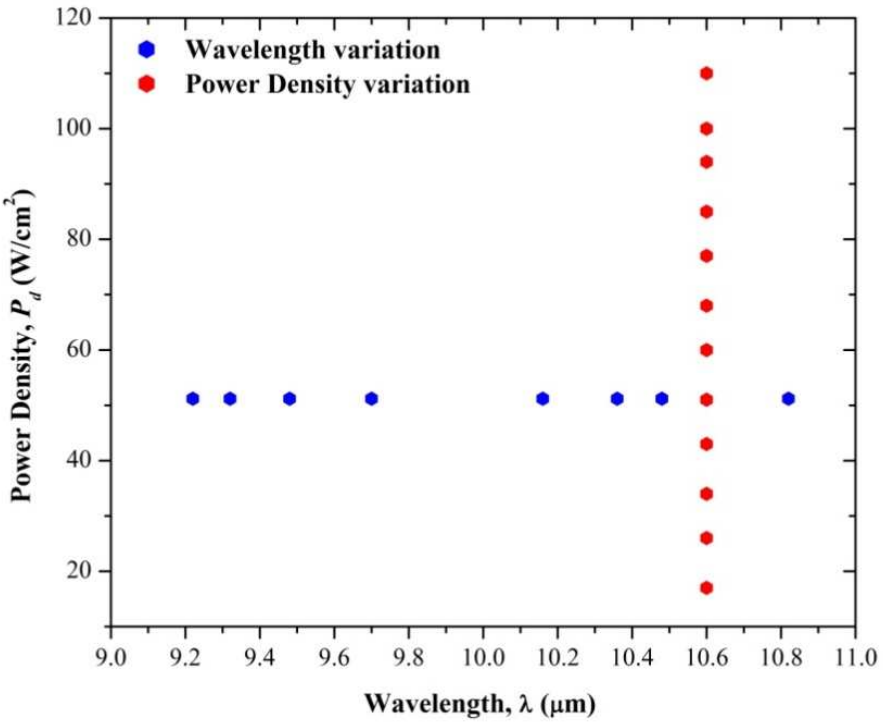


Figure 6.1 The varying laser parameters are represented by the respective points on the graph, used to investigate the effects on the morphology and chemical composition of the products.

The unfocused laser beam, which has a larger beam area, was used here to increase the time (or residence time) that the precursor spends in the laser beam and so threshold effects can also be investigated. The threshold effects reveal at what power and wavelength a chemical

composition will form, and so it is not imperative to cover a larger laser pyrolysis parameter space. The constant power of 30 W was chosen so that all the varied wavelength branches could have the same power, and this is better understood by referring to Figure 4.16 which shows the maximum power output for every wavelength. The 10.6 μm wavelength was chosen as this is the optimum wavelength for state preparation and the highest power is available at this wavelength [2].

The 2.4 mM tungsten (VI) ethoxide precursor was used, and the optimal flow rates (relative to the densities of the gases and precursor) for the precursor carrier gas (oxygen), acetylene and argon gas according to the flow meters, were found to be 8 sccm ±35%, 50 sccm ±10% and 30 sccm ±19%, respectively. The selected flow rates and arrangement of the adjacent flowing gases in the setup described in the previous chapter were successful in making uniform films [21]. Various nanostructures grew within the films during annealing for 17 hours at 500^{o}C in argon atmosphere, in agreement with literature [45] which reported that 500^{o}C was the optimum temperature to grow rod-like nanostructures.

The residence time was estimated from the precursor flow rate (8 sccm) and the interaction volume (which was found to be 0.29 cm^3 from equation (5.1) for the unfocused PL6 beam). By taking the ratio of the interaction volume to the flow rate, the residence time was found to be 3.7 ms and this is in the range of the relaxation times of excited state gases. For example, the metastable lifetime of carbon dioxide gas, which was shown in Figure 4.3, is 2 milliseconds [101]. This implies that the precursor gas spends an amount of time that is almost equivalent to its excited state lifetime, such that the precursor may not de-excite within the laser beam but dissociate.

The precursor molecule is composed of 49 atoms, which means the precursor has a possible 141 degrees of freedom (see discussion in section 2.2.2.1). Each degree of freedom has its own vibrational and associated rotation-vibration levels, and so the laser beam can distribute its energy in various ways, according to the power and wavelength in the estimated residence time. It is thus possible for several chain reactions and chemical pathways to be considered. The resulting nanostructures that form after annealing can be owed to state preparation as discussed in section 2.2.2, or a polarization change in the precursor associated with the laser parameters as discussed in section 1.1.1.

6.2 Sample Morphology and Topography

6.2.1 *Wavelength Variation*

The first set of experiments involved keeping the power density fixed, and so the direct effect of laser wavelength could be investigated. The results of the wavelength variation will be explained with reference to Figure 6.2, which shows the absorbance of the precursor as a function of wavelength with the corresponding part of the FTIR transmission spectrum of tungsten (VI) ethoxide. The absorbance of the precursor was obtained by taking the ratio of the laser power before laser-precursor interaction to the power observed during laser-precursor interaction. The figure also indicates the possible resonant, near-resonant and non-resonant interaction between laser and precursor.

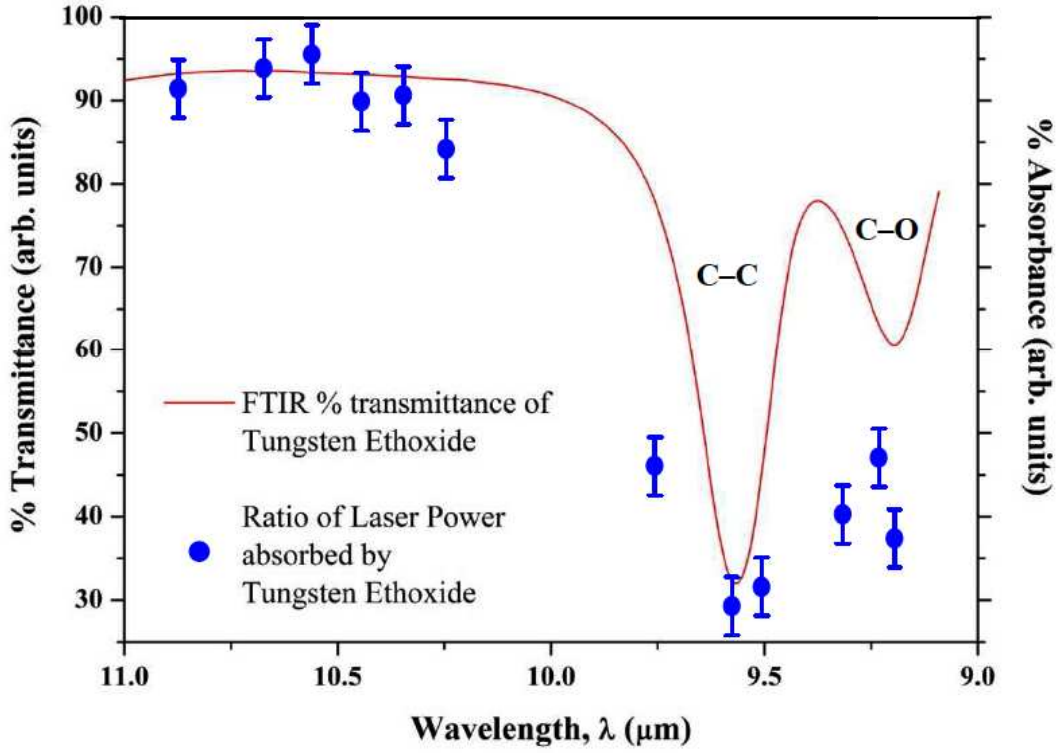


Figure 6.2 The comparison of the FTIR transmittance spectrum of the tungsten ethoxide precursor and the CO_2 laser radiation absorbance data of tungsten (VI) ethoxide as a function of wavelength.

Morphology studies were carried out using a Jeol JSM-5600 Scanning Electron Microscope which has EDX capability in-situ. The SEM micrographs for the annealed samples prepared at various wavelengths are shown in Appendix B.1. The sample prepared at 9.22 μm wavelength and power density of 51.2 W/cm^2 is shown in Figure 6.3 (a) as an example, with

its corresponding EDX spectrum in Figure 6.3 (b). The EDX spectrum will be discussed in conjunction with XRD studies. A study of the morphology from SEM for the various laser parameters reveals many different shaped micro and nanostructures within the thin film after annealing. The structures observed vary from fibres, spheres, discs, bundles of fibres, to structures shaped like an *H*.

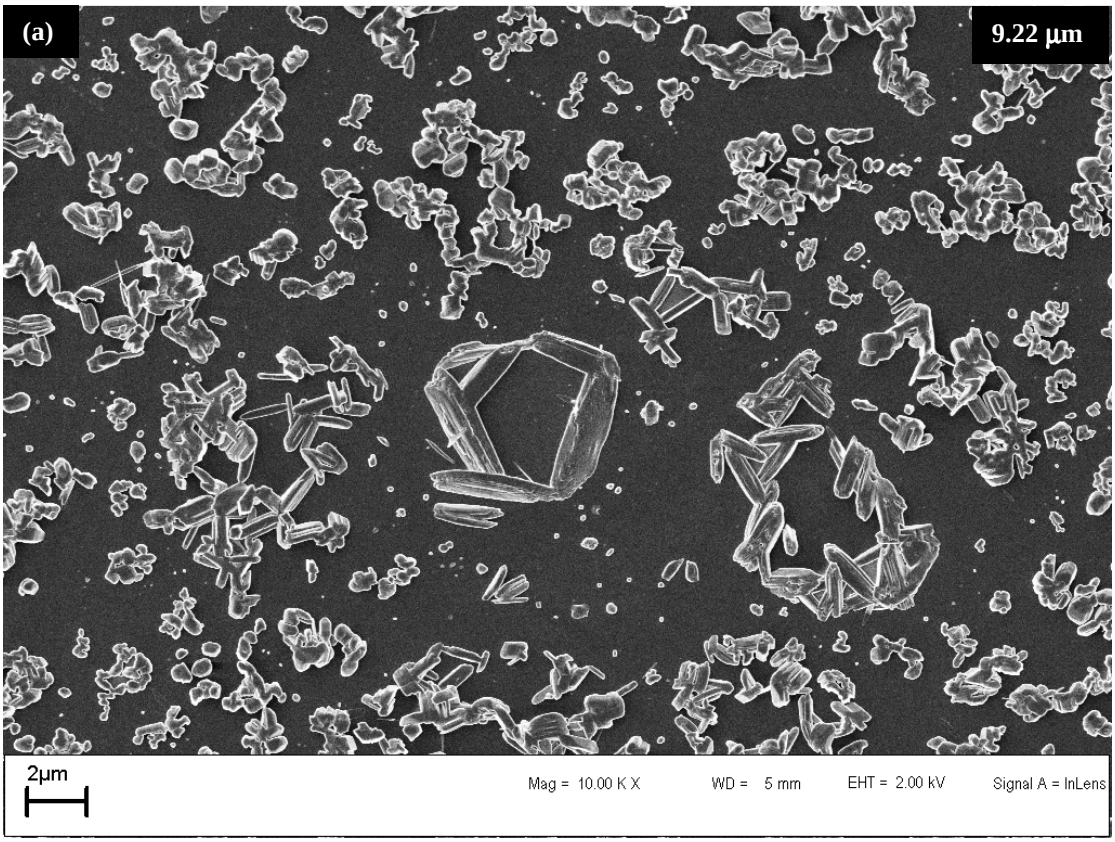


Figure 6.3 (a) The annealed sample prepared at the 9.22 µm wavelength and 51.2 W/cm^2.

The growth mechanism that was looked at that could explain the formation of the different shaped nanostructures of different sizes during annealing was the Gibbs–Thompson effect [1], which proposes that the size of the critical radius is dependent on the precursor concentration and aims to explain the increase (Ostwald ripening) or decrease (Tiller's formula) in size of nanostructures. This behavior is depicted in Figure 6.4 and 6.6, as well as Figure 6.9 (a-b), which shows the sample particle size variation as a function of the laser parameters.

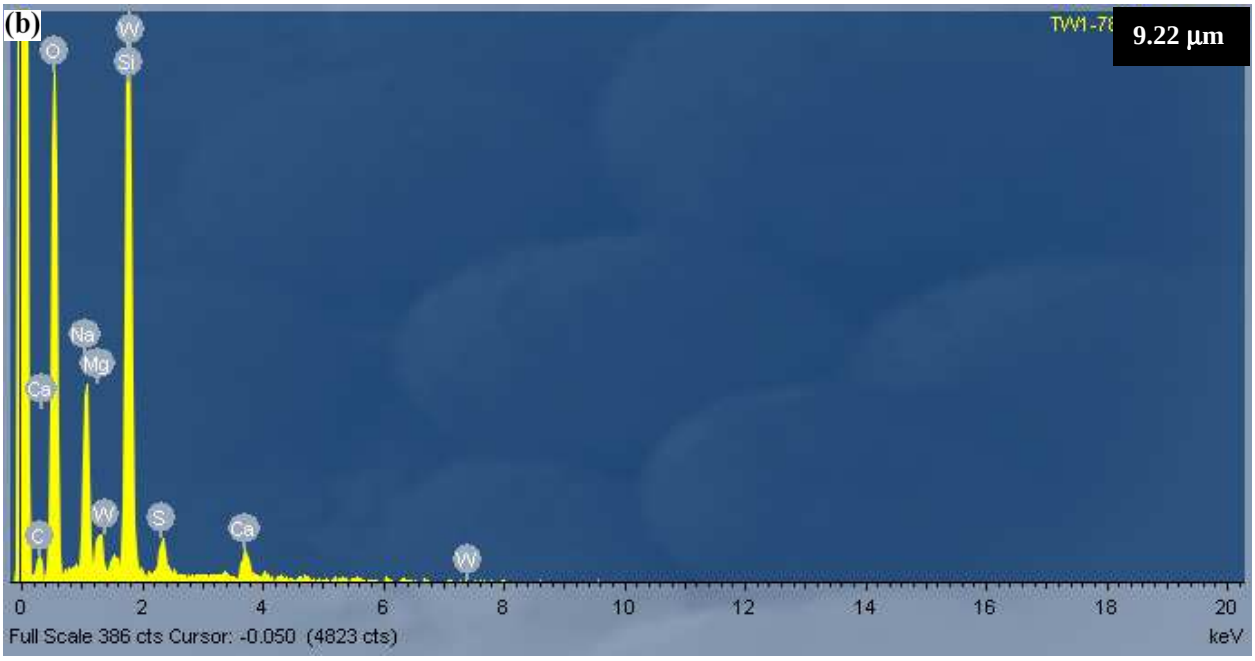


Figure 6.3 (b) The EDX spectrum on the area of the sample prepared at the 9.22 µm wavelength and constant power density of 51.2 W/cm^2, which shows the presence of calcium (Ca), magnesium (Mg), carbon coating (C), sodium (Na), silicon (Si) and sulphur (S), which most probably come from the Corning glass. The oxygen (O) could have come from the substrate and the sample and tungsten (W) results from the sample.

Before looking at the number of photons absorbed by the precursor in the residence time, the number of precursor molecules present in the interaction volume was estimated. Assuming that the precursor was nebulized into droplets with a radius r of 2.5 µm, the volume of a droplet sphere ($4/3\ \pi r^3$) was found to be 6.5×10^{-11} cm^3. The number of molecules present in each droplet was then calculated by multiplying the droplet volume by the precursor density to get the precursor mass in the droplet which was found to be 5.1×10^{-11} g. Dividing this mass by the precursor molar mass of 454.2 g/mol, and multiplying by Avogadro's number N_A, it was found that 6.9×10^{10} tungsten (VI) ethoxide molecules were present in one nebulized droplet.

The interaction volume of the unfocused laser beam of 0.29 cm^3, was divided by the volume of a droplet sphere. It was found that approximately 4.6×10^{10} droplets could fit in the interaction volume at any given time. Multiplying the number of droplets by the number of precursor molecules contained in each droplet, it was found that 3.2×10^{21} precursor molecules are present in the laser beam. From this estimation, it can be speculated that the

number of photons absorbed by the precursor near a resonant wavelength will be close to 3.2×10^{21}.

It was found that the precursor absorbed approximately 3.3×10^{18} photons (calculated by dividing the power absorbed by the precursor by the energy of the photon, and then dividing by the residence time of 3.7 ms) from the 9.22 µm wavelength. The number of photons is two-orders of magnitude less than the estimated number of precursor molecules present in the beam which could imply that the residence time is not long enough to allow for more photons to be transferred to the precursor. The FTIR spectrum in Figure 6.2 speculates that the C–O bond absorbed these near-resonant photons. The average sphere diameter of the particles found in this sample measured approximately 355 nm. Only the spheres were measured accurately in all the micrographs because the micrographs gave a good 2D representation of the structures. The corresponding micrograph shows many agglomerations and what appear to be bundles of fibres scattered over the sample. TEM will be used to verify if the larger agglomerations are composed of bundles of fibres.

The precursor was found to absorb approximately 3.3×10^{18} photons from the 9.32 µm wavelength. The FTIR spectrum reveals that this absorption could be owed to the C–O bond of the precursor. The average sphere diameter of the particles found in this sample measured approximately 163 nm, and it appears when the laser wavelength is near the C–C absorption band of the precursor, the sphere diameters tend to be smaller. It should be noted here that the relative number of photons absorbed by the precursor at the different wavelengths also depends on the quantity of that bond in the precursor, that is, the C–C absorption peak is larger than the C–O absorption peak because there are more C–C bonds in the precursor as depicted by the FTIR spectrum. The corresponding micrograph shows a uniform distribution of spherical particles.

The maximum absorbance by the precursor was found at the 9.48 µm wavelength, where approximately 3.9×10^{18} photons were taken in by the precursor. According to the FTIR spectrum of the precursor, the C–C bond has a strong absorption near this wavelength, and so it is speculated that the high absorption is owed to this bond. The average sphere diameter of the particles in this sample was found to be the smallest in the range at around 123 nm, as

measured in the SEM micrograph. The corresponding micrograph is similar to the 9.32 µm wavelength, which shows a uniform distribution of spherical particles or discs.

The next wavelength that showed high absorbance by the precursor was the 9.70 µm, where it was found that approximately 3.1×10^{18} photons were taken in by the precursor. The FTIR spectrum speculates that the C–C bond of the precursor absorbed these photons. The average sphere diameter of the particles found in this sample measured approximately 385 nm, which was similar to the 9.22 µm sample, where the precursor also absorbed a similar number of photons. The corresponding micrograph shows a non-uniform distribution of random structures.

Moving up to the 10 µm wavelengths, at which none of the precursor bonds are resonant, some interesting results were found. At the 10.16 µm wavelength, approximately 7.6×10^{17} photons were absorbed by the precursor which was unexpected. It is speculated that since this wavelength lies at the end of the C–C absorption band, the absorbed photons could have been channelled into this band. The average sphere diameter of the particles found in this sample measured approximately 380 nm, which is similar to the sphere diameters measured in the 9.22 µm and 9.70 µm samples. Despite the similarity in average sphere diameters, the number of photons absorbed at the 9.22 µm and 9.70 µm wavelengths was much more than that absorbed at the 10.16 µm wavelength. This could mean that the way in which the 10.16 µm energy photons is distributed into the bond of the precursor is very similar to the way the 9.22 µm and 9.70 µm wavelengths distributes its energy. The corresponding micrograph is similar to the 9.70 µm wavelength, which shows a non-uniform distribution of random structures.

The precursor absorbed 3.9×10^{17} photons of the 10.36 µm wavelength. It is not clear into which precursor bond this energy was distributed into, because the FTIR spectrum shows no absorption band at this wavelength. Furthermore, the average sphere diameters were found to be the largest at this wavelength, measuring in at approximately 680 nm. A similar pattern was found for the 10.82 µm wavelength at which 3.0×10^{17} photons were absorbed by the precursor, but the chemical bond into which these photons are distributed is unknown. The average sphere diameter was also large in this sample and measured approximately 560 nm.

The corresponding micrograph shows *H*-structures scattered over the sample with smaller rod-like structures distributed between the *H*-structures.

The 10.48 µm wavelength, which lies somewhere between the 10.36 µm and 10.84 µm, showed no observable absorption of photons. It appears that the laser beam just passed through the precursor unaffected, but it was found that this sample did show spheres with an average diameter of 440 nm. In the absence of laser light, the annealed sample did not show nanostructures, so it is safe to assume that laser light does contribute to the formation of nanostructures even when the light is not absorbed. The Grotthus-Draper law is disobeyed in this case, which implied that neither a photophysical nor photochemical process was possible, and so it can be speculated that the laser energy facilitated for state preparation which caused the distribution and growth of the observed nanostructures. The corresponding micrograph shows a uniform distribution of spheres or discs across the sample and a mixture of agglomerations and fibre-bundles.

For the 10.82 µm wavelength, 3.0×10^{17} photons were absorbed by the precursor, but the chemical bond into which these photons are distributed is unknown like the previous sample. The average sphere diameter was also large in this sample and measured approximately 560 nm. The corresponding micrograph shows many random structures and agglomerations scattered over the sample.

The non-resonant interactions appeared to promote the formation of larger nanoparticles. This could have occurred because the latent heat supplied to the precursor decreased as a result of the non-resonance with the laser wavelength, thus decreasing the evapouration and nucleation rate, which leads to a greater growth and agglomeration rate during annealing [1]. It is thus speculated that resonant interactions between laser and precursor causes a higher spontaneous reaction temperature, which induces the formation of smaller nanoparticles. This is a sensible speculation, as there are multiple vibrational levels in the precursor and the photons that are resonant or near-resonant with these vibrational levels causes more and more excitations, such that the temperature of the system increases rapidly. This result is further confirmed by the large number of multiphotons absorbed in the given time.

The average sphere diameters as a function of wavelength are tabulated in Figure 6.4.

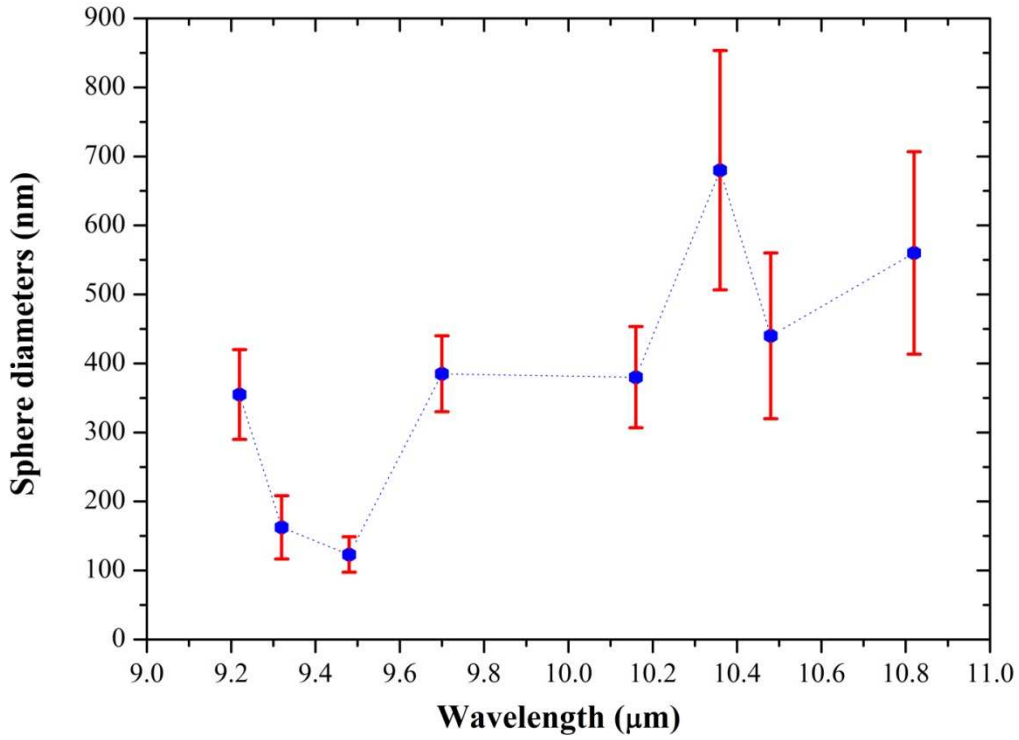


Figure 6.4 The average spherical particle sizes as a function of wavelength at the 51.2 W/cm^2 power density.

To verify if the nanostructures shown in Figure 6.3 (a) contain bundles of fibres, TEM was carried out using a Jeol JEM-2100 Transmission Electron Microscope which has EDX capability in-situ. The TEM micrograph with the corresponding EDX spectra is shown in Figure 6.5 (See Appendix C for TEM micrographs and EDX spectra). The EDX is shown to confirm that the sample is the tungsten oxide in question and not an impurity.

The TEM shows a tungsten containing nanorod in Figures 6.5. This structure possibly confirms the presence of fibre-bundles which could have separated during sonication. The copper (Cu) in the EDX spectrum result from the copper grid on which the sample sits, and the potassium (K) and calcium (Ca) probably result from the glass substrate. Calcium was also confirmed in the EDX spectra from the Scanning Electron Microscope.

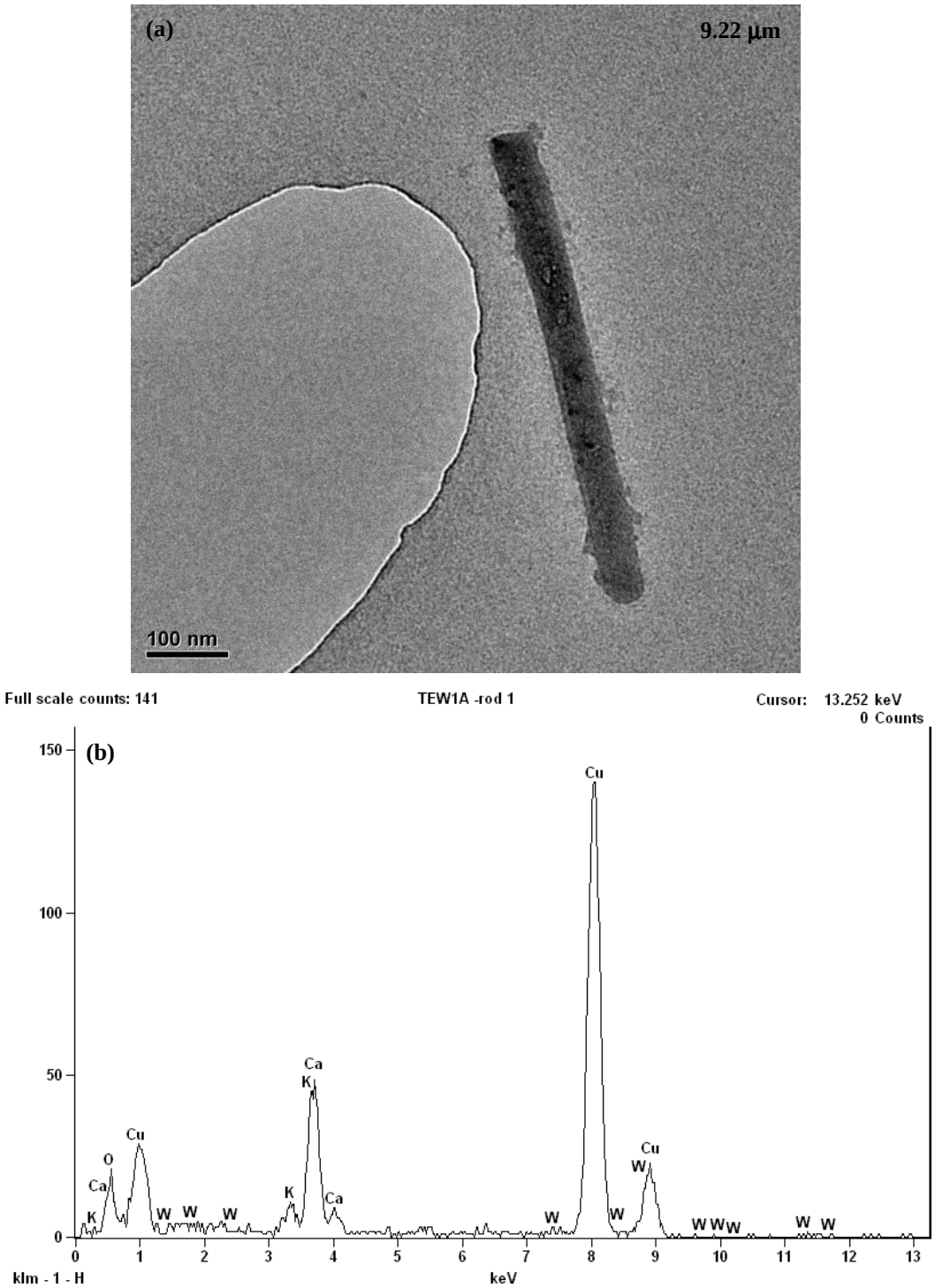


Figure 6.5 (a) A TEM micrograph showing a nanorod and **(b)** the EDX spectrum taken of the rod.

6.2.2 *Power Variation*

The second set of experiments involved keeping the wavelength fixed so the direct effect of power density could be investigated. The SEM micrographs corresponding to these laser parameters are given in Appendix B.2. The morphology of the power varied samples showed many similarities to the wavelength varied samples, probably due to similar state preparation by the laser parameters. Unlike the previous experiment with varying laser wavelengths, all the photons in this experiment have the same energy (a 10.6 μm photon has an energy of 1.88×10^{-20} J) and the precursor appeared to always absorb 1.9×10^{17} photons in 3.7 ms, irrespective of the power density. This behaviour was discussed in section 1.1.2 on linear and nonlinear absorption by a material system. According to equation (1.3) for linear absorption, the absorption by the precursor is independent of the laser intensity. In this case the number of photons absorbed by the precursor does not appear to change constantly or is not laser intensity dependent, and so it follows the relationship in equation (1.3) for linear absorption.

The average sphere diameters as a function of power density are tabulated in Figure 6.6. It was established that the precursor appears to linearly absorb the 10.6 μm photons and this result can be explained by referring to region II on Figure 1.6 which shows the transitions involved in multiphoton infrared absorption. This region is characterized by quasi-continuum behaviour, and so successive photons can be absorbed in a series of energetically allowed single-photon transitions where energy is conserved at each step. This allows the molecule to exist for a short lifetime at each step before absorbing the next photon. This implies that excitation through this region does not necessitate the increasing photon flux, which is the case with increasing power at constant wavelength, and so the number of photons absorbed in a given time remains relatively constant. However, the changing flux can possibly induce a change in the series of steps and its associated lifetimes, leading to the various types of structures formed, and their respective sizes. The overall average sphere diameters for the varying power density samples were found to be 40% smaller than the average sphere diameters found for the varying wavelength samples. This could be due to the way the vibrational levels are excited according to the wavelength and photon flux.

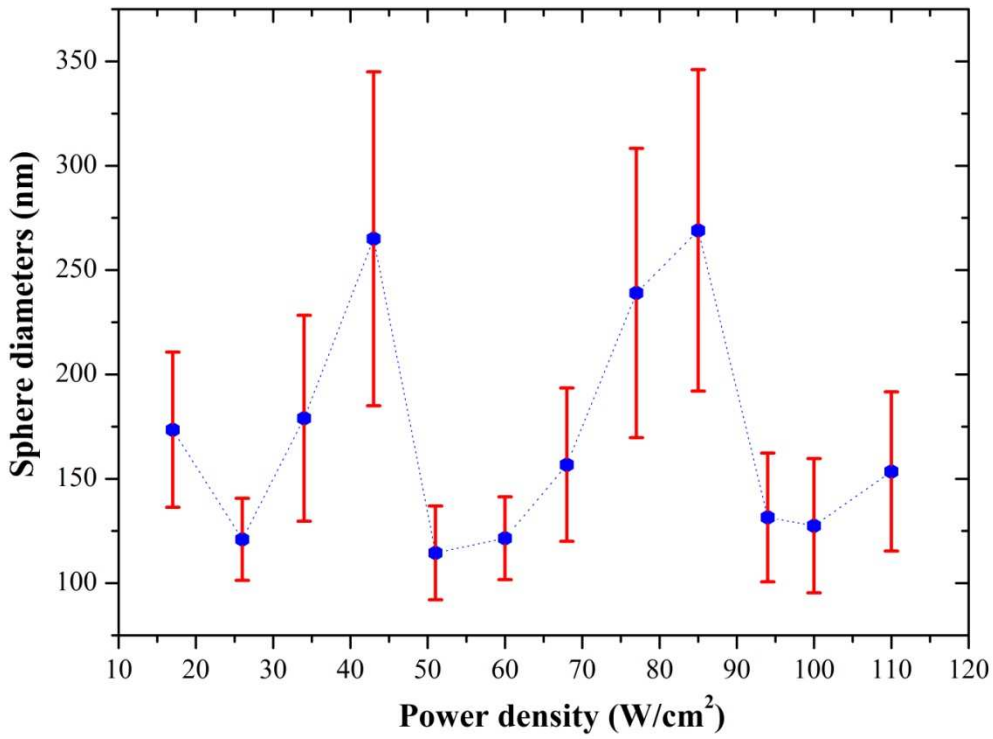


Figure 6.6 The average spherical particle sizes as a function of power density at the 10.6 µm wavelength

From Figure 6.6, it appears that the average sphere diameters changes sinusoidally with increasing power density, which was unexpected since particle sizes usually decrease with increasing power density [79]. Another explanation for this behaviour could be the result of a competing photochemical and photophysical processes that is brought about by the combination of laser wavelength and power, and the particle sizes depends on which process dominates. The overall lack in trend can be owed to resonant, near-resonant and non-resonant processes (laser wavelength), and photon distribution within the precursor vibrational levels (laser beam intensity), or a combination of both.

6.3 Sample Phase Composition and Crystal Structure

Crystallographic studies were carried out using a Philips Xpert powder diffractometer equipped with a CuK_{α} wavelength of 154.184 pm, on the prepared samples. The diffraction

angle of the x-ray source was varied from 5^o to 95^o for an exposure time of 15 minutes. The corresponding XRD spectra for the samples prepared at varying laser parameters are shown in Appendix D.1. Figure 6.7 shows the XRD spectrum for the sample prepared at 9.22 µm wavelength and power density of 51.2 W/cm^2, corresponding to the SEM micrograph in Figure 6.3 (a). The combinations of XRD peaks in the spectra were compared to standard Powder Diffraction Files (PDF) to identify the most probable phase and composition. In the case of tungsten oxides, it was noticed that XRD peaks at smaller diffraction angles refers to the abundance of oxygen, while XRD peaks at the larger diffraction angles refers to an abundance of tungsten. The XRD results for all the samples are tabulated in Table 6.1 with each samples most probable PDF number and phase composition.

The PDF numbers, phase and composition of the corresponding samples are shown on the XRD spectra for the various laser parameters (see Appendix D.1 and D.2). The samples matched spectra with either monoclinic *m*, or triclinic *t* phases, with various ratios of tungsten to oxygen compositions at the different laser parameters. Most of the samples had a crystalline arrangement as seen by the strong peaks in the XRD spectra, and the broad peak between 15^o and 40^o diffraction angle resulted from the nanocrystalline arrangement of the silicon oxide substrate. The 60 W/cm^2 and 85 W/cm^2 power density samples could not be positively identified due to the substrate contribution, and so Raman spectroscopy will be used to verify the compositions.

It is known that tungsten oxides can self assemble into many stoichiometric and non-stoichiometric compositions and phases, depending on the conditions under which it is prepared. According to the XRD analysis, the $W_{18}O_{49}$ (=$WO_{2.72}$ Magneli phase) [38, 110] appears to be most stable and preferred stoichiometry of the prepared samples at 500^oC in inert atmosphere as shown previously [36].

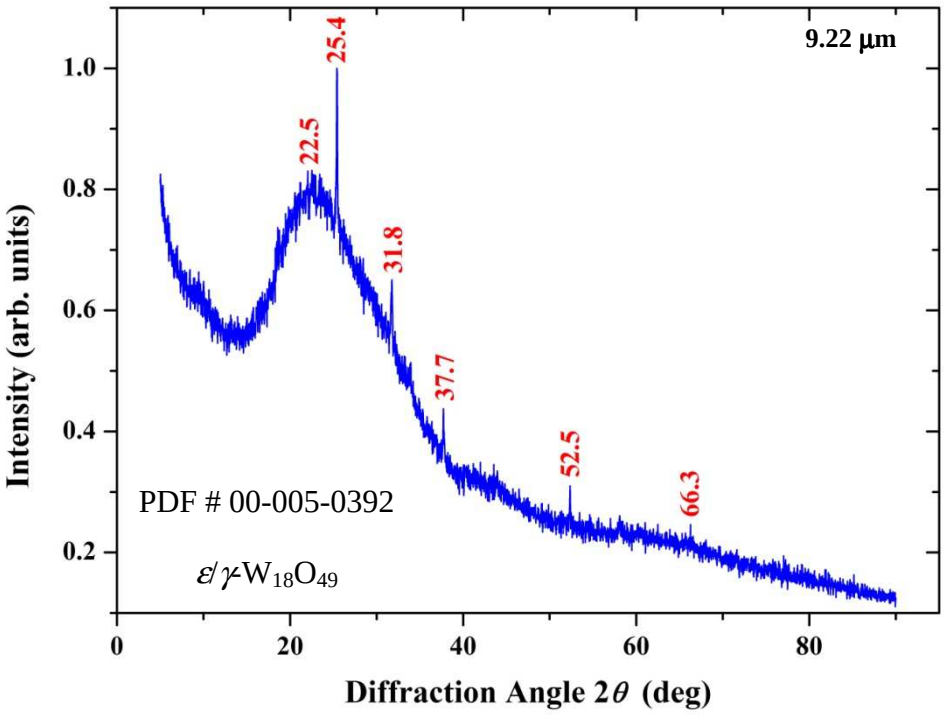


Figure 6.7 The XRD spectrum for the post-annealed sample, prepared at the 9.22 μm wavelength and 51.2 W/cm^2 power density.

The impurities that were found in the glass by EDX, probably stabilized the tungsten oxide crystal structure during annealing, as the XRD peaks and PDF did suggest that the tungsten oxide was combined to potassium and calcium. It is also not known at this stage if the impurities could have promoted the growth of the various structures observed in the SEM micrographs [111]. It was found that only the 10.48 μm wavelength sample resulted in the formation of monoclinic WO_3, and it was observed in the previous section that the precursor absorbed no photons at this wavelength. This wavelength probably caused the formation of the different nanostructures on the substrate, but did not induce any photochemical reactions (in agreement with the Grotthus-Draper law) on the basis that annealing the tungsten (VI) ethoxide precursor above 100^{o}C forms WO_3 [108].

Table 6.1. The results obtained from the XRD spectra for the varied set of laser parameters.

Wavelength Variation ($P_{density}$ = 51.2 W/cm^2)			**Power Density Variation (λ = 10.6 μm)**		
Wavelength, λ (μm)	***PDF number***	***Composition***	***Power Density, P_d (W/cm^2)***	***PDF number***	***Composition***
9.22	00-005-0392	*m/t*-$W_{18}O_{49}$	17	00-041-1431	*m/t*-$CaWO_4$
9.32	00-013-0057	*m/t*–$Na_2WO_4.2H_2O$	26	00-021-0696	*m*-K_2WO_4
9.48	00-012-0727	(Fe) WO_4	34	00-033-1387	*m*-WO_3
9.70	00-041-1431	*m/t*-$CaWO_4$	43	00-033-1387	*m*-WO_3
10.16	00-005-0392	*m/t*-$W_{18}O_{49}$	51	00-005-03792	*m/t*-$W_{18}O_{49}$
10.36	00-027-0789	*t*- $MgWO_4$	60	No match	-
10.48	00-033-1387	*m*-WO_3	68	00-005-0381	*m/t*-$W_{10}O_{29}$
10.82	00-005-0392	*m/t*-$W_{18}O_{49}$	77	00-005-0386	*m/t*-$W_{10}O_{29}$
			85	No match	-
m ≡ monoclinic phase			94	00-021-0696	*m*-K_2WO_7
t ≡ triclinic phase			100	00-032-0696	*m*-WO_2
			110	00-032-0696	*m*-WO_2

It is worth mentioning here that the XRD spectra can be used to determine the average particle size of crystals making up the nanostructures. The samples prepared here, however, do not have a distribution of uniform structures, and so the results obtained are an average over all the different structures. The formula used to do this estimation is called Scherrer's formula [112], which is given by (see derivation in Appendix E)

$$\sigma = \frac{0.9\lambda}{\beta \cos \theta_b}, \tag{6.1}$$

where σ is the thickness of the crystallites in the sample, λ is the incident x-ray wavelength, θ_b is known as Bragg's angle (the angle that satisfies Bragg's law) and β is the angular width in radians, measured at an intensity equal to half the maximum intensity.

By fitting a Gaussian function to the most intense peak of a XRD spectrum, the angle θ_b and the full width at half maximum β at this angle can be extracted. Since the x-ray wavelength (154.184 pm) is known, an estimate of the crystal size in each sample can be made from Equation (6.1), and then used to draw comparisons with SEM measurements. Looking at Figure 6.7, the most intense XRD peak is found at $2\theta \approx 25.4$, so zooming into this part of the spectrum looks like that shown in Figure 6.8. Fitted to this data is a Gaussian curve, and the relevant data is extracted. After converting the data from degrees to radians, β was found to be 1.65×10^{-3} rad and θ_b was found to be 0.22 rad. Inputting these parameters into Scherrer's formula, the average crystallite size in this sample is found to be 86 nm±12%, which is 25% smaller than the average sphere diameter measured in the SEM micrograph.

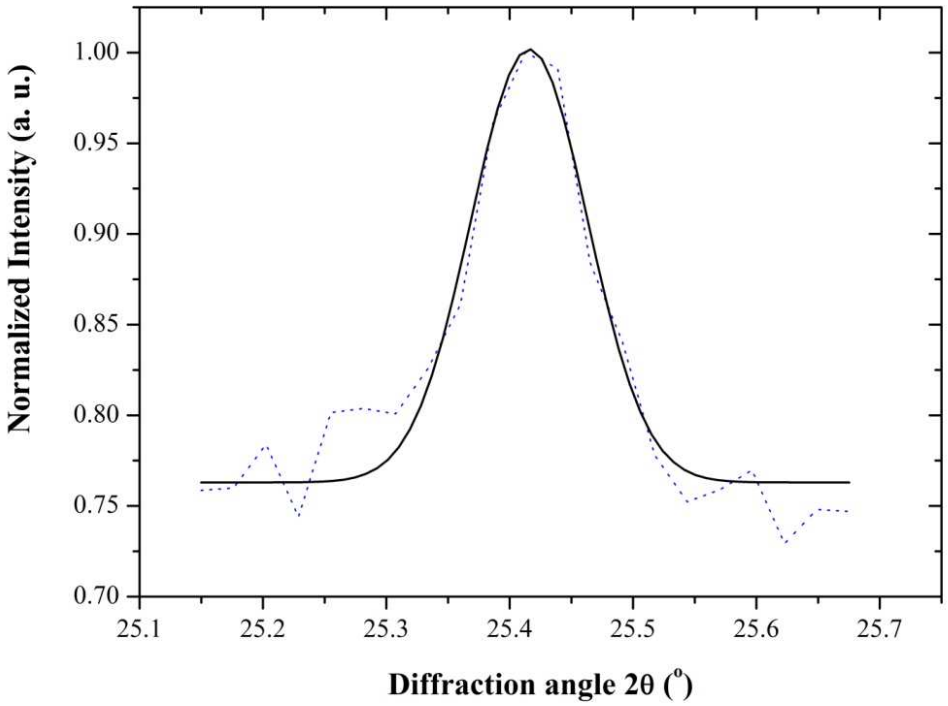


Figure 6.8 A zoomed in view of the most intense XRD peak of Figure 6.7 with a Gaussian fit to this peak. The full width at half maximum, and the angle at which the peak is most intense, are then extracted and converted to radians.

The Scherrer analysis was carried out on all the XRD spectra and the estimated crystal sizes for each sample wavelength are illustrated in Figure 6.9 (a) and the estimated crystal thickness for varying power density samples are illustrated in Figure 6.9 (b). Note the points at the 60 W/cm^2 and 85 W/cm^2 on Figure 6.9 (b) could be outliers, as there were not enough intense peaks in the respective XRD spectra, and these two samples could also not be identified with XRD.

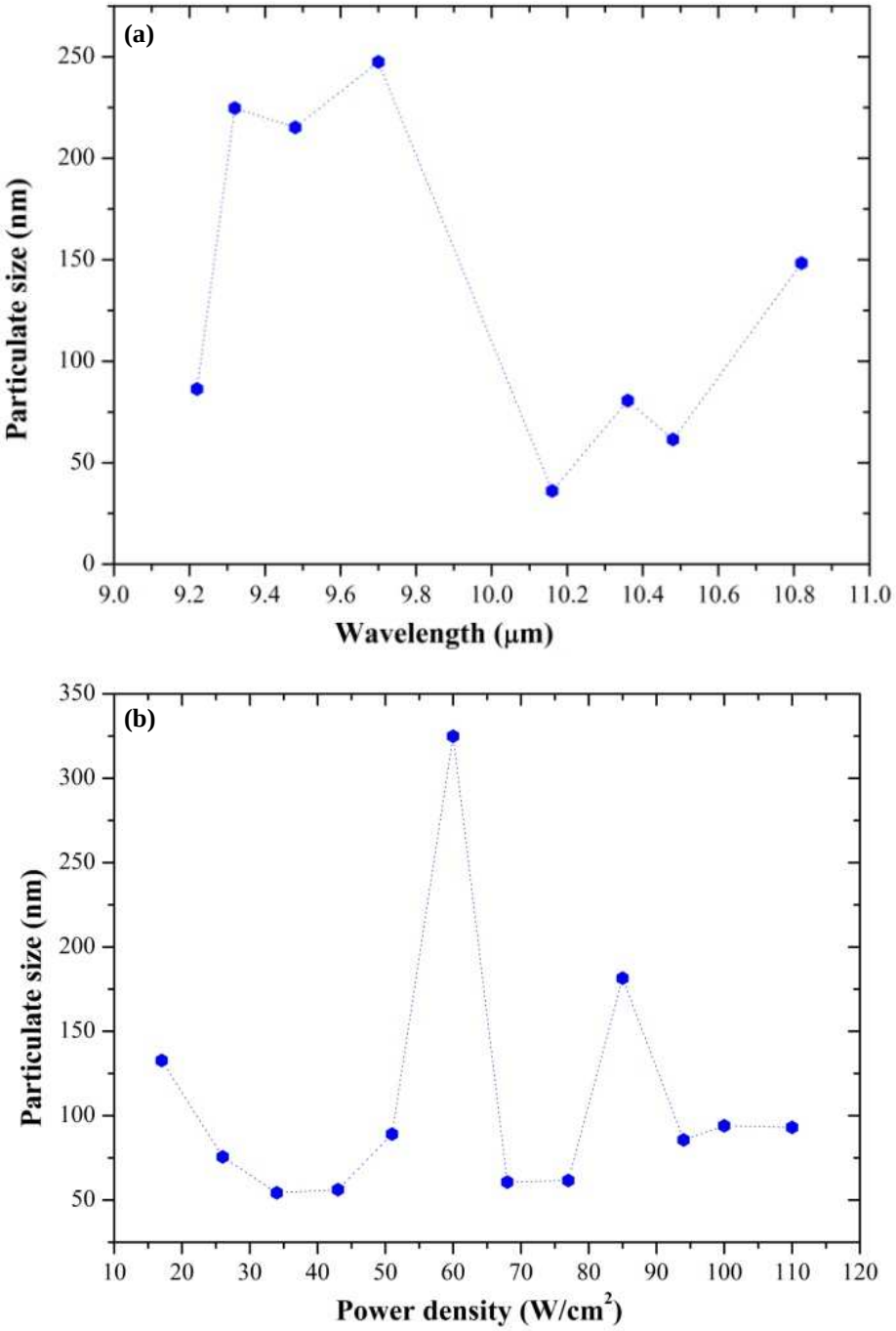


Figure 6.9 The particulate sizes for the samples shown in the SEM micrographs above, were calculated from the XRD spectra for the respective samples and Scherrer's formula, for the various **(a)** wavelengths at the 51.2 W/cm^2 power density and **(b)** power densities at the 10.6 μm wavelength.

6.4 Sample Vibrational Information and Molecular Identification

The combinations of Raman peaks in the spectra are compared to literature and known samples to identify vibrational information that is specific to chemical bonds and molecular symmetry. The combination of Raman peaks in a spectrum, acts as a fingerprint in identifying a molecule. Raman spectroscopy is an excellent tool for identifying tungsten oxides because the different phases and ratios of tungsten to oxygen can be accurately determined. The most probable composition for each sample is shown on the corresponding Raman spectra, and the samples that were not very crystalline gave Raman spectra with a low signal-to-noise ratio.

There are three wavenumber regions that can be individuated in the Raman spectra of tungsten oxide crystalline phases [38, 113-115]. The first region is found at very low wavenumbers (<200 cm^{-1}), and is associated with lattice mode vibrations from WO_6 octahedra units within the same unit cell. Raman peaks found at ~143 cm^{-1} is characteristic of monoclinic (*m*) phase WO_3, while Raman peaks found at ~183 cm^{-1} is characteristic of monoclinic *m* phase or triclinic (*t*) phase WO_3.

The second region is found at intermediate wavenumbers (200-400 cm^{-1}), and is associated with O–W–O bending modes features. Raman peaks found at ~207 cm^{-1} or ~275 cm^{-1} is characteristic of monoclinic (*m*) phase or triclinic (*t*) phase WO_3, and Raman peaks found at ~271 cm^{-1} or ~321 cm^{-1} is characteristic of crystalline WO_3. Raman peaks found at ~308 cm^{-1} is characteristic of monoclinic (*m*) phase WO_3, while Raman peaks found at ~349 cm^{-1} represents a WO_3 group.

The third region is found at the higher wavenumbers (600-900 cm^{-1}), and is associated to W–O stretching modes. Raman peaks found at ~626 cm^{-1} is characteristic of hydrated tungsten oxide, such as $WO_3.1/3H_2O$. Raman peaks found at ~645 cm^{-1} or ~678 cm^{-1} is characteristic of monoclinic (*m*) phase WO_3, and Raman peaks found at ~712 cm^{-1} and ~806 cm^{-1} is characteristic of crystalline WO_3 (the latter wavenumber positively identifies the presence of WO_3). Raman peaks found at ~775 cm^{-1} is characteristic of tetrahedral borate and WO_6 groups, and is confirmed if a Raman peak is present at ~945 cm^{-1}. Raman peaks found at

~960 cm^{-1} is characteristic of terminal W=O stretching mode, and the presence of a hydrated and nanocrystalline tungsten oxide.

To tie up and find correlations with the XRD analysis, Raman spectra was obtained using a Jobin-Yvon T64000 Raman Spectrograph with a wavelength of 514.5 nm from an argon ion laser set at a laser power of 0.384 mW at the sample, in order to minimize local heating during the Raman analysis. Raman spectroscopy was first carried out on a blank Corning glass (silicon oxide) substrate to eliminate its contribution to the Raman spectra of the samples. The Raman spectrum of the Corning glass and its Raman peaks are shown in Figure 6.10.

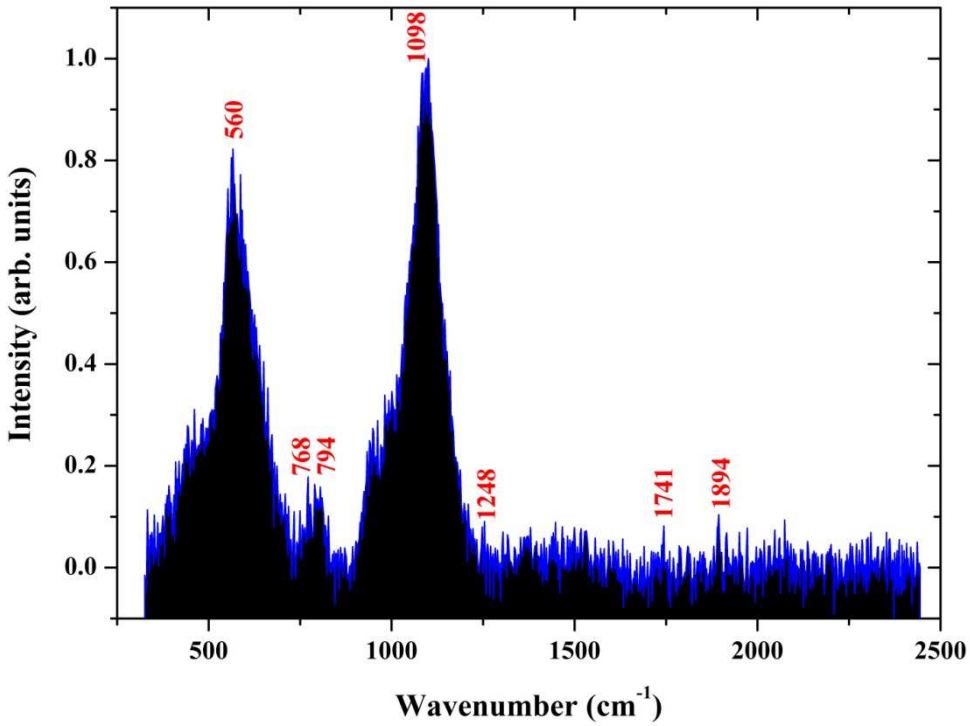


Figure 6.10 The Raman spectrum of a cleaned corning glass substrate.

The corresponding Raman spectra for the samples are shown in Appendix F. Figure 6.11 shows the Raman spectrum for the sample prepared at 9.22 µm wavelength and power density of 51.2 W/cm^2, corresponding to the SEM micrograph in Figure 6.3 (a). The results obtained from the Raman spectra are tabulated in Table 6.2.

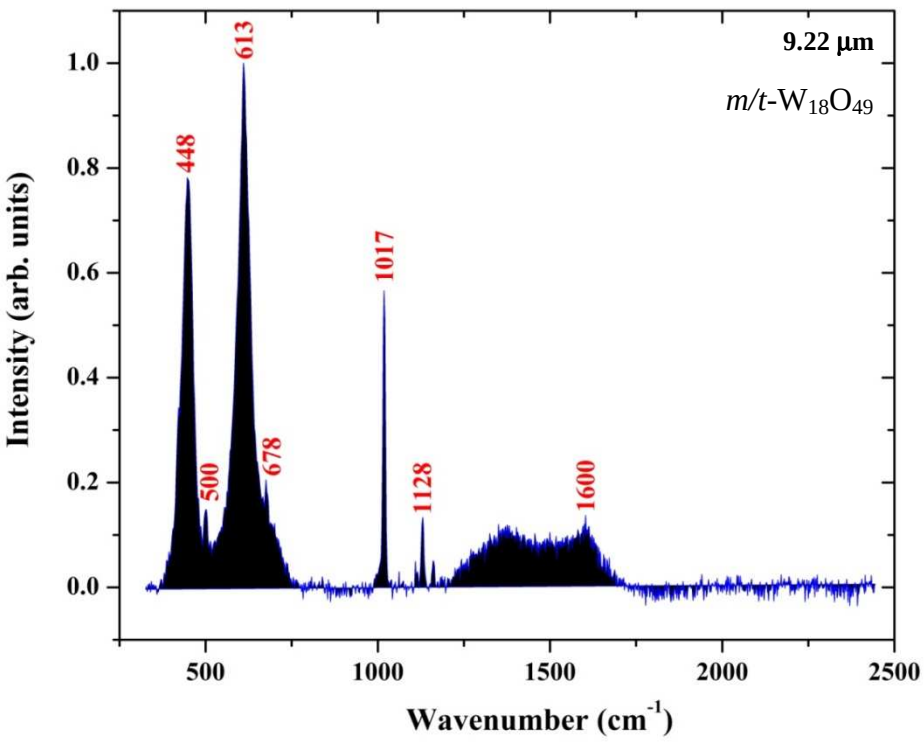


Figure 6.11 The Raman spectrum for the post-annealed sample, prepared at the 9.22 µm wavelength and 51.2 W/cm^2 power density.

Looking at the wavelength varied samples, the 9.32 µm and 9.48 µm wavelengths appeared to favour the formation of hydrated WO_3, while the 10.48 µm wavelength favoured the formation of crystalline WO_3. The wavelengths above 10.48 µm led to the formation of a mixture of $W_{18}O_{49}$ (=$WO_{2.72}$ Magneli phase) and *t*-WO_3, but XRD peaks suggest that $W_{18}O_{49}$ appears to be the more stable stoichiometry of tungsten oxides.

Looking at the power varied samples, the 26 W/cm^2 sample did not show enough peaks to match a tungsten oxide stoichiometry, and the 60 W/cm^2 sample could not be identified for similar reasons. For the power density variation, it appears that the formation of WO_3 is favoured at the 10.6 µm wavelength [2], as well as stoichiometries close to WO_3 such as $W_{10}O_{29}$ (=$WO_{2.9}$ Magneli phase), as expected. These results show some correlation with XRD.

Table 6.2. The results obtained from the Raman spectra for the varied set of laser parameters.

Wavelength Variation ($P_{density}$ = 51.2 W/cm^2)		**Power Density Variation (λ = 10.6 µm)**	
***Wavelength, λ* (µm)**	***Composition***	***Power Density, P_d* (W/cm^2)**	***Composition***
9.22	*m/t*-$W_{18}O_{49}$	17	*m/t*-$W_{18}O_{49}$
9.32	*m/t*-$WO_3.1/3H_2O$	26	-
9.48	*m/t*-$WO_3.1/3H_2O$	34	*m*-WO_3
9.70	*m/t*-$W_{18}O_{49}$	43	*m*-WO_3
10.16	*m/t*-$W_{18}O_{49}$	51	*m/t*-$W_{18}O_{49}$
10.36	*m/t*-$W_{18}O_{49}$	60	-
10.48	*m*-WO_3	68	*m*-WO_3
10.82	*m/t*-$W_{18}O_{49}$	77	*m*-WO_3
		85	*m/t*-$W_{10}O_{29}$
m ≡ monoclinic phase		94	*m/t*-$W_{10}O_{29}$
t ≡ triclinic phase		100	*m*-WO_3
		110	*m*-WO_3

6.5 Repetition experiments at the Higher Power Regime

From literature, it was found that tungsten trioxide nanowires were produced by laser pyrolysis [2, 21], and an attempt to obtain the same result was carried out here. From the literature [21], the quoted tungsten (VI) ethoxide precursor concentration was 27.23 µM (5.4 mg tungsten hexachloride in 500 mL ethanol), the laser wavelength was 10.6 µm and the power density was 2.2 kW/cm^2 (50 W power in a beam waist of 1.2 mm). Inserting the laser parameters from section 4.4.3 for the focused laser beam into equation (5.1), and noting that l = 2.5 mm, the interaction volume was found to be 11.3×10^{-3} cm^3. The stated flow rates for the precursor carrier gas (oxygen), acetylene and argon gas were 8 sccm, 8 sccm and variable, respectively, for the same experimental setup used in this study. This means that the residence time in this particular experiment was 1.4 ms, which is believed to be equivalent to the metastable state lifetime in an excited gas.

After several attempts using the quoted experimental parameters, no film or nanostructures were observed under SEM. It is believed that the discrepancy resulted from the relative flow

rates which were found to be impossible to emulate with literature, despite using the same setup.

The flow rates were then varied but the result remained the same. The only factor that could have led to this result is the relative density of the precursor, and so it was decided to use the more concentrated precursor of 2.5 mM from the previous experiments (concentration is proportional to density). Using the 2.5 mM tungsten (VI) ethoxide precursor at the flow rates stated in the literature, again led to no result. Changing the flow rates to those stated in section 6.1 and using the literature's laser parameters finally led to the formation of products, but the products differed from literature.

At the higher power densities, the linear absorption behaviour appeared to be consistent with what was seen at the lower power densities. The precursor again appeared to always absorb 1.9×10^{17} photons, even in the 1.4 ms residence time. It was seen in section 1.1.2.3 where the steady-state response of an atom to a laser field was derived, that the saturation intensity of an atomic transition is very low. The relaxation and dephasing time of the precursor used here has not yet been determined, but the results suggest that the 2.2 kW/cm^2 is probably more than the saturation intensity of the atomic transition in the short residence time, based on the linear response of the precursor to the laser field. However, this only holds true if the precursor is a saturable absorber, which is uncertain at this stage.

It was also noticed that the thin films that formed on the substrates in this set of experiments was less dense than the thin films formed at the lower power density. Apart from the multiphoton absorption by the precursor, it seems that the increased temperature gradient, which is proportional to the laser power, becomes more prominent in the laser–precursor interaction. This is expected to cause many unorthodox reaction pathways towards product formation, and so it is expected that the state preparation by these laser parameters will be very different from the low power density experiments.

The SEM micrographs of the pre-annealed samples, after laser pyrolysis was carried out, are shown in Figure 6.12. The sample is uniformly distributed with patches composed of smaller structures. As was expected, the distribution of 'ablated' material could be owed to the state preparation influenced by the high power density. Annealing this sample should lead to the

uniform growth of interesting structures, as it was seen before for less dense and uniformly distributed patches of agglomerations on the samples [2].

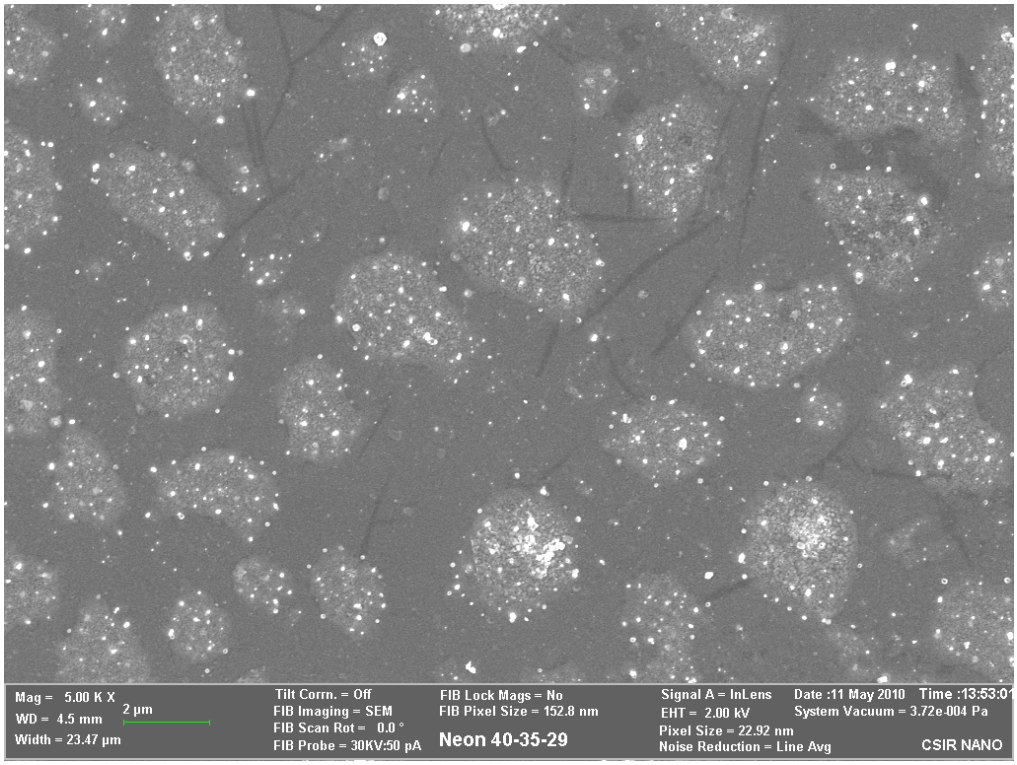


Figure 6.12 SEM micrographs of the pre-annealed sample, at 5000 times magnification, prepared at the 10.6 µm wavelength and power density of 2.2 kW/cm^2.

After annealing the sample shown in Figure 6.12 for 17 hours at 500^{o}C, it was found that six-sided stars grew out of the patches that are composed of smaller structures. Figure 6.13 shows the SEM micrographs of the stars (see Appendix G for more SEM micrographs of this sample). From the micrograph, it looks like the stars start to form on the agglomerated patch, and slowly grow out away from the agglomeration, while constantly being fed by the material in the agglomeration over time. It is not yet known if the predominant valency of +6 of tungsten has any correlation with the number of sides that the stars prefer to form.

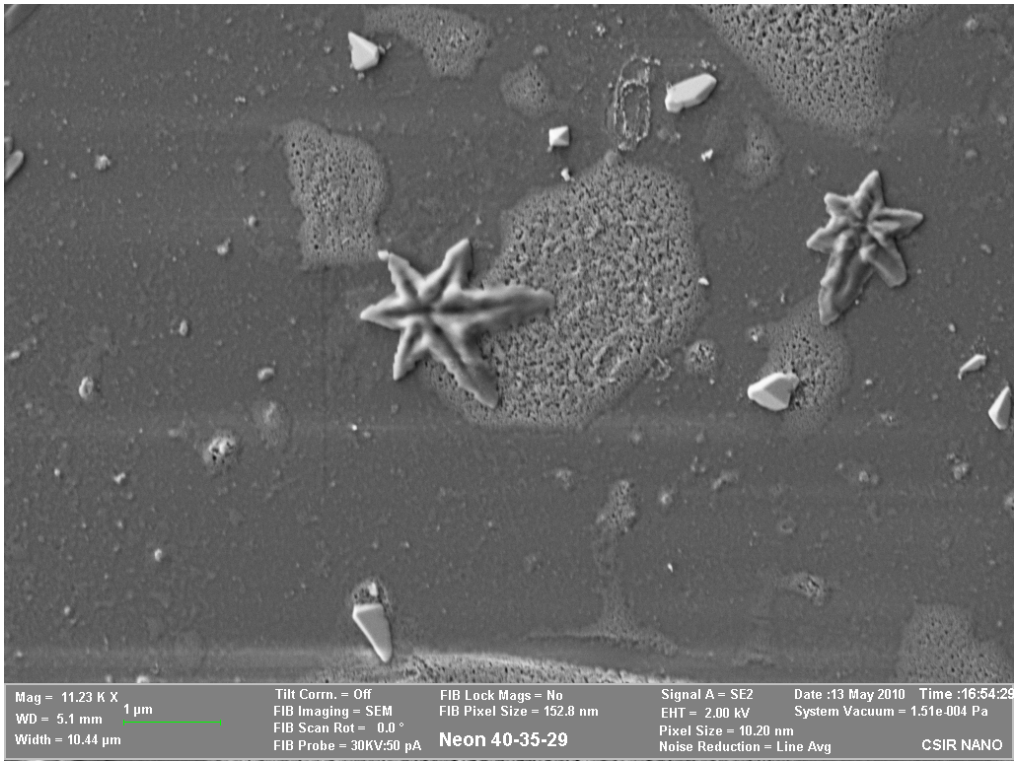


Figure 6.13 SEM micrographs (× 11230) of the post-annealed sample showing the stars that formed during annealing, prepared at the 10.6 µm wavelength and power density of 2.2 kW/cm^2.

The growth mechanism that is proposed for stars [116, see Appendix H] is based on the concentration difference and gradient (CDG) technique. The CDG technique speculates that a high local concentration of one reactant mixed with a low concentration of another reactant under ambient conditions, where the high concentration favoured the thermodynamic conditions for crystal growth and the low concentration resulted in a diffusion-controlled kinetic environment for growth of hierarchical structures. This mechanism was chosen because the laser beam profile contains regions of varying intensity, which could lead to the concentration difference in dissociated precursor [111].

At another region of the sample containing the stars, a thin film of orderly slabs was found, with numerous nanowires in between the slabs as depicted in Figure 6.14. This was similar to what was expected from literature [21] which was illustrated in Figure 2.2. However, it appears that the more concentrated precursor (~93 times more concentrated) used in this experiment, provided a surplus of dissociated material after laser interaction, and so rapid growth resulted during annealing. The proposed mechanism that was used to explain this growth of such structures was the Solid-Vapour-Solid (SVS) mechanism [21, 45], which was proposed because no catalyst for the growth of these structures could be identified with

certainty, and there was an inverse proportionality between length and diameter of the nanowires.

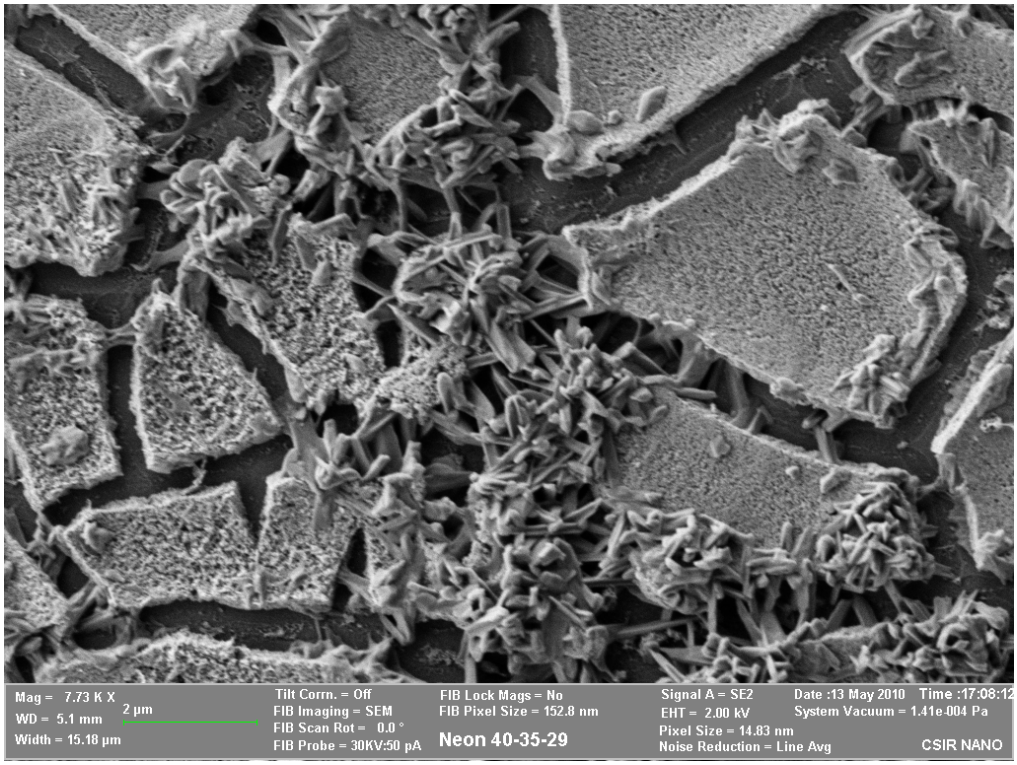


Figure 6.14 SEM micrographs of the post-annealed sample showing structures growing between slabs, at 10130 times magnification, prepared at the 10.6 µm wavelength.

XRD studies were then carried out on the sample shown in Figure 6.13, and the corresponding XRD spectrum is shown in Figure 6.15. The XRD peaks were very weak, but it was still possible to find a PDF matching this spectra. The most probable chemical composition was found to be K_2WO_4 (PDF number 00-024-0905), which raises the question as to whether potassium from the substrate (which was seen in the EDX spectra) catalyzes the growth of tungsten oxide nanostructures as observed by [111]. The grain or particulate size was calculated from the XRD peak at 44^o and Scherrer's formula, and found to be 467.9 nm ±5%.

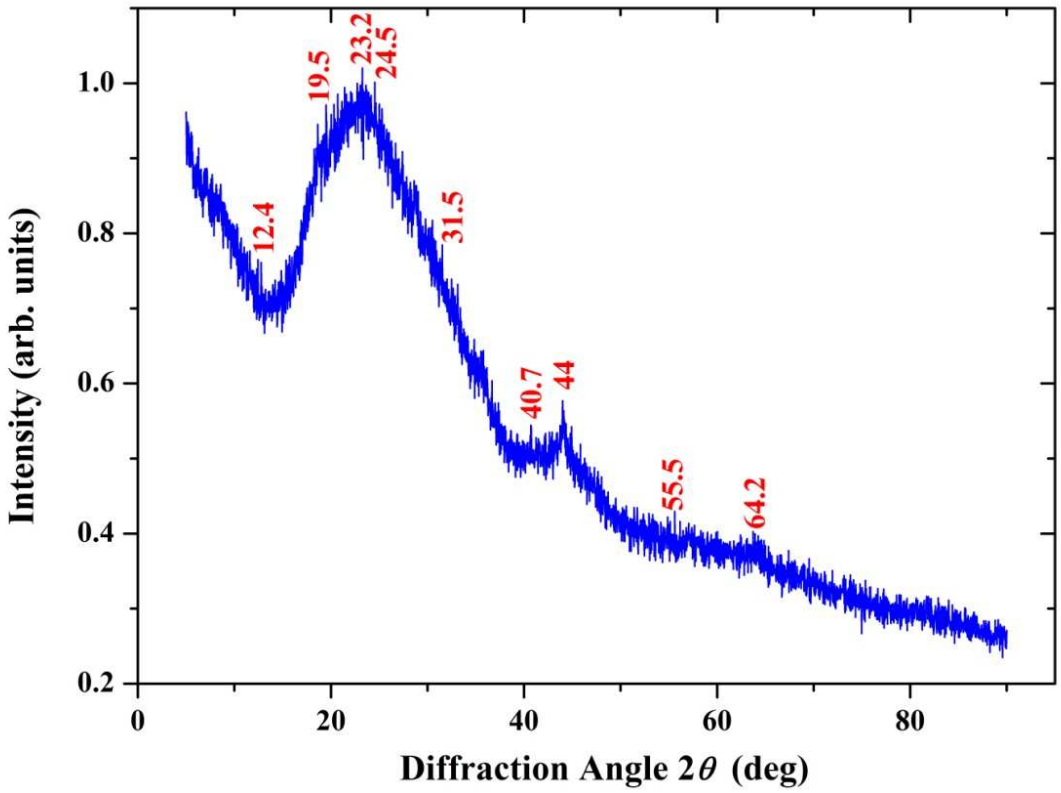


Figure 6.15 The XRD spectrum for the post-annealed sample containing the stars, slabs and the growths between the slabs.

Raman studies were carried out to verify the composition of the samples at the higher power density. The Raman spectrum is shown in Figure 6.16 for various spots on the sample, covering the stars, slabs and growths between the slabs. The wavenumbers at 224 cm^{-1}, 288 cm^{-1} and 320 cm^{-1} suggests the presence of varying grain sized WO_3 [115]. The Raman peak at 700 cm^{-1} suggests the presence of a WO_3 compound, but the lack of the peak at ~800 cm^{-1} confirms that the product is not a tungsten trioxide, and so the most probable stoichiometry is a Magneli phase that's close to WO_3 tungsten to oxygen ratio [45, 114]. The peak at 965 cm^{-1} represents a terminal W=O stretching mode of a hydrated and nanocrystalline tungsten oxide [113]. The most probable composition of the analyzed sample according to XRD and Raman spectroscopy is *m*-$W_{18}O_{49}$. Note that the peak at 700 cm^{-1} is asymmetric and makes it a candidate for phonon confinement but it was decided not to cover this topic in this study.

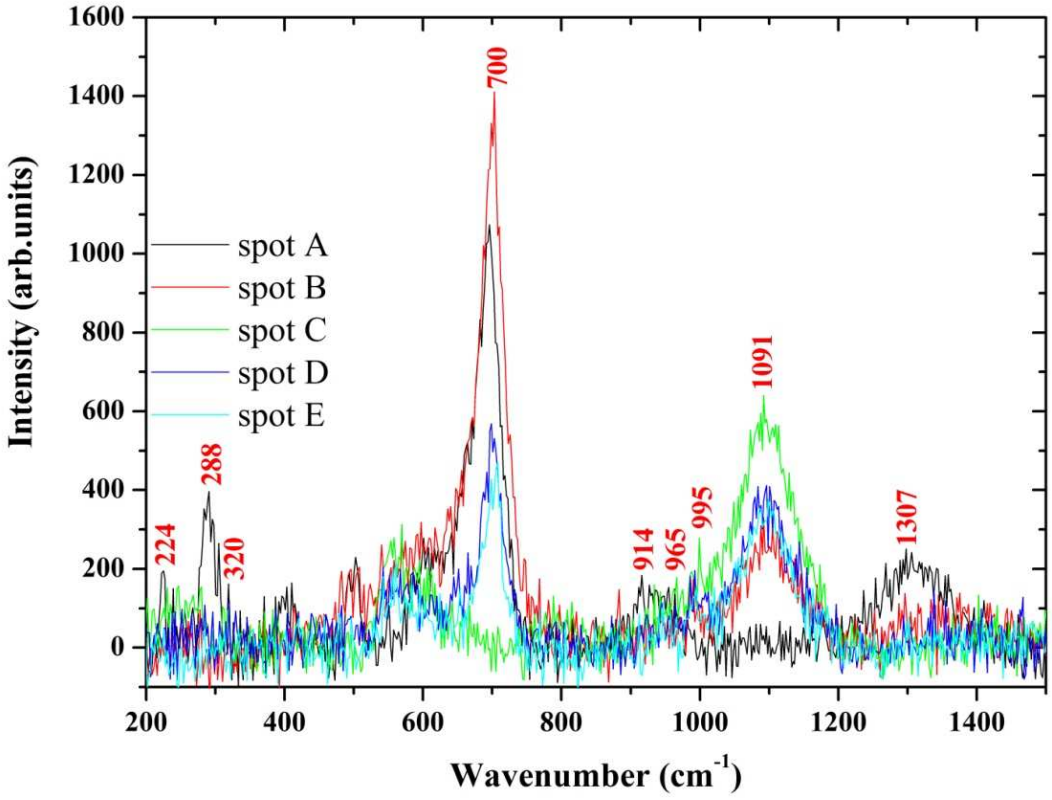


Figure 6.16 The Raman spectrum for the post-annealed sample containing the stars, slabs and the growths between the slabs.

6.6 Conclusion

Laser pyrolysis was carried out at different laser powers and wavelengths to investigate the dynamics of the laser–precursor interaction and its corresponding influence on morphology and formation of nanostructures. SEM and TEM were used to carry out morphology studies on the samples and to measure the size distributions of the spherical structures in the sample. XRD was used to determine the phase and composition of the sample material, and it was also used to obtain an average size distribution of the samples using Scherrer's formula [112]. Raman spectroscopy was successful in identifying most of the sample compositions and there was also evidence of phonon confinement observed in some samples by the asymmetric peaks. EDX was also used to confirm the presence of certain elements in the samples.

It was found that resonant and near-resonant overlapping of laser wavelength with an absorption band of the precursor resulted in the distribution of smaller nanostructures, whereas non-resonant overlapping showed an increase in the sizes of nanostructures. The

precursor showed linear absorption of laser power. The resonant and linear behavior of the precursor resulted in the lack of any trends. Linear and nonlinear optical processes, as well as photochemistry and photophysics were evident for the different laser parameters.

$W_{18}O_{49}$ six-sided stars were grown for the first time by laser pyrolysis, and the growth mechanism used to explain the formation of the stars was the CDG mechanism. Even though nanowires were grown previously using the same laser parameters, the change in concentration appeared to have made all the difference. It is known that the very dilute precursor used to make the nanowires, was too dilute to follow the CDG mechanism and follows the SVS mechanism instead. However, when using a 93 times more concentrated precursor, the CDG mechanism is applicable, and so hierarchical structures tend to grow. It was speculated previously that potassium, which was present in the substrate according to EDX, could have catalyzed the growth of the stars. It is not yet understood if the predominant valency of tungsten, which is +6, influenced the number of sides on the stars.

The results have shown the basics of the complex dynamics involved when a polyatomic molecule with 141 vibrational modes interacts with a far infrared laser beam. The possible structures that can be grown by this technique were shown, as well as the different tungsten oxide compositions. The technique does appear to have potential as a nano-synthesis alternative, and by applying it to make other materials, discloses remarkable capabilities.

Chapter 7

Conclusions and Future Work

In Chapter 1, the advancements in the emerging field of nanoscience and nanotechnology were covered. One material that stands out in this field is tungsten trioxide, and it was shown that the size of this material down to the nanoscale influences its properties. The methods used to produce this material on the nanoscale were highlighted, and the laser pyrolysis nanosynthesis method was one of the recommended methods. Laser pyrolysis began as early as 1975, and the progress thus far was looked at, and so some perspective for this project was brought into light. In this dissertation, it was shown that laser pyrolysis was successful in making tungsten trioxide and tungsten oxide nanomaterials with many different shapes.

This is the first work that attempts to understand the effects of wavelength in laser pyrolysis. The study revealed that resonant and near-resonant processes between the precursor absorption bands and laser wavelength gave smaller nanostructures when compared to non-resonant processes which gave larger nanostructures. The resonant and non-resonant processes also influenced the trend in nanostructure sizes. The chemical compositions that came out for the different wavelengths appeared to prefer the $W_{18}O_{49}$ composition. The 10.48 µm and 10.6 µm wavelengths exhibit threshold effects and favoured the WO_3 composition. The variation in power did not show the expected trend in size variation, which is increasing structure size with increasing power density, and this was verified using the multiphoton infrared excitation theory. The chemical compositions that came out for the different power densities appeared to prefer the WO_3 composition and threshold effects began to show at the 34 W/cm^2 power density.

In Chapter 2, the theory on light and laser–matter interactions was dealt with from a linear and nonlinear optical process perspective to the photophysical and photochemical processes, and formed the critical point of this study. The various photophysical processes were illustrated and the possible photochemical schemes were outlined. The exception of the Stark-Einstein law was detailed, where infrared multiphoton absorption and excitation is possible, and this theory was explained using a simple diatomic molecule. The theory on the

diatomic molecule was insufficient in explaining the more complex precursor compound, and it was observed that for a polyatomic compound the theory becomes very complicated as more dynamics are involved when the number of molecules increases.

In Chapter 3, a broad overview of the characterization techniques that was used to identify and examine the produced nanomaterial was given. The techniques that were used are FTIR, Raman spectroscopy, XRD, EDX, TEM and SEM. The applications of these techniques were discussed in Chapter 6 to explain the experimental results.

In Chapter 4, the PL6 CO_2 laser that was used and the theory of how it operates was covered. The scanning slit technique and the pyrocam technique was used to determine the parameters of the laser beam. The PL6 laser produced a beam that was not near-Gaussian before and after the focal plane of a focusing mirror, and so the scanning slit method could not be implemented. The pyrocam method became the primary technique to characterize the beam. The beam waist was found to be 1.05 mm using a 1 m radius of curvature mirror while the unfocused beam was found to have a beam waist of 6.11 mm. The beam quality factor was 4.93 and the beam was found to diverge quickly. Laser polarization theory was introduced and a polarization based attenuator was used to determine the polarization of the laser beam. It was found that the beam had 93% vertical polarization and 7% horizontal polarization. The PL6 laser is wavelength tunable and a CO_2 spectrum analyzer was used to map out the wavelength spectrum.

In Chapter 5, the laser pyrolysis experimental methodology and setup was illustrated, and the cross-flow geometry was chosen as the best. The reaction chamber operates at atmospheric pressure in this experiment whereas most of the literature reports on pressure-controlled reaction chambers. The lack of pressure monitoring inside the chamber would have lead to the discrepancies observed in the repetition experiments from literature to that observed experimentally.

The interaction volume (the volume of the laser occupied by the precursor) was found to be 0.29 cm^3 for the 6.11 mm beam waist. It was estimated that 3.2×10^{21} tungsten (VI) ethoxide molecules were present in the interaction volume but the number of photons absorbed in the residence time were two orders of magnitude less than the number of molecules.

The process and reaction steps for making the tungsten (VI) precursor were discussed and the properties of the precursor were determined. The calculation revealed that the precursor had 141 degrees of freedom which gives an idea of the complexity of such a compound, especially when interacting with a laser. A more concentrated and dense precursor was made (2.5 mM) as well as a more dilute and less dense precursor (27 µM).

The use of a larger beam waist created a longer residence time (time precursor spends in laser beam) to determine threshold effects, and it is believed that the residence time in this case was equivalent to the metastable lifetime of the precursor gas. On the other hand, when the smaller beam waist was used, the residence time is believed to be less than the metastable lifetime of the precursor gas. This result could have influenced the "state preparation" of the laser pyrolyzed material before annealing.

In Chapter 6, for the wavelength and power varied samples, SEM showed different shaped nanostructures. Some structures appeared to be bundles of rod-like structures, so TEM was used to verify this and found that there are rod-like structures as suggested. XRD was used to obtain an average size distribution for the laser parameters, and this was done using Scherrer's formula. There was good agreement when the results from Scherrer's formula were compared to the measurements made by SEM. XRD, Raman spectroscopy and EDX were successful in obtaining the chemical compositions of the synthesized material and showed good correlation. The threshold wavelength to form WO_3 was observed around 10.48 µm and 10.6 µm and threshold effects of power density was observed at 34 W/cm^2.

It was found that a repetition of the experiments in literature to make tungsten trioxide nanowires could not be achieved; it thus goes back to the pressure in the reaction chamber during the experiment, which is believed to be an important parameter in this process. However, using a more concentrated precursor at an increased flow rate resulted in the formation of tungsten oxide nanostars for the first time. The growth mechanism chosen for the stars was the concentration difference and gradient mechanism which applied in this case for the higher concentrated precursor, whereas the proposed growth mechanism for a dilute precursor was the solid-vapour-solid mechanism.

The future work will involve the study of the physical, electrical and optical properties of the synthesized products that were obtained and presented here. Techniques such as atomic force

spectroscopy and ultraviolet spectroscopy can be applied on the sample at different temperatures. When all the properties have been determined, the materials can be tailored to make specific devices, where all the properties can be harnessed. Another aspect to be considered is the scalability of the laser pyrolysis process, which can be engineered in the future since laser pyrolysis appears to be a promising method for nanotechnological advancement.

Appendix A

Steady-State Response of a Two-Level Atom to a Monochromatic Field

A.1 *Density Matrix Equations of Motion for a Two-Level Atom*

The density matrix equations for the motion of a two-level system in the absence of damping effects will be considered. There is no unique way, however, to include damping in the model, because damping mechanisms can be very different under different physical conditions. The formulation that follows, serves as a starting point for the inclusion of damping by any mechanism.

The Hamiltonian for this system can be represented as [86]

$$\hat{H} = \hat{H}_0 + \hat{V}(t), \tag{A.1}$$

where $\hat{H}_0$ denotes the atomic Hamiltonian and $\hat{V}(t)$ denotes the energy of interaction of the atom with the electromagnetic field. The energies of the states ***a*** and ***b*** are denoted as

$$E_a = \hbar\omega_a \quad \text{and} \quad E_b = \hbar\omega_b. \tag{A.2}$$

The Hamiltonian $\hat{H}_0$ can thus be represented by the diagonal matrix, and its elements can be given by

$$H_{0,nm} = E_n\delta_{nm}. \tag{A.3}$$

It is assumed that the electric dipole approximation can adequately describe the interaction energy, and so the interaction Hamiltonian is given by

$$\hat{V}(t) = -\hat{\mu}\vec{E}(t). \tag{A.4}$$

It is also assumed that the atomic wave functions corresponding to the states ***a*** and ***b*** have definite parity, such that the diagonal matrix elements $\hat{\mu}$ are eliminated, and so $\mu_{aa} = \mu_{bb} = 0$. From this, it follows that

$$V_{aa} = V_{bb} = 0. \tag{A.5}$$

The only elements of $\vec{V}$ that are not eliminated are V_{ba} and V_{ab}, which can be written explicitly as

$$V_{ba} = {V_{ab}}^{*} = -\mu_{ba}\vec{E}(t). \tag{A.6}$$

The state of the system can be described by means of a density matrix, which is given explicitly by

$$\hat{\rho} = \begin{bmatrix} \rho_{aa} & \rho_{ab} \\ \rho_{ba} & \rho_{bb} \end{bmatrix}, \tag{A.7}$$

where $\rho_{ba} = {\rho_{ab}}^{*}$. The time evolution of the density matrix in the absence of damping effects is given by

$$\begin{aligned} \dot{\rho}_{nm} = \frac{-i}{\hbar}\left[\hat{H}, \hat{\rho}\right]_{nm} &= \frac{-i}{\hbar}\left[\left(\hat{H}\hat{\rho}\right)_{nm} - \left(\hat{\rho}\hat{H}\right)_{nm}\right] \\ &= \frac{-i}{\hbar}\sum_{v}\left(H_{nv}\rho_{vm} - \rho_{nv}H_{vm}\right). \end{aligned} \tag{A.8}$$

The decomposition of the Hamiltonian into atomic and interaction parts (equation (A.1)) are introduced into equation (A.8), and is given by

$$\dot{\rho}_{nm} = -\omega_{nm}\rho_{nm} - \frac{-i}{\hbar}\sum_{v}\left(V_{nv}\rho_{vm} - \rho_{nv}V_{vm}\right), \tag{A.9}$$

where the transition frequency ($\omega_{nm} = (E_n - E_m)/\hbar$) has been introduced.

For the case of the two-level atom, the indices *n*, *m* and ν can take the values *a* and *b* only, and the equations of motion for the density matrix elements are given explicitly by

$$\dot{\rho}_{ba} = -\omega_{ba}\rho_{ba} + \frac{i}{\hbar}V_{ba}(\rho_{bb} - \rho_{aa}), \tag{A. 10 a}$$

$$\dot{\rho}_{bb} = \frac{i}{\hbar}(V_{ba}\rho_{ab} - \rho_{ba}V_{ab}), \tag{A. 10 b}$$

$$\dot{\rho}_{aa} = \frac{i}{\hbar}(V_{ab}\rho_{ba} - \rho_{ab}V_{ba}). \tag{A. 10 c}$$

It can be seen by inspection that

$$\dot{\rho}_{bb} + \dot{\rho}_{aa} = 0, \tag{A.11}$$

which implies that the total population $(\rho_{bb} + \rho_{aa})$ is a conserved quantity. The definition of the density matrix reveals that the diagonal elements of $\hat{\rho}$ represent probabilities of occupation, such that

$$\rho_{aa} + \rho_{bb} = 1. \tag{A.12}$$

Due to the relation $\rho_{ab} = \rho_{ba}{}^{*}$, no separate equation of motion is required for ρ_{ab}.

Equations (A.10 a-c) constitute the density matrix equations of motion in the absence of relaxation processes for a two-level atom. These equations provide a description of resonant nonlinear optical processes in the absence of relaxation processes. An example of such a case occurs for the material excitation with short laser pulses, where the duration is much less than the material relaxation time. The next section covers the case where relaxation processes are taken into account.

A.2 *Closed Two-Level Atom*

The relaxation processes for a closed two-level system is illustrated schematically in Figure A.1, where the upper and lower levels are not allowed to exchange population with each

other. It is assumed that the upper level ***b*** decays at a rate Γ_{ba} to the lower level ***a***, such that the lifetime of the upper level can be written as $T_1 = 1/\Gamma_{ba}$ [86]. The decay of the upper level would typically be due to spontaneous emission, and this system is called a closed system, because any population that leaves the upper level, enters the lower level. It is also assumed that the atomic dipole moment is dephased in the characteristic time T_2, leading to a transition line width (in the case of weak applied fields) of characteristic width $\gamma_{ba} = 1/T_2$.

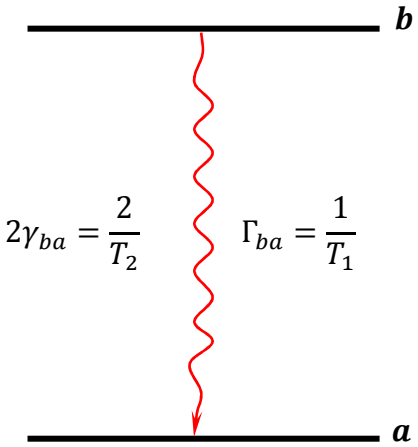


Figure A.1 Relaxation processes of the closed two-level atom [86].

The relaxation processes can be described mathematically, by adding decay terms to Equations (A.10 a-c), and are given by

$$\dot{\rho}_{ba} = -\left(\omega_{ba} + \frac{1}{T_2}\right)\rho_{ba} + \frac{i}{\hbar}V_{ba}(\rho_{bb} - \rho_{aa}), \qquad \text{(A. 13 a)}$$

$$\dot{\rho}_{bb} = \frac{-\rho_{bb}}{T_1} - \frac{i}{\hbar}(V_{ba}\rho_{ab} - \rho_{ba}V_{ab}), \qquad \text{(A. 13 b)}$$

$$\dot{\rho}_{aa} = \frac{\rho_{bb}}{T_1} + \frac{i}{\hbar}(V_{ab}\rho_{ba} - \rho_{ab}V_{ba}). \qquad \text{(A. 13 c)}$$

The forms of the relaxation terms that were included in equations (A.13 a-c) will now be justified. By inspection it can be seen that the condition

$$\dot{\rho}_{bb} + \dot{\rho}_{aa} = 0, \qquad \text{(A.14)}$$

is still satisfied.

Since the population difference $(\rho_{bb} - \rho_{aa})$ in equation (A.13 a) depends on the populations ρ_{bb} and ρ_{aa} only, it is useful to consider the equation of motion that satisfies this difference. Firstly, to formulate the equation of motion, equation (A.13 c) is subtracted from equation (A.13 b) to give

$$\frac{d}{dt}(\rho_{bb} - \rho_{aa}) = \frac{-2\rho_{bb}}{T_1} - \frac{2i}{\hbar}(V_{ba}\rho_{ab} - \rho_{ba}V_{ab}). \qquad (A.15)$$

The term $\frac{-2\rho_{bb}}{T_1}$ can be rewritten using the relation $2\rho_{bb} = (\rho_{bb} - \rho_{aa}) + 1$ (which follows from equation (1.16)), and is given by

$$\frac{d}{dt}(\rho_{bb} - \rho_{aa}) = -\frac{(\rho_{bb} - \rho_{aa}) + 1}{T_1} - \frac{2i}{\hbar}(V_{ba}\rho_{ab} - \rho_{ba}V_{ab}). \qquad (A.16)$$

This relation can be generalized by allowing the possibility that the population difference in thermal equilibrium $(\rho_{bb} - \rho_{aa})^{(eq)}$ can have some value other than -1, which is the value taken from the assumption that only spontaneous transitions could occur. The generalized version of equation (A.16) is then given by

$$\frac{d}{dt}(\rho_{bb} - \rho_{aa}) = -\frac{(\rho_{bb} - \rho_{aa}) - (\rho_{bb} - \rho_{aa})^{(eq)}}{T_1} - \frac{2i}{\hbar}(V_{ba}\rho_{ab} - \rho_{ba}V_{ab}). \qquad (A.17)$$

It is seen therefore, that for a closed two-level system, the density matrix equations of motion reduce to two coupled equations, namely, equations (A.13 a) and (A.17).

To justify the relaxation terms in equations (A.13 a) and (A.17), the nature of the solutions are examined in the absence of an applied field $(V_{ba} = 0)$. The solution to equation (A.17) is given by

$$[\rho_{bb}(t) - \rho_{aa}(t)] = (\rho_{bb} - \rho_{aa})^{(eq)} + \{[\rho_{bb}(0) - \rho_{aa}(0)] - (\rho_{bb} - \rho_{aa})^{(eq)}\}e^{-t/T_1}. \qquad (A.18)$$

Equation (A.18) shows that the population inversion $[\rho_{bb}(t) - \rho_{aa}(t)]$ relaxes from its initial value $\rho_{bb}(0) - \rho_{aa}(0)$ to its equilibrium value $(\rho_{bb} - \rho_{aa})^{(eq)}$ in a time of the order T_1. It is for this reason that T_1 is called the relaxation time.

In a similar manner, the solution to equation (A.13 a) for the case $V_{ba} = 0$, is written as

$$\rho_{ba}(t) = \rho_{ba}(0)e^{-(i\omega_{ba}+1/T_2)t}. \tag{A.19}$$

The result in equation (A.19) can be interpreted more directly by considering the expectation value of the induced dipole moment, which is given by

$$\begin{aligned}\langle\vec{\mu}(t)\rangle &= \mu_{ab}\rho_{ba}(t) + \mu_{ba}\rho_{ab}(t) \\ &= \mu_{ab}\rho_{ba}(0)e^{-(i\omega_{ba}+1/T_2)t} + \mu_{ba}\rho_{ab}(0)e^{+(i\omega_{ba}+1/T_2)t} \\ &= \left[\mu_{ab}\rho_{ba}(0)e^{-i\omega_{ba}t} + \mu_{ba}\rho_{ab}(0)e^{i\omega_{ba}t}\right]e^{-t/T_2}. \end{aligned} \tag{A.20}$$

Equation (A.20) shows that, for an undriven atom, the dipole moment oscillates at frequency ω_{ba} and decays to zero in the characteristic time T_2. It is for this reason that T_2 is known as the dephasing time.

T_1 and T_2 are related to the collisional dephasing rate γ_c by

$$\frac{1}{T_2} = \frac{1}{2T_1} + \gamma_c. \tag{A.21}$$

A.3 *Steady-State Response of a Closed Two-Level Atom to a Monochromatic Field*

The solution to the density matrix equations of motion for a closed two-level atom in the presence of a monochromatic and steady-state field will now be examined. Recall that the density matrix equations for the closed two-level atomic system were given in equations (A.13 a) and (A.17).

The interaction Hamiltonian for an applied field in the form of a monochromatic wave of frequency ω (according to the electric dipole approximation) is given by [86]

$$\hat{V} = -\hat{\mu}\left(Ee^{-i\omega t} + E^{*}e^{i\omega t}\right), \tag{A.23}$$

and the matrix elements of the interaction Hamiltonian are given by

$$V_{ba} = -\mu_{ba}\left(Ee^{-i\omega t} + E^{*}e^{i\omega t}\right). \tag{A.24}$$

Equations (A.13 a) and (A.17) cannot be solved exactly for V_{ba} from equation (A.24), and so the rotating-wave approximation is used to find a solution. Recall the discussion for equation (A.20), which stated that in the absence of a driving field, ρ_{ba} tends to evolve in time as $e^{-i\omega_{ba}t}$. It is for this reason, when ω is approximately equal to ω_{ba}, the part of V_{ba} that oscillates as $e^{-i\omega t}$ acts as a far more effective driving term for ρ_{ba} than does the part that oscillates as $e^{i\omega t}$. It is thus a good approximation to write equation (A.24) as

$$V_{ba} = -\mu_{ba}Ee^{-i\omega t}. \tag{A.25}$$

This approximation is called the rotating-wave approximation. Within this approximation, the density matrix equations of motion in (A.13 a) and (A.17) are written as

$$\frac{d}{dt}\rho_{ba} = -\left(i\omega_{ba} + \frac{1}{T_2}\right)\rho_{ba} + \frac{i}{\hbar}\mu_{ba}Ee^{-i\omega t}(\rho_{bb} - \rho_{aa}), \tag{A.26}$$

and

$$\frac{d}{dt}(\rho_{bb} - \rho_{aa}) = -\frac{(\rho_{bb} - \rho_{aa}) - (\rho_{bb} - \rho_{aa})^{(eq)}}{T_1} + \frac{2i}{\hbar}\left(\mu_{ba}Ee^{-i\omega t}\rho_{ab} - \mu_{ba}E^{*}e^{i\omega t}\rho_{ba}\right). \tag{A.27}$$

Note that (in the rotating wave approximation) ρ_{ab} is driven only near its resonance frequency ω_{ba}, and $(\rho_{bb} - \rho_{aa})$ is driven only near zero frequency, which is its natural frequency.

The steady-state solutions for equations (A.26) and (A.27) will now be solved, where the solution is valid long after the transients associated with the turn-on of the driving field have expired. This can be done by introducing the slowly varying quantity σ_{ba}, defined by

$$\rho_{ba}(t) = \sigma_{ba} e^{-i\omega t}. \tag{A.28}$$

Applying equation (A.28) to equations (A.26) and (A.27), gives

$$\frac{d}{dt}\sigma_{ba} = \left(i(\omega - \omega_{ba}) + \frac{1}{T_2}\right)\sigma_{ba} + \frac{i}{\hbar}\mu_{ba}E(\rho_{bb} - \rho_{aa}), \tag{A.29}$$

and

$$\frac{d}{dt}(\rho_{bb} - \rho_{aa}) = -\frac{(\rho_{bb} - \rho_{aa}) - (\rho_{bb} - \rho_{aa})^{(eq)}}{T_1} + \frac{2i}{\hbar}(\mu_{ba}E\sigma_{ab} - \mu_{ba}E^*\sigma_{ba}). \tag{A.30}$$

The steady-state solutions can now be obtained by equating the left-hand side of equations (A.29) and (A.30) to zero. Two coupled equations are then obtained, which are solved algebraically to obtain

$$(\rho_{bb} - \rho_{aa}) = \frac{(\rho_{bb} - \rho_{aa})^{(eq)}[1 + (\omega - \omega_{ba})^2 T_2^2]}{1 + (\omega - \omega_{ba})^2 T_2^2 + (4/\hbar^2)|\mu_{ba}|^2 |E|^2 T_1 T_2}, \tag{A.31}$$

and

$$\rho_{ba} = \sigma_{ba} e^{-i\omega t} = \frac{\mu_{ba} E e^{-i\omega t}(\rho_{bb} - \rho_{aa})}{\hbar(\omega - \omega_{ba} + i/T_2)}. \tag{A.32}$$

The result of equations (A.31) and (A.32) are used to calculate the polarization, which is given by the off-diagonal elements of the density matrix given by

$$\vec{P}(t) = N\langle\vec{\mu}\rangle = N\,\mathrm{Tr}\left(\hat{\hat{\rho}}\hat{\hat{\mu}}\right) = N(\mu_{ab}\rho_{ba} + \mu_{ba}\rho_{ab}), \tag{A.33}$$

where N is the number density of atoms.

The complex amplitude P of the polarization is introduced now, through the relation

$$\vec{P}(t) = Pe^{-i\omega t} + P^{*}e^{i\omega t}. \tag{A.35}$$

The susceptibility χ is defined as the constant of proportionality relating P and E by

$$P = \epsilon_0\chi E. \tag{A.34}$$

Hence, from equations (A.32) through to (A.36), it is found that the susceptibility is given by

$$\chi = \frac{N|\mu_{ba}|^2(\rho_{bb} - \rho_{aa})}{\epsilon_0\hbar(\omega - \omega_{ba} + i/T_2)}, \tag{A.36}$$

where $(\rho_{bb} - \rho_{aa})$ is given by equation (A.32). The expression for $(\rho_{bb} - \rho_{aa})$ is introduced into equation (A.36) and the denominator is rationalized to obtain the result given by

$$\chi = \frac{N(\rho_{bb} - \rho_{aa})^{(eq)}|\mu_{ba}|^2(\omega - \omega_{ba} - i/T_2)\,T_2^2/\epsilon_0\hbar}{1 + (\omega - \omega_{ba})^2T_2^2 + (4/\hbar^2)|\mu_{ba}|^2|E|^2T_1T_2}. \tag{A.37}$$

Note that equation (A.37) gives the total susceptibility, including the linear and nonlinear contributions.

A new notation is introduced to simplify equation (A.37), and the first expression is given by

$$\Omega = 2|\mu_{ba}||E|/\hbar, \tag{A.38}$$

which is known as the on-resonance Rabi-frequency, and the second expression is given by

$$\Delta = \omega - \omega_{ba}, \tag{A.39}$$

which is known as the detuning factor, so that the susceptibility is now given by

$$\chi = \left[N(\rho_{bb} - \rho_{aa})^{(eq)}|\mu_{ba}|^2 \frac{T_2}{\epsilon_0 \hbar}\right] \frac{\Delta T_2 - i}{1 + \Delta^2 T_2^2 + \Omega^2 T_1 T_2}. \tag{A.40}$$

The combination of factors in the square brackets in equation (A.40) will now be expressed in terms of the linear absorption coefficient of the material system, which is a directly measurable quantity. The absorption coefficient is given in general by

$$\alpha = \frac{2\omega}{c} \mathrm{Im}\, n = \frac{2\omega}{c} \mathrm{Im}\left[(1+\chi)^{1/2}\right], \tag{A.41 a}$$

and, whenever the condition $|\chi| \ll 1$ is valid, the absorption coefficient can be expressed by

$$\alpha = \frac{\omega}{c} \mathrm{Im}\, \chi. \tag{A.41 b}$$

By letting $\alpha_0(\Delta)$ denote the absorption coefficient experienced by a weak optical wave detuned from the atomic resonance by an amount Δ, it is found that by ignoring the contribution $\Omega^2 T_1 T_2$ in the denominator of equation (A.40), so that $\alpha_0(\Delta)$ can be expressed as

$$\alpha_0(\Delta) = \frac{\alpha_0(0)}{1 + \Delta^2 T_2^2}, \tag{A.42 a}$$

where the unsaturated, line-center absorption coefficient is given by

$$\alpha_0(0) = -\frac{\omega_{ba}}{c}\left[N(\rho_{bb} - \rho_{aa})^{(eq)}|\mu_{ba}|^2 \frac{T_2}{\epsilon_0 \hbar}\right]. \quad \text{(A. 42 b)}$$

By introducing equations (A.42 a) and (A.42 b) into equation (A.40), it is found that the susceptibility can be written as

$$\chi = -\frac{\alpha_0(0)}{\omega_{ba}/c}\frac{\Delta T_2 - i}{1 + \Delta^2 T_2^2 + \Omega^2 T_1 T_2}. \quad \text{(A. 43)}$$

To interpret the result in equation (A.43), it is useful to express the susceptibility as $\chi = \chi' + i\chi''$ where its real and imaginary parts are given by

$$\chi' = -\frac{\alpha_0(0)}{\omega_{ba}/c}\frac{1}{\sqrt{1 + \Omega^2 T_1 T_2}}\frac{\Delta T_2 / \sqrt{1 + \Omega^2 T_1 T_2}}{1 + \Delta^2 T_2^2/\left(1 + \Omega^2 T_1 T_2\right)}, \quad \text{(A. 44 a)}$$

and

$$\chi'' = \frac{\alpha_0(0)}{\omega_{ba}/c}\left(\frac{1}{1 + \Omega^2 T_1 T_2}\right)\frac{1}{1 + \Delta^2 T_2^2/\left(1 + \Omega^2 T_1 T_2\right)}. \quad \text{(A. 44 b)}$$

The expressions in equation (A.44 a) and (A.44 b) suggests that even in the presence of an intense laser field, χ' has a dispersive lineshape and χ'' has a Lorentzian lineshape. However, each of these lines has been broadened by the factor $\left(1 + \Omega^2 T_1 T_2\right)^{1/2}$ with respect to the weak-field width. The width of the absorption line (full width at half maximum) is thus given by

$$\Delta\omega_{\mathrm{FWHM}} = \frac{2}{T_2}\left(1 + \Omega^2 T_1 T_2\right)^{1/2}. \quad \text{(A. 45)}$$

Spectral lines tend to become broadened when measured using intense optical fields, and is known as power broadening. The line center value of χ'' (and absorption coefficient α) is decreased with respect to its weak-field value by the factor $\left(1+\Omega^2 T_1 T_2\right)^{1/2}$. The absorption tends to decrease when measured using an intense optical field, and is known as saturation. This behaviour is illustrated in Figure A.2.

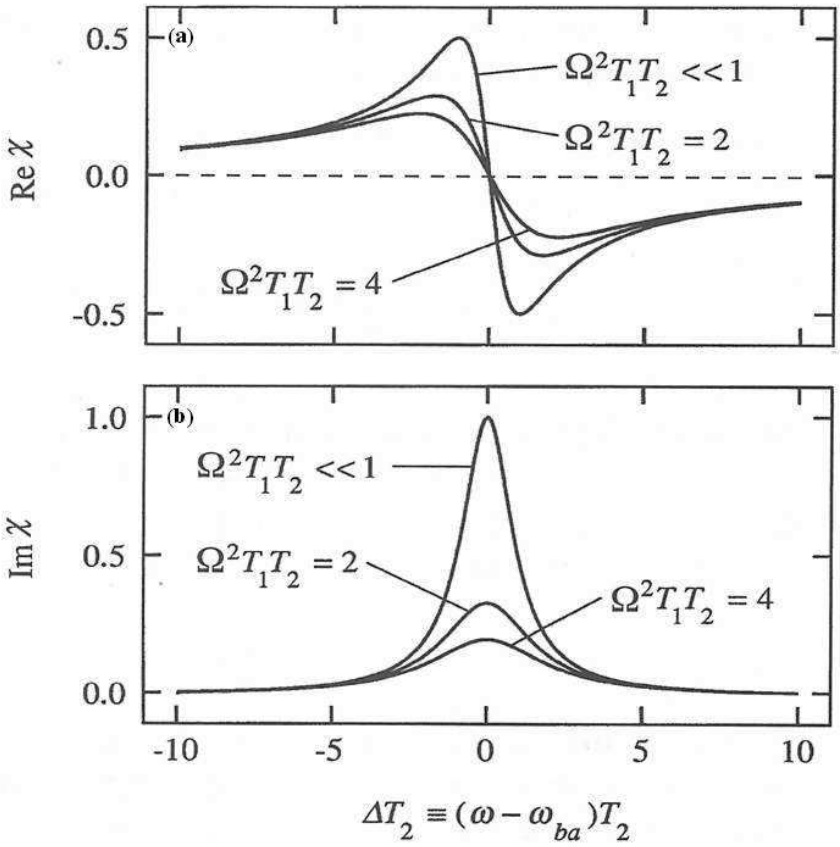


Figure A.2 (a) Real and **(b)** imaginary parts of the susceptibility (in units $\alpha_0 c/\omega_{ba}$) plotted as functions of the optical frequency ω for several values of the saturation parameter $\Omega^2 T_1 T_2$ [86].

It is convenient to define the quantity E_S^0 which is known as the line-center saturation field strength, by means of the relation

$$\Omega^2 T_1 T_2 = \frac{|E|^2}{|E_S^0|^2}\,. \qquad \text{(A. 46)}$$

Using equation (A.38), it is found that E_S^0 is given explicitly by

$$|E_S^0|^2 = \frac{\hbar^2}{4|\mu_{ba}|^2 T_1 T_2}\,. \tag{A.47}$$

The expression in equation (A.43) for the susceptibility can be rewritten in terms of the saturation field as

$$\chi = -\frac{\alpha_0(0)}{\omega_{ba}/c}\frac{\Delta T_2 - i}{1 + \Delta^2 T_2^2 + |E|^2/|E_S^0|^2}. \tag{A.48}$$

The expression in equation (A.48) suggests that the significance of E_S^0 is that the absorption experienced by an optical wave tuned to line center (which is proportional to Im χ evaluated at $\Delta = 0$) drops to one-half its weak-field value when the optical field has a strength of E_S^0. Similarly, a saturation field for a wave of arbitrary detuning can be defined, which is denoted by E_S^Δ, by means of the relation

$$\left|E_S^\Delta\right|^2 = |E_S^0|^2\left(1 + \Delta^2 T_2^2\right). \tag{A.49}$$

It is now clear that in equation (A.49), Im χ drops to one-half its weak-field value when a field of detuning Δ has a field strength of E_S^Δ.

It is also useful to define the saturation intensity for a wave at line center (assuming that $|n-1| \ll 1$) as

$$I_S^0 = 2\epsilon_0 c|E_S^0|^2, \tag{A.50}$$

and the saturation intensity for a wave of arbitrary detuning can be defined as

$$I_S^\Delta = 2\epsilon_0 c\left|E_S^\Delta\right|^2 = I_S^0\left(1 + \Delta^2 T_2^2\right). \tag{A.51}$$

To better understand and relate the nonlinear optical susceptibility treatment to the perturbative treatment, the first and third-order contributions to the susceptibility of a collection of two-level atoms will be calculated. By expanding equation (A.48) using a power series in the quantity $|E|^2/|E_S^0|^2$ and retaining only the first and second terms, it is found that the susceptibility can be approximated as

$$\chi \cong \frac{-\alpha_0(0)}{\omega_{ba}/c}\left(\frac{\Delta T_2 - i}{1+\Delta^2 T_2^2}\right)\left(1 - \frac{1}{1+\Delta^2 T_2^2}\frac{|E|^2}{|E_S^0|^2}\right). \qquad (A.52)$$

The expression in equation (A.52) can now be equated to the usual power series expansion $\chi = \chi^{(1)} + 3\chi^{(3)}|E^2|$ (where $\chi^{(3)} \equiv \chi^{(3)}(\omega = \omega + \omega - \omega)$), and so it is found that the first and third-order susceptibilities are given by

$$\chi^{(1)} = \frac{-\alpha_0(0)}{\omega_{ba}/c}\frac{\Delta T_2 - i}{1+\Delta^2 T_2^2}, \qquad (A.53\text{ a})$$

and

$$\chi^{(3)} = \frac{\alpha_0(0)}{3\omega_{ba}/c}\left[\frac{\Delta T_2 - i}{\left(1+\Delta^2 T_2^2\right)^2}\right]\frac{1}{|E_S^0|^2}. \qquad (A.53\text{ b})$$

The frequency dependence of $\chi^{(3)}$ as given by equation (A.53 a) and (A.53 b) are illustrated in Figure A.3. Note that the sign of $\chi^{(3)}$ is opposite to that of $\chi^{(1)}$, and can be understood by noting that $\chi^{(3)}$ represents a saturation of the optical response.

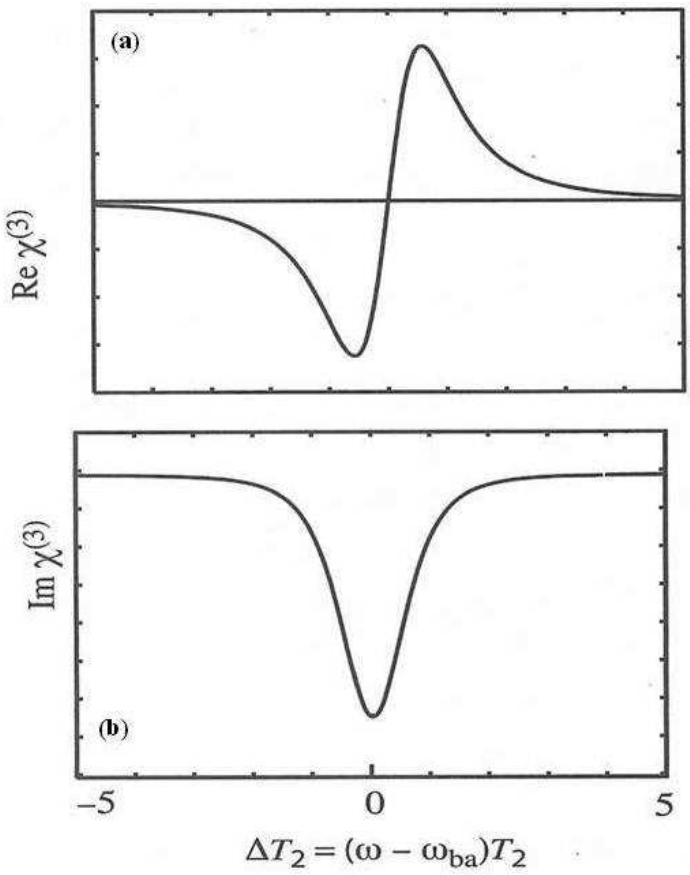


Figure A.3 (a) Real and **(b)** imaginary parts of the susceptibility $\chi^{(3)}$ plotted as functions of the optical frequency ω [86].

For some purposes, the nonlinear susceptibility can be expressed in terms of the line-center saturation intensity, and is given by

$$\chi^{(3)} = \frac{\alpha_0(0)}{3\omega_{ba}/c}\left[\frac{\Delta T_2 - i}{\left(1+\Delta^2 T_2^2\right)^2}\right]\frac{2\epsilon_0 c}{I_S^0}, \qquad \text{(A. 54 a)}$$

or, through the use of equations (A.42 a) and (A.51), in terms of the saturation intensity and absorption coefficient at the laser frequency as

$$\chi^{(3)} = \frac{\alpha_0(\Delta)(\Delta T_2 - i)}{3\omega_{ba}/c}\frac{2\epsilon_0 c}{I_S^{\Delta}}. \qquad \text{(A. 54 b)}$$

Note also that the third-order susceptibility can be related to the linear susceptibility by

$$\chi^{(3)} = \frac{-\chi^{(1)}}{3\left(1+\Delta^2 T_2^2\right)^2 |E_S^0|^2} = \frac{-\chi^{(1)}}{3\left|E_S^{\Delta}\right|^2}. \tag{A.55}$$

Furthermore, through the use of equations (A.42 b) and (A.47), the first and third-order susceptibilities can be expressed in terms of microscopic quantities as

$$\chi^{(1)} = \left[N(\rho_{bb}-\rho_{aa})^{(eq)}|\mu_{ba}|^2 \frac{T_2}{\epsilon_0 \hbar}\right] \frac{\Delta T_2 - i}{1+\Delta^2 T_2^2}, \tag{A.56 a}$$

and

$$\chi^{(3)} = -\frac{4}{3} N(\rho_{bb}-\rho_{aa})^{(eq)}|\mu_{ba}|^4 \frac{T_1 T_2}{\epsilon_0 \hbar^3} \frac{\Delta T_2 - i}{\left(1+\Delta^2 T_2^2\right)^2}. \tag{A.56 b}$$

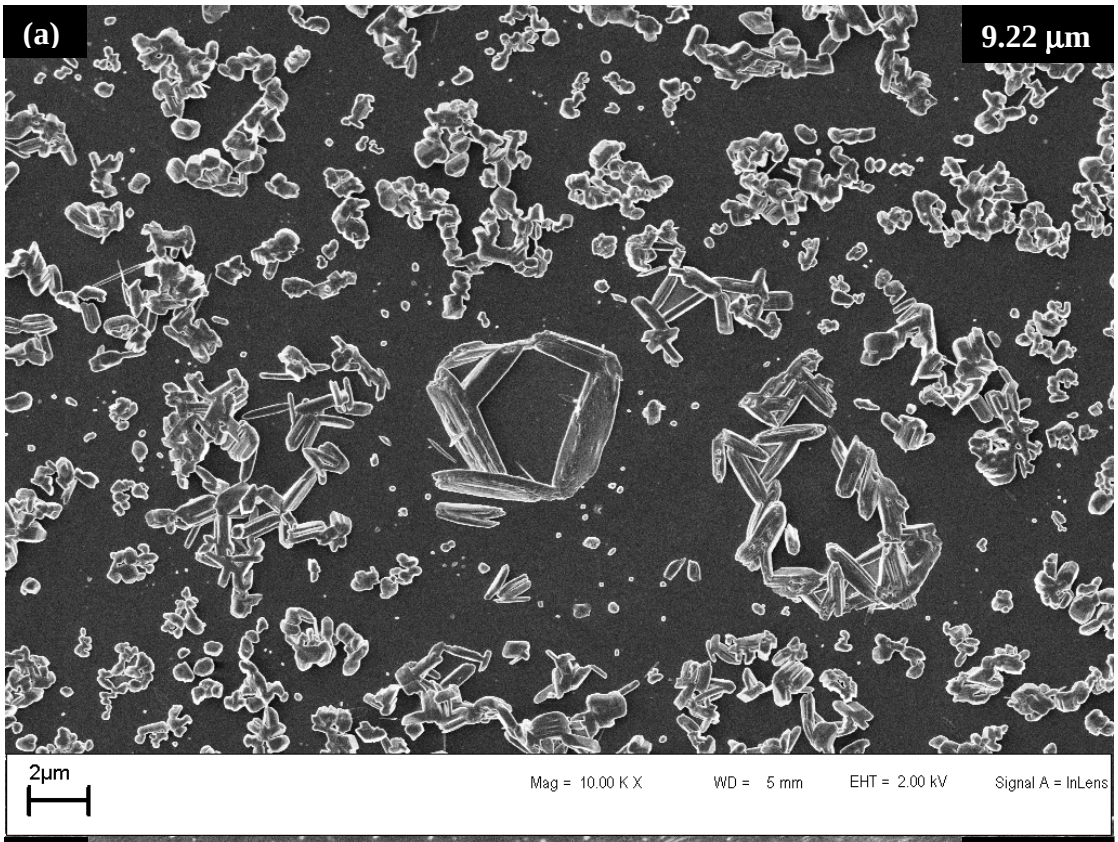
In the limit $\Delta T_2 \gg 1$, the expression for $\chi^{(3)}$ reduces to

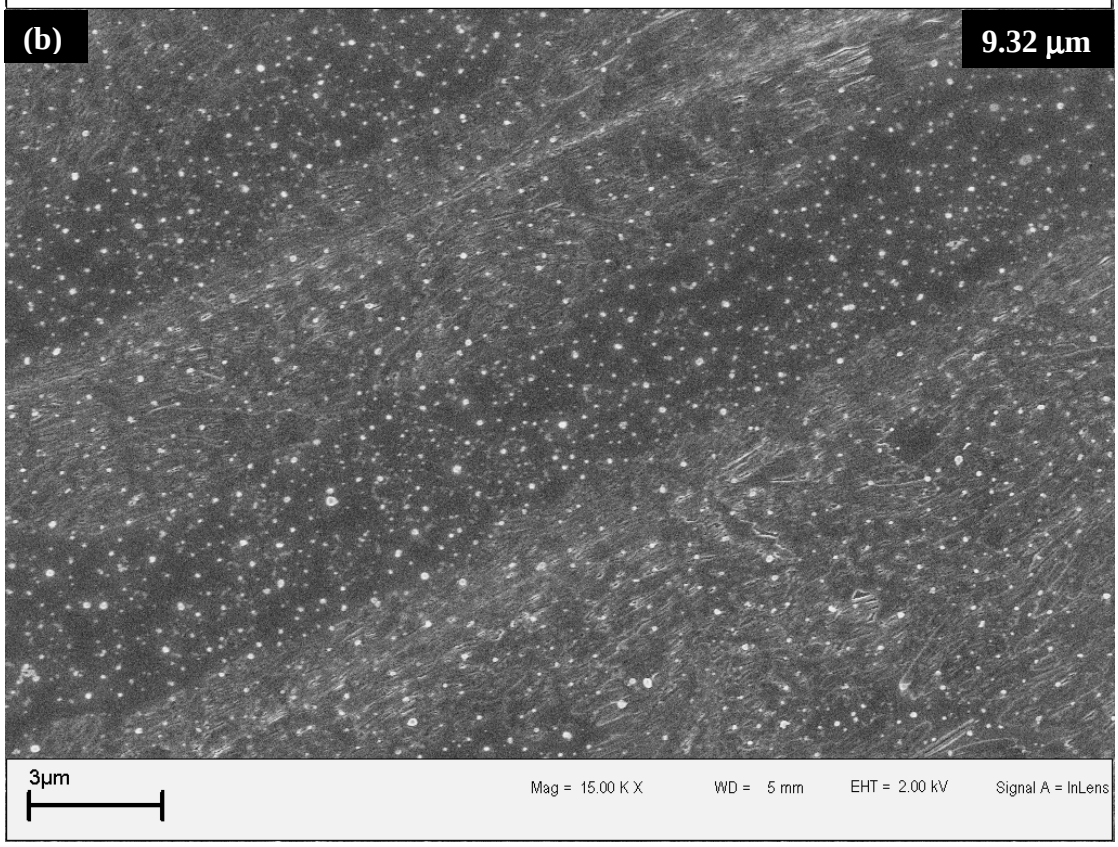
$$\chi^{(3)} = -\frac{4}{3} N(\rho_{bb}-\rho_{aa})^{(eq)}|\mu_{ba}|^4 \frac{1}{\hbar^3 \Delta^3} \frac{T_1}{T_2}. \tag{A.57}$$

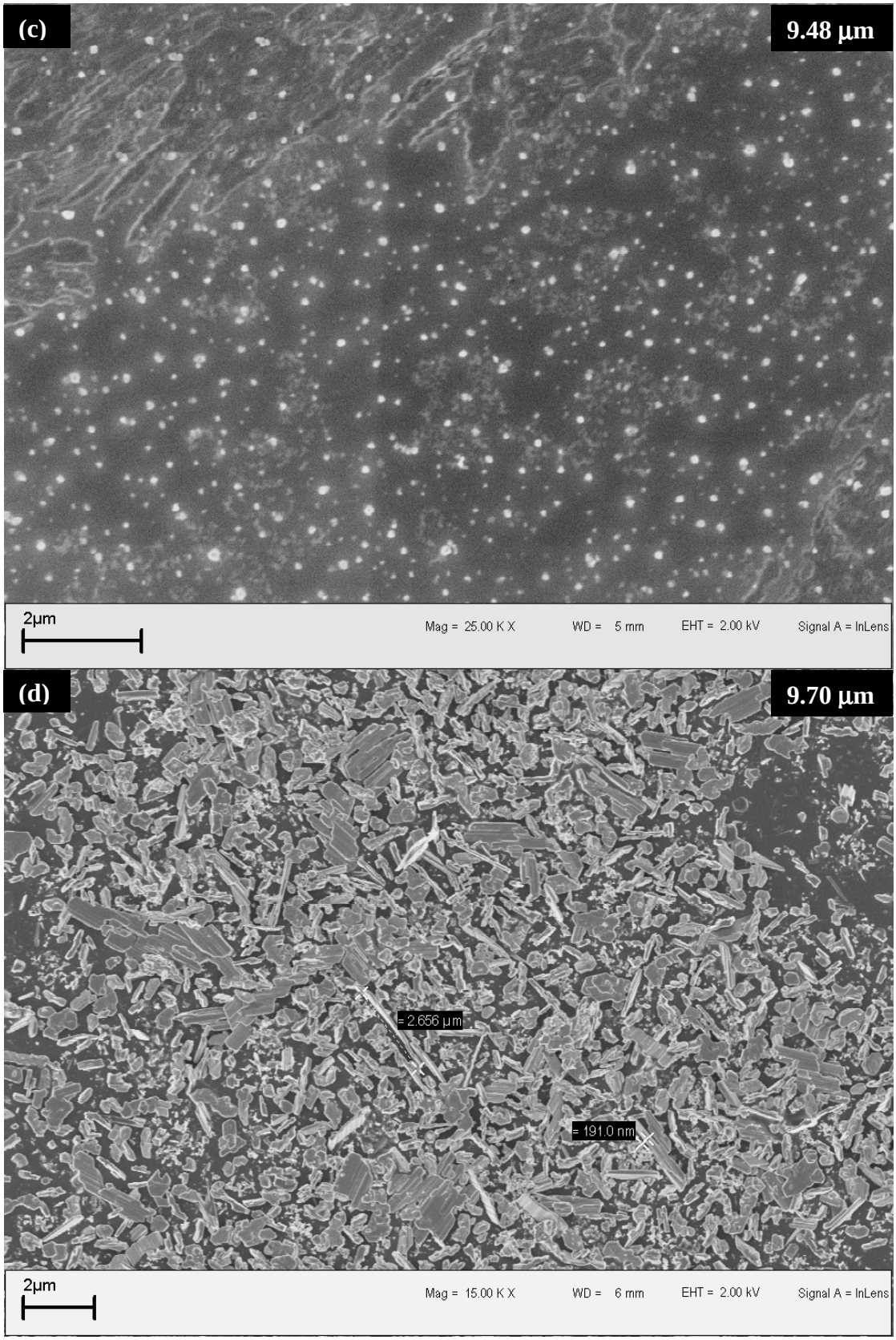
To get an idea of the magnitudes of some of the physical quantities that were introduced, an example will be considered. Since (for $n = 1$) the intensity of an optical wave field strength E is given by $I = 2\epsilon_0 c|E|^2$, the Rabi frequency of equation (A.38) is given by

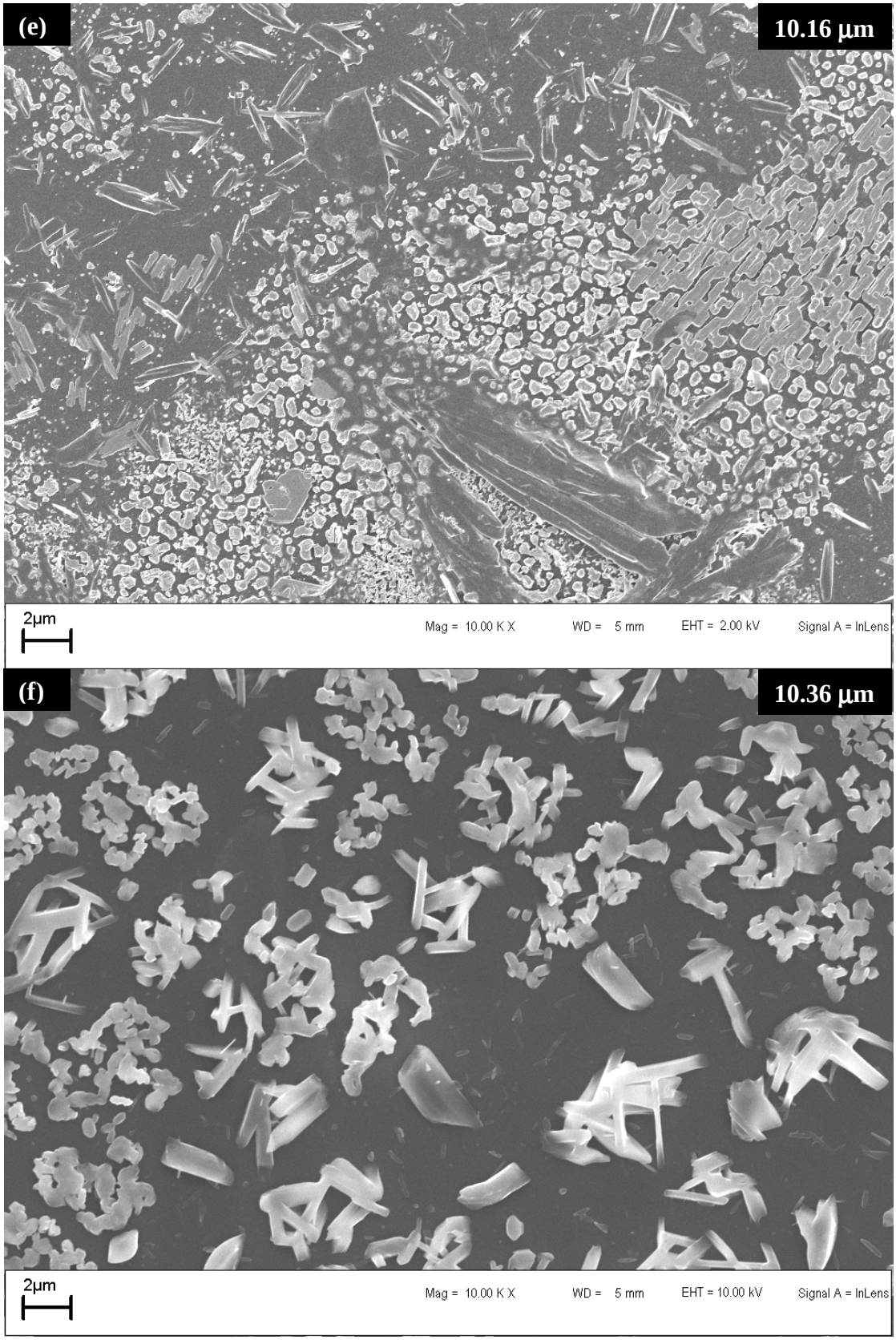
$$\Omega = \frac{2|\mu_{ba}|}{\hbar}\left(\frac{I}{2\epsilon_0 c}\right)^{1/2}. \tag{A.58}$$

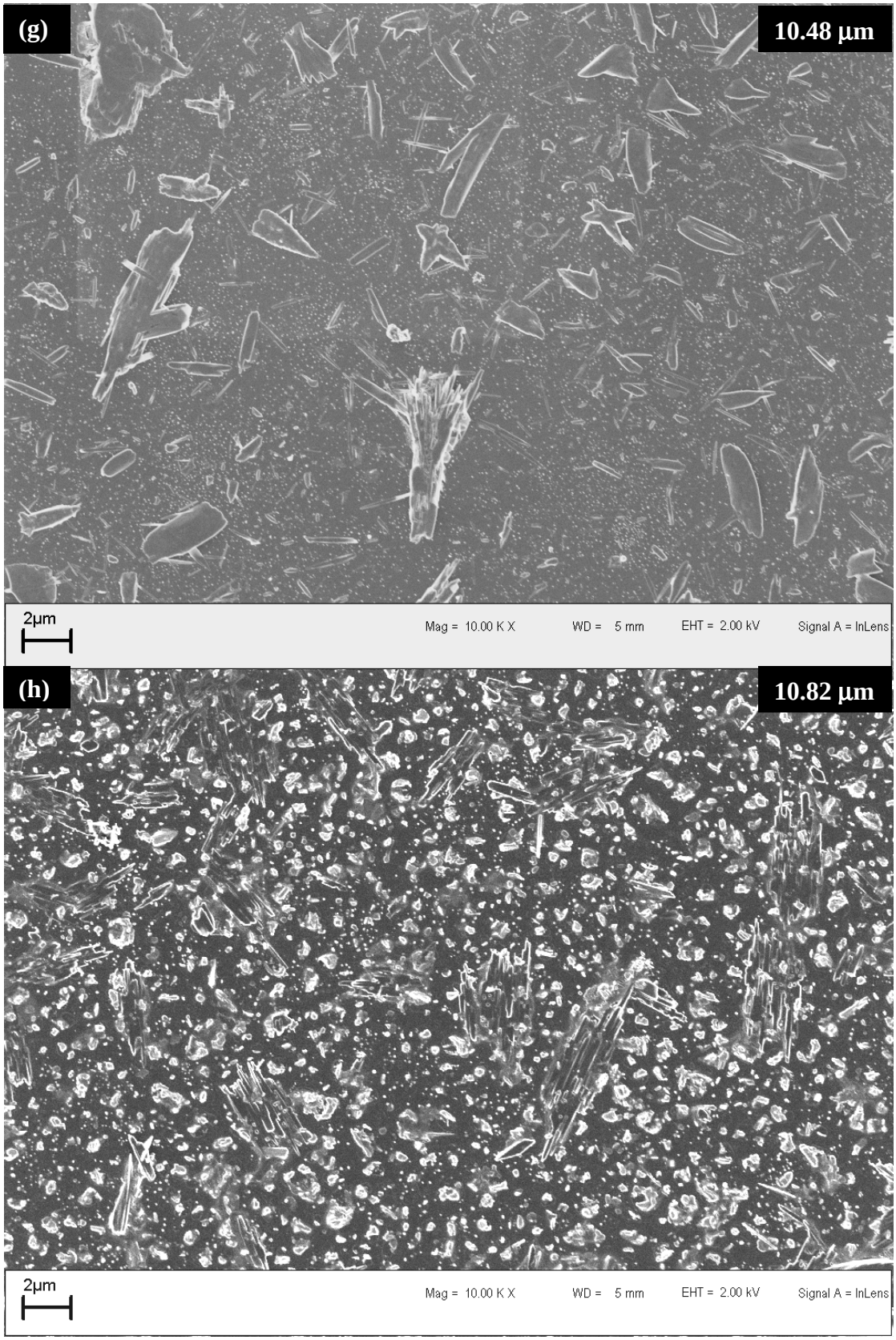
Appendix B - SEM Micrographs



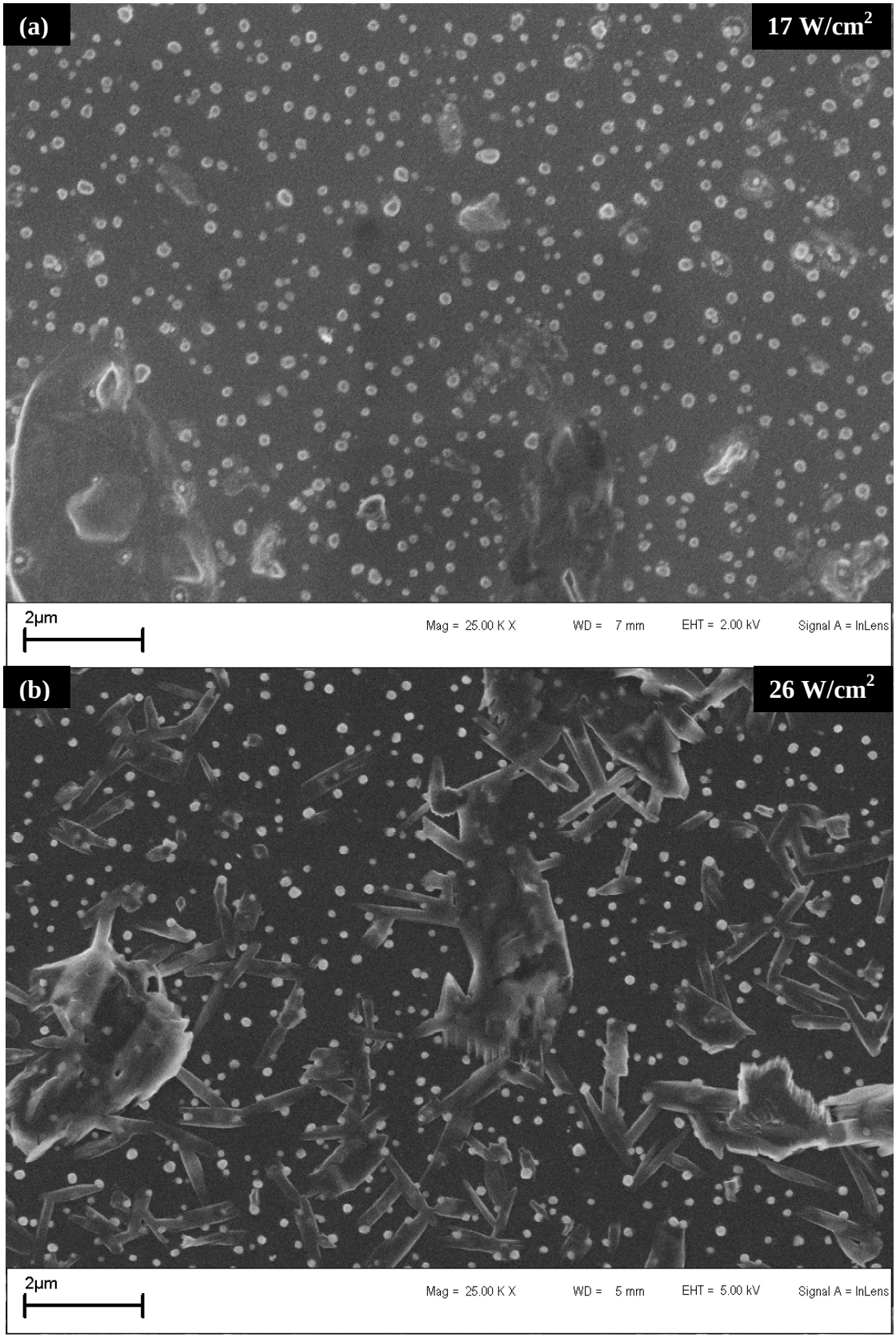


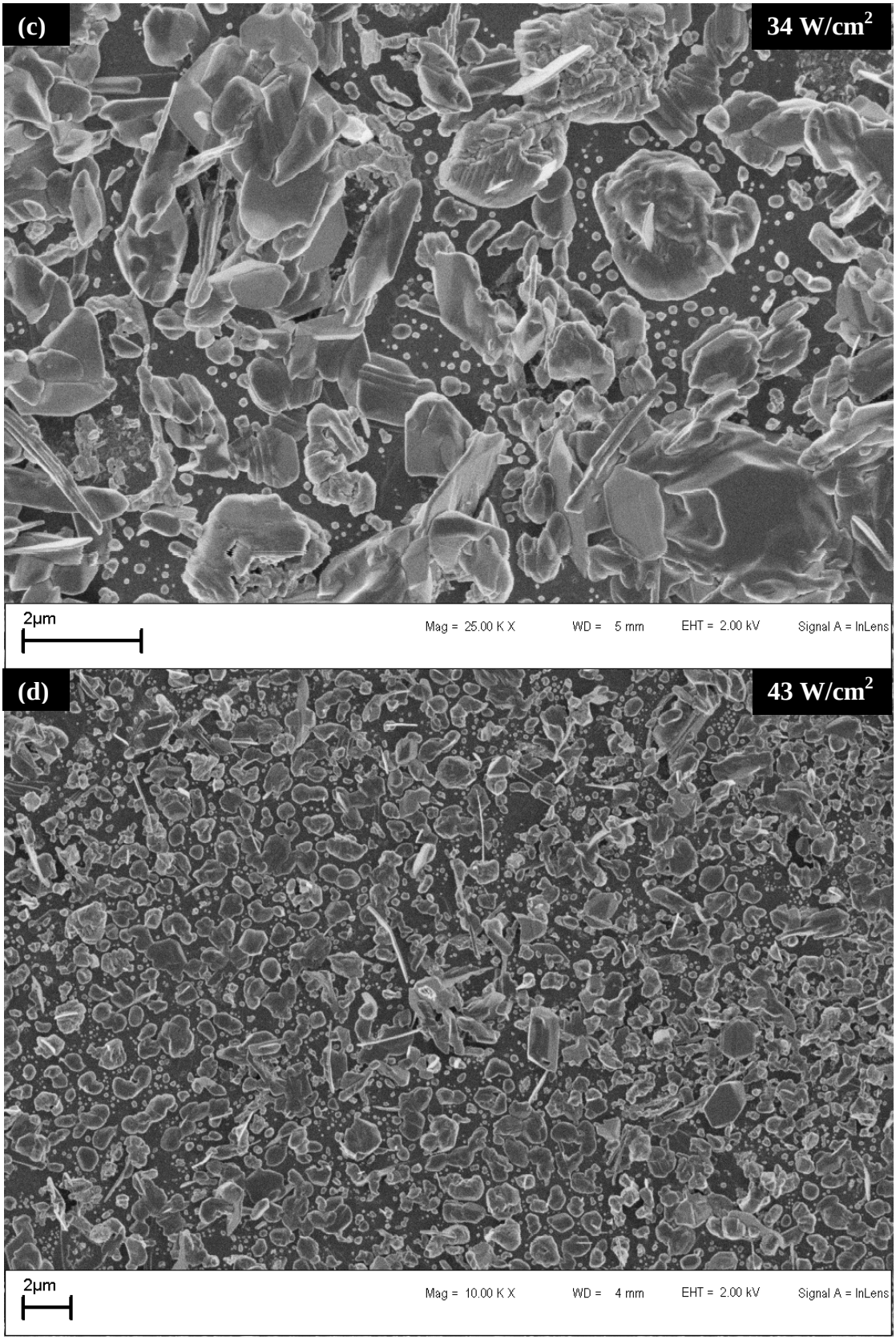

(c)
9.48 µm
2µm
Mag = 25.00 K X
WD = 5 mm
EHT = 2.00 kV
Signal A = InLens
(d)
9.70 µm
= 2.656 µm
= 191.0 nm
2µm
Mag = 15.00 K X
WD = 6 mm
EHT = 2.00 kV
Signal A = InLens

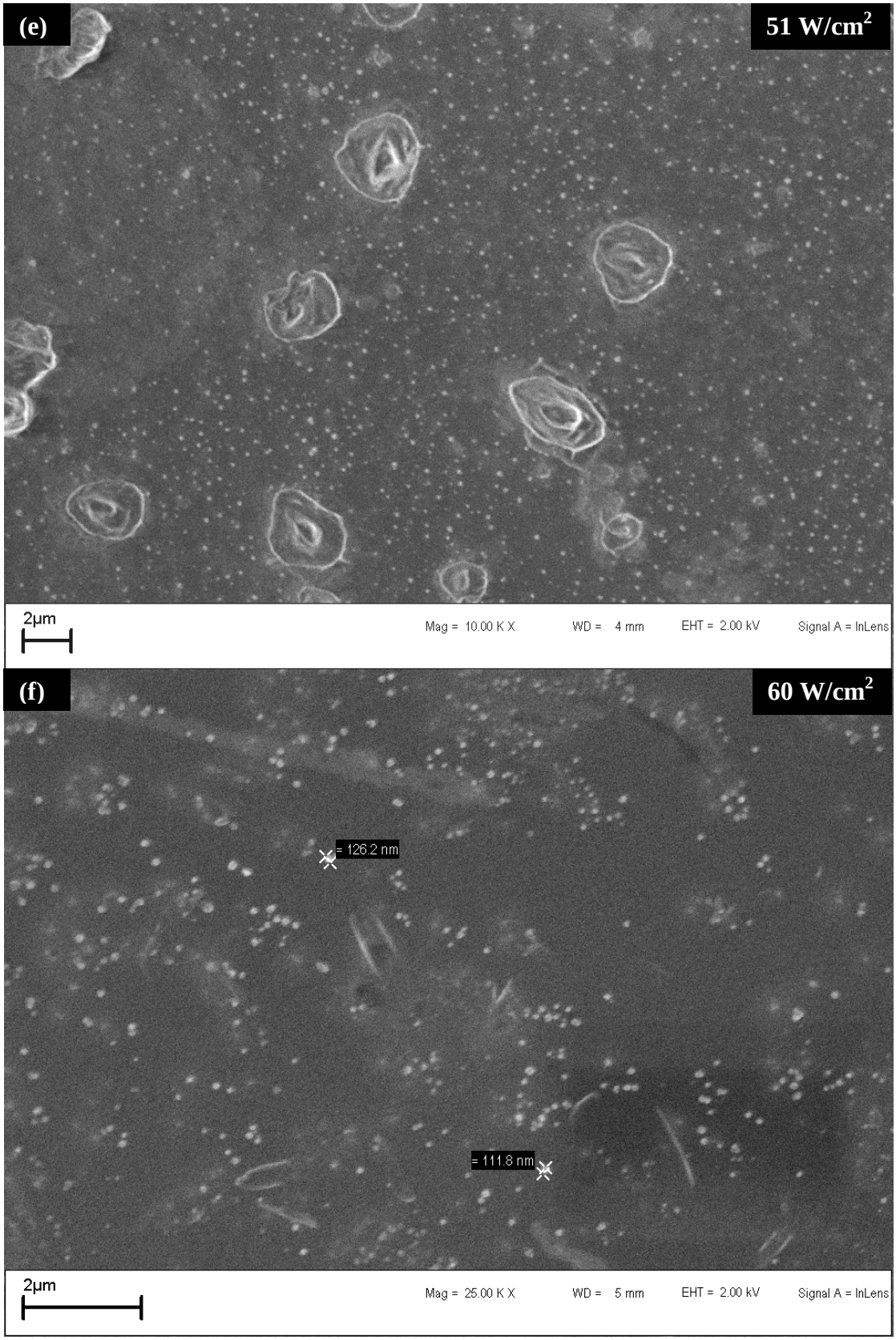

(e)
10.16 µm
2µm
Mag = 10.00 K X
WD = 5 mm
EHT = 2.00 kV
Signal A = InLens
(f)
10.36 µm
2µm
Mag = 10.00 K X
WD = 5 mm
EHT = 10.00 kV
Signal A = InLens

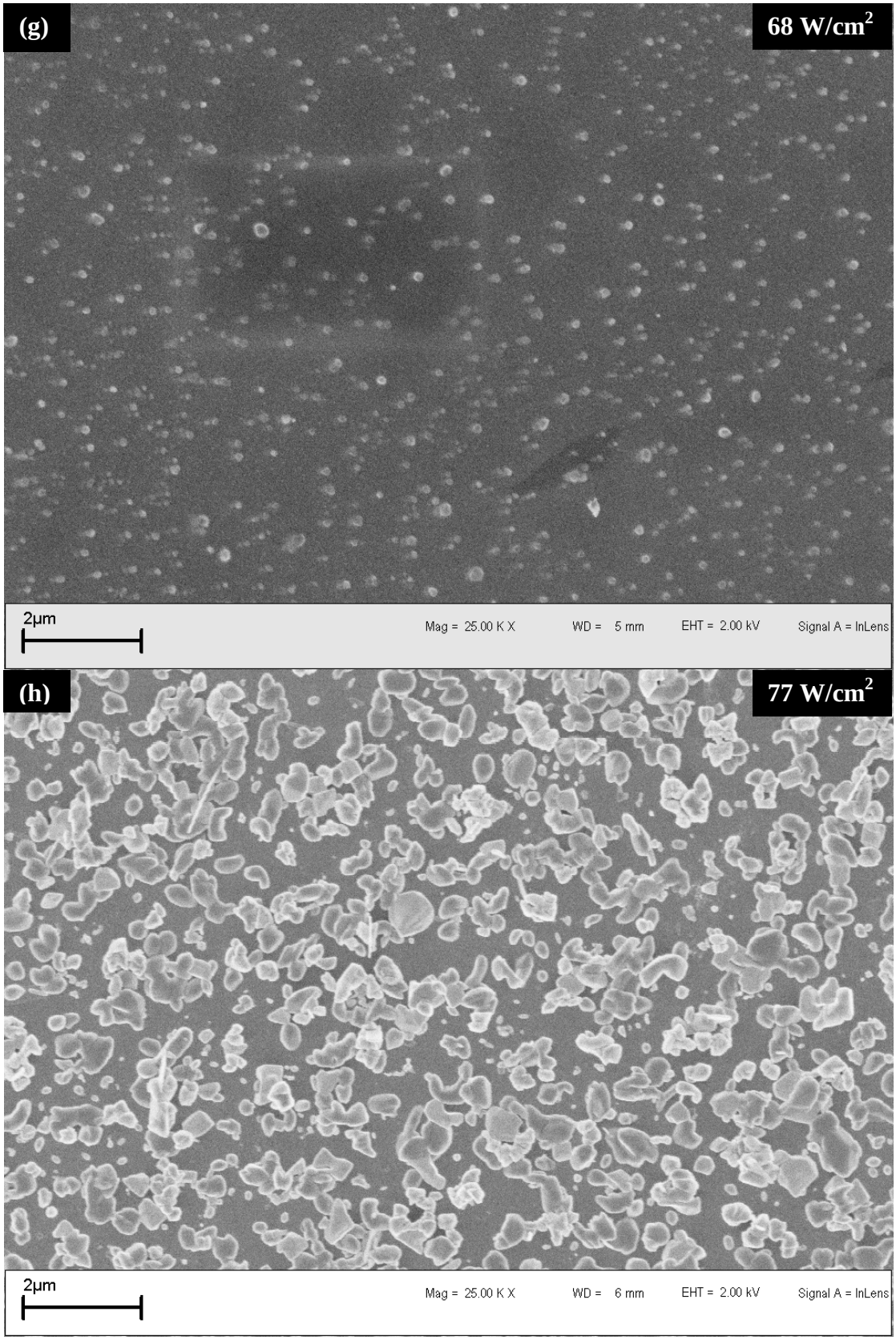


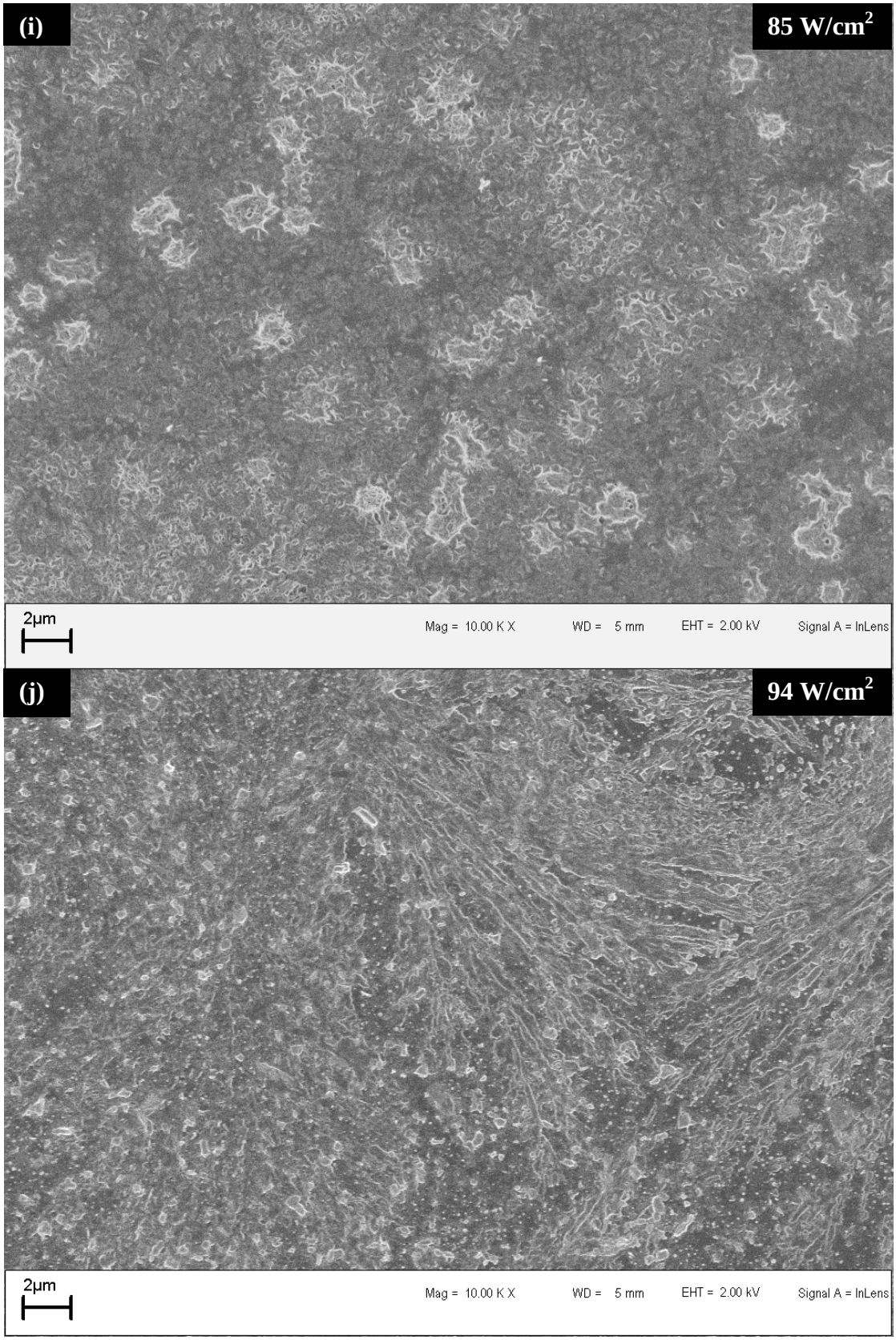
Appendix B.1 (a-h) The annealed sample prepared at the 10.82 µm wavelength and 51.2 W/cm^2.

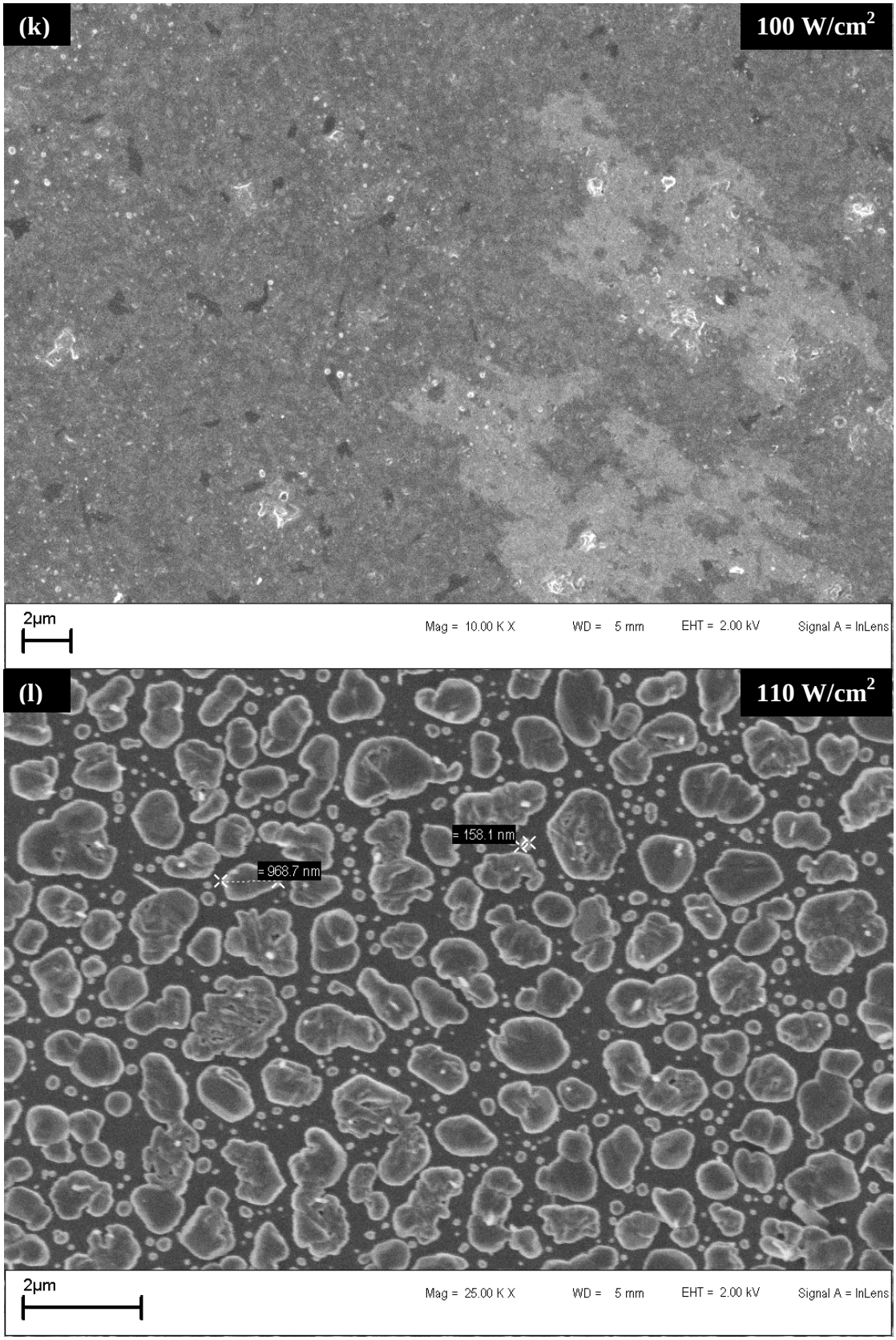

(a)
17 W/cm2
2µm
Mag = 25.00 K X
WD = 7 mm
EHT = 2.00 kV
Signal A = InLens
(b)
26 W/cm2
2µm
Mag = 25.00 K X
WD = 5 mm
EHT = 5.00 kV
Signal A = InLens


(c)
34 W/cm2
2µm
Mag = 25.00 K X
WD = 5 mm
EHT = 2.00 kV
Signal A = InLens
(d)
43 W/cm2
2µm
Mag = 10.00 K X
WD = 4 mm
EHT = 2.00 kV
Signal A = InLens


(e)
51 W/cm2
2µm
Mag = 10.00 K X
WD = 4 mm
EHT = 2.00 kV
Signal A = InLens
(f)
60 W/cm2
= 126.2 nm
= 111.8 nm
2µm
Mag = 25.00 K X
WD = 5 mm
EHT = 2.00 kV
Signal A = InLens

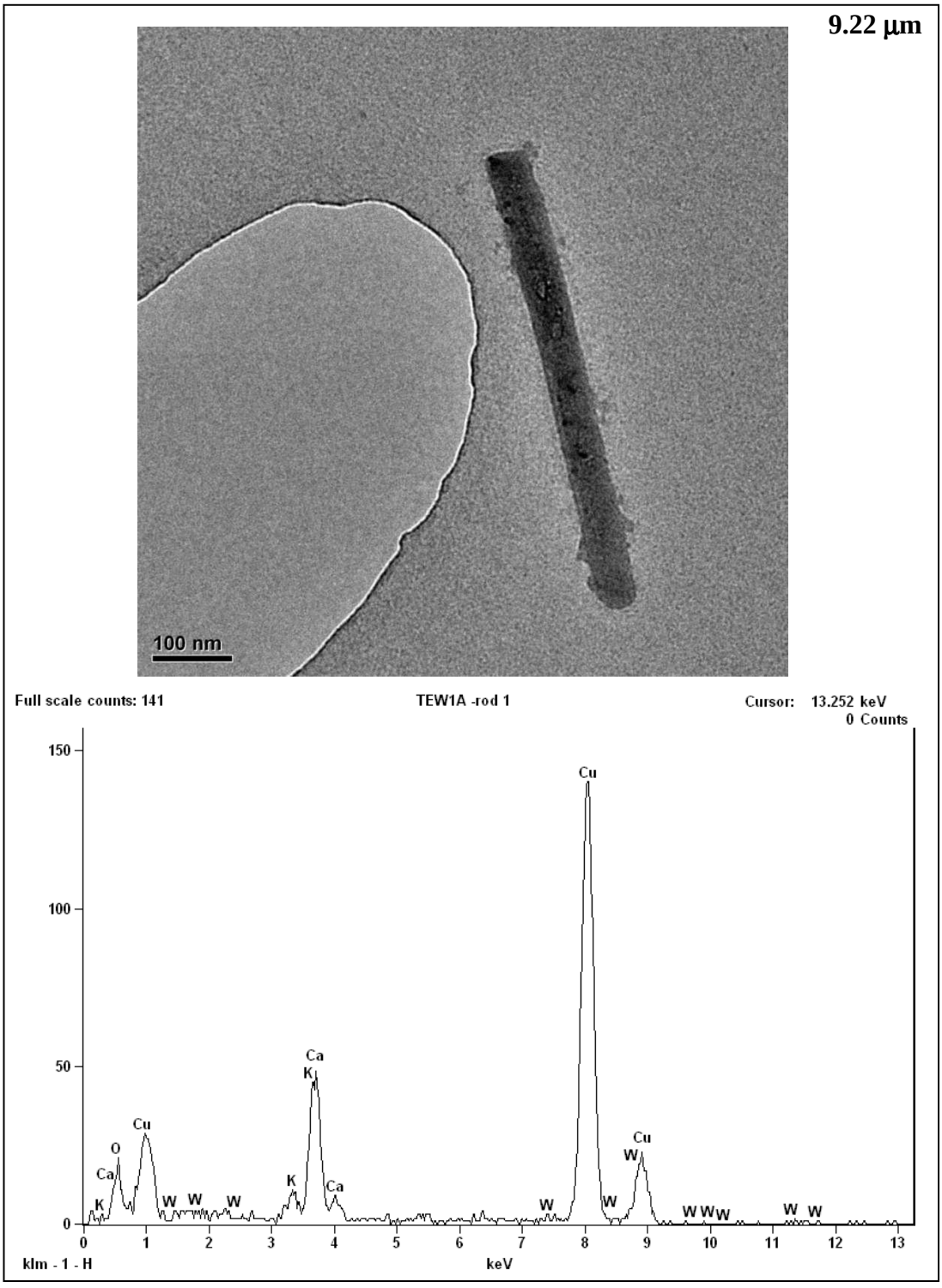

(g)
68 W/cm2
2µm
Mag = 25.00 K X
WD = 5 mm
EHT = 2.00 kV
Signal A = InLens
(h)
77 W/cm2
2µm
Mag = 25.00 K X
WD = 6 mm
EHT = 2.00 kV
Signal A = InLens


(i)
85 W/cm2
2µm
Mag = 10.00 K X
WD = 5 mm
EHT = 2.00 kV
Signal A = InLens
(j)
94 W/cm2
2µm
Mag = 10.00 K X
WD = 5 mm
EHT = 2.00 kV
Signal A = InLens

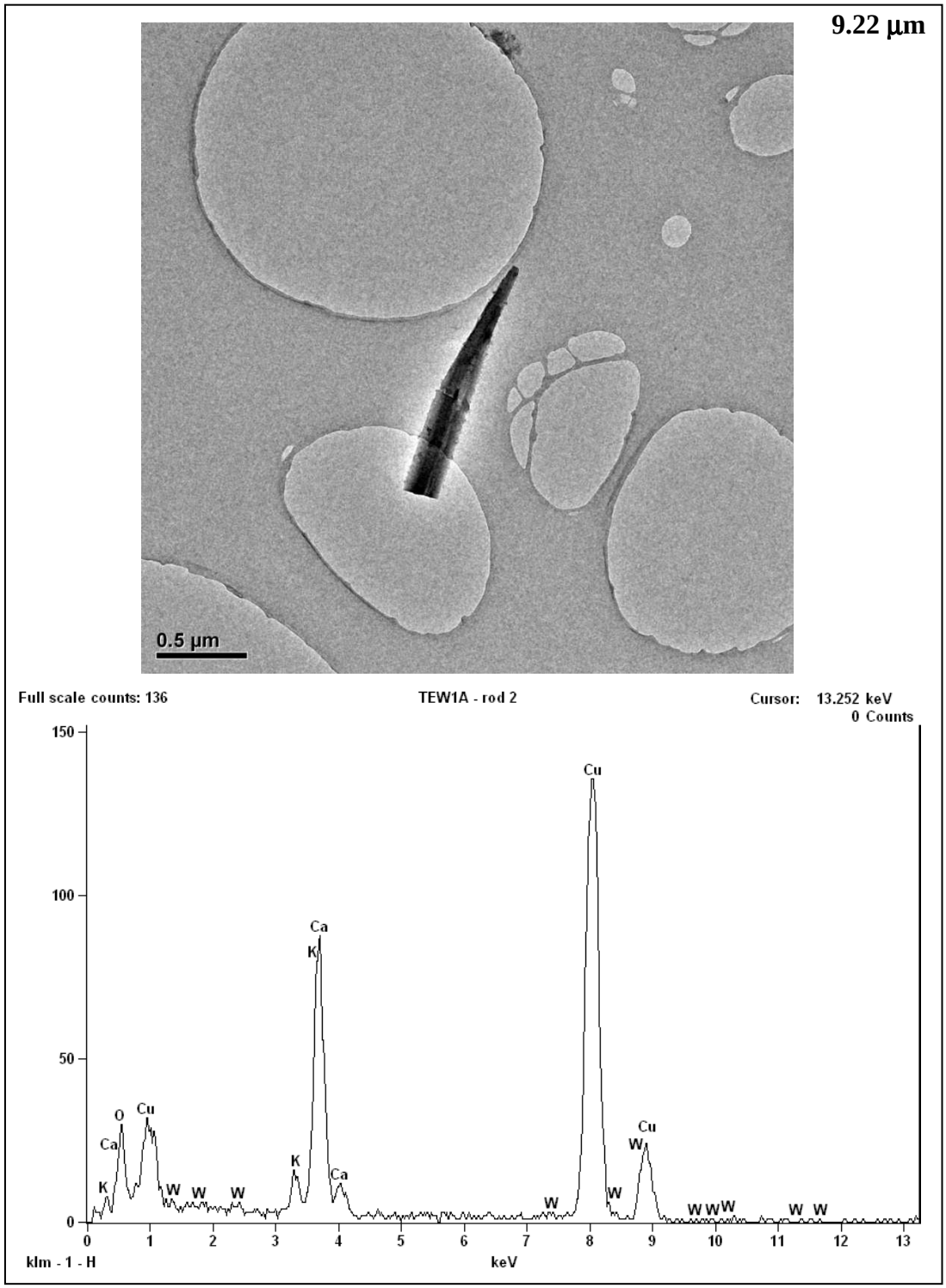


Appendix B.2 (a)-(l) The SEM micrographs for the post-annealed samples, prepared at different power densities as represented on the respective micrographs, and constant wavelength of 10.6 µm.

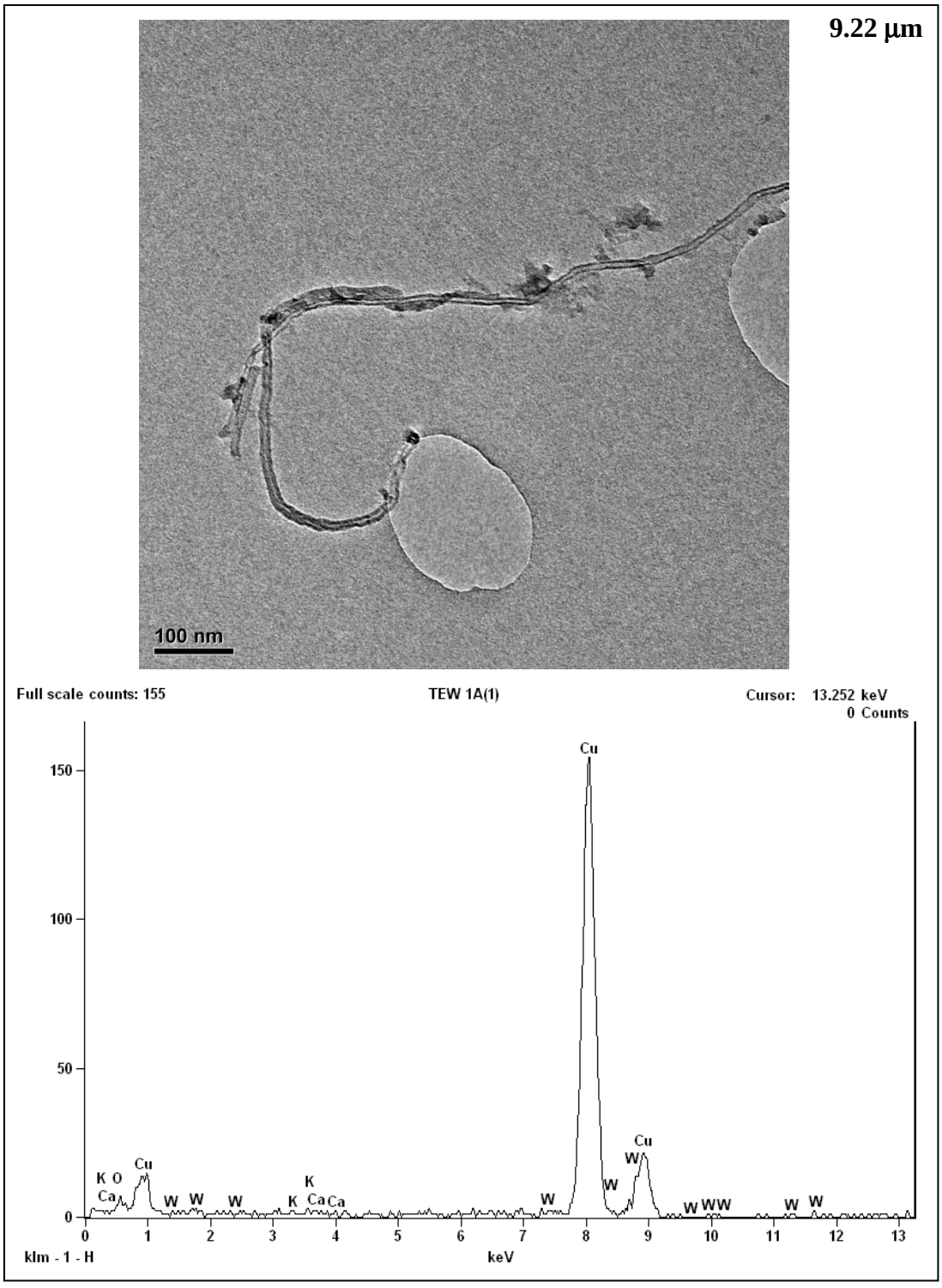
Appendix C - TEM Micrographs



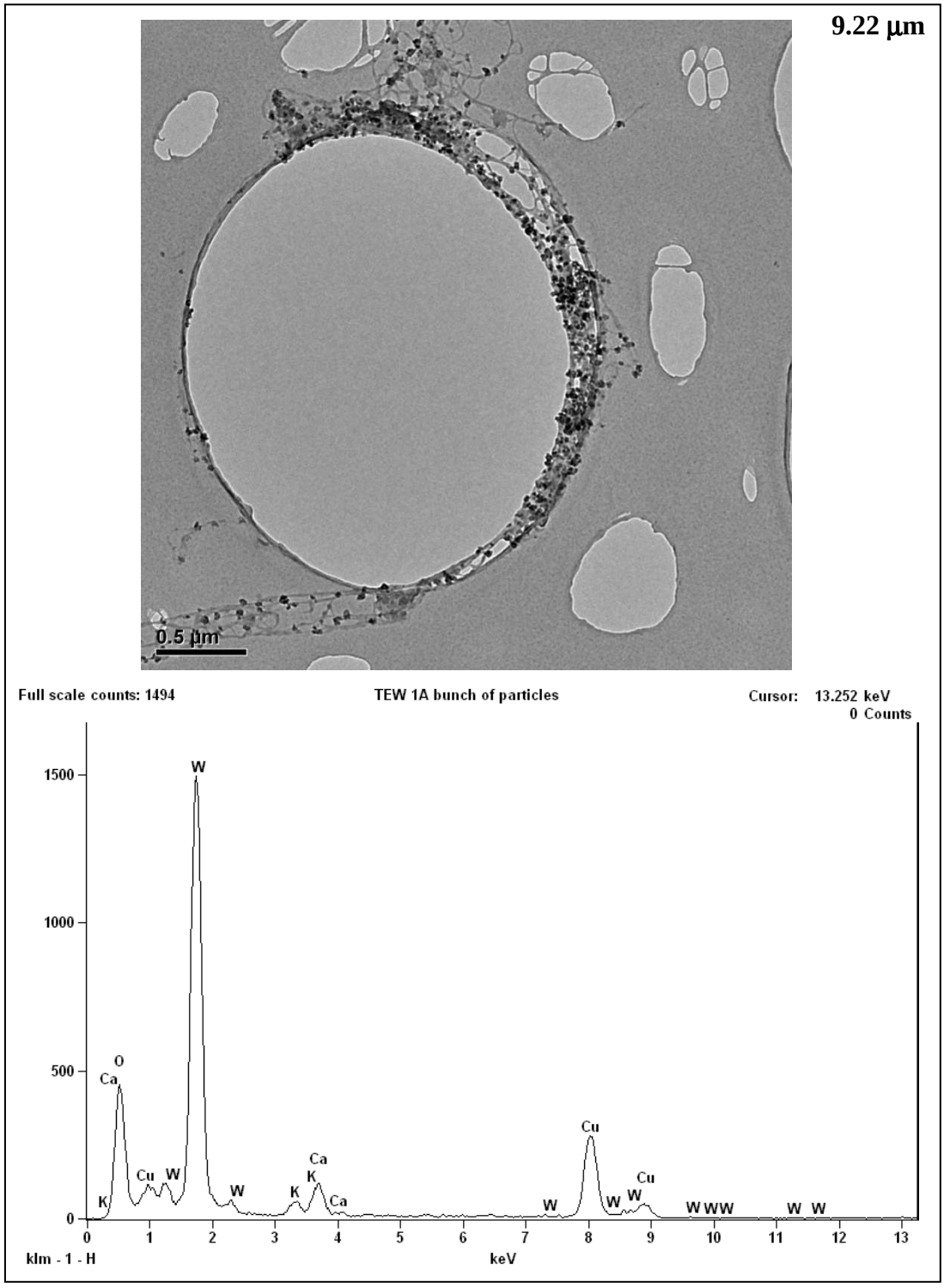
Appendix C.1 ***Top*****:** A TEM micrograph showing a nanorod and ***Bottom*****:** the EDX spectrum taken of the rod.



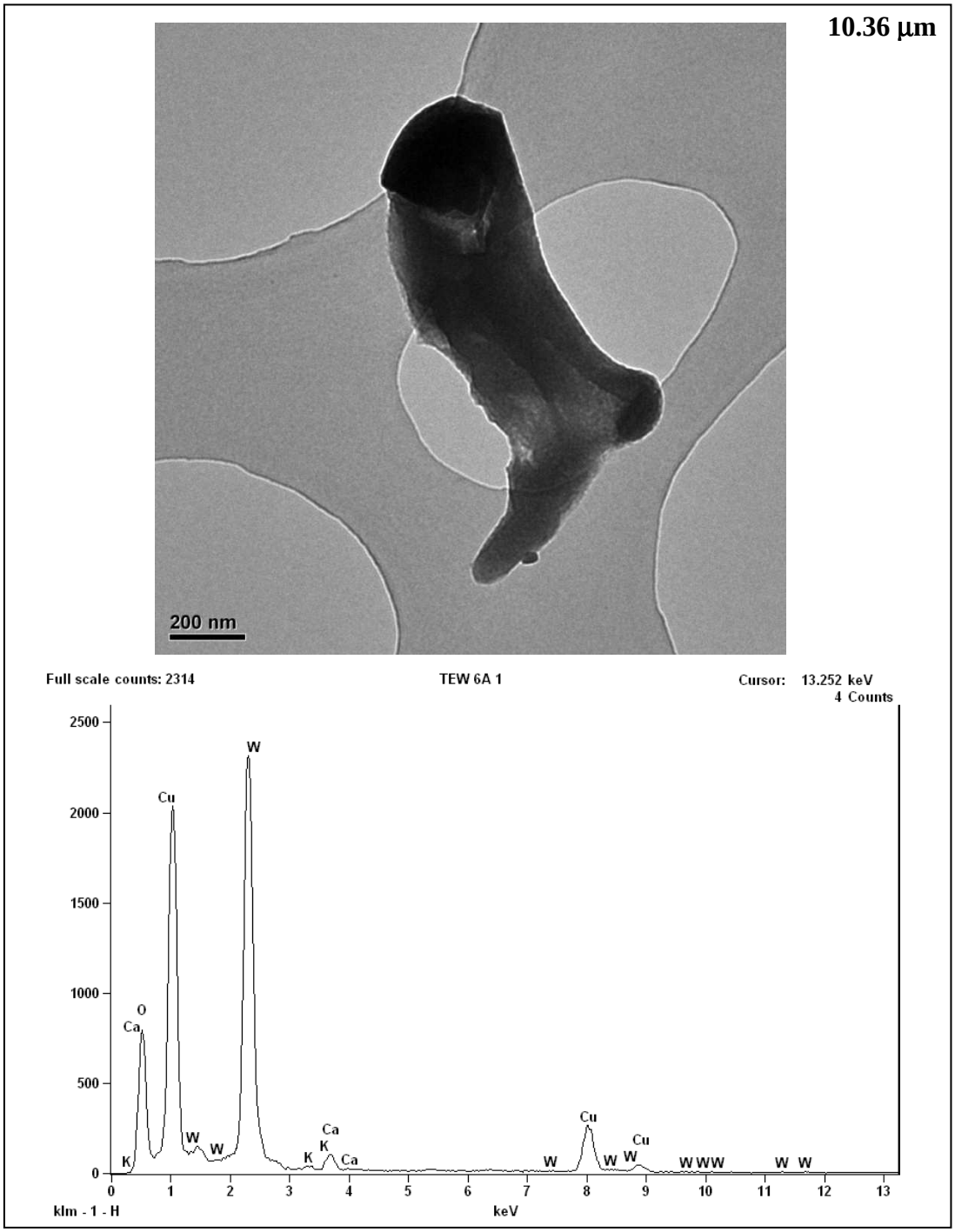
Appendix C.2 ***Top*****:** A TEM micrograph showing a nanospike and ***Bottom*****:** the EDX spectrum taken of the spike.



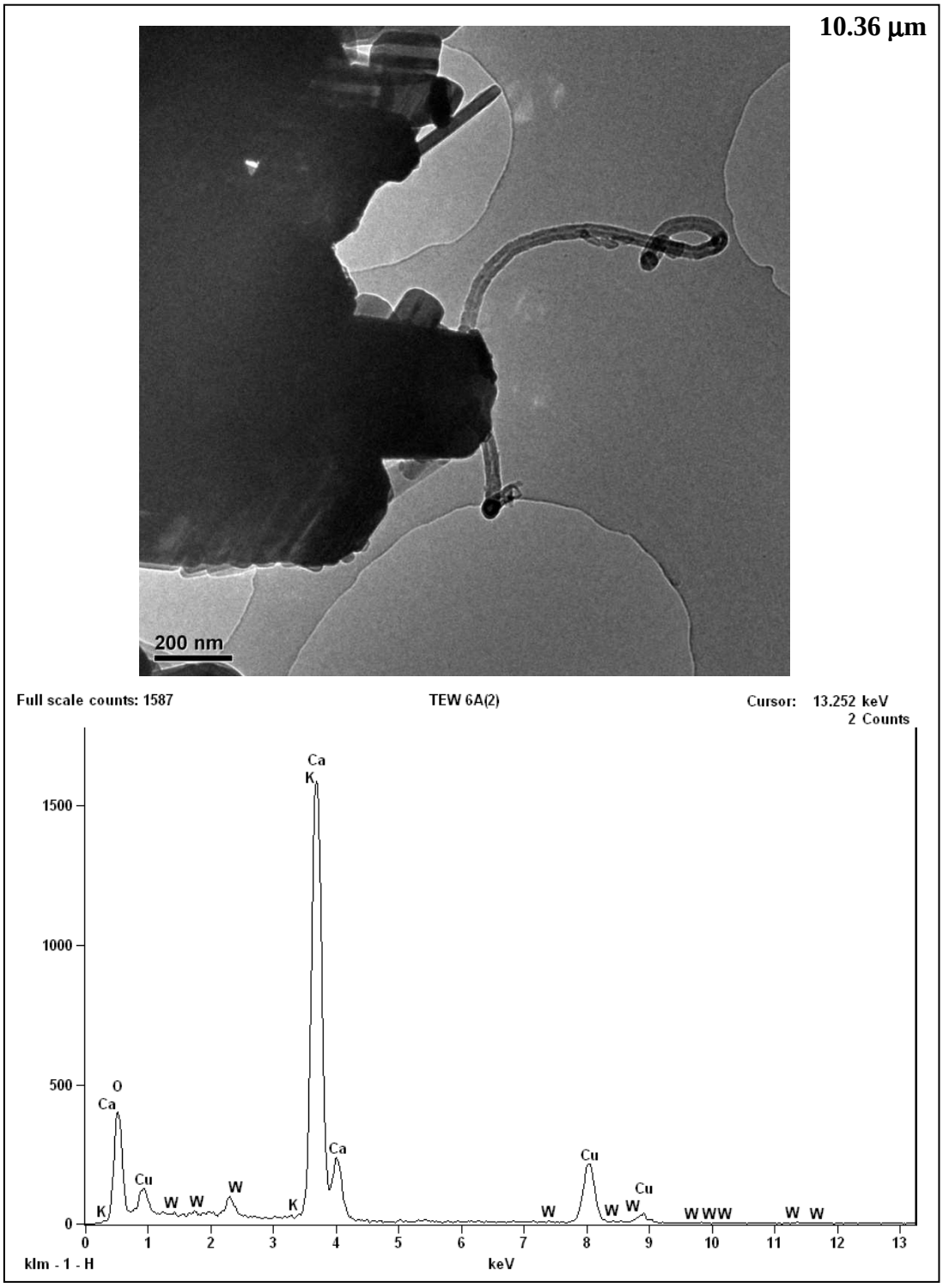
Appendix C.3 ***Top*****:** A TEM micrograph showing a nanotube and ***Bottom*****:** the EDX spectrum taken of the tube.



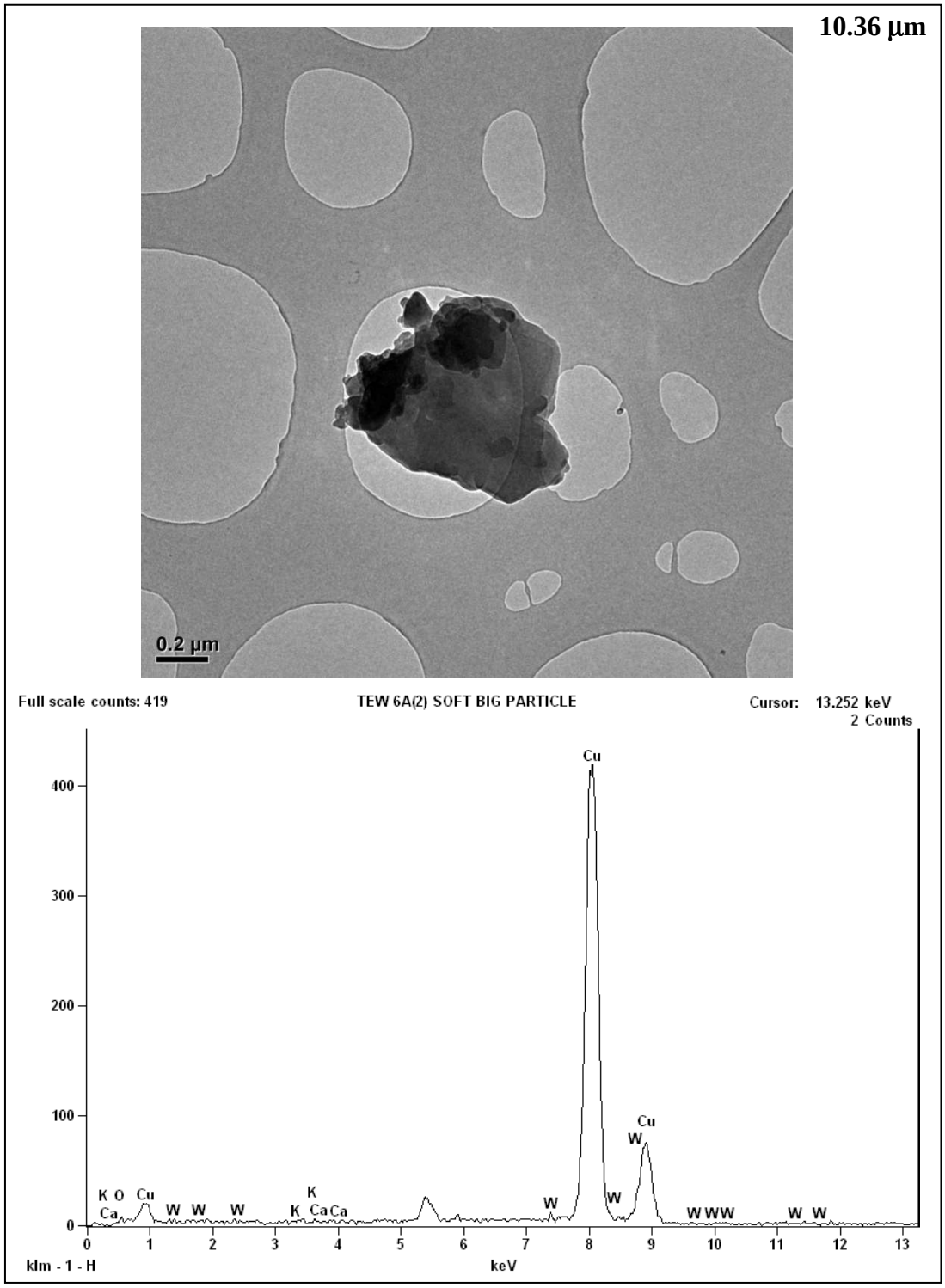
Appendix C.4 ***Top*****:** A TEM micrograph showing a stream of particles and ***Bottom*****:** the EDX spectrum taken of the particles.



Appendix C.5 ***Top*****:** A TEM micrograph showing an agglomeration of particles in the shape of a leg and ***Bottom*****:** the EDX spectrum taken of the agglomerated particles.

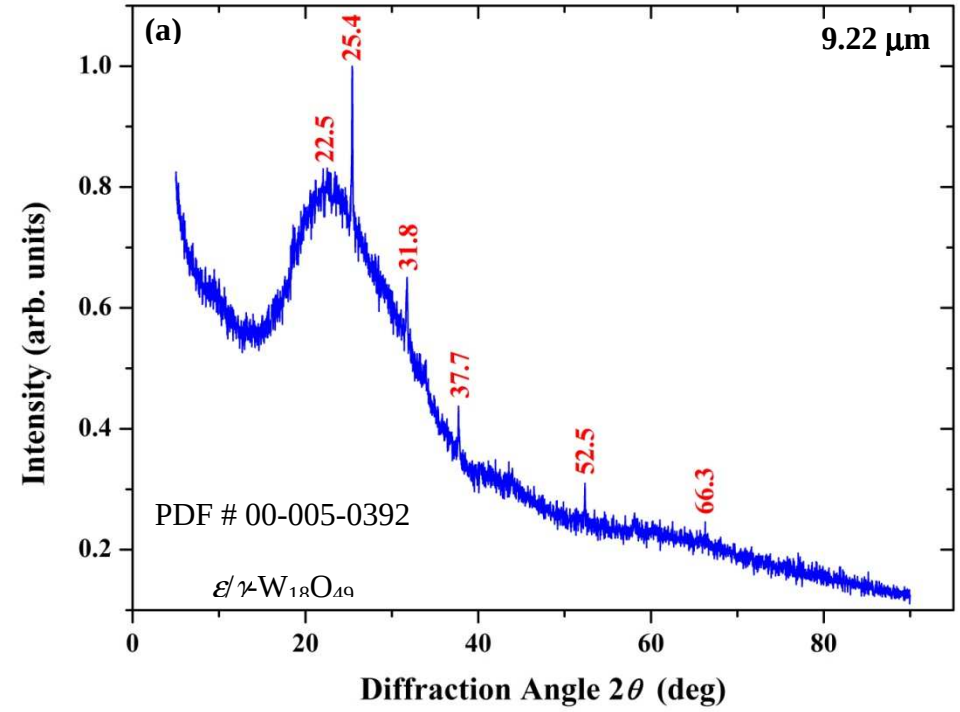


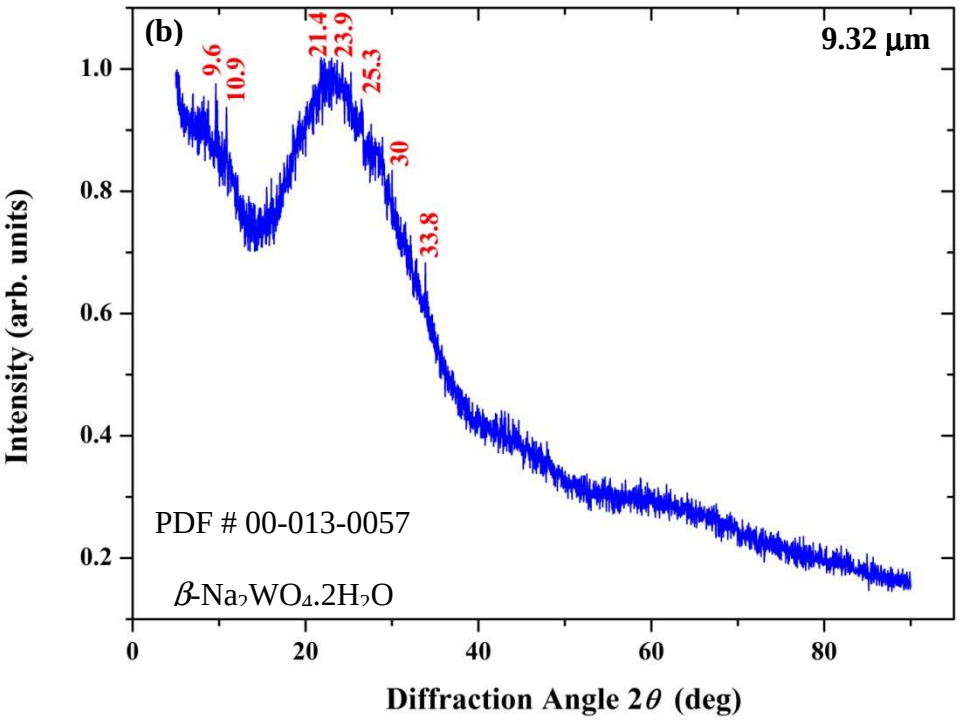
Appendix C.6 ***Top*****:** A TEM micrograph showing a clump of particles and a nanotube and ***Bottom*****:** the EDX spectrum of the various structures.

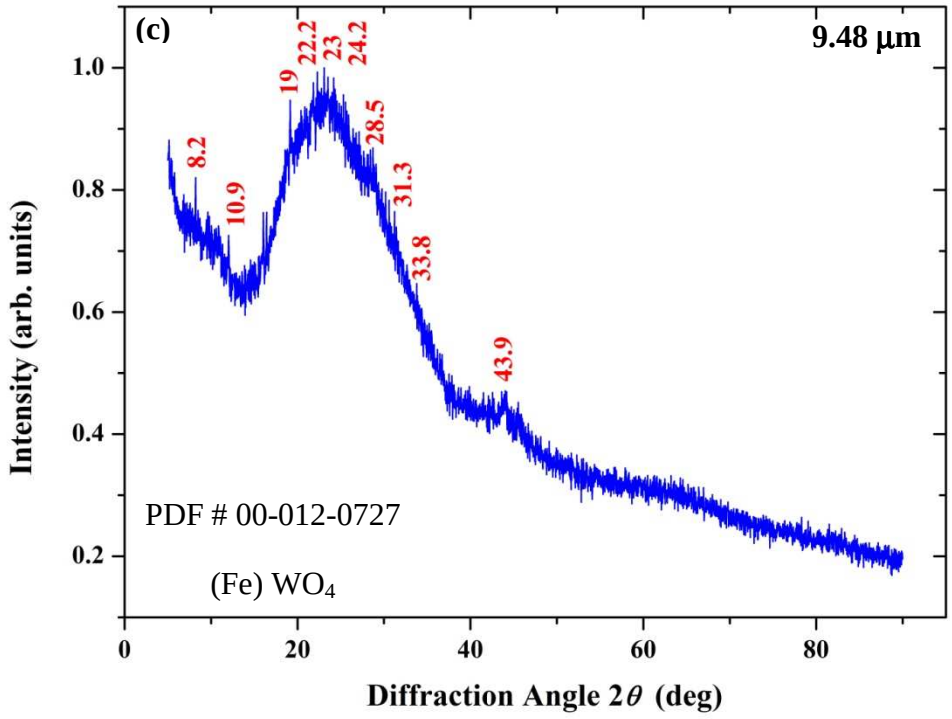


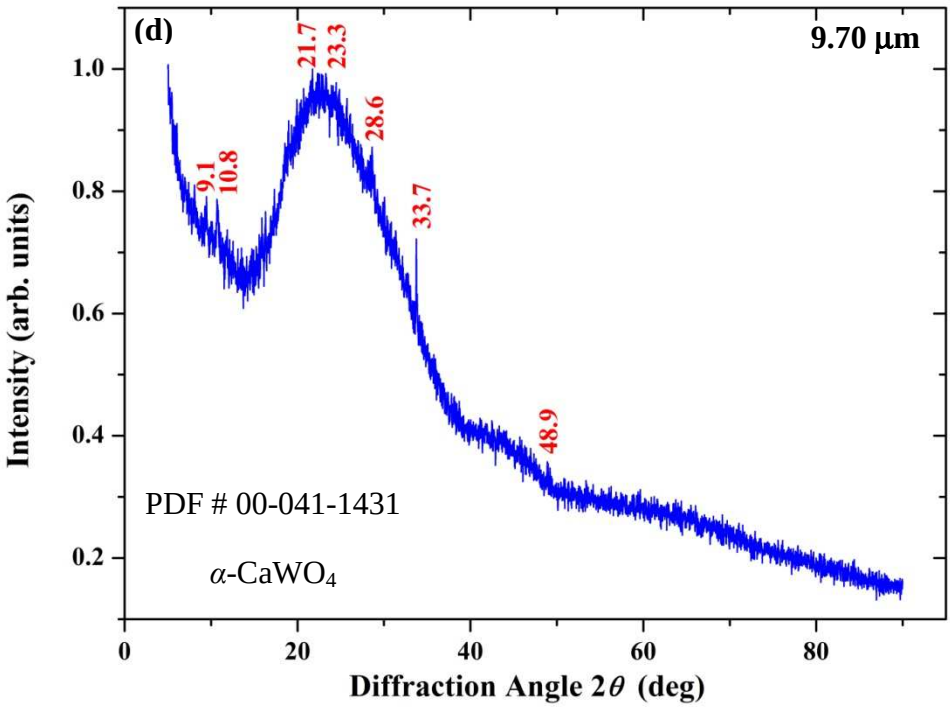
Appendix C.7 ***Top*****:** A TEM micrograph showing an agglomeration of particles and ***Bottom*****:** the EDX spectrum of the agglomeration.

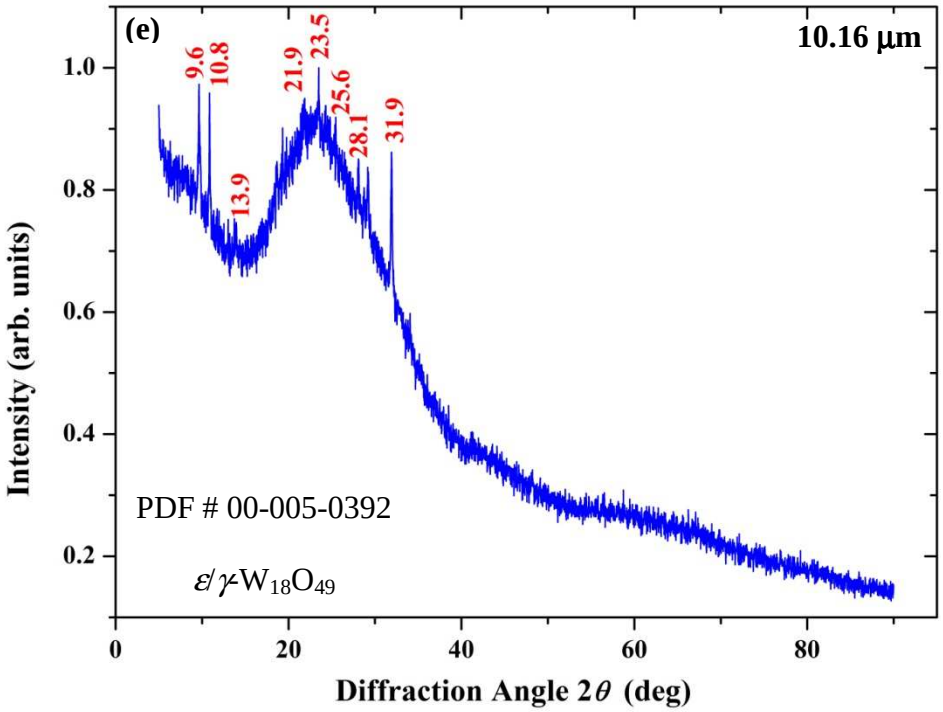
Appendix D - XRD Spectra

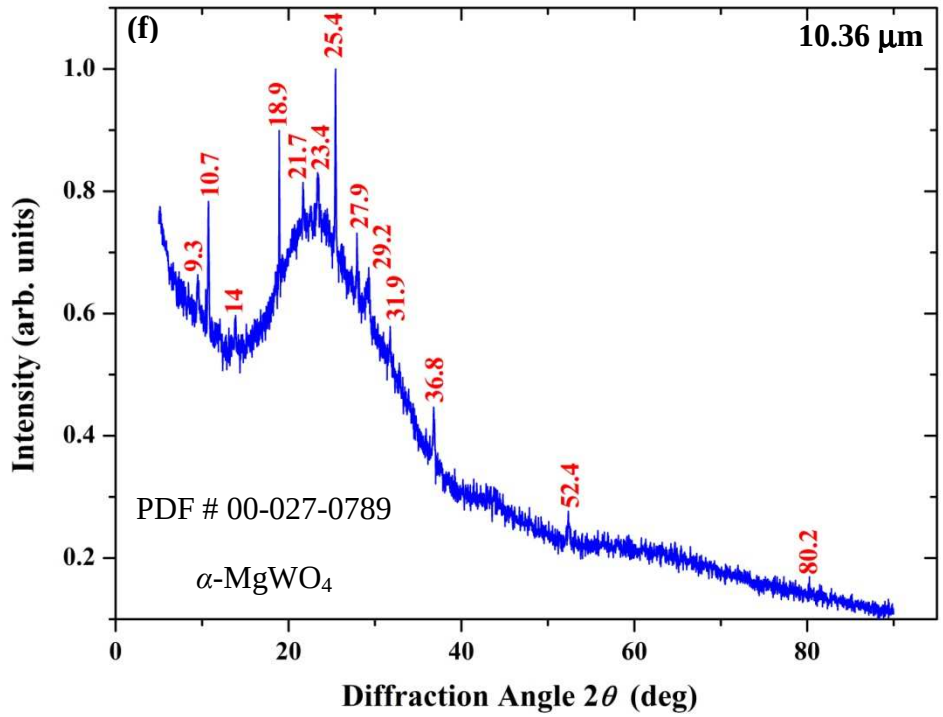


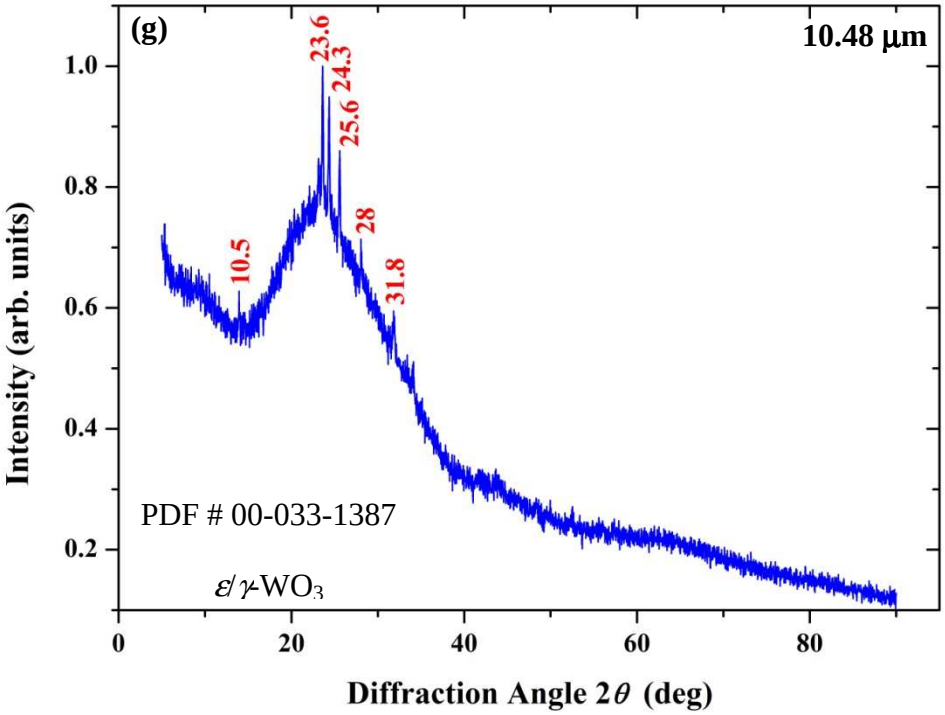


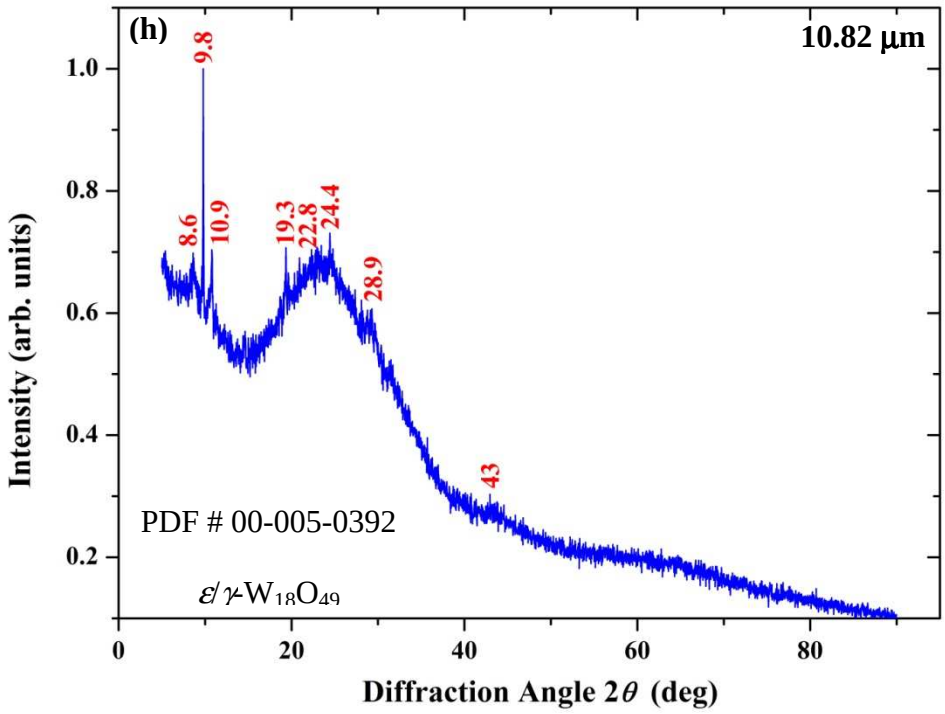

(c)
9.48 μm
8.2
10.9
19
22.2
23
24.2
28.5
31.3
33.8
43.9
PDF # 00-012-0727
(Fe) WO4
Intensity (arb. units)
Diffraction Angle 2θ (deg)


(d)
9.70 μm
9.1
10.8
21.7
23.3
28.6
33.7
48.9
PDF # 00-041-1431
α-CaWO4
Intensity (arb. units)
Diffraction Angle 2θ (deg)

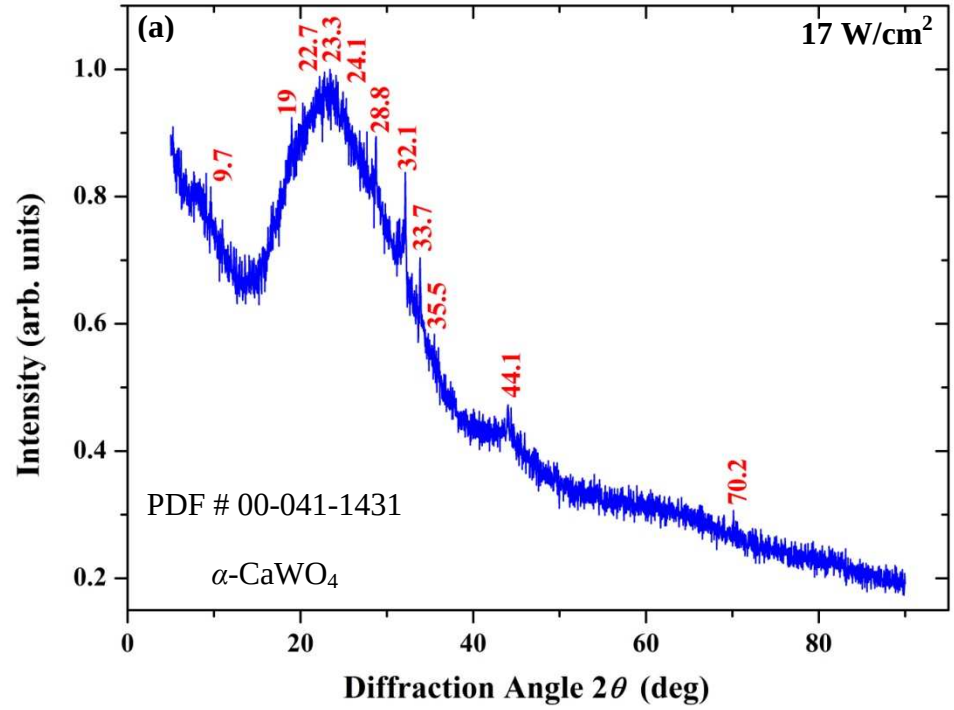

(e)
10.16 μm
9.6
10.8
13.9
21.9
23.5
25.6
28.1
31.9
PDF # 00-005-0392
ε/γ-W18O49
Intensity (arb. units)
Diffraction Angle 2θ (deg)

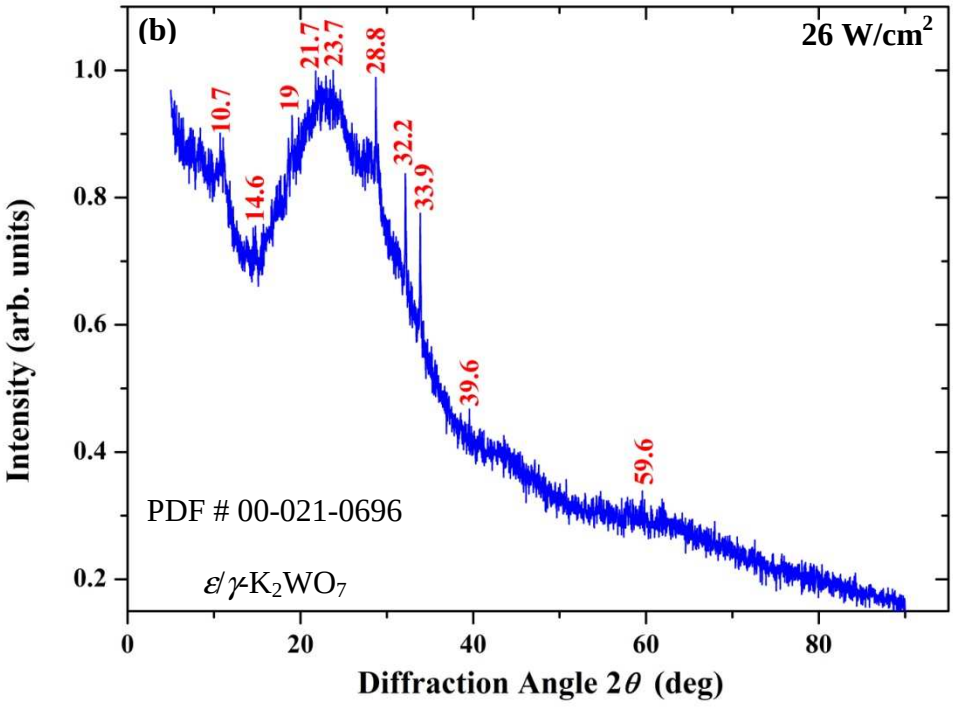

(f)
10.36 μm
9.3
10.7
14
18.9
21.7
23.4
25.4
27.9
29.2
31.9
36.8
52.4
80.2
PDF # 00-027-0789
α-MgWO4
Intensity (arb. units)
Diffraction Angle 2θ (deg)

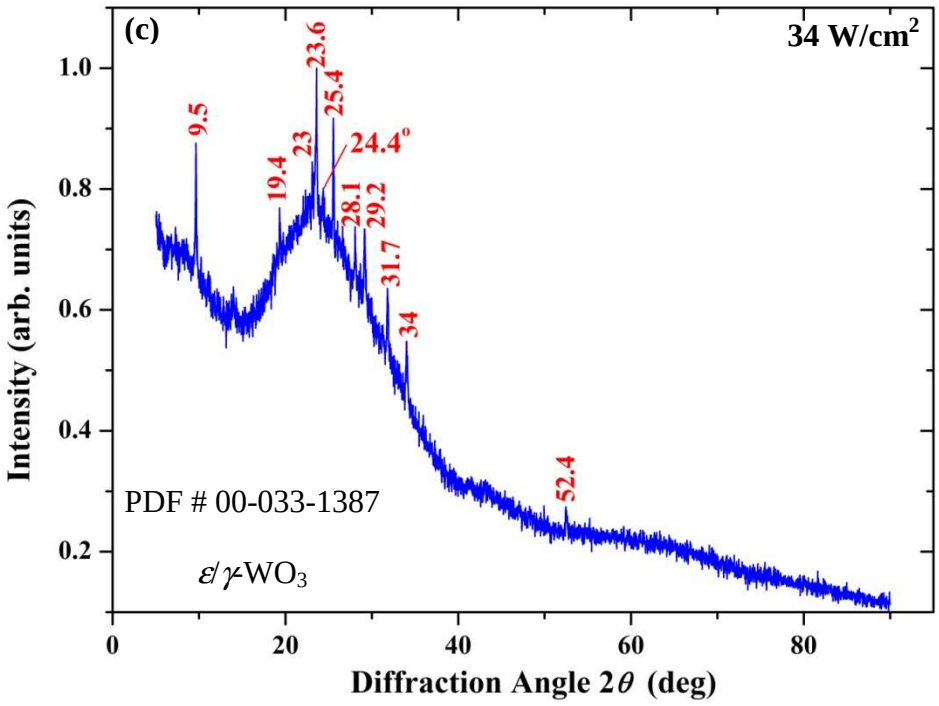


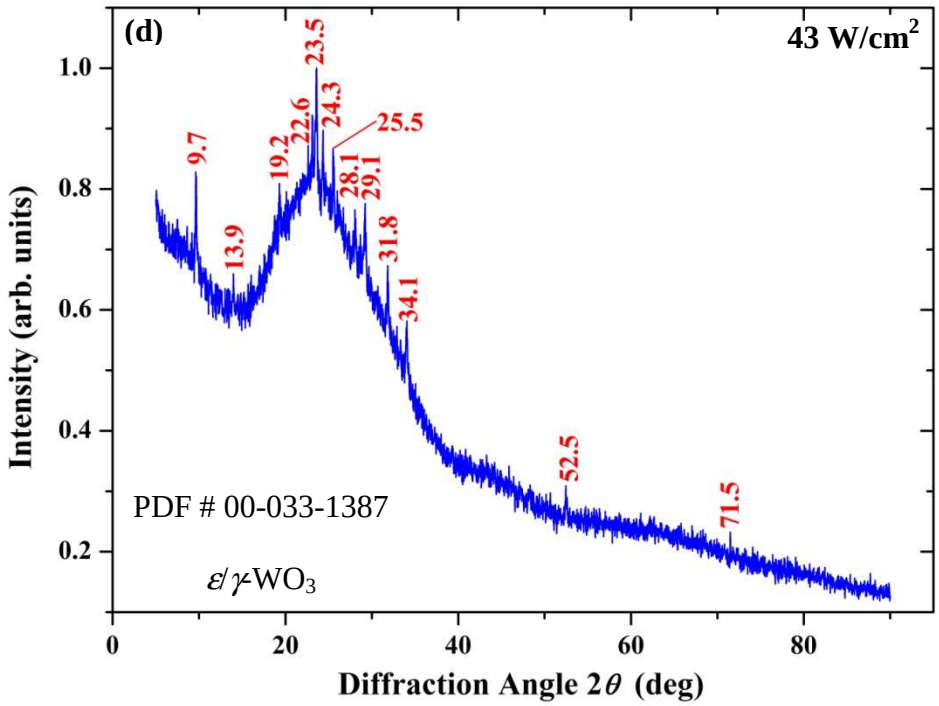


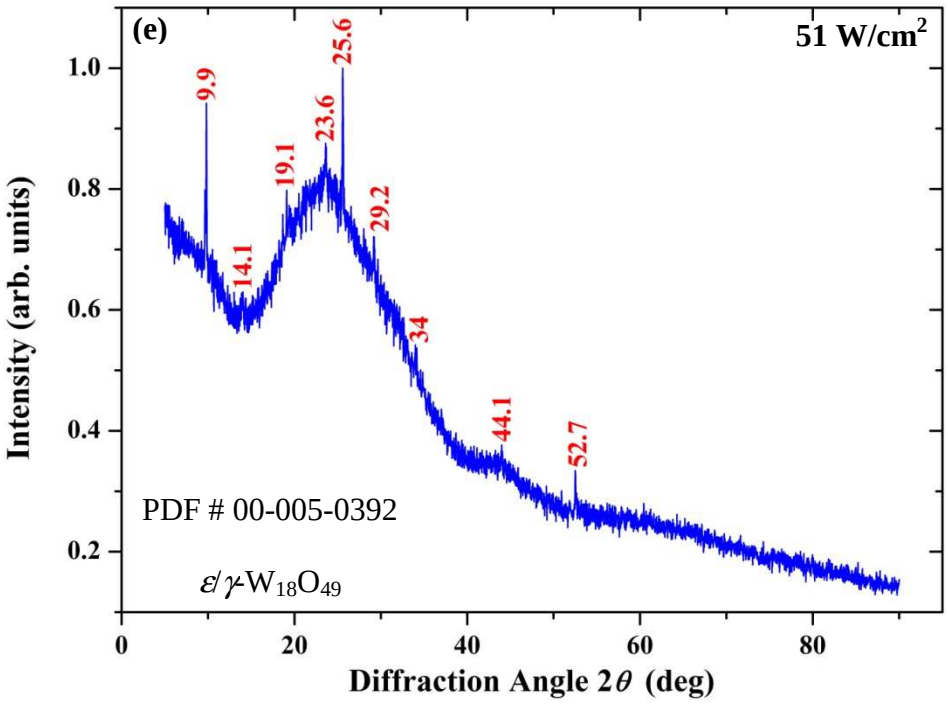
Appendix D.1 (a)-(h) The XRD spectra for the post-annealed samples, prepared at different wavelengths and constant power density of 51.2 W/cm^2.

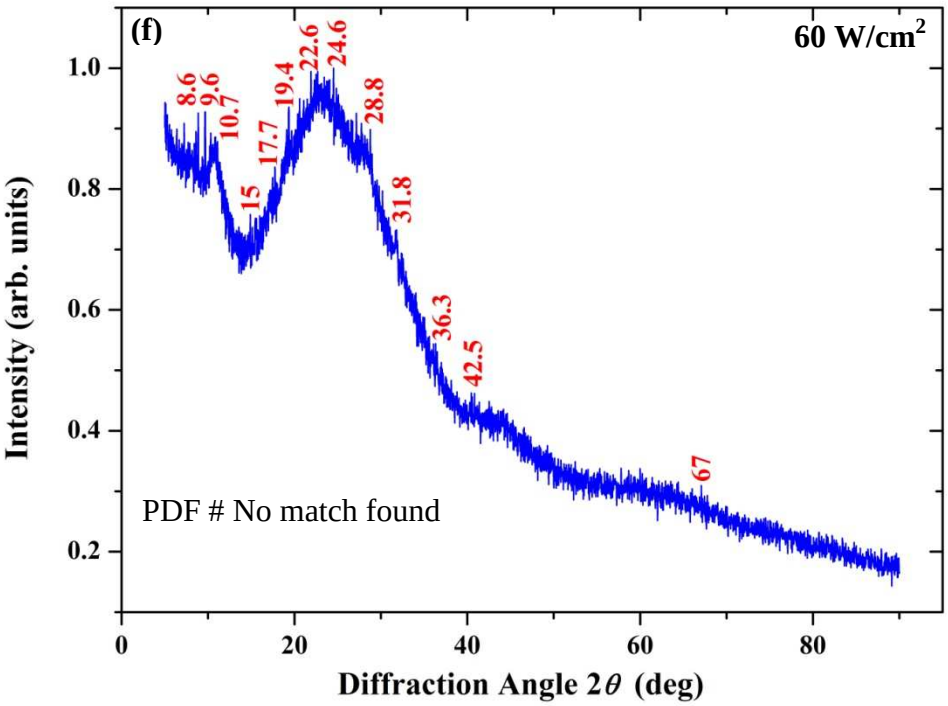

(a)
17 W/cm2
9.7
19
22.7
23.3
24.1
28.8
32.1
33.7
35.5
44.1
70.2
PDF # 00-041-1431
α-CaWO4
Intensity (arb. units)
Diffraction Angle 2θ (deg)

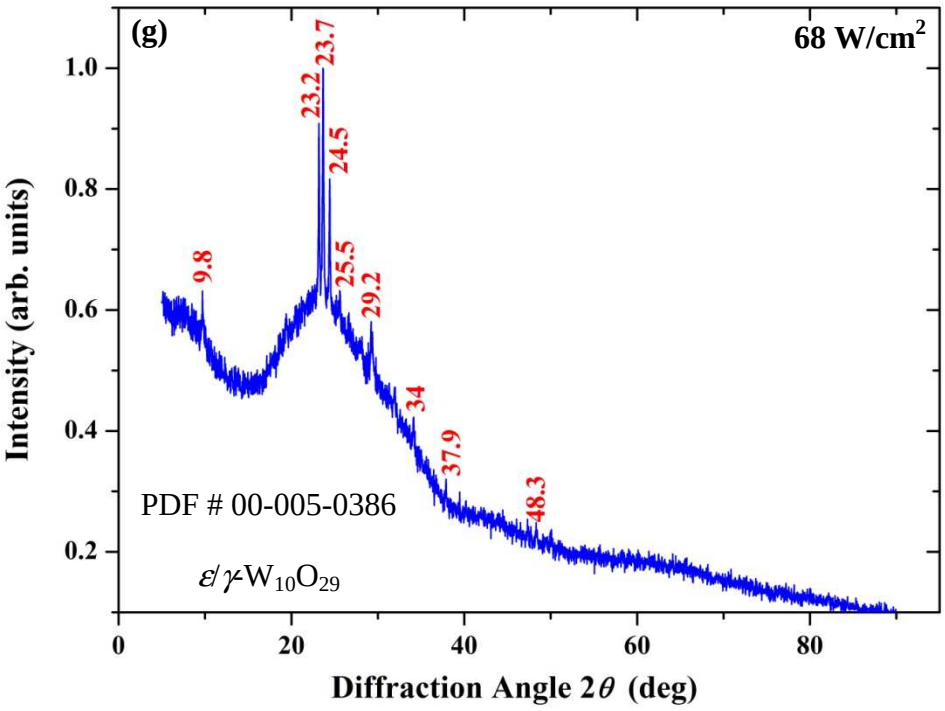

(b)
26 W/cm2
10.7
14.6
19
21.7
23.7
28.8
32.2
33.9
39.6
59.6
PDF # 00-021-0696
ε/γ-K2WO7
Intensity (arb. units)
Diffraction Angle 2θ (deg)

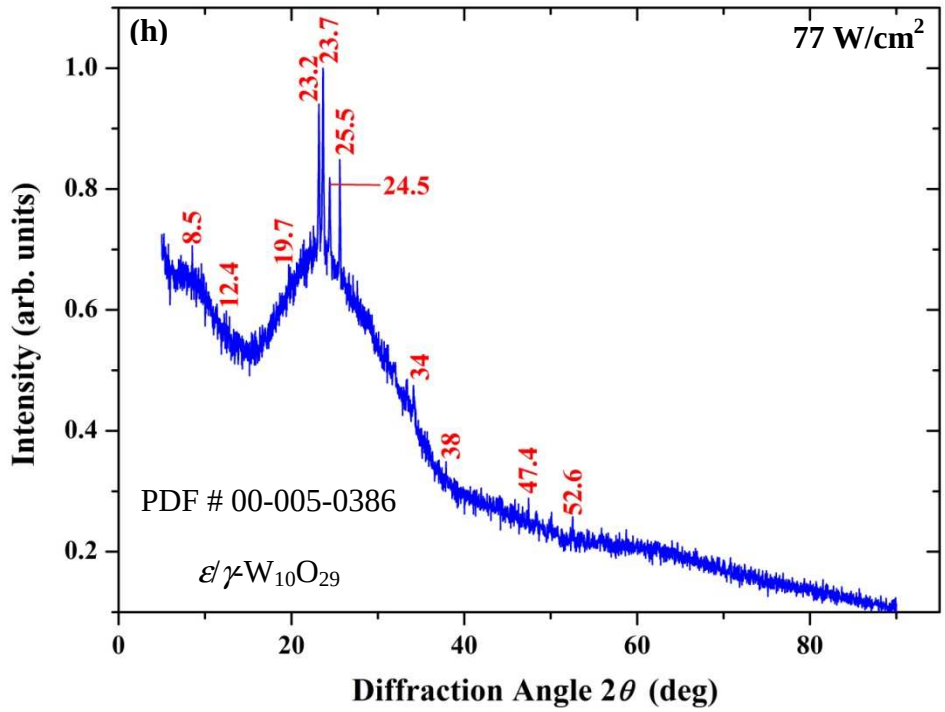

(c)
34 W/cm2
9.5
19.4
23
23.6
25.4
24.4°
28.1
29.2
31.7
34
52.4
PDF # 00-033-1387
ε/γ-WO3
Intensity (arb. units)
Diffraction Angle 2θ (deg)

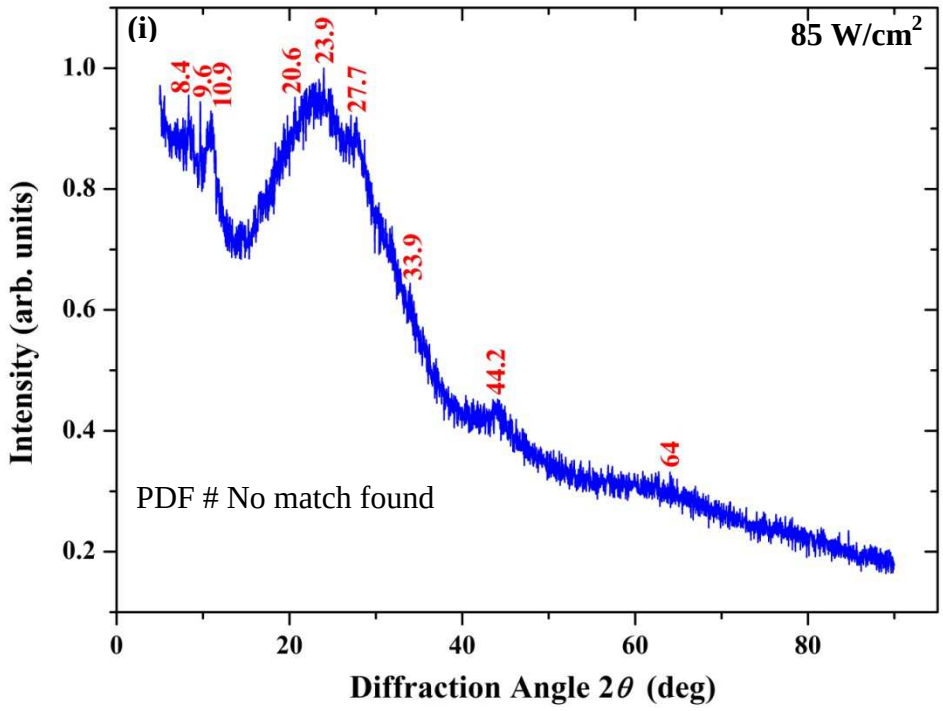

(d)
43 W/cm2
9.7
13.9
19.2
22.6
23.5
24.3
25.5
28.1
29.1
31.8
34.1
52.5
71.5
PDF # 00-033-1387
ε/γ-WO3
Intensity (arb. units)
Diffraction Angle 2θ (deg)

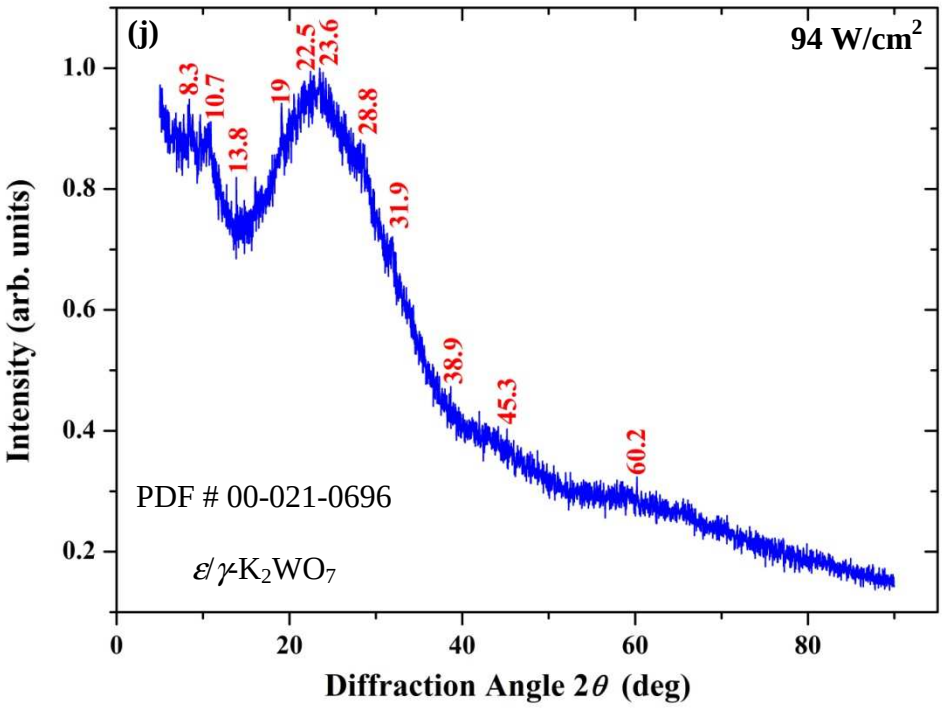

(e)
51 W/cm2
9.9
14.1
19.1
23.6
25.6
29.2
34
44.1
52.7
PDF # 00-005-0392
ε/γ-W18O49
Intensity (arb. units)
Diffraction Angle 2θ (deg)

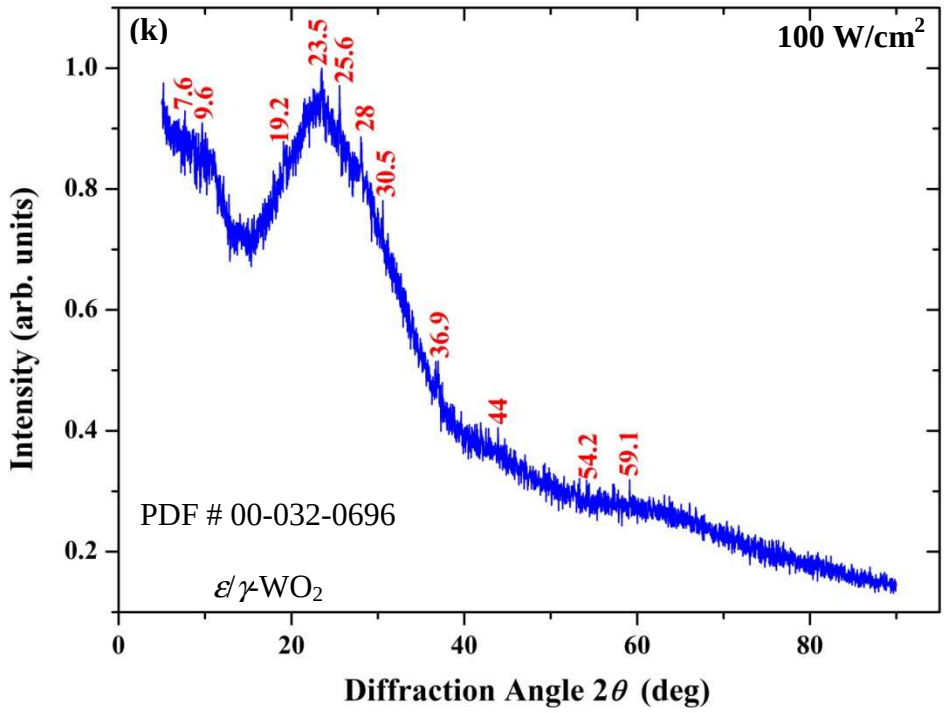

(f)
60 W/cm2
8.6
9.6
10.7
15
17.7
19.4
22.6
24.6
28.8
31.8
36.3
42.5
67
PDF # No match found
Intensity (arb. units)
Diffraction Angle 2θ (deg)

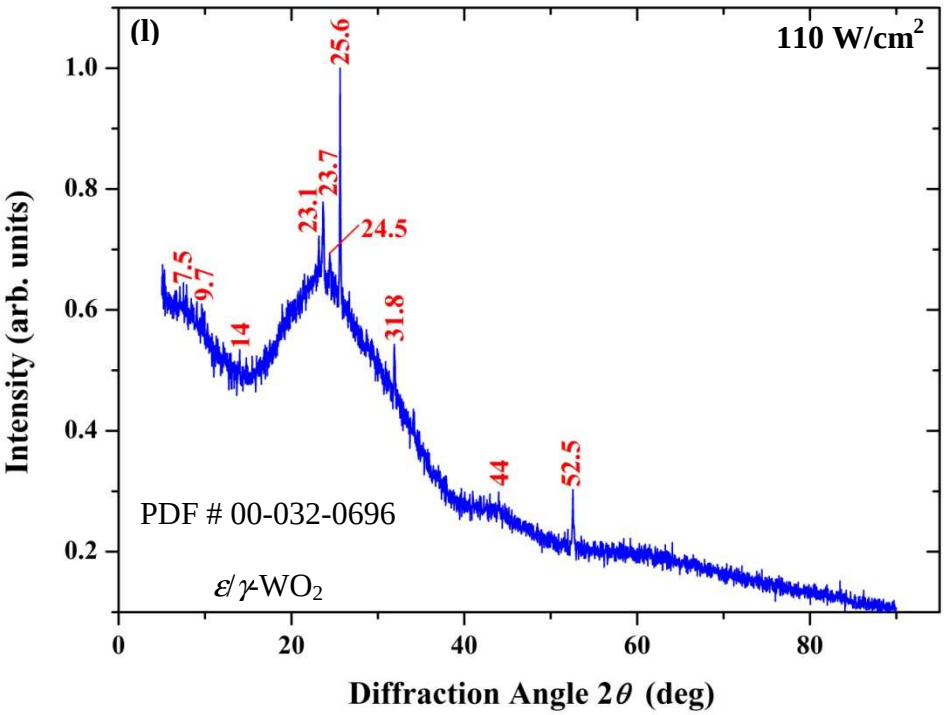

(g)
68 W/cm2
23.7
23.2
24.5
25.5
29.2
9.8
34
37.9
48.3
PDF # 00-005-0386
ε/γ-W10O29
Intensity (arb. units)
Diffraction Angle 2θ (deg)


(h)
77 W/cm2
23.7
23.2
25.5
24.5
8.5
19.7
12.4
34
38
47.4
52.6
PDF # 00-005-0386
ε/γ-W10O29
Intensity (arb. units)
Diffraction Angle 2θ (deg)


(i)
85 W/cm2
8.4
9.6
10.9
20.6
23.9
27.7
33.9
44.2
64
PDF # No match found
Intensity (arb. units)
Diffraction Angle 2θ (deg)


(j)
94 W/cm2
8.3
10.7
13.8
19
22.5
23.6
28.8
31.9
38.9
45.3
60.2
PDF # 00-021-0696
ε/γ-K2WO7
Intensity (arb. units)
Diffraction Angle 2θ (deg)



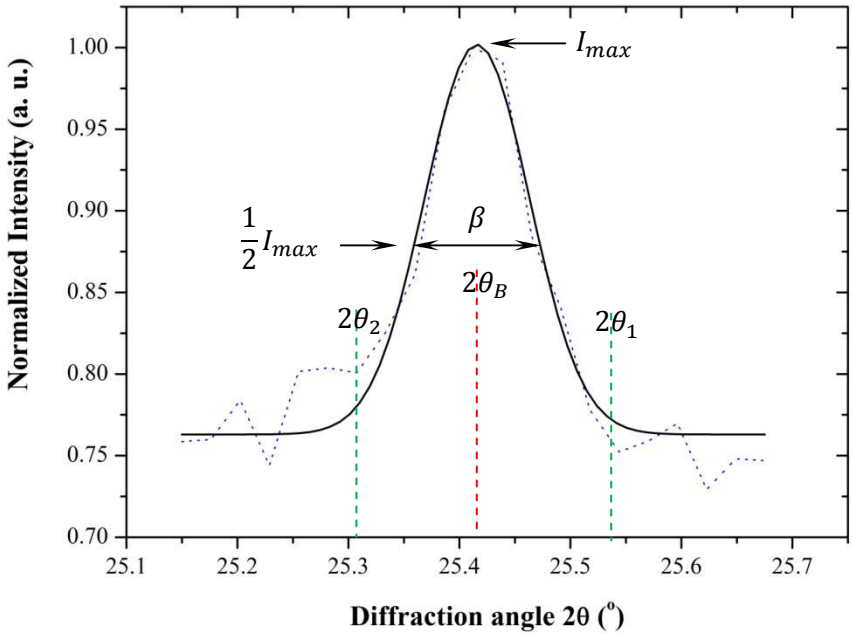


Appendix D.2 (a)-(l) The XRD spectra for the post-annealed samples, prepared at different power densities and constant wavelength of 10.6 μm.

Appendix E

Derivation of the Scherrer Formula

The width of the XRD diffraction curve shown in Figure E.1, increases as the thickness of the crystal decreases, because the angular range $(2\theta_1 - 2\theta_2)$ increases as *m* decreases. The width β is measured in radians at an intensity equal to half the maximum intensity. Note that β is an angular width in terms of 2θ. As an estimate of β, one can take half the difference between the two extreme angles at which the intensity is zero, which amounts to assuming that the diffraction line is triangular in shape. This means that $\beta = \frac{1}{2}(2\theta_1 - 2\theta_2) = \theta_1 - \theta_2$.



Appendix E.1 A XRD diffraction curve.

The path-difference equations can now be written for the two angles, which is related to the entire thickness of the crystal rather than the distance between adjacent planes (see Figure E.1). The relationships are given by [112]

$$2d \sin\theta_1 = (m+1)\lambda, \qquad (E.1)$$

and

$$2d \sin\theta_2 = (m-1)\lambda. \qquad (E.2)$$

where d is the thickness of the crystal.

Subtracting equations (E.1) from (E.2), gives

$$d(\sin\theta_1 - \sin\theta_2) = \lambda, \tag{E.3}$$

and using trigonometric co-functions gives

$$2d\cos\left(\frac{\theta_1 + \theta_2}{2}\right)\sin\left(\frac{\theta_1 - \theta_2}{2}\right) = \lambda. \tag{E.4}$$

But θ_1 and θ_2 are both nearly equivalent to Bragg's angle θ_B, so that

$$\theta_1 + \theta_2 = 2\theta_B, \tag{E.5}$$

and

$$\sin\left(\frac{\theta_1 - \theta_2}{2}\right) = \left(\frac{\theta_1 - \theta_2}{2}\right). \tag{E.6}$$

It follows that

$$2d\left(\frac{\theta_1 - \theta_2}{2}\right)\cos\theta_B = \lambda, \tag{E.7}$$

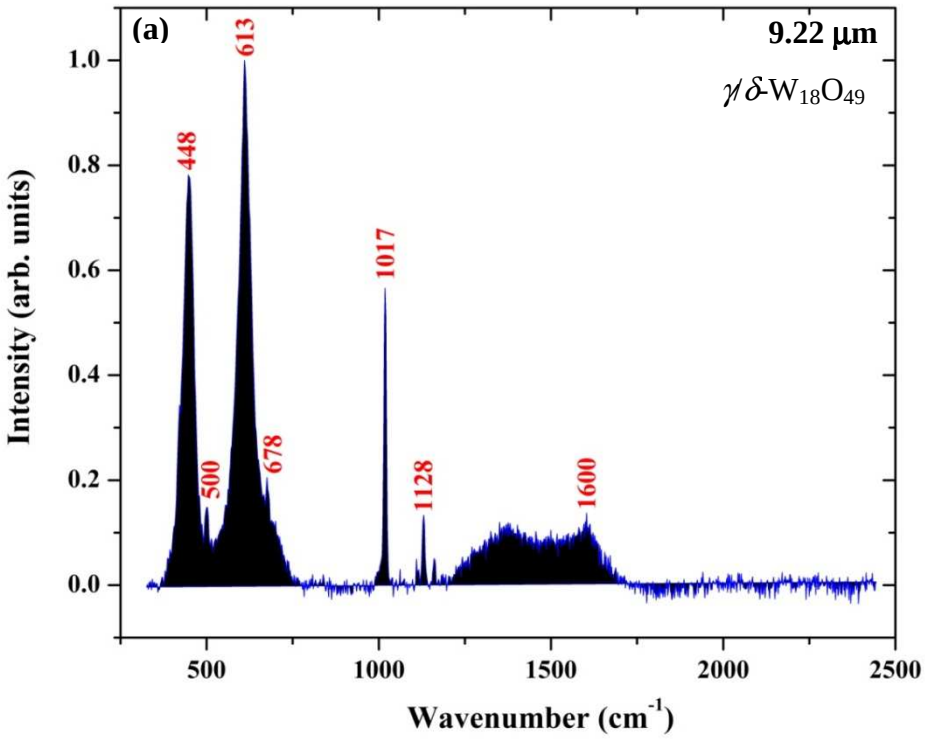
and so equation (E.7) can be written as

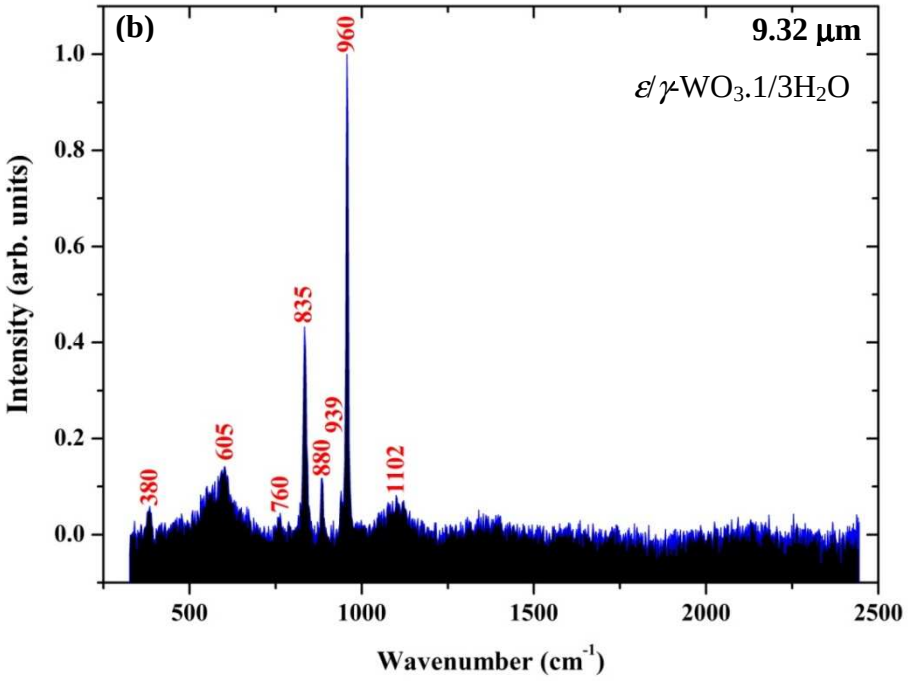
$$d = \frac{\lambda}{\beta\cos\theta_B}. \tag{E.8}$$

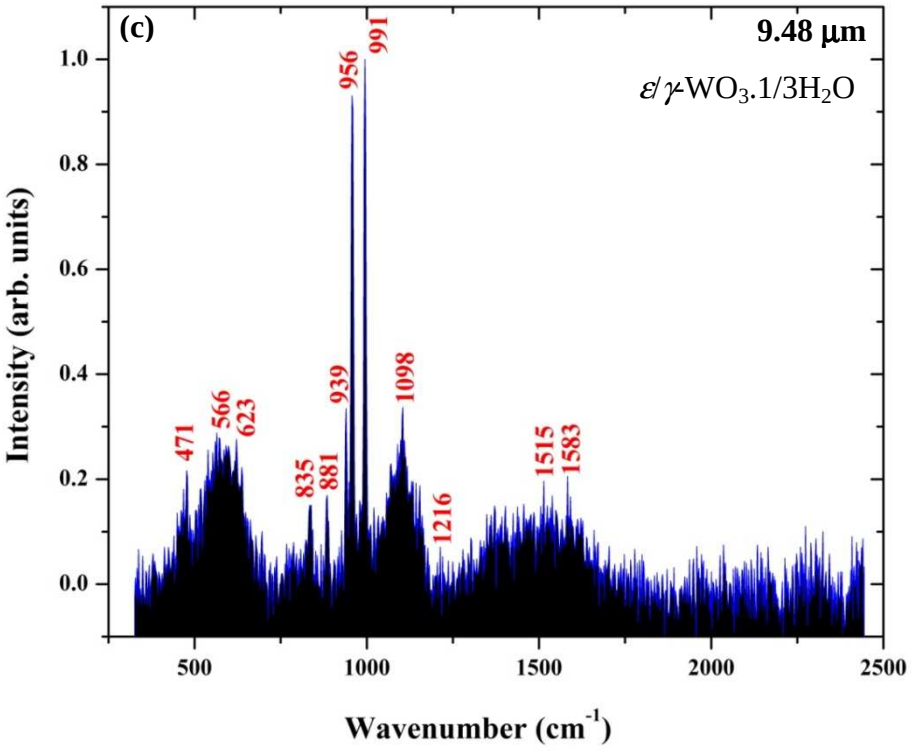
A more exact treatment of the problem leads to Scherrer's formula, given by

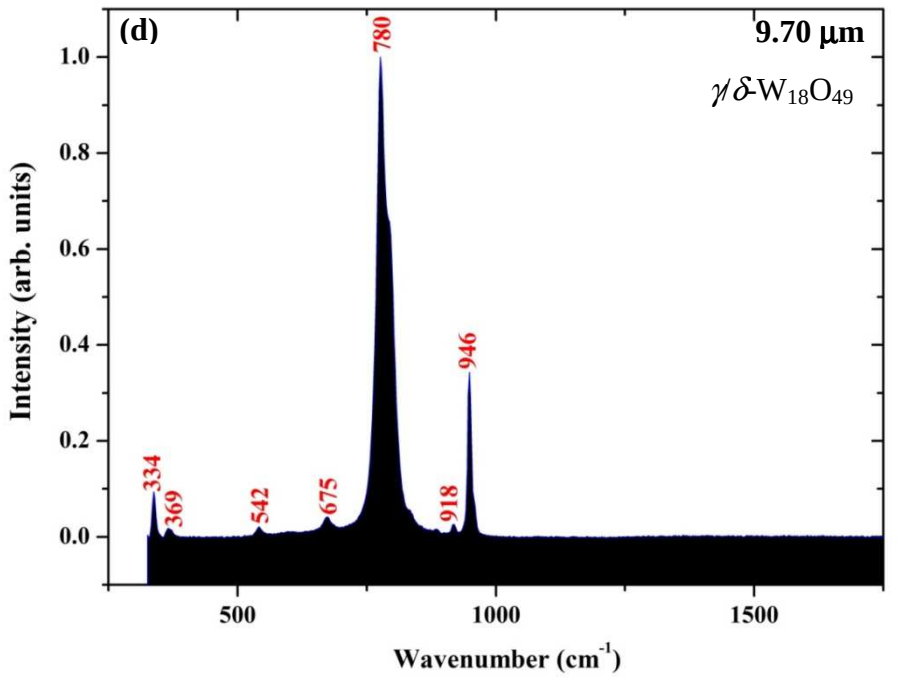
$$d = \frac{0.9\lambda}{\beta\cos\theta_B}. \tag{E.9}$$

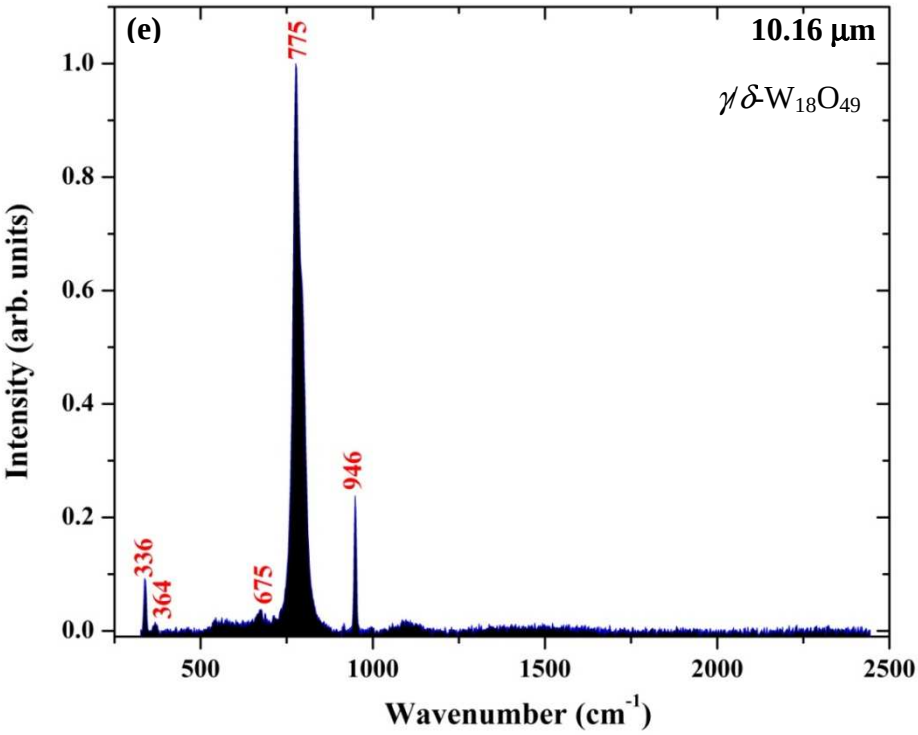
Appendix F - Raman Spectra

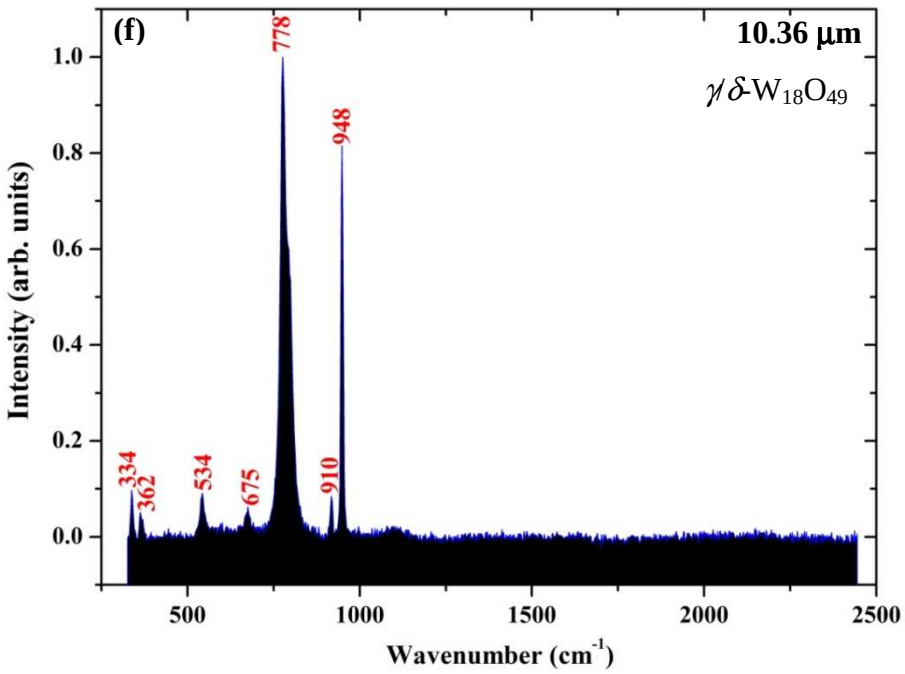


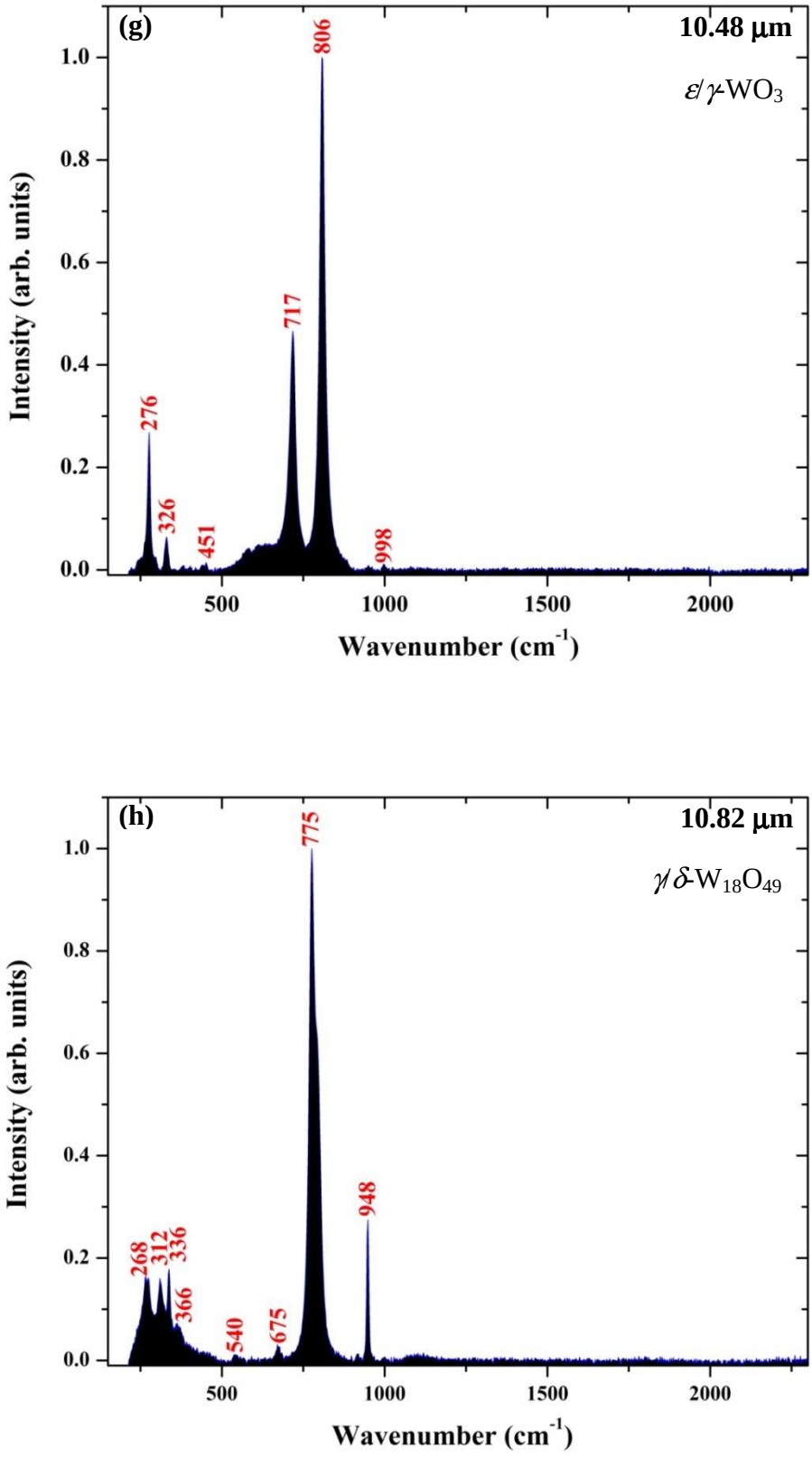



(c)
9.48 μm
ε/γ-WO3.1/3H2O
Intensity (arb. units)
Wavenumber (cm-1)
471
566
623
835
881
939
956
991
1098
1216
1515
1583

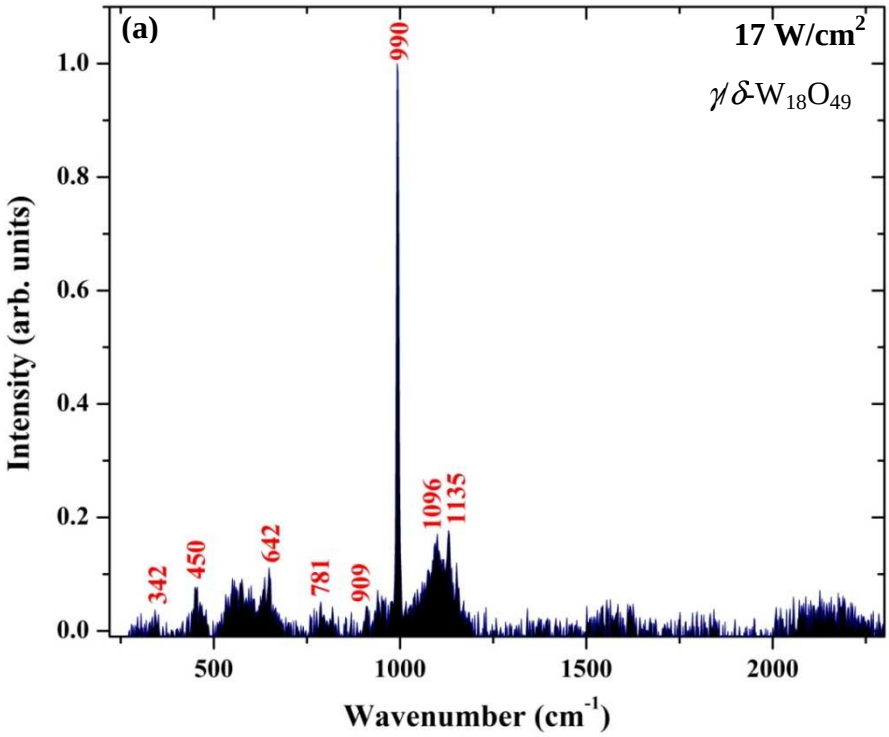

(d)
9.70 μm
γ/δ-W18O49
Intensity (arb. units)
Wavenumber (cm-1)
334
369
542
675
780
918
946

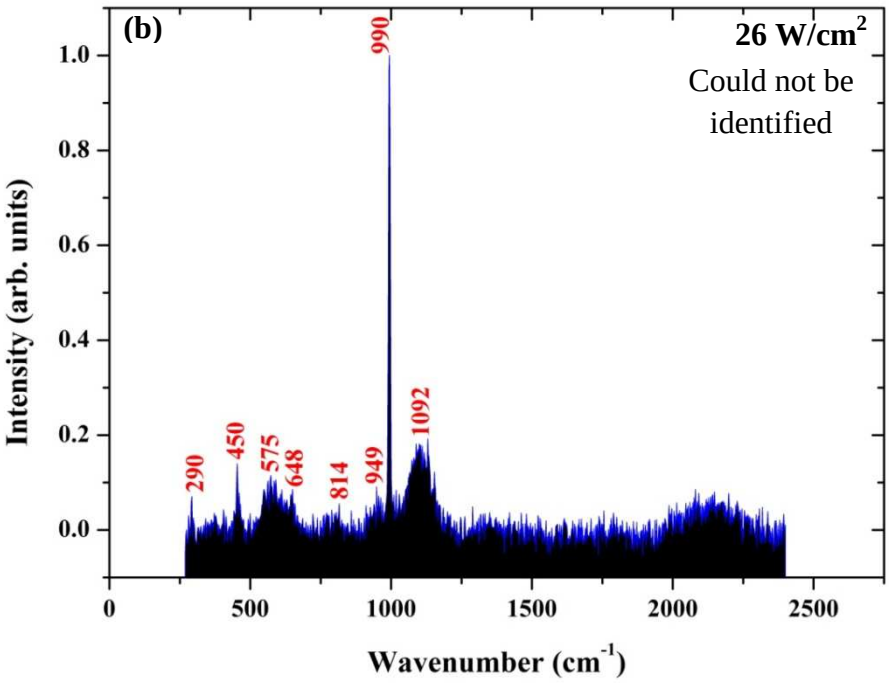

(e)
10.16 μm
γ/δ-W18O49
775
946
336
364
675
Intensity (arb. units)
Wavenumber (cm-1)
0.0
0.2
0.4
0.6
0.8
1.0
500
1000
1500
2000
2500

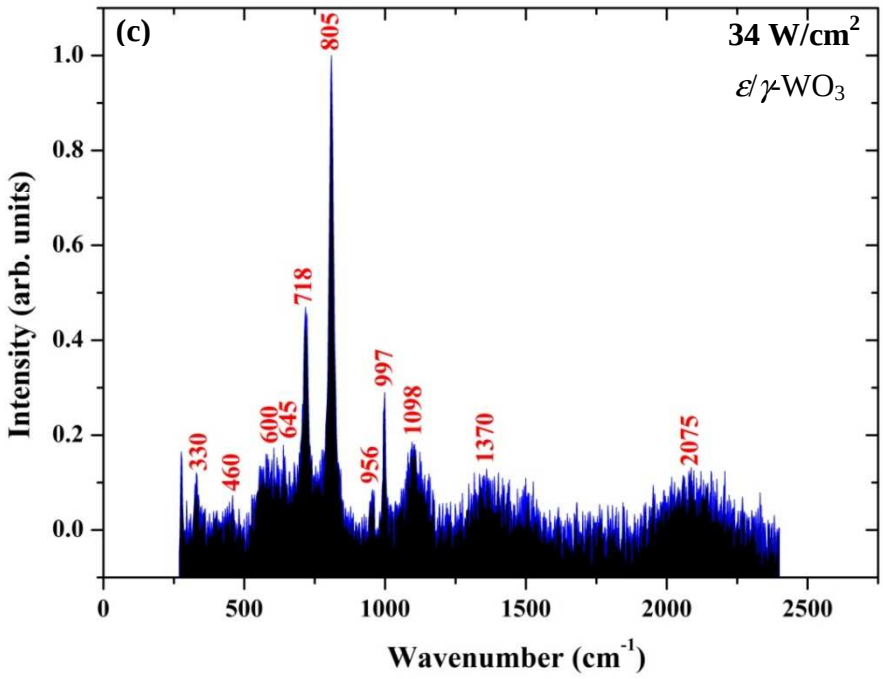

(f)
10.36 μm
γ/δ-W18O49
778
948
334
362
534
675
910
Intensity (arb. units)
Wavenumber (cm-1)
0.0
0.2
0.4
0.6
0.8
1.0
500
1000
1500
2000
2500

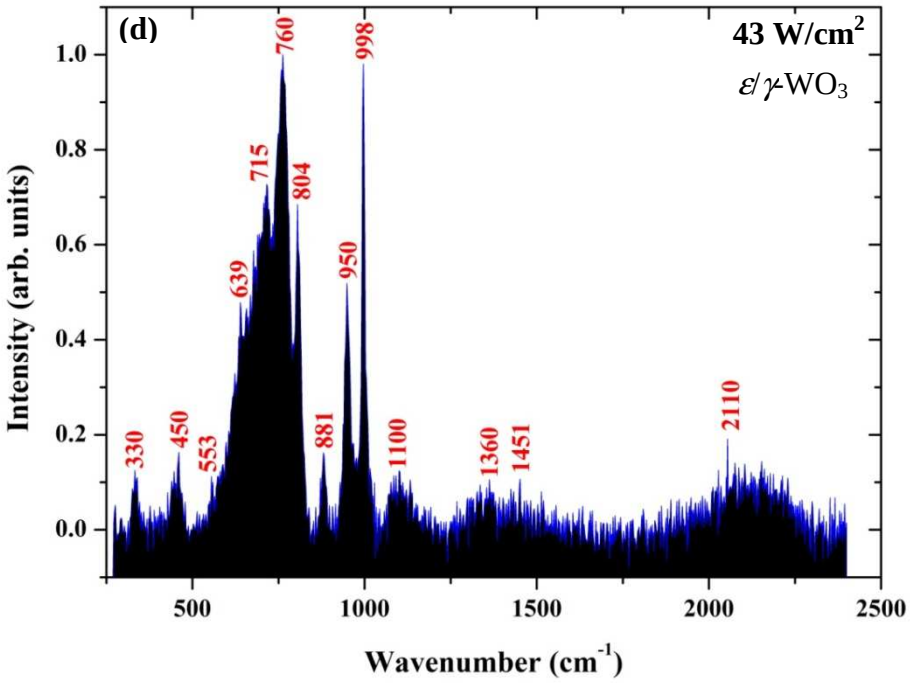


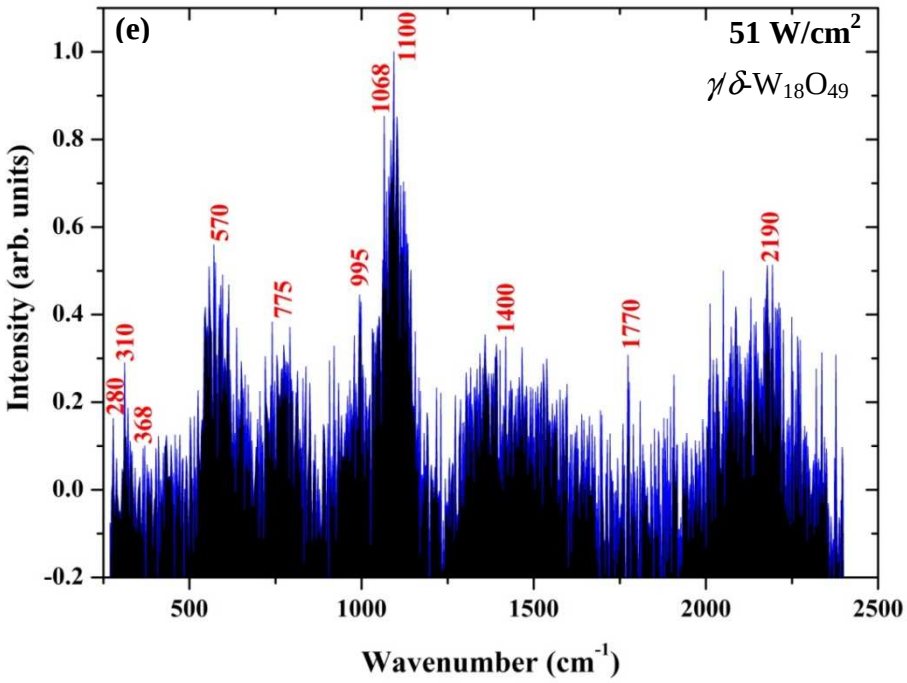
Appendix F.1 (a)-(h) The Raman spectra of the post-annealed samples, prepared at different wavelengths and constant power density of 51.2 W/cm^2.

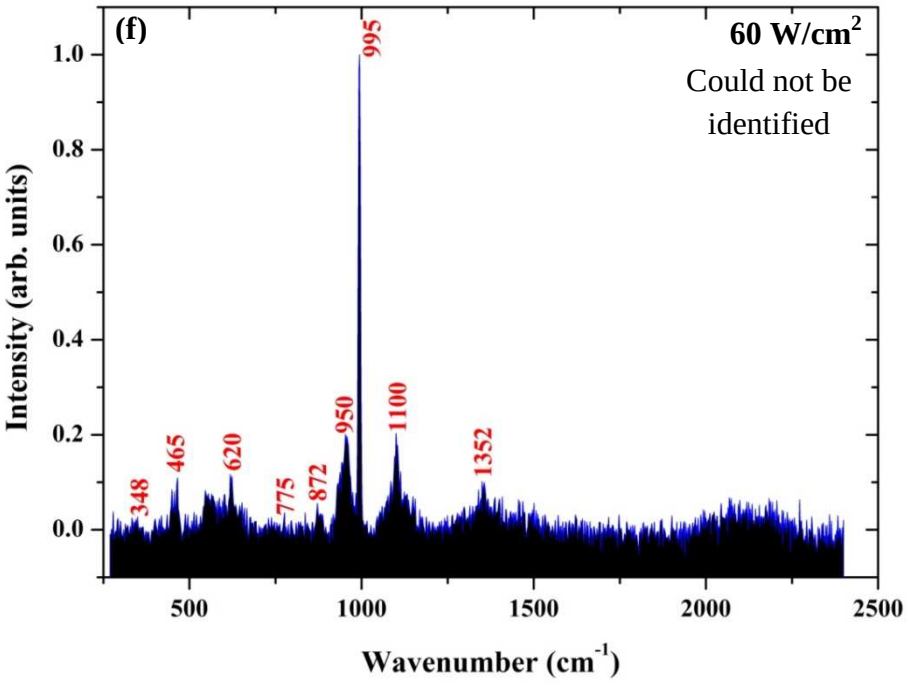

(a)
17 W/cm2
γ/δ-W18O49
990
1096
1135
642
450
342
781
909
Intensity (arb. units)
Wavenumber (cm-1)

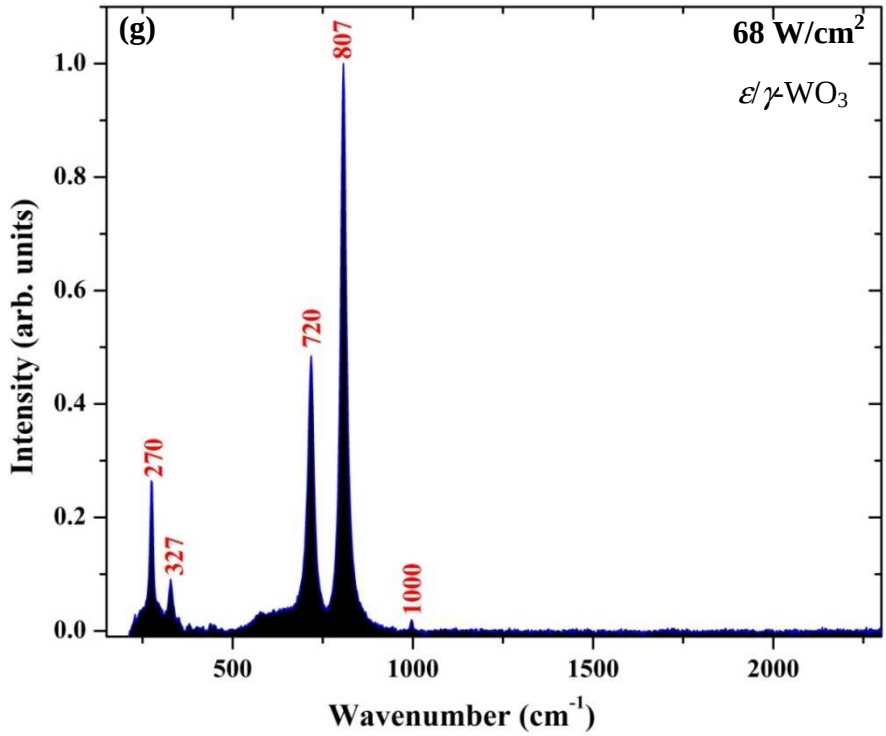

(b)
26 W/cm2
Could not be identified
990
1092
450
575
648
290
814
949
Intensity (arb. units)
Wavenumber (cm-1)

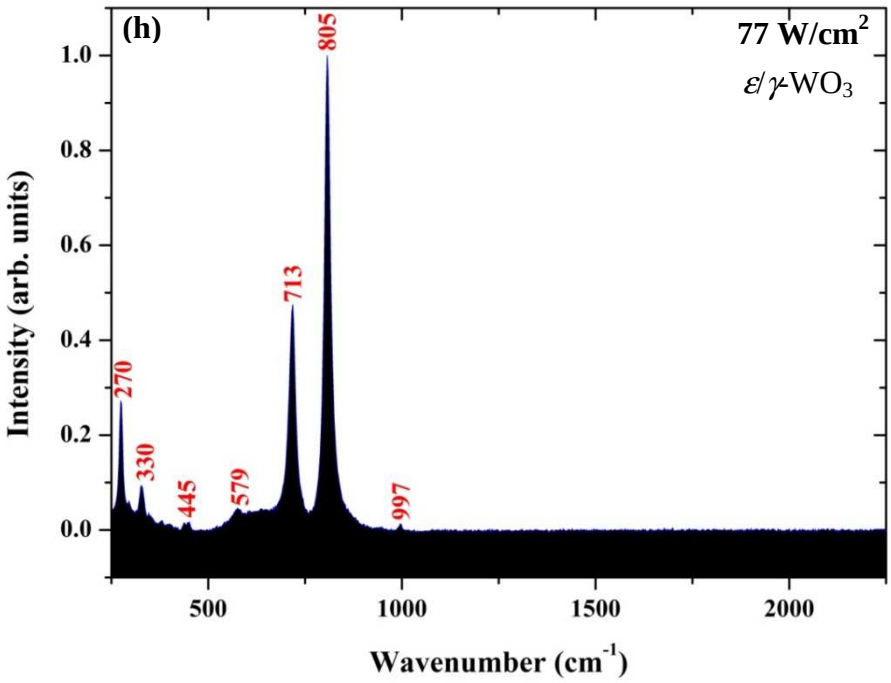

(c)
34 W/cm2
ε/γ-WO3
Intensity (arb. units)
Wavenumber (cm-1)
330
460
600
645
718
805
956
997
1098
1370
2075

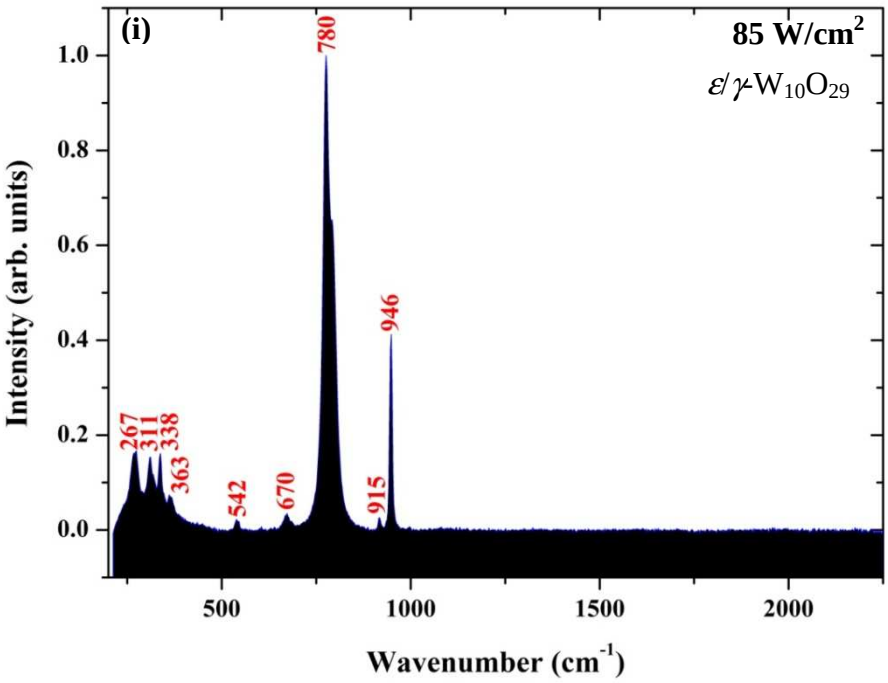

(d)
43 W/cm2
ε/γ-WO3
Intensity (arb. units)
Wavenumber (cm-1)
330
450
553
639
715
760
804
881
950
998
1100
1360
1451
2110

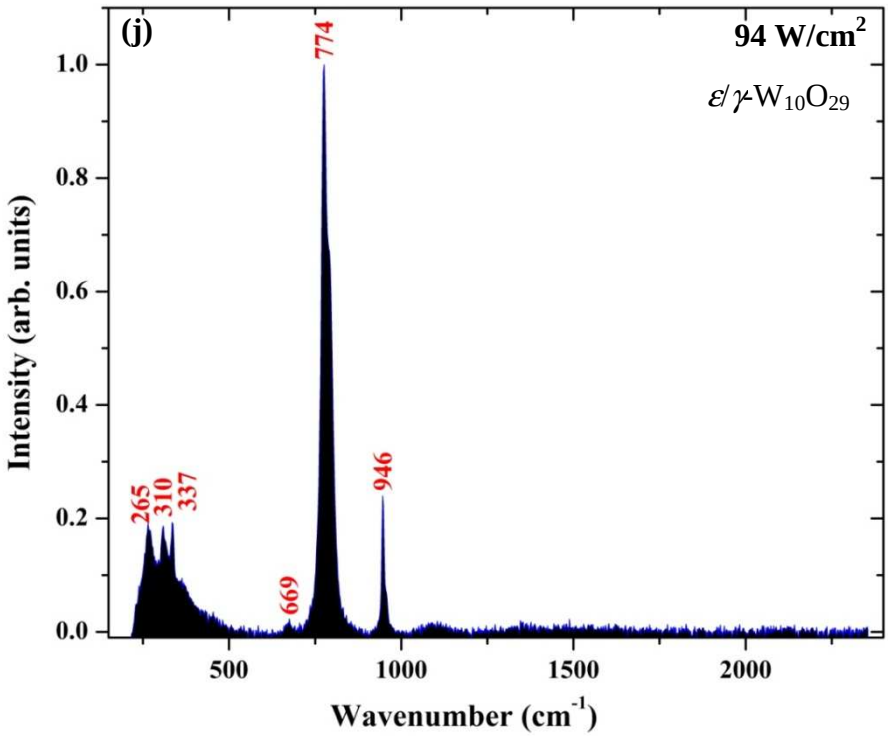

(e)
51 W/cm2
γ/δ-W18O49
Intensity (arb. units)
Wavenumber (cm-1)
280
310
368
570
775
995
1068
1100
1400
1770
2190

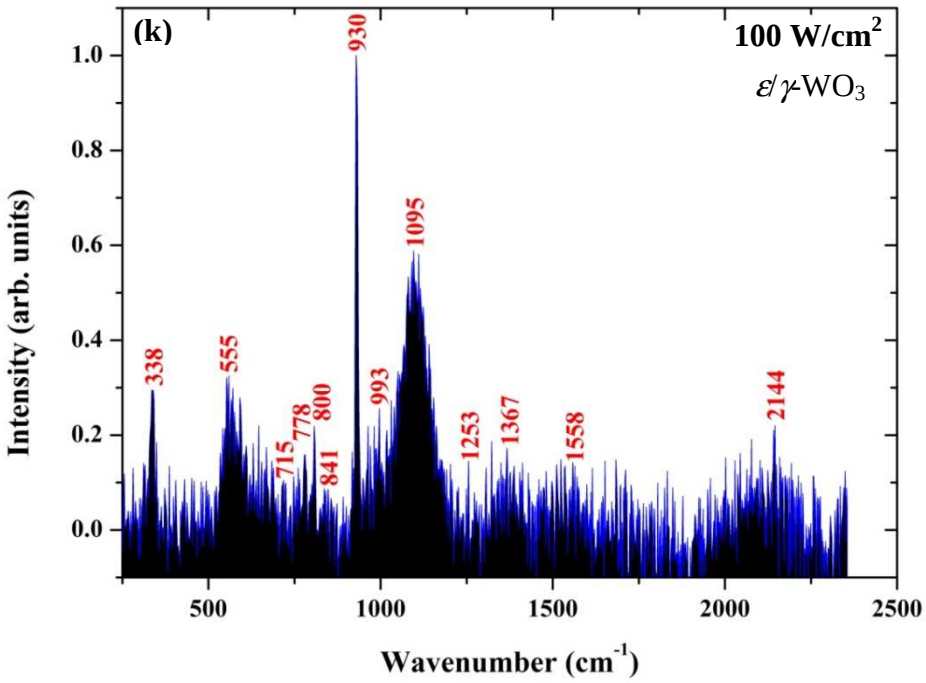

(f)
60 W/cm2
Could not be identified
Intensity (arb. units)
Wavenumber (cm-1)
348
465
620
775
872
950
995
1100
1352

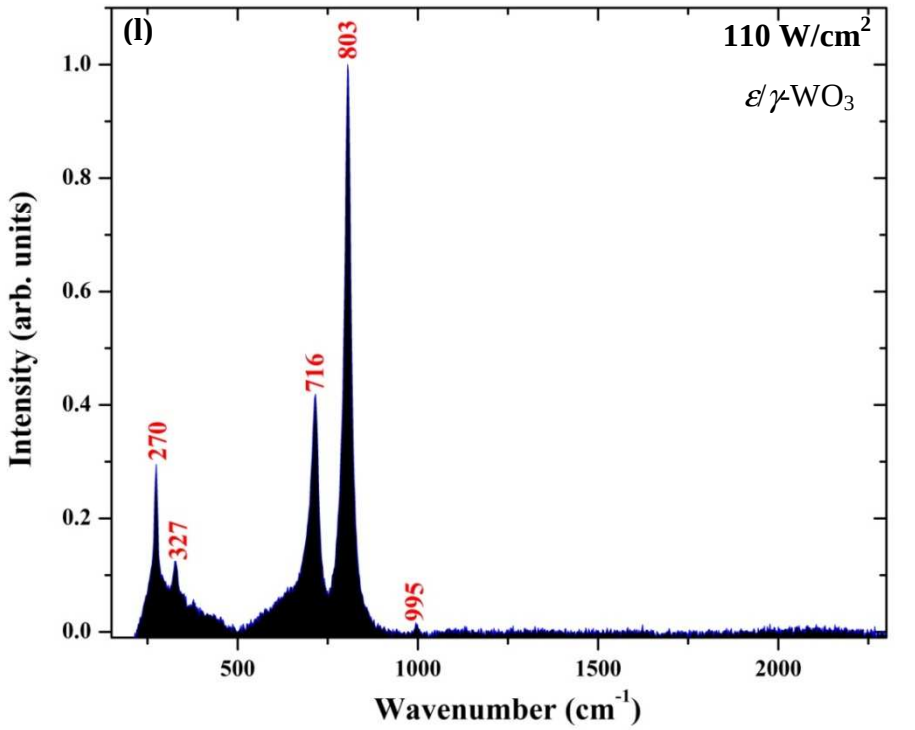

(g)
68 W/cm2
ε/γ-WO3
807
720
270
327
1000
Intensity (arb. units)
Wavenumber (cm-1)


(h)
77 W/cm2
ε/γ-WO3
805
713
270
330
445
579
997
Intensity (arb. units)
Wavenumber (cm-1)


(i)
85 W/cm2
ε/γ-W10O29
Intensity (arb. units)
Wavenumber (cm-1)
780
946
267
311
338
363
542
670
915
0.0
0.2
0.4
0.6
0.8
1.0
500
1000
1500
2000

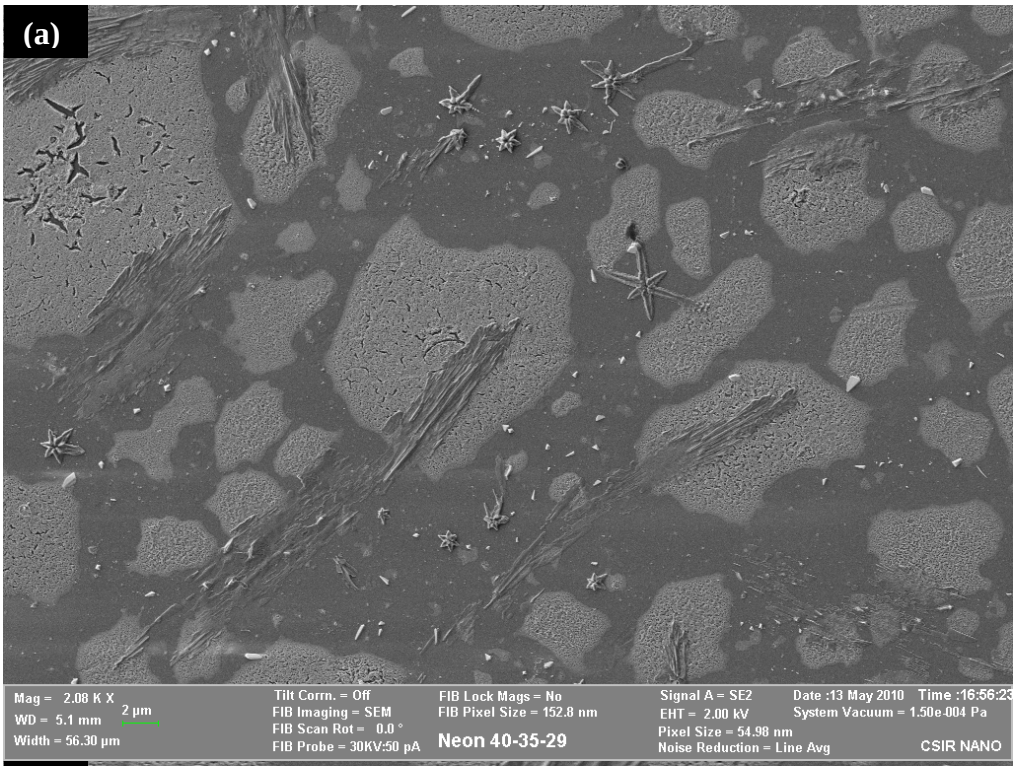

(j)
94 W/cm2
ε/γ-W10O29
Intensity (arb. units)
Wavenumber (cm-1)
774
946
265
310
337
669
0.0
0.2
0.4
0.6
0.8
1.0
500
1000
1500
2000

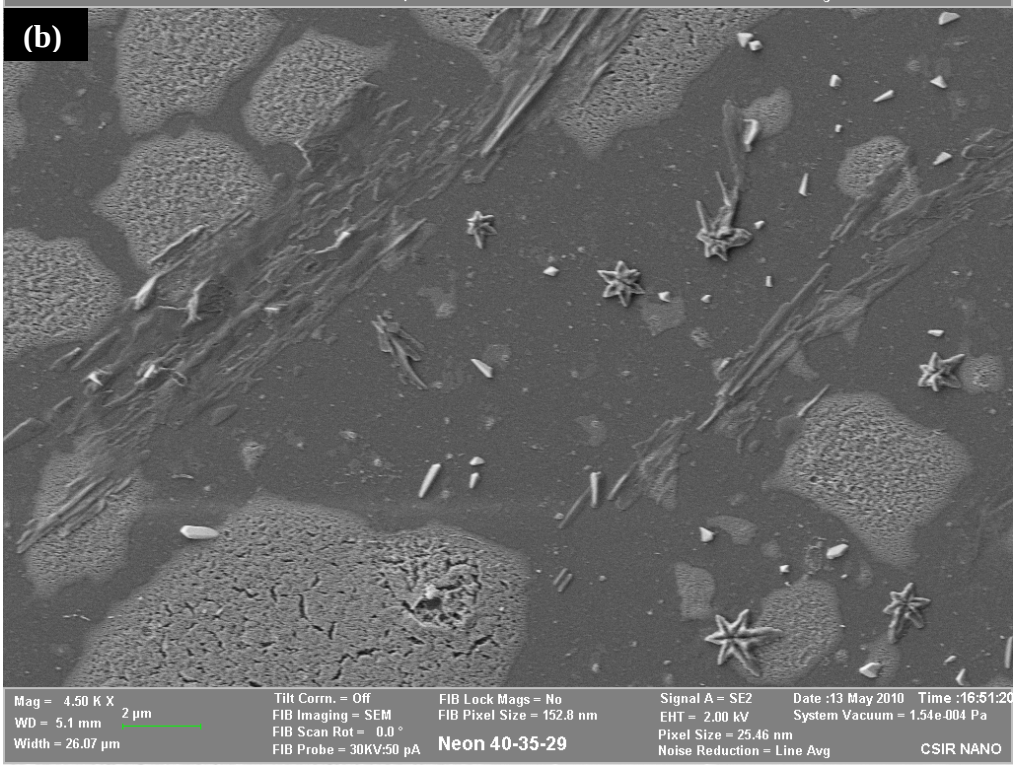


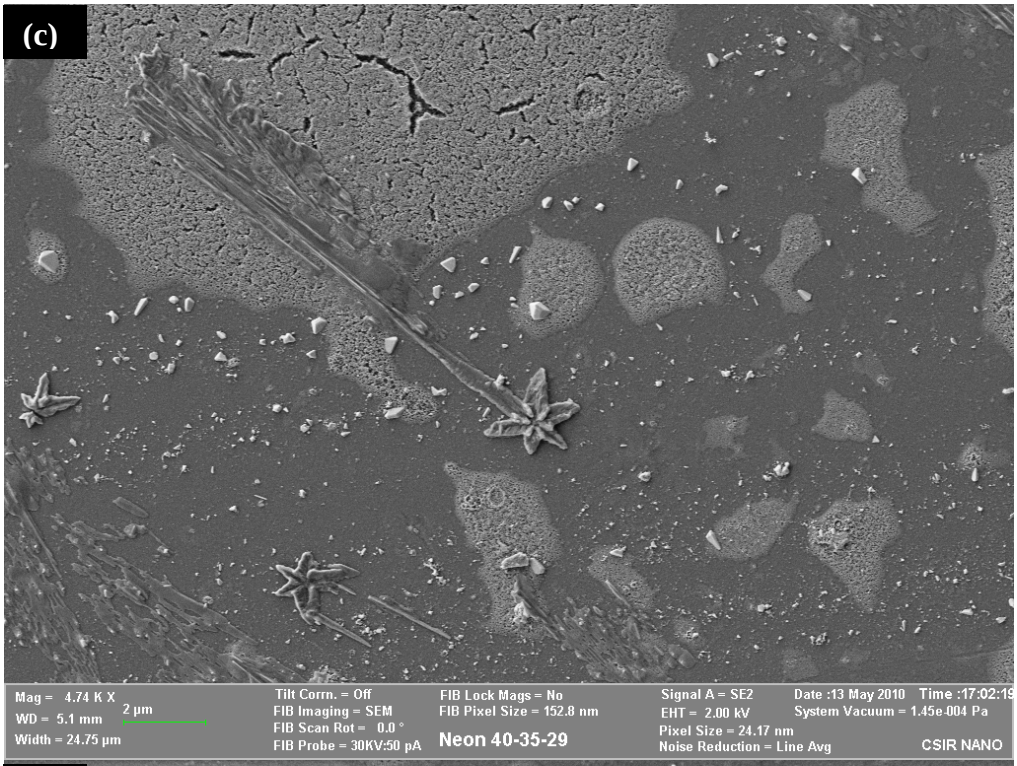


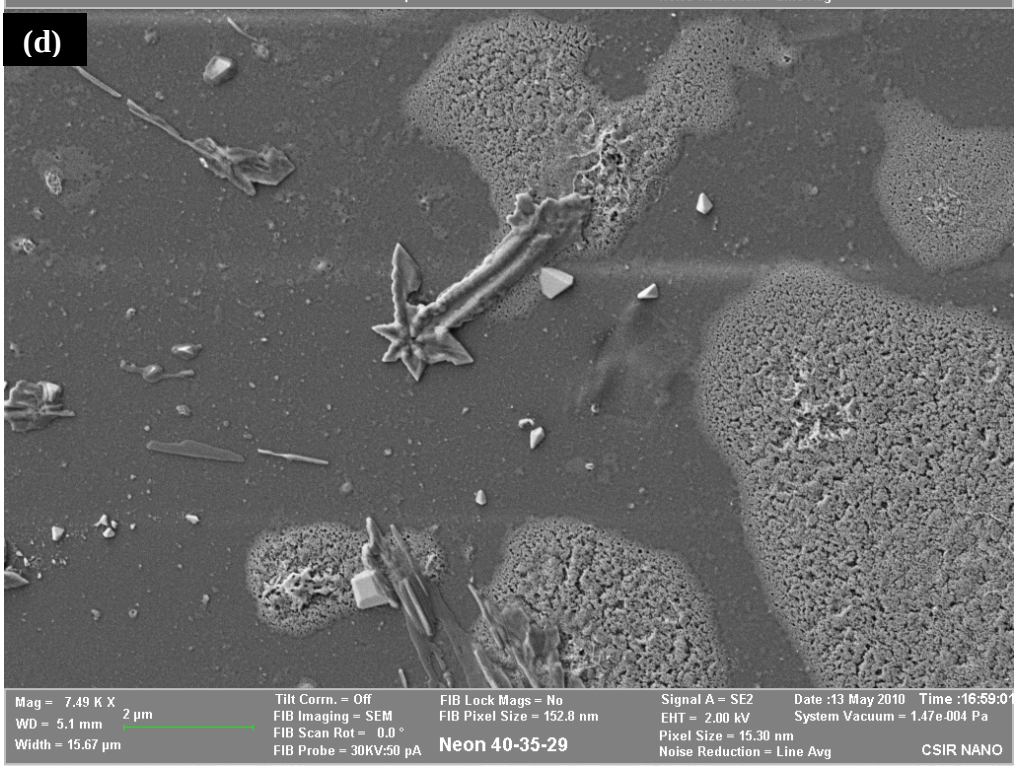
Appendix F.2 (a)-(l) The Raman spectra of the post-annealed samples, prepared at different power densities and constant wavelength of 10.6 μm.

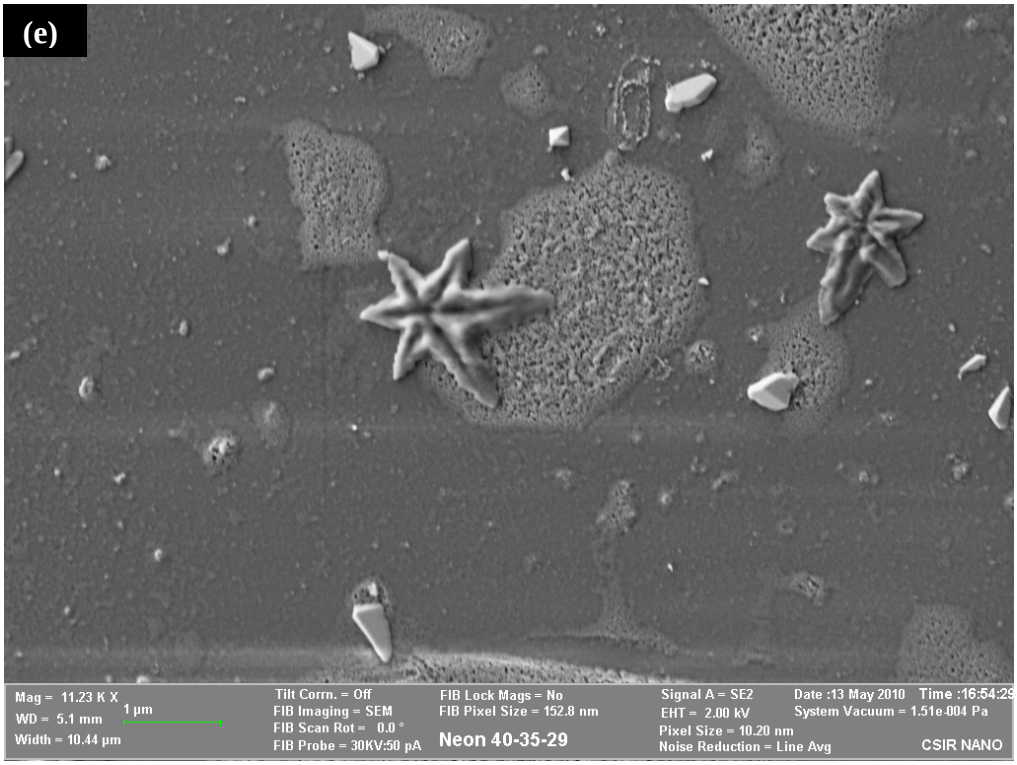
Appendix G - SEM Micrographs






(c)
Mag = 4.74 K X
WD = 5.1 mm
Width = 24.75 µm
2 µm
Tilt Corrn. = Off
FIB Imaging = SEM
FIB Scan Rot = 0.0 °
FIB Probe = 30KV:50 pA
FIB Lock Mags = No
FIB Pixel Size = 152.8 nm
Neon 40-35-29
Signal A = SE2
EHT = 2.00 kV
Pixel Size = 24.17 nm
Noise Reduction = Line Avg
Date :13 May 2010
System Vacuum = 1.45e-004 Pa
CSIR NANO


(d)
Mag = 7.49 K X
WD = 5.1 mm
Width = 15.67 µm
2 µm
Tilt Corrn. = Off
FIB Imaging = SEM
FIB Scan Rot = 0.0 °
FIB Probe = 30KV:50 pA
FIB Lock Mags = No
FIB Pixel Size = 152.8 nm
Neon 40-35-29
Signal A = SE2
EHT = 2.00 kV
Pixel Size = 15.30 nm
Noise Reduction = Line Avg
Date :13 May 2010
System Vacuum = 1.47e-004 Pa
CSIR NANO



Appendix E.1 SEM micrographs of the post-annealed sample showing the stars that formed during annealing, at **(a)** 2000 times magnification, **(b)** 4500 times magnification, **(c)** 4740 times magnification, **(d)** 7490 times magnification, and **(e)** 11230 times magnification, prepared at the 10.6 µm wavelength and power density of 2.2 kW/cm^2.

Appendix H - Publication

Govender et al. Nanoscale Research Letters 2011, 6:166
http://www.nanoscalereslett.com/content/6/1/166

Nanoscale Research Letters
a SpringerOpen Journal

NANO EXPRESS Open Access

Formation of tungsten oxide nanostructures by laser pyrolysis: stars, fibres and spheres

Malcolm Govender[1,2], Lerato Shikwambana[1,2], Bonex Wakufwa Mwakikunga[1*], Elias Sideras-Haddad[2,3], Rudolph Marthinus Erasmus[2], Andrew Forbes[1,4]

Abstract

In this letter, the production of multi-phase WO_3 and WO_{3-x} (where x could vary between 0.1 and 0.3) nanostructures synthesized by CO_2-laser pyrolysis technique at varying laser wavelengths (9.22-10.82 mm) and power densities (17-110 W/cm^2) is reported. The average spherical particle sizes for the wavelength variation samples ranged between 113 and 560 nm, and the average spherical particle sizes for power density variation samples ranged between 108 and 205 nm. Synthesis of $W_{18}O_{49}$ (= $WO_{2.72}$) stars by this method is reported for the first time at a power density and wavelength of 2.2 kW/cm^2 and 10.6 μm, respectively. It was found that more concentrated starting precursors result in the growth of hierarchical structures such as stars, whereas dilute starting precursors result in the growth of simpler structures such as wires.

Introduction

Tungsten trioxide is known as a 'smart material', because it exhibits excellent electrochromic, photochromic and gasochromic properties. Nano-sized tungsten trioxide has been applied in many nano-photonic devices for applications such as photo-electro-chromic windows [1], sensor devices [2,3] and optical modulation devices [4]. Many techniques for synthesizing nano-sized tungsten trioxide have been reported [5-8] and this article concerns with laser pyrolysis.

Laser pyrolysis is more advantageous than most methods because the experimental orientation does not allow the reactants to make contact with any side-walls, so that the products are of high quality and purity [9]. Laser pyrolysis is based on photon-induced chemical reactions, which is believed to rely on a resonant interaction between a laser beam's emission line and a precursor's absorption band, such that a photochemical reaction is activated [10]. The photochemical reaction enables an otherwise inaccessible reaction pathway towards a specific product, either by dissociation, ionization or isomerisation of the precursor compound. It was shown [8,11] that low laser power densities can also achieve the same desired products as the high power densities, presumably because of the way photon-energy is distributed into the energy levels of the precursor.

In this letter, the formation of $W_{18}O_{49}$ (= $WO_{2.72}$) and the effect of the laser power, the wavelength on the morphology and structural properties of tungsten oxide nano-structured and thin films are reported.

Experimental

The laser pyrolysis experimental setup was discussed in detail in [10], and a schematic description of the experiment during laser-precursor interaction is depicted in Figure 1. The laser pyrolysis method is carried out within a custom-made stainless steel chamber at atmospheric pressure. A wavelength tunable Continuous Wave CO_2 laser was used in the experiments (Edinburgh Instruments, model PL6, 2 Bain Square, Kirkton Campus, Livingston, UK) and the beam was focused into the reaction chamber with a 1-m radius of curvature concave mirror which is effectively a lens with a focal length of 500 mm. For low power densities, an unfocused beam was used by replacing the concave mirror with a flat mirror. An IR-detector (Ophir-Spiricon, model PY-III-C-A, Ophir Distribution Center, Science-Based Industrial Park, Har Hotzvim, Jerusalem, Israel) was used to trace out the laser beam profile at various propagation distances from the flat or concave mirror to determine the beam properties.

* Correspondence: BMwakikunga@csir.co.za
[1]CSIR National Laser Centre, P. O. Box 395, Pretoria 0001, South Africa
Full list of author information is available at the end of the article

SpringerOpen

© 2011 Govender et al; licensee Springer. This is an Open Access article distributed under the terms of the Creative Commons Attribution License (http://creativecommons.org/licenses/by/2.0), which permits unrestricted use, distribution, and reproduction in any medium, provided the original work is properly cited.

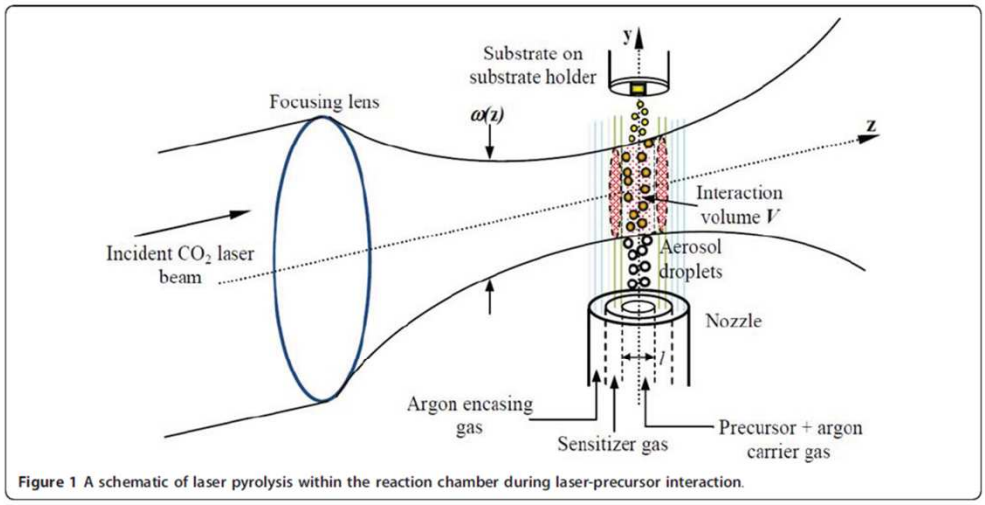


Figure 1 A schematic of laser pyrolysis within the reaction chamber during laser-precursor interaction.

The laser power was varied using a polarization-based attenuator, and the wavelength variation was achieved with an intra-cavity mounted grating in the laser. The different wavelengths were identified using a spectrum analyzer (Macken Instruments Inc., model 16A, Coffey Lane, Santa Rosa, California, USA) and the power output was measured with a power meter (Coherent Inc., 5100 Patrick Henry Drive, Santa Clara, CA 95054, USA).

The synthesis of WO_3 and WO_{3-x} commenced by mixing 0.1 g of greyish-blue anhydrous tungsten hexachloride (WCl_6, >99.9%, Sigma Aldrich, 3050 Spruce Street, St. Louis, MO 63103, USA) powder in 100 mL of absolute ethanol (C_2H_5OH, >99.9%, Sigma Aldrich) to give a tungsten ethoxide $W(OC_2H_5)_6$ starting precursor [12]. Optical absorption properties of the precursor were determined using a Perkin Elmer Spotlight 400 FTIR Imaging System in the wavelength range 500-4000 cm^{-1}.

The liquid precursor was decanted into an aerosol generator (Micro Mist, model EN, Research Triangle Park, NC 27709, USA) which was attached to the laser pyrolysis system via a multiflow nozzle that allows argon gas to carry the stream of very fine precursor droplets (5 μm droplet diameter according to the manufacturer) into the laser beam. Acetylene (C_2H_2) sensitizer gas and argon encasing gas flowed adjacent to the precursor, guiding it towards a substrate. The gas flow rates are chosen such that the ablated precursor collects on the substrate after interacting with the laser.

The sample was annealed for 17 h at 500°C under argon atmosphere [10]. Morphology studies were carried out using a Jeol JSM-5600 Scanning Electron Microscopy (SEM) microscope (using the secondary electron mode). Raman spectroscopy was carried out using a Jobin-Yvon T64000 Raman Spectrograph with a wavelength of 514.5 nm from an argon ion laser set at a laser power of 0.384 mW at the sample to minimize local heating of the sample during the Raman analysis. X-ray diffraction (XRD) was carried out using a Philips Xpert powder diffractometer equipped with a CuK_α wavelength of 154.184 pm. The reproducibility of the experimental procedure was not verified.

Results

When the CO_2 laser beam was focused with a 1-m radius of curvature mirror, it produced a minimum beam radius or a beam waist of 1.2 mm, and at a laser power of 50 W on the 10.6-μm emission line, a power density of 2.2 kW/cm^2 was achieved. These parameters were consistent with those obtained when synthesizing WO_3 nanowires using a very dilute precursor of 27 μM [10]. Laser pyrolysis of the more concentrated 2.5 mM precursor showed many uniform agglomerations composed of nanospheres (40 nm) before annealing, as depicted in the SEM micrograph in the inset of Figure 2. The sample was annealed, and from the agglomerates, stars grew with six points as seen in the SEM micrographs of Figure 2.

The Raman and XRD spectra of the samples containing the stars are shown in Figure 3. The stars were not visible under the Raman microscope and so various spots were analyzed on the sample. The Raman study shows that the sample is amorphous after annealing,

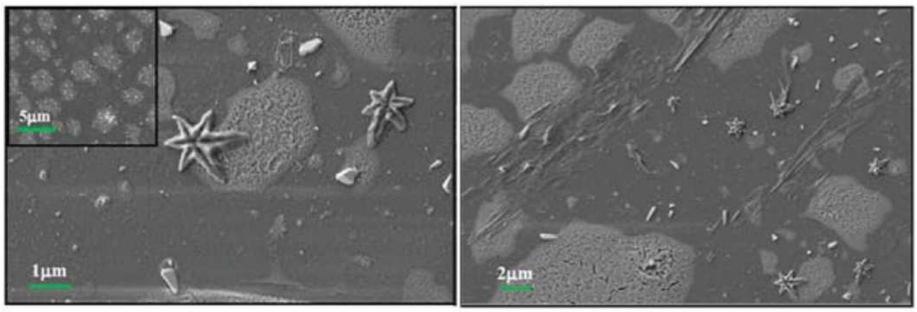


Figure 2 Scanning electron micrographs of the post-annealed sample showing the growth of six-sided stars from the agglomerations of the pre-annealed sample depicted in the inset.

and the lack of a dominant peak at 800 cm^{-1} suggests the absence of monoclinic phase tungsten trioxide and possibly oxygen deficiency [13,14]. The Raman peaks found near 224 cm^{-1}, 288 cm^{-1} and 320 cm^{-1} are indicative of a W-O-W stretching mode of a tungsten oxide. The Raman peak at 700 cm^{-1} is designated to the bridging O-W-O vibrations in tungsten trioxide, and the asymmetry in this phonon peak shows that there are a number of phonons confined in the tungsten oxide layer of particles. This indicates that the product is composed of particles less than 20 nm in size [15,16]. The peak near 960 cm^{-1} is assigned to the W^{6+} = O symmetric stretching mode.

The XRD studies revealed peaks at 23° and 24° diffraction angles which suggests a tungsten oxide compound, but the lack of a triplet peak confirms the absence of monoclinic tungsten trioxide [17]. The broad hump at 22° resulted from SiO_2 of the substrate, and this substantially decreased the signal-to-noise ratio making it difficult to identify the peaks. XRD peaks at 11, 40 and 64° diffraction angles are also evident in tungsten oxides [17], but the 44° diffraction angle suggests that the tungsten oxide has a deficiency of oxygen [18]. Based on the information from Raman spectroscopy and XRD, the most probable stoichiometry of this sample is monoclinic phase $W_{18}O_{49}$ (= $WO_{2.72}$). According to the Powder Diffraction File (PDF 00-005-0392) that best matches the XRD spectrum in Figure 3, the lattice constants *a*, *b* and *c* are 18.28, 3.78 and 13.98 Å, respectively and the lattice angles are α = γ = 90° and β = 115.20°. The Miller indices are shown on the XRD spectrum in Figure 3.

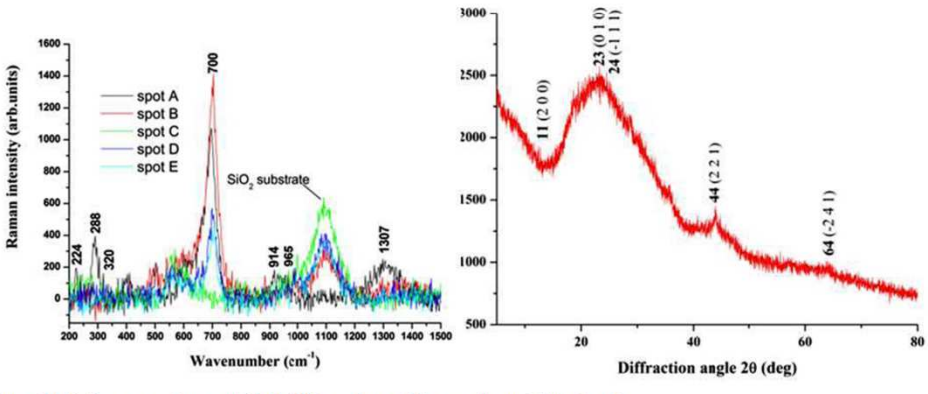


Figure 3 Left: Raman spectrum and Right: XRD spectrum of the sample containing the stars.

Previously solid-vapour-solid (SVS) [8] and solution-liquid-solid (SLS) [19] mechanisms were proposed to explain the growth of nanowires of tungsten trioxide and platinum, respectively. Since the tungsten trioxide nanowires were grown with a low precursor concentration using a similar laser beam and laser parameters, the precursor concentration is seemingly the main contributor to hierarchical structure. This was confirmed by the 100 times more concentrated precursor that was used for the growth of the stars. The six-sided stars that were grown in Figure 2 looked very similar to lead (II) sulphide (PbS) stars that were grown by a concentration difference and gradient (CDG) technique [20]. This CDG technique used a high local concentration of one reactant mixed with a low concentration of another reactant under ambient conditions, where the high concentration favoured the thermodynamic conditions for crystal growth and the low concentration resulted in a diffusion-controlled kinetic environment for growth of hierarchical structures.

It is possible that due to a Gaussian laser beam profile, which has a high intensity at the beam's centre and low intensity at the edges, the region of intensity in the beam experienced by the precursor could vary the concentration of the decomposed material. It is speculated that this variation in concentration could have led to the growth of the hierarchical structures according to the CDG technique. The growth of stars has also been reported before for gold and molybdenum oxide [21,22], but not as yet for tungsten oxide. The literature proposes that star-shaped structures can be grown from agglomerates of more simple nanoforms under an inert atmosphere, which conditions were similar for this experiment [21,22]. One growth mechanism of nanostructures could be due to Gibbs-Thompson effect [9,23,24], which proposes that the size of the critical radius is dependent on the precursor concentration and explains the increase (Ostwald ripening) or decrease (Tiller's formula) in size of nanostructures.

The higher concentration probably provided a critical radius which resulted in simple nanoforms and the growth of stars as opposed to a lower concentration which resulted in microspheres and the growth of wires. It is speculated that the critical radius influences the thermodynamic and kinetic conditions as predicted by the CDG technique. Thus, the laser beam properties together with the relative precursor concentration contribute to the growth of stars. Some stars may form with four-sides and others with six-sides depending on the crystalline plane arrangement and the elements composing the structures [20]. It is not yet understood if the observed deficiency of oxygen plays a role in the formation of the six-sided stars or if the higher tungsten content, with a predominant valency of +6, has some correlation with the number of sides formed.

It is thought that acetylene gas acts as a photosensitizer [10] in laser pyrolysis, yet no evidence of absorption in the laser wavelength range 9.19-10.82 μm was found. This was verified by passing the acetylene gas through the laser beam at atmospheric pressure, and monitoring the power change during this interaction. The laser power did not appear to show any change, which implied that no radiation was absorbed by this gas. This does not, however, discount the possibility of some short-lived metastable state in acetylene induced by the laser which was undetectable by the power meter. The argon-precursor mixture, however, showed a change in power which indicated that the radiation was being absorbed, and the maximum absorbance was found at a wavelength of 9.54 μm. The absorbance of the precursor was given by the ratio of the laser power before laser-precursor interaction to the power observed during laser-precursor interaction.

Figure 4 shows the absorbance by the precursor as a function of wavelength with the corresponding part of the FTIR transmission spectrum of tungsten ethoxide. This determination gives us an idea if the laser pyrolysis mechanism is a resonant process or if the precursor is decomposed by collisions with excited photosensitizer molecules. However, the results indicate that the laser energy gets transferred to the precursor and should cause decomposition by a resonant process, thus leading to the formation of the predicted products. Therefore, acetylene probably provides a reducing atmosphere in the laser-precursor interaction that influences the reaction pathway towards the formation of the products.

To determine how the laser wavelength plays a role in laser pyrolysis, it was varied between 9.19 and 10.84 μm at a constant power of 30 W and power density of 51.2 W/cm^2. The lower power density was achieved by replacing the focusing mirror with a flat mirror to obtain a beam radius of 6.11 mm. The low power density was chosen such that all the *R*- and *P*-branches of the CO_2 laser supplied a constant power output for the varying wavelengths. It was also assumed that at such low power density, minimum heating effects are involved in the laser-precursor interaction. It was found that only the 10.48-μm wavelength formed monoclinic phase WO_3 according to the Raman and XRD spectra shown in Figure 5 with the corresponding SEM micrograph.

The nanosphere diameters of this sample, which were easiest to measure on SEM micrograph, were distributed in the range 50-250 nm as depicted in inset of Figure 5, and micron-sized fibres were also present in this sample. The theory speculates that if the laser wavelength is resonant with the C-O absorption band of the precursor (W-O-C_2H_5), then the C-O bond would break and lead to the formation of tungsten oxide. However, FTIR showed that the C-O absorption band is found between

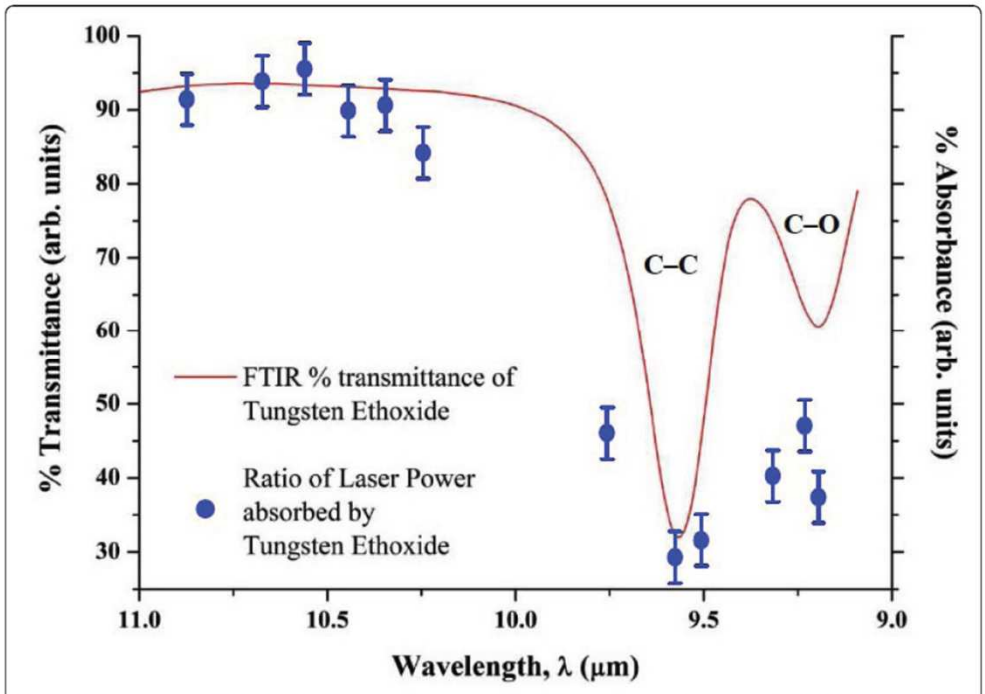


Figure 4 The comparison of the FTIR transmittance spectrum of the tungsten ethoxide precursor and the CO_2 laser radiation absorbance data of tungsten ethoxide as a function of wavelength.

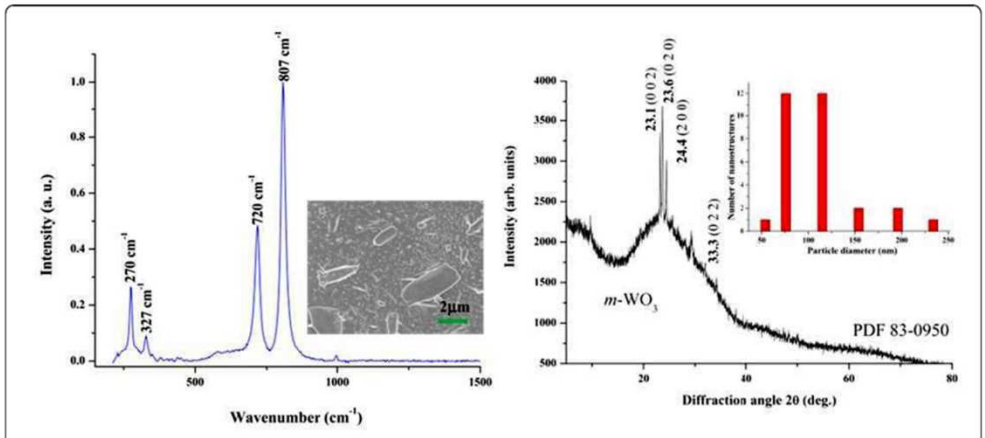


Figure 5 Left: the Raman spectrum of the sample prepared at the 10.48-μm wavelength and 51.2 W/cm^2 power density with a SEM micrograph in the inset showing the morphology. Right: the corresponding XRD spectrum with the histogram of the diameters of a selection of the nanostructures of the corresponding SEM micrograph in the inset. The Raman and XRD suggest a monoclinic phase WO_3.

9.00-9.38 μm (see Figure 4), and despite argon carrier gas presumably broadening the precursor absorption bands to some extent [25], the result could correspond to a non-resonant energy transfer. A 10.48-μm wavelength photon carries 0.1 eV of energy, and so 29 photons are required to dissociate a C-O bond [26] which corresponds to a multi-photon process. It is known, however, that tungsten ethoxide precursor can form WO_3 upon heat treatment [12], which implies that the 10.48-μm wavelength could have had similar effects as annealing had. We believe that the shorter wavelengths, which had higher energy photons, dissociated various bonds which led to the formation of triclinic phase or a mixture of monoclinic and triclinic phase WO_{3-x} where x can vary between 0.1 and 0.3, depending on the laser parameters. It was also observed that the morphology of the samples became more randomized and of a disordered arrangement as the wavelength increased, and this is believed to be an effect of a corresponding decrease in energy.

Unlike the increasing wavelength, the increase in power density led to more ordered and shaped nanostructures, presumably because of the increase in energy rate. The 10.6 μm wavelength appeared to favour the formation of monoclinic phase tungsten oxide Furthermore, it was observed that at high enough power densities, it was more likely for helping nanostructure growth. At such low power densities (17-110 W/cm^2) on the 10.6 μm wavelength, the particle sizes did not show a decrease with increasing power density as predicted [27] for the higher power density range (1-100 kW/cm^2). The nanosphere diameters of this sample were found to be in the range 150-400 nm as depicted in inset of Figure 6. It was observed that the overall particle sizes were smaller for the power variation experiment, while the wavelength variation experiment showed larger particle sizes. The increase in power density did not always favour the formation of WO_3, and since the photon energy was constant, only the number of photons per unit time varied.

Figure 6 shows the Raman and XRD spectra with the corresponding SEM micrograph of a sample prepared at a power density of 85 W/cm^2 at the 10.6-μm wavelength, which appeared to form a monoclinic phase WO_3 according to the characteristic peaks.

Table 1 summarizes all the results obtained for the varying laser parameters. The average particle sizes observed for the wavelength variation was in the range 113-560 nm, while the average particle sizes for the power density variation were in the range 108-205 nm. The compositions of some samples were uncertain, and so it is written as WO_{3-x} where x most likely attains values between 0.1 and 0.3. There were no obvious trends as to how the laser parameters affected the product size or composition, and thus, it is believed that some possible competing reactions taking place during the laser-precursor interaction or during annealing.

Conclusion

Six-sided monoclinic phase $WO_{2.72}$ stars were synthesized by laser pyrolysis technique using a more concentrated starting precursor and near-Gaussian laser beam profile.

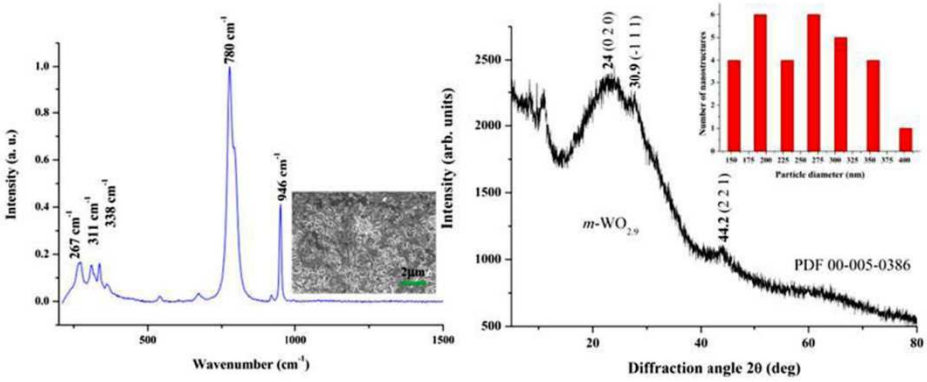


Figure 6 Left: the Raman spectrum of the sample prepared at the 10.6-μm wavelength and 85 W/cm^2 power density with a SEM micrograph in the inset showing the morphology. Right: the corresponding XRD spectrum with the histogram of the diameters of a selection of the nanostructures with the corresponding SEM micrograph in the inset. The Raman and XRD suggest a monoclinic phase WO_{3-x} (x~0.1).

Table 1 A summary of the results obtained for the laser power and wavelength variation

Wavelength Variation ($P_{density}$ = 51.2 W/cm^2)			Power Density Variation (λ = 10.6 μm)		
Wavelength, λ (mm)	*Average sphere particle size (nm)*	*Composition*	*Power Density, P_{peak} (W/cm^2)*	*Average sphere particle size (nm)*	*Composition*
9.22	343	*m/t*-WO_{3-x}	17	157	*m*-WO_{3-x}
9.32	125	*m/t* -WO_{3-x}	26	122	*m*-WO_{3-x}
9.48	113	*m/t* -WO_{3-x}	34	140	*m*-WO_3
9.70	403	*m/t*-WO_{3-x}	43	193	*m*-WO_3
10.16	360	*t*-WO_3	51	108	*m*-WO_{3-x}
10.36	560	*t*-WO_3	60	122	*m*-WO_{3-x}
10.48	347	*m*-WO_3	68	136	*m*-WO_3
10.82	453	*t*-WO_3	77	180	*m*-WO_3
			85	205	*m*-WO_{3-x}
			94	114	*m*-WO_{3-x}
			100	106	*m*-WO_3
			110	128	*m*-WO_3
			2200	100	*m*-$WO_{2.72}$

M, monoclinic phase; *t*, triclinic phase.

The higher concentrated precursors are required to obtain hierarchical structures as predicted by the literature. Laser wavelengths above 10 μm seem to favour the formation of stoichiometric WO_3, but only at certain power densities, presumably to overcome possible competing reactions. Owing to the nature of photochemical reactions and the many stoichiometries and multi-phases that tungsten oxides can form, some product compositions were written as WO_{3-x} where x most probably assumes values between 0.1 and 0.3. The higher power densities were found to be essential for the further growth of structures and for smaller particle sizes. The authors now have an idea of the possible shapes of nanostructures that can be synthesized with possible chemical compositions, and the determination of the electrical and optical properties of these structures to observe possible unique characteristics allows for the tailoring of sensor devices that operate at room temperature for example.

Author details
[1]CSIR National Laser Centre, P. O. Box 395, Pretoria 0001, South Africa [2]School of Physics, University of the Witwatersrand, Private Bag 3, P. O. Wits 2050, Johannesburg, South Africa [3]iThemba Labs, Private Bag 11, Wits 2050, Jan Smuts and Empire Road, Johannesburg, South Africa [4]School of Physics, University of KwaZulu-Natal, Private Bag X54001, Durban 4000, South Africa

Authors' contributions
MG carried out all the experiments in conjunction with LS. MG also initiated the first draft manuscript. BWM assisted with the production of thin films by laser pyrolysis, characterization, analysis, interpretation of experimental results and manuscript handling. AF performed the optical alignment of the laser pyrolysis and discussion of the manuscript. ESH contributed through discussion of the manuscript and RE provided the Raman spectral data from all samples.

Conflicts of interest
The authors declare that they have no conflict of interests.

Received: 25 October 2010 Accepted: 23 February 2011
Published: 23 February 2011

References

1. Bittencourt C, Landers R, Llobet E, Molas G, Correig X, Silva MAP, Sueiris JE, Calderer J: **Effects of Oxygen Partial Pressure and Annealing Temperature on the Formation of Sputtered Tungsten Oxide Films.** *Electrochem Soc* 2002, **149**:H81.
2. Kawasaki H, Namba J, Iwatsuji K, Suda Y, Wada K, Ebihara K, Ohshima T: **NO_x gas sensing properties of tungsten oxide thin films synthesized by pulsed laser deposition method.** *Appl Surf Sci* 2002, **197-198**:547-551.
3. Guidi V, Butturi MA, Blo M, Carotta MC, Galliera S, Giberti A, Malagù C, Martinelli G, Piga M, Sacerdoti M, Vendemiati B: **Aqueous and alcoholic syntheses of tungsten trioxide powders for NO_2 detection.** *Sens Actuators B* 2004, **100**:277.
4. Wang SW, Chou TC, Liu CC: **Nano-crystalline tungsten oxide NO_2 sensor.** *Sens Actuators B* 2003, **94**:343.
5. Wang XP, Yang BQ, Zhang HX, Feng PX: **Tungsten Oxide Nanorods Array and Nanobundle Prepared by Using Chemical Vapor Deposition Technique.** *Nanoscale Res Lett* 2007, **2**:405-409.
6. Rajagopal S, Nataraj D, Mangalaraj D, Djaoued Y, Robichaud J, Khyzhun O: **Controlled Growth of WO_3 Nanostructures with Three Different Morphologies and Their Structural, Optical, and Photodecomposition Studies.** *Nanoscale Res Lett* 2009, **4**:1335-1342.
7. Mwakikunga BW, Forbes A, Sideras-Haddad E, Scriba M, Manikandan E: **Self assembly and properties of C:WO_3 nano-platelets and C:VO_2/V_2O_5 triangular capsules of C:VO_2/V_2O_5 fullerenes and quantum dots produced by laser solution photolysis.** *Nanoscale Res Lett* 2010, **5**:389-397.
8. Mwakikunga BW, Forbes A, Sideras-Haddad E, Arendse C: **Optimization, yield studies and morphology of WO_3 nanowires synthesized by laser pyrolysis in C_2H_2 and O_2 ambients - validation of a new growth mechanism.** *Nanoscale Res Lett* 2008, **3**:372-380.
9. Haggerty JS, Cannon WR: **Sinterable powders from laser-driven reactions.** In *Laser Induced Chemical Reactions*. Edited by: J. I. Steinfield. New York, Plenum Press; 1981:165-241.
10. Mwakikunga BW, Forbes A, Sideras-Haddad E, Erasmus RM, Katumba G, Masina B: **Synthesis of tungsten oxide nanostructures by laser pyrolysis.** *Int J Nanopart* 2008, **1**:185-200.
11. Bowden CM, Stettler JD, Witriol NM: **An excitation model for laser-induced photochemical reactions.** *J Phys B Atom Mol Phys* 1977, **10**:1789.
12. Sakka S: **Handbook of Sol-Gel Science and Technology: Processing, Characterization and Applications.** Boston: Kluwer Academic Publishers; 2004.
13. Lu DY, Chen J, Zhou J, Deng SZ, Xu NS, Xu JB: **Raman spectroscopic study of oxidation and phase transition in $W_{18}O_{49}$ nanowires.** *J Raman Spectrosc* 2007, **38**:176-180.
14. Lu DY, Chen J, Deng SZ, Xu NS, Zhang WH: **The most powerful tool for the structural analysis of tungsten suboxide nanowires: Raman spectroscopy.** *J Mater Res* 2008, **23**:402-408.

Impact factor = 2.894

References

1. Haggerty J.S., Cannon W.R., Sinterable powders from laser-driven reactions, In J. I. Steinfield (Ed) Laser Induced Chemical Reactions, New York, Plenum Press; 1981, pp. 165-241.

2. Mwakikunga B.W., Forbes, A., Sideras-Haddad, E., Erasmus, R.M., Katumba, G., and Masina B. Synthesis of tungsten oxide nanostructures by laser pyrolysis, *Int. J. Nanoparticles*, Vol. 1, No. 3, 2008, pp. 195.

3. Boulova, M., and Lucazeau, G. Crystallite Nanosize Effect on the Structural Transitions of WO_3 Studied by Raman Spectroscopy, *Journal of Solid State Chemistry*, **167**, 2002, pp. 425-434.

4. Cele, L.M., Ray, S.S., and Coville, N.J. Nanoscience and Nanotechnology in South Africa, *South African Journal of Science*, vol. 105, No. 7/8, 2009.

5. Hornyak, G.L., Dutta, J., Tibbals, H.F., and Rao, A.K. Introduction to Nanoscience, CRC Press, Taylor and Francis Group, 2008.

6. Rempel, A.A., Nanotechnologies: Properties and applications of nanostructured materials, *Russian Chemical Reviews*, **76** (5), 2007, pp. 435-461.

7. Caltech Engineering and Science, **23** (5), 1960, pp. 22-36.

8. Buzea, C., Pacheco, I., and Robbie, K. Nanomaterials and Nanoparticles: Sources and Toxicity, *Biointerphases*, **2** (4), 2007, pp. MR17-MR71.

9. Tikhomirov, V., and Lidor, A. Notes on Electrolysis, *Journal of Russian Physical Chemistry Society*, **15**, 1883, pp. 421-423.

10. Gunther, B., and Kampman, A. Ultrafine oxide powders prepared by inert gas evapouration, *Nanostruc. Mater.* **1**, 1992, pp. 27-30.

11. Faraday, M. Experimental Relations of Gold (and Other Metals) to Light, Philos. Trans. R. Soc. London **147**, 1857, pp. 145.

12. Wade, T., Park, J., Garza, E.G., Ross, C.B., Smith, D.M., and Crooks, R.M. Synthesis of Aluminium Nitride Nanopowder by Gas-Reduction-Nitridation Method, *J. Am. Chem. Soc.*, **114**, 1992, pp.9457.

13. Butyagin, P.Y. *Usp. Khim.*, **63**, 1994, pp. 1031.

14. De Carli, P.S. Formation of Diamond by Explosive Shock, *J C Jamieson Science*, **133**, 1961, pp. 1821.

15. Merzanov, A.G., and Sharivker, S.Y. Self-Propagating High-Temperature Synthesis of Carbides, Nitrides and Borides, Kluwer Academic, 1999, pp. 205.

16. Gleiter, H. Deformation of Polycrystals: Mechanisms and Microstructures, Roskilde, Denmark: Risø Natl. Laboratory, 1981, 15.

17. Herth, S., Rosner, H., Rempel, A.A., Schaefer, H-E., and Wurschum, R. Z. Metallkd., **94**, 2003, pp. 1073.

18. Smirnova, N.A., Levit, V.I., Pilyugin, V.P., Kuznetsov, R.I., and Degtyarev, M.V. *Fiz. Met. Metalloved.*, **62**, 1986, pp. 566.

19. Martynyuk, M.M. *Zh. Tekhn. Fiz.*,**44**, 1974, pp.1262.

20. Worthy, W. Coulomb Explosion Techniques Unlocks Molecular Ion Secrets, *American Chemical Society*, **65**(49), 1987, pp. 25-28.

21. Mwakikunga, B.W., Forbes, A., Sideras-Haddad, E., and Arendse, C. Optimization, Yields Studies and Morphology of WO_3 Nano-Wires Synthesized by Laser Pyrolysis in C_2H_2 and O_2 Ambients-Validation of a New Growth Mechanism, *Nanoscale Res Lett*, **3,** 2008, pp. 372–380.

22. Salem, A.K., Searson, P.C., and Leong, K.W. Multifunctional nanorods for gene delivery, *Nature Materials*, 2, 2003, pp. 668–671.

23. Wang, Z., Daemen, L.L., Zhao, Y., Zha, C.S., Downs, R.T., Wang, X., Wang, Z.L., and Hemley, R.J. Morphology-tuned wurtzite-type ZnS nanobelts, *Nature Materials*, 4, 2005, pp. 922–927.

24. Zheng, L.X., O'Connell, M.J., Doorn, S.K., Liao, X.Z., Zhao, Y.H., Akhadov, E.A., Hoffbauer, M.A., and B. Roop, J. Ultralong Single-Wall Carbon Nanotubes, *Nature Materials* **3** (10), 2004, pp. 673–676.

25. Jiao, L., Zhang, L., Wang, X., Diankov, G., and Dai, H. Narrow graphene nanoribbons from carbon nanotubes, *Nature* **458**, 2009, pp. 877-880.

26. Du, J., Liu, Z., Li, Z., Han, B., Sun, Z., and Huang, Y. Carbon nanoflowers synthesized by a reduction–pyrolysis–catalysis route, *Material Letters*, **59**, 2005, pp. 456-458.

27. Kharissova, O.V., Kharisov, B.I., Garcia, T.H., and Méndez, U.O. A Review on Less-common Nanostructures, *Synthesis and Reactivity in Inorganic, Metal-Organic, and Nano-Metal Chemistry*, **39**, 2009, pp. 662-684.

28. Polleux, J., Pinna, N., Antonietti, M., and Niederberger, M. Growth and Assembly of Crystalline Tungsten Oxide Nanostructures Assisted by Bioligation, *J. AM. CHEM. SOC.*, **127**, 2005, pp. 15595-15601.

29. Lassner, E., and Schubert, W. Tungsten: Properties, Chemistry, Technology of the Element, Alloys, and Chemical Compounds, Kluwer Academic, 1999.

30. Lee., W.J. Effects of surface porosity on tungsten trioxide (WO3) films electrochromic performance, *Journal of Electronic Materials*, **29**, 2000, pp. 183.

31. Tungsten trioxide, *The Merck Index*, Vol. 14, 2006.

32. Patnaik, P. Handbook of Inorganic Chemical Compounds, McGraw-Hill, 2003.

33. Vijayalakshmi, R. Jayachandran, M., and Sanjeeviraja, C. Structural, electrochromic and FT-IR studies on electrodeposited tungsten trioxide films, *Current Applied Physics*, **3**, 2003, pp. 171-175.

34. http://www.3rd1000.com/elements/Tungsten.htm (2010-01-11)

35. Xin-Sheng, Y., Yu, W., Liang, D., Li-Zhen, Q., and Feng, Z. Defect and electrical properties of nanocrystalline tungsten trioxide, *Chin. Phys. Soc. and IOP Publishing Ltd*. Vol 13, No. 9, 2004, pp. 1516-1519.

36. Sun, Q., Rao, B.K., Jena, P., Stolcic, D., Kim, Y.D., Gantefor, G., and Castleman Jr., A.W. Appearance of bulk properties in small tungsten oxide clusters, *Journal of Chemical Physics* **121** (19), 2004, pp. 9417-9422.

37. Sharma, N., Deepa, M., Varshney, P., and Agnihotry, S.A. FTIR and absorption edge studies on tungsten oxide based precursor materials synthesized by sol-gel technique, *Journal of Non-Crystalline Solids*, **306**, 2002, pp. 129-137.

38. El-Batal, F.H. Gamma ray interaction with lithium borate glasses containing WO_3, *Indian Journal of Pure & Applied Physics*, **47**, 2009, pp. 471-480.

39. Huang, X., Zhai, H., Li J., and Wang, L. On the Structure and Chemical Bonding of Tri-Tungsten Oxide Clusters $W_3O_n^-$ and W_3O_n (n = 7-10): W_3O_8 As A Potential Molecular Model for O-Deficient Defect Sites in Tungsten Oxides, *J. Phys. Chem. A* **110**, 2006, pp. 85-92.

40. Sun, S., Zou, Z., and Min, G. Synthesis of bundled tungsten oxide nanowires with controllable morphology, *Materials Characterization*, **60**, 2009, pp. 437-440.

41. Blyholoerand, G., and Tanaka, M. Infrared Spectra of CO and O_2 Adsorbed on Tungsten, *Bulletin of the Chemical Society of Japan*, Vol. 46, 1973, pp. 1876-1878.

42. Lemire, C., Lollman, D.B.B., Al Mohammad, A., Gillet, E., Aguir, K. Reactive R. F. Magnetron sputtering deposition of WO_3 thin films. *Sensores and Actuators B*, **84**, 2002, pp. 43-48.

43. Rajeswari, J., Viswanathan, B., and Varadarajan, T.K. Tungsten trioxide nanorods as supports for platinum in methanol oxidation, *Materials Chemistry and Physics*, **106**, 2007, pp. 168-174.

44. Choi, H.G., Jung, Y.H., and Kim, D.K. Solvothermal Synthesis of Tungsten Oxide Nanorod/Nanowire/Nanosheet, *J. Am. Ceram. Soc.* **88** (6), 2005, pp. 1684-1686.

45. Mwakikunga, B.W., Sideras-Haddad, E., Arendse, C., Witcomb, M.J., and Forbes, A. WO_3 Nano-Spheres into $W_{18}O_{49}$ One-Dimensional Nano-Structures Through Thermal Annealing, *J. Nanosci. Nanotechnol.,* **8**, 2008, pp. 1-9.

46. Bachmann, H.R., Noth, H., Rinck, R., and Kompa, K.S. BCl_3 by laser synthesis, *Chem. Phys. Lett.* **29**, 1975, pp. 627.

47. Allen, S.D. Direct-Write Pyrolytic Laser Depostion, *IEEE Circuits And Devices Magazine*, 1986, pp. 32-36.

48. Mwakikunga, B.W., Sideras-Haddad, E., Forbes, A., and C. Arendse, Raman spectroscopy of WO_3 nano-wires and thermo-chromism study of VO_2 belts produced by ultrasonic spray and laser pyrolysis techniques, *Phys. Stat. Sol. (a)*, **205**, No. 1, 2008, pp. 150-154.

49. Li-Bin, L., Tie-Cheng, L., Yong, L., and Qiang, L. Variation of morphology and color of VO_2 thin filmsinduced by excimer laser, *Nuclear Instruments and Methods in Physics Research B*, **191**, 2002, pp. 102-105.

50. Von Hoesslin, M., Förster, J., Schäfer, J.H., and Uhlenbusch, J. CARS diagnostics of a CO_2-laser pyrolytic experiment for the production of nanosized ceramic powders, *Appl. Phys. B*, **61**, 1995, pp. 367-375.

51. Förster, J., Von Hoesslin, M., and Uhlenbusch, J. Temperature measurements in CO_2-laser-induced pyrolysis flames for SiC and tenary SiC/C/B powder synthesis by means of CARS, *Appl. Phys. B*, **62**, 1996, pp. 609-612.

52. Huisken, F., Kohn, B., Alexandrescu, R., Cojocaru, S., Crunteanu, A., Ledoux, G., and Reynaud, C. Silicon carbide nanoparticles produced by CO_2 laser pyrolysis of SiH_4/C_2H_2 gas mixtures in a flow reactor, *Journal of Nanoparticle Research*, **1**, 1999, pp. 293-303.

53. Herlin-Boime, N., Vicens, J., Dufour, C., Ténégal, F., Reynaud, C., and Rizk, R. Flame temperature effect on the structure of SiC nanoparticles grown by laser pyrolysis, *Journal of Nanoparticle Research*, **6**, 2004, pp. 63-70.

54. Leconte, Y., Maskrot, H., Herlin-Boime, N., Porterat, D., Reynaud, C., Swiderska-Sroda, A., Grzanka, E., Gierlotka, S., and Palosz, B., Elaboration of SiC, TiC, and ZrC Nanopowders by Laser Pyrolysis: From Nanoparticles to Ceramic Nanomaterials, *Glass Physics and Chemistry*, Vol. 31, No. 4, 2005, pp. 510-518.

55. Combemale, L., Leconte, Y., Portier, X., Herlin-Boime, N., and Reynaud, C. Synthesis of nanosized zirconium carbide by laser pyrolysis route, *J. Alloys Compd.*, **483**, 2009, pp. 468.

56. Veintemillas-Verdaguer, S., Morales, M.P., and Serna, C.J. Continuous production of γ-Fe_2O_3 ultrafine powders by laser pyrolysis, *Materials Letters*, **35**, 1998, pp. 227-231.

57. Huisken, F., Kohn, B., Alexandrescu, R., and Morjan, I. Mass spectrometric characterization of iron clusters produced by laser pyrolysis and photolysis of $Fe(CO)_5$ in a flow reactor, *Eur. Phys. J. D*, **9**, 1999, pp. 141-144.

58. Alexandrescu, R., Morjan, I., Voicu, I., Dumitrache, F., Albu, L., Soare, I., and Prodan, G. Combining resonant/non-resonant processes: Nanometer-scale iron-based material preparation via CO_2 laser pyrolysis, *Applied Surface Science*, **248**, 2005, pp. 138-146.

59. Jäger, C., Mutschke, H., Huisken, F., Alexandrescu, R., Morjan, I., Dumitrache, F., Barjega, R., Soare, I., David, B., and Schneeweiss, O. Iron-carbon nanoparticles prepared by CO_2 laser pyrolysis of toluene and iron pentacarbonyl, Appl. Phys. A, **85**, 2006, pp. 53-62.

60. Tomescu, A., Alexandrescu, R., Morjan, I., Dumitrache, F., Gavrila-Florescu, L., Birjega, R., Soare, I., Prodan, G., Bastl, Z., Galikova, A., and Pola, J. Structural and sensing properties of a novel Fe/Fe_2O_3/polyoxocarbosilane core shell nanocomposite powder prepared by laser pyrolysis, J. Mater. Sci., **42**, 2007, pp. 1838-1846.

61. Dumitrache, F., Alexandrescu, R., Morjan, I., Sandu, I., Soare, I., Voicu, I., Fleaca, C.T., Plascaru, M., Savoiu, M., Vasile, E., and Ciupina, V. Mixed phases of TiO_2 nanopowders prepared by laser pyrolysis, *Proc. Of SPIE*, Vol. 5581, 2004, pp. 292-296.

62. Alexandrescu, R., Dumitrache, F., Morjan, I., Sandu, I., Savoiu, M., Voicu, I., Fleaca, C., and Piticescu, R. TiO_2 nanosized powders by $TiCl_4$ laser pyrolysis, *Nanotechnology*, **15**, 2004, pp. 537-545.

63. Scarisoreanu, M., Morjan, I., Alexandrescu, R., Birjega, R., Voicu, I., Fleaca, C., Popvici, E., Soare, I., Gavrila-Florescu, L., Cretu, O., Prodan, G., Ciupina, V., and Figgemeier, E. Effects of some synthesis parameters on the structure of titiania nanoparticles obtained by laser pyrolysis, *Applied Surface Science*, **253**, 2007, pp. 7908-7911.

64. Figgemeier, E., Kylberg, W., Constable, E., Scarisoreanu, M., Alexandrescu, R., Morjan, I., Soare, I., Birjega, R., Popovici, E., Fleaca, C., Gavrila-Florescu, L., and Prodan, G. Titanium dioxide nanoparticles prepared by laser pyrolysis: Synthesis and photocatalytic properties, *Applied Surface Science*, **254**, 2007, pp. 1037-1041.

65. Alexandrescu, R., Scarisoreanu, M., Morjan, I., Birjega, R., Fleaca, C., Luculescu, C., Soare, I., Cretu, O., Negrila, C.C., Lazarescu, N., and Ciupina, V. Preparation and characterization of nitrogen-doped TiO_2 nanoparticles by the laser pyrolysis of N_2O-containing gas mixtures, *Applied Surface Science*, **255**, 2009, pp. 5373-5377.

66. Huisken, F., Ledoux, G., Guillois, O., and Reynaud, C. Light-Emitting Silicon Nanocrystals from Laser Pyrolysis, *Adv. Mater.*, **14**, No. 24, 2002, pp. 1861-1865.

67. Li, X., He. Y., Talukda, S.S., and Swihart, M.T. Process for Preparing Macroscopic Quantities of Brightly Photoluminescent Silicon Nanoparticles with Emission Spanning the Visible Spectrum, *Langmuir*, **19**, 2003, pp. 8490-8496.

68. Trave, E., Bello, V., Mattei, G., Mattiazzi, M., Borsella, E., Carpanese, M., Fabbri, F., Falconieri, M., D' Amato, R., and Herlin-Boime, N. Surface control of optical properties in silicon nanocrystals produced by laser pyrolysis, *Applied Surface Science*, **252**, 2006, pp. 4467-4471.

69. Sublemontier, O., Lacour, F., Leconte, Y., Herlin-Boime, N., and Reynaud, C. CO_2 laser-driven pyrolysis of silicon nanocrystals and applications, *J. Alloys Compd.*, **483**, 2009, pp. 499-502.

70. Bi, X., Lee, W., and Eklund, P.C. Laser Pyrolysis Production of Nanoscale Carbon Black, *American Chemical Society*, **205**, 1993, pp. 444-451.

71. Galvez, A., Herlin-Boime, N., Reynaud, C., Clinard, C., and Rouzaud, J.–N. Carbon nanoparticles from laser pyrolysis, *Carbon*, **40**, 2002, pp. 2775-2789.

72. Morjan, I., Voicu, I., Dumitrache, F., Sandu, I., Soare, I., Alexandrescu, R., Vasile, E., Pasuk, I., Brydson, R.M.D., Daniels, H., and Rand, B. Carbon nanopowders from the continuous-wave CO_2 laser-induced pyrolysis of ethylene, *Carbon*, **41**, 2003, pp. 2913-2921.

73. Kim, Y.J., Lee, S., Pikhitsa, P., and Choi, M. Laser induced transition from soot generation to shell shaped carbon nanoparticles in an acetylene flow: aerosol characterization, *Journal of Mechanical Science and Technology*, **22**, 2008, pp. 134-140.

74. Morjan, I., Soare, I., Alexandrescu, R., Gavrila-Florescu, L., Morjan, R.–E., Prodan, G., Fleaca, C., Sandu, I., Voicu, I., Dumitrache, F., and Popvici, E. "Carbon nanotubes grown by catalytic CO_2 laser-induced chemical vapour deposition on core-shell Fe/C composite nanoparticles", *Infrared Physics and Technology*, **51**, 2008, pp. 186-197.

75. Llamas-Jansa, I., Jäger, C., Mutschke, H., and Henning, T. Far-ultraviolet to near-infrared optical properties of carbon nanoparticles produced by pulsed-laser pyrolysis of hydrocarbons and their relation with structural variations, *Carbon*, **45**, 2007, pp. 1542-1557.

76. Bystrzejewski, M., Lange, H., Huczko, A., Baranowski, P., Hübers, H.–W., Gemming, T., Pichler, T., Büchner, B., and Rümmeli, M.H. One-step catalyst-free generation of carbon nanospheres via laser-induced pyrolysis of anthracene, *Journal of Solid State Chemistry*, **181**, 2008, pp. 2796-2803.

77. Flynn, G.W., Parmenter, C.S., and Wodtke, A.M. Vibrational energy transfer, *Journal of Physical Chemistry*, Vol. 100, No. 31, 1996, pp. 12817-12838.

78. El-Diasty, F. Simulation of CO_2 laser pyrolysis during preparation of SiC nanopowders, *Optics Communications*, **241**, 2004, pp. 121-135.

79. Bomatí-Miguel, O., Zhao, X.Q., Martelli, S., Di Nunzio, P.E., and Veintemillas-Verdaguer, S. Modeling of the laser pyrolysis process by means of the aerosol theory: Case of iron nanoparticles, *Journal of Applied Physics*, **107**, 2010, pp. 0149061-0149067.

80. Botcher, T.R., and Wight, C.A. Transient Thin Film Laser Pyrolysis of RDX, *J. Phys. Chem.*, **97**, 1993, pp. 9149-9153.

81. Peters, G., Jerg, K., and Schramm, B. Characterization of chromium (III) oxide powders prepared by laser-induced pyrolysis of chromyl bromide, *Materials Chemistry and Physics*, **55**, 1998, pp. 197-201.

82. Poondi, D., Dobbins, T., and Singh, J. A novel laser-liquid-solid interaction technique for synthesis of silver, nickel and immisciblesilver-nickel alloys from liquid precursors, *Journal of Materials Science*, **35**, 2000, pp. 6237-3243.

83. Pingali, K.C., Deng, S., Rockstraw, D.A. Direct synthesis of Ru-Ni core-and-shell nanoparticles by spray-pyrolysis: Effects of temperature and precursor constituent ratio, *Powder Technology*, **183**, 2008, pp. 282-289.

84. Bell, J.P., Edwards, R.V., Nott, B.R., and Angus, J.C. Pyrolysis of Ethylene with 10.6-Micron Laser Radiation, *Ind. Eng. Chem. Fundamen.*, **13** (1), 1974, pp. 89-91.

85. Boyd, R.W. Nonlinear Optics, Academic Press Elsevier, 3rd Edition, 2008.

86. Roberts, R., Ouellette, R.P., Muradaz, M.M., Cozzens, R.F., and Cheremisinoff, P.N. Applications of Photochemistry, TECHNOMIC Publishing Co., Inc. 1984.

87. Guillet, J. Polymer photophysics and photochemistry: an introduction to the study of photoprocesses in macromolecules, CUP Archive-Technology and Engineering, 1987.

88. Wells, C.H.J. Introduction to Molecular Photochemistry, Chapman and Hall Chemistry Textbook Series, 1972.

89. Andrews, D.L. Lasers in Chemistry, Springer, 3rd Edition, 1997.

90. Markovich, R.J., and Pidgeon, C. Introduction to Fourier Transform Infrared Spectroscopy and Applications in the Pharmaceutical Sciences, *Pharmaceutical Research*, Vol. 8, No. 6, 1991, pp. 663-674.

91. Haynes, W., and Loudon, R. Scattering of light by crystals, Wiley, New York, 1978.

92. Cullity, B.D. Elements of X-Ray Diffraction, 2nd Ed., Addison-Wesley, Don Mills Canada, 1978.

93. Egerton, R.F. Physical Principles of Electron Microscopy: An Introduction to TEM, SEM, and AEM, Springer Science, Business Media Inc. 2005.

94. Long, D.A. Introduction to Raman Spectroscopy, *Cambridge Royal Society of Chemistry*, 2005, pp. 17-40.

95. Raman, C.V. The molecular scattering of light, *Nobel Lecture*, 1930, pp. 267-275.

96. Raman, C.V., and Krishnan, K.S. A New Type of Secondary Radiation, *Nature*, 1928, pp. 501-502.

97. Santiago Rivera, M.A. Operating the Siemens XRD Diffraktometer D5000 (Manual), http://geology.uprm.edu/facilities/xrdforms/SOP-Siemens-XRD-Diffraktometer-D5000.pdf

98. Csele, M. Fundamentals Of Light Sources And Lasers, John Wiley and Sons Inc. Hoboken, New Jersey, 2004.

99. spaceplace.nasa.gov/en/kids/**laser**/index.shtml

100. Patel, C. Continuous wave laser action on vibrational rotational transition of CO_2, *Physics Review*, **136A**, 1964, pp. 1187-1193.

101. Patel, C. High Power Carbon Dioxide Lasers: An excellent introduction to the CO_2 laser, *Scientific American*, T1-S5, 1968.

102. Wright, D., Greve, P., Fleischer, J., and Austin, L. Laser beam width, divergence and beam propagation factor – an international standardization approach, *Opt. Quantum Electron*, **24**, 1992, pp. 993–1000.

103. Chapple, P.B. Beam waist and M^2 measurement using a finite slit, *Optical Engineering*, **33**(7), 1994, pp. 2461-2466.

104. Pyrocam III Operators Manual, Ophir-Spiricon Inc., Version 1.06, Manual No. 10903-001, 2008.

105. Mellendorf, K. EM Waves and Polarization, *Physics Archive*, 2004.

106. http://www.macken.com/CO_2.shtml (2010-01-20).

107. Sublemontier, O., Lacour, F., Leconte, Y., Herlin-Boime, N., and Reynaud, C. CO_2 laser-driven pyrolysis synthesis of silicon nanocrystals and applications, *Journal of Alloys and Compounds* 483, 2009, pp. 499-502.

108. Sakka, S. Handbook of sol-gel science and technology: processing, characterization and applications, Boston: Kluwer Academic Publishers, 2004.

109. Glockler, G. Carbon Halogen Bond Energies and Bond Distances, *J. Phys. Chem*, **62** (9), 1958, pp. 1049-1054.

110. Solonin, Y.M., Khyzhun, O.Yu., and Graivoronskaya, E.A. Nonstoichiometric Tungsten Oxide Based on Hexagonal WO_3. *Crystal Growth & Design*, **1** (6), 2001, pp. 473-477.

111. Gillet, M., Delamare, R., and Gillet, E. Structure and electrical conduction of WO_3 nanorods grown on mica, *Eur. Phys. J*, D **43**, 2007, pp. 295-298.

112. Cullity, B.D. Elements of X-Ray Diffraction, *Addison-Wesley Publishing Company, Inc.*, 2nd Edition, year.

113. Nonaka, K., Takase, A., and Miyakawa, K. Raman spectra of sol-gel-derived tungsten oxides, *Journal of Materials Science Letters*, **12**, 1993, pp. 274-277.

114. Baserga, A., Russo, V., Di Fonzo, F., Bailini, A., Cattaneo, D., Casari, C.S., Li Bassi, A., and Bottani, C.E. Nanostructured tungsten oxide with controleed properties: Synthesis and Raman caharacterization, *Thin Solid Films*, **515**, 2007, pp. 6465-6469.

115. Lu, D.Y., Chen, J., Deng, S.Z., Xu, N.S., and Zhang, W.H. The most powerful tool for the structural analysis of tungsten suboxide nanowires: Raman spectroscopy, *J. Mater. Res.*, **23** (2), 2008, pp. 402-408.

116. Govender, M., Shikwambana, L., Mwakikunga, B.W., Sideras-Haddad, E., Erasmus, R.M., and Forbes, A. Formation of tungsten oxide nanostructures by laser pyrolysis: stars, fibres and spheres, *Nanoscale Research Letters*, **6** (166), 2011, pp. 1-8.